DIAGRAMMATIC MANY-BODY METHODS FOR ANHARMONIC MOLECULAR VIBRATIONAL PROPERTIES

BY

MATTHEW R. HERMES

DISSERTATION

Submitted in partial fulfillment of the requirements
for the degree of Doctor of Philosophy in Chemistry
in the Graduate College of the
University of Illinois at Urbana-Champaign, 2015

Urbana, Illinois

Doctoral Committee:

Professor So Hirata, Chair
Professor Nancy Makri
Professor Catherine Murphy
Professor Josh Vura-Weis

Abstract

Diagrammatic many-body methods for computing the energies and other properties of anharmonic vibrations have been developed based on the Dyson equation formalism for the single-particle vibrational Green's function and the many-body perturbation theory for the total zero-point energy. Unlike similar methods based on the vibrational self-consistent field (VSCF) approximation, these XVSCF and XVMP2 methods are guaranteed to be size-consistent at the formalism level, meaning that they are applicable not only to small molecules but also to larger systems including condensed phases.

The XVSCF method, initially developed by Keçeli and Hirata, is extended to calculate anharmonic corrections to geometries as well as vibrational frequencies and energies, and rendered identical to the VSCF method in the thermodynamic limit despite orders of magnitude lower computational cost. When XVSCF is formulated in terms of the Dyson equation, it is additionally revealed to be an approximation to the self-consistent phonon (SCP) method which is commonly used in solid-state physics. Furthermore, the development of XVSCF in terms of Green's functions enables the formulation of the concept of Dyson coordinates and Dyson geometries, conceived as anharmonic generalizations of the normal coordinates and equilibrium geometries of the harmonic approximation, which represent a formally exact effectively harmonic treatment of molecular and crystal vibrations, similar to the concept of Dyson orbitals from the field of electronic structure theory.

Many-body perturbation theory based on XVSCF is referred to as XVMP2 and is showed to be both more efficient and more powerful than standard VMP2 methods. XVMP2 inherits the computational efficiency and manifest size-consistency of XVSCF, and additionally, through the Dyson-equation formalism, it is able to directly compute vibrational fundamental, overtone, and combination frequencies directly even in the presence of anharmonic resonance. This makes XVMP2 a rare example of a perturbative method which can defeat strong correlation.

The XVSCF and XVMP2 methods are formulated in both deterministic algorithms which rely on the computation of a large number of anharmonic force constants, and stochastic algorithms which require no stored representation of the PES. This is a significant advance because the computation and storage of the PES is a significant bottleneck in terms of accuracy and computational cost. The Monte Carlo XVSCF and Monte Carlo XVMP2 methods, as they are called, are uncommon among stochastic methods in that they can compute anharmonic frequencies directly, without

noisy, small differences between large total vibrational energies and without sign problems that plague other forms of quantum Monte Carlo such as DMC.

To those who find joy in this world.

Acknowledgments

I first must acknowledge my advisor, So Hirata, whose guidance, insight, and inspiration both pushed and pulled me forward throughout the last four years. His genuine fascination with his field reinforced and alloyed mine, and his patience with my learning process helped to drive my success.

I also must acknowledge my past and present colleauges in the Hirata group, who not only helped me tackle difficult scientific problems, but also helped me feel at home while at work. Seni, Murat, Kiyoshi, Jacob, Alex, Misha, Ryan, Cole, Xiao, and everyone else assisted me both in figuring out what to make of those tricky semi-reducible diagrams and in blowing off steam through fascinating philosophical conversation. Murat Keçeli and Kiyoshi Yagi especially are largely responsible for the whole existence of my thesis, having laid the groundwork before I joined the Hirata group, and I owe them a great deal.

My previous advisors, including Roman Boulatov and Keith Kuwata, also provided invaluable guidance and as I was beginning my scientific career and I most certainly owe them for a great deal of mentoring. Additionally, my friendly and helpful colleagues throughout the Chemistry department at the University - including but not limited to Tyler Takeshita, Lu Xu, Ben McCall, and many others - are simply too numerous to name. Most importantly, they have kept me connected with the enormous breadth and depth of chemical and physical inquiry going on in this department that is outside my narrow little focus. Everyone's eagerness to share their science and to share their passion helped keep the metaphorical fires lit.

My friends and family outside the department also proved endlessly supportive. My mother has routinely offered helping hands with my living situation which proved absolutely essential to my ability to make progress on my work. My friends in Urbana-Champain have made me feel astonishingly at home here, for which I am inexpressibly grateful.

Table of Contents

List of Abbreviations

AVM	Antithetic variate method.
CC	Coupled cluster.
CI	Configuration interaction.
CPU	Central processing unit.
HF	Hartree–Fock.
MBPT	Many-body perturbation theory.
MP	Møller-Plesset.
MPI	Message-Passing Interface.
PES	Potential energy surface.
QFF	Quartic force field.
RSPT	Rayleigh–Schrödinger perturbation theory.
SCP	Self-consistent phonon.
VCI	Vibrational configuration interaction.
VCC	Vibrational coupled cluster.
VH	Vibrational harmonic (perturbation theory; of a form defined in Chapter 4).
VMP	Vibrational Møller–Plesset.
VPT	Vibrational perturbation theory (based on the harmonic approximation, conventional form).
VSCF	Vibrational self-consistent field.
XVSCF	Size-extensive vibrational self-consistent field.
ZPE	Zero-point energy.

Chapter 1

Introduction

The vibrational motion of nuclei in molecules and solids is fundamentally a quantum-mechanical phenomenon and is described by the Schrödinger equation with a high-rank many-body Hamiltonian operator. Sophisticated quantum-mechanical simulations are necessary to surpass the accuracy of the harmonic approximation in reproducing or predicting, for example, infrared and Raman spectra as well as vibrationally averaged properties. For systems with a few atoms, it is now feasible to perform nearly exact variational calculations of vibrational wave functions using efficient diagonalizers such as the Lanczos algorithm and compact representations of the potential energy surface (PES) such as the discrete variable representation.[1–3] However, for larger molecules or solids, these brute-force methods are infeasible and systematic hierarchies of approximations with different cost-accuracy trade-offs are required for practical calculations.

The hierarchies of methods developed for treating the electronic structure problem, such as Hartree–Fock (HF), Møller–Plesset perturbation (MP), coupled-cluster (CC), and configuration-interaction (CI) methods, have been adapted for the vibrational structure problem. The vibrational self-consistent field (VSCF) method,[4–6] analogous to the HF method, variationally minimizes a trial wave function composed of a single Hartree product of one-dimensional vibrational wave functions. The vibrational Møller–Plesset (VMP) method[7–9] uses the Rayleigh–Schrödinger perturbation theory (RSPT)[10] with the VSCF wave function as a reference. Vibrational CC (VCC)[11–15] and vibrational CI (VCI)[16] based on a VSCF reference wave function have also been implemented.

However, there are two critical problems affecting the formal and practical aspects of all of these methods. The first is the problem of size consistency. According to thermodynamics, observable quantities of chemical systems are either extensive (i.e. with numerical values asymptotically proportional to K^1, where K represents the size of the system) or intensive (numerical values asymptotically proportional to K^0). Extensive properties include total energy or mass, and intensive properties include excitation energies or temperature. In order to be meaningfully applicable to large molecules or solids, any approximate treatment of a many-body electronic or vibrational wave function must reproduce these size dependencies, i.e., must be size consistent. This can be assessed most expediently if the equations for observables using a given method can be expressed in the form of Feynman-Goldstone diagrams.[17] With a few exceptions,[12–15,18,19] however, the vibrational many-body methods mentioned above are defined in terms of

first quantization, i.e., formalisms derived using vibrational equivalents of Slater-Condon rules, which offers no insight into size consistency. An investigation of the equations of the VSCF method has revealed that this method lacks size consistency:[20] the equations for total energy and vibrational frequencies contain many terms which asymptotically vanish in the thermodynamic limit, so that there is a large wastage in the evaluation of these quantities for large molecules or solids, and the accuracy of the VSCF approximation differs for systems of different sizes. This is the case not only with VSCF, but also in any 'correlation' method which uses the VSCF wave function as a reference.

The second issue is the treatment of the PES. Most anharmonic vibrational methods suffer from the requirement of a stored representation of the PES, which must be evaluated prior to performing the vibrational calculation. This is generally a high-dimensional array, such as a set of high-rank force constants or numerical values of the PES on a grid, which becomes too massive to evaluate or store for large molecules and solids. It is necessary to completely eliminate this computational bottleneck.

Here, we review several new methods we have developed during the past few years which are designed to address these two critical issues. The remainder of this chapter introduces background information. In Sec. 1.1, we derive the vibrational Schrödinger equation and discuss the form of the vibrational Hamiltonian operator as well as the harmonic approximation. In Sec. 1.2, we discuss the standard VSCF method, it's shortcomings from the perspective of size-consistency, and the manifestly size-consistent form of VSCF known as XVSCF(n) which was developed by Keçeli and Hirata in 2011, which can calculate anharmonic corrections to total energies and vibrational frequencies, but not geometries.[21] In Sec. 1.3, we describe the diagrammatic formalism of the vibrational Green's function and Dyson self-energies[10,22–26] for vibrational frequencies and the many-body perturbation theory (MBPT)[27] for zero-point energies (ZPE) which is used to expand XVSCF and to develop new vibrational many-body methods throughout the rest of this document, and which guarantees size-consistency through the use of linked diagrams.[17,28,29]

Chapter 2 discusses an extension to the XVSCF method to allow it to calculate anharmonic corrections to geometries, and introduces the XVSCF[n] method, which unlike XVSCF(n) is identical to the standard VSCF method in the bulk (or "thermodynamic") limit, but is vastly more computationally efficient.[30] Chapter 3 compares XVSCF(n), XVSCF[n], and the self-consistent phonon (SCP) method of solid-state physics[31,32] in terms of the different approximations each makes to the Dyson self-energies and introduces the concepts of Dyson coordinates and Dyson geometries, vibrational counterparts to the Dyson orbitals[33,34] of electronic structure theory.[35] Chapter 4 introduces second-order size-extensive vibrational Møller-Plesset perturbation (XVMP2) methods for anharmonic total energies and vibrational frequencies. XVMP2 can compute frequencies directly and in a size-consistent manner, unlike VMP2, which computes them as small differences between the ground and excited state energies. By solving the Dyson equation self-consistently with frequency-dependent Dyson self-energies, XVMP2 can calculate frequencies of not only fundamentals but also overtones and combinations from a single equation. It also resists divergence in the presence

of resonances.[36] Chapters 5 and 6 discuss alternate stochastic algorithms for XVSCF and XVMP2, designed to address the issues of the PES calculation, denoted as Monte Carlo XVSCF (MC-XVSCF) and Monte Carlo XVMP2 (MC-XVMP2).[37,38] They do away with any explicit references to anharmonic force constants and require only the values of the PES obtained on the fly during a Metropolis walk[39] over the PES. MC-XVSCF and MC-XVMP2 belong to a new branch of quantum Monte Carlo (QMC),[40–43] in which the theoretical advantages of systematic, convergent hierarchies of many-body electronic and vibrational methods are wed to the algorithmic advantages of highly parallel-scalable QMC methods.[44–55]

Together, these developments represent significant theoretical progress towards performing practical many-body vibrational calculations on large molecules and, in the future, condensed-phase systems using cutting-edge high-performance computing resources.

1.1 The Schrödinger equation for vibrations of molecules and crystals

1.1.1 The molecular Hamiltonian

The fundamendal equation of quantum chemistry is the Schrödinger equation with the molecular Hamiltonian, which in the time-independent form is

$$\hat{H}_{\text{mol}}\Psi_{\text{mol}}(\boldsymbol{r},\boldsymbol{R}) \quad = \quad E_{\text{mol}}\Psi_{\text{mol}}(\boldsymbol{r},\boldsymbol{R}), \tag{1.1}$$

where Ψ_{mol} is a molecular wave function of the spatial coordinates of n electrons, $\boldsymbol{r}$, and N atomic nuclei, $\boldsymbol{R}$, E_{mol} is the total energy, and the molecular Hamiltonian operator, $\hat{H}_{\text{mol}}$, is

$$\hat{H}_{\text{mol}} \quad = \quad -\sum_{I=1}^{N}\frac{1}{2m_I}\nabla_I^2 - \frac{1}{2}\sum_{i=1}^{N}\nabla_i^2 + \sum_{I=1}^{N-1}\sum_{J=I+1}^{N}\frac{Z_I Z_J}{r_{IJ}} + \sum_{i=1}^{n-1}\sum_{j=i+1}^{n}\frac{1}{r_{ij}} - \sum_{i=1}^{n}\sum_{I=1}^{N}\frac{Z_I}{r_{iI}}, \tag{1.2}$$

where indices I and J label atomic nuclei, indices i and j label electrons, r_{pq} is the distance between particles p and q, Z_I and m_I are respectively the atomic number and mass of nucleus I, and ∇_p^2 is the Laplace operator for the real-space coordinates of the particle labeled p. Atomic units are used here and throughout this document; i.e., the electron mass, the elementary charge, the reduced Planck constant, and Coulomb's constant are all unity. The first two terms of Eq. (1.2) are the kinetic energy operators of nuclei and electrons, the second and third terms are the pairwise Coulomb repulsion among nuclei and electrons, and the last term is the pairwise Coulomb attraction between nuclei and electrons.

1.1.2 The Born-Oppenheimer approximation

Equation (1.1) can be solved exactly for up to two-particle systems with one nucleus and one electron such as neutral hydrogen atoms, but not for any larger system. Quantum chemical models of molecules and solids typically make use of the Born-Oppenheimer approximation, which exploits the fact that the nuclear atomic masses, m_I, are much larger (about 10^3-10^5 in atomic units) than the mass of the electron. Therefore, to a first approximation, the nuclear kinetic energy term can be dropped, leading to the electronic Hamiltonian,

$$\hat{H}_{\text{elec}} = -\frac{1}{2}\sum_{i=1}^{N}\nabla_i^2 + \sum_{I=1}^{N-1}\sum_{J=I+1}^{N}\frac{Z_I Z_J}{r_{IJ}} + \sum_{i=1}^{n-1}\sum_{j=i+1}^{n}\frac{1}{r_{ij}} - \sum_{i=1}^{n}\sum_{I=1}^{N}\frac{Z_I}{r_{iI}}. \tag{1.3}$$

The eigenvalue equation for this Hamiltonian,

$$\hat{H}_{\text{elec}}\Psi_{\text{elec}}(\boldsymbol{r};\boldsymbol{R}) = V(\boldsymbol{R})\Psi_{\text{elec}}(\boldsymbol{r};\boldsymbol{R}), \tag{1.4}$$

is solved for the electronic wave function, Ψ_{elec}. Equation (1.4) describes the electronic structure problem and approximately solving it is the objective of electronic structure methods such as HF, MP, CI, CC, and density functional theory (DFT). The electronic energy eigenvalue of Eq. (1.4), labeled V, depends on the nuclear coordinates, $\boldsymbol{R}$, and is referred to as the PES.

The PES replaces the terms corresponding to $\hat{H}_{\text{elec}}$ in Eq. (1.2), leading to the nuclear-motion Hamiltonian operator,

$$\hat{H}_{\text{nuc}} = -\sum_{I=1}^{N}\frac{1}{2m_I}\nabla_I^2 + V(\boldsymbol{R}), \tag{1.5}$$

which has the eigenvalue equation

$$\hat{H}_{\text{nuc}}\Psi_{\text{nuc}}(\boldsymbol{R}) = E_{\text{mol}}\Psi_{\text{nuc}}(\boldsymbol{R}), \tag{1.6}$$

where Ψ_{nuc} is the wave function of atomic nuclear motion. The total molecular wave function, Ψ_{mol} which solves Eq. (1.1), is then given in the Born-Oppenheimer approximation as the product of the nuclear and electronic wave functions,

$$\Psi_{\text{mol}}(\boldsymbol{r},\boldsymbol{R}) \approx \Psi_{\text{nuc}}(\boldsymbol{R})\Psi_{\text{elec}}(\boldsymbol{r};\boldsymbol{R}). \tag{1.7}$$

1.1.3 The vibrational Hamiltonian

The PES, $V(\boldsymbol{R})$, is invariant with respect to overall rotation and translation of the molecule or solid. Equation (1.6) can therefore be simplified by expressing the two operators of $\hat{H}_{\text{nuc}}$ in terms of linear combinations of nuclear spatial coordinates, $\boldsymbol{R}$, corresponding to overall molecular translation, rotation, and vibration. This was accomplished by Watson,[56] who derived the Hamiltonian in these terms as

$$\hat{H}_{\text{mol}} = -\frac{1}{2}\sum_i \frac{\partial^2}{\partial Q_i^2} + V(\boldsymbol{Q}) + \frac{1}{2m_{\text{tot}}}\nabla^2_{\text{CM}} + \sum_{\alpha,\beta}\mu_{\alpha\beta}\left(\Pi_\alpha - \pi_\alpha\right)\left(\Pi_\beta - \pi_\beta\right) - \frac{1}{8}\sum_\alpha \mu_{\alpha\alpha}, \tag{1.8}$$

where $\boldsymbol{Q} = \{Q_1, Q_2, \ldots, Q_M\}$ are M orthonormal mass-weighted (i.e. effective mass defined as unity) vibrational coordinates, m_{tot} is the total mass of the molecule or crystal, ∇^2_{CM} is the Laplace operator for the center of mass of the molecule or crystal, α and β are summed over the three Cartesian directions x, y, and z, μ is the reciprocal inertia tensor, and Π and π are angular momentum operators.[56] The first, third, and fourth and fifth terms in Eq. (1.8) correspond to vibrational, translational, and rotational kinetic energy, respectively. The translational degrees of freedom are rigorously separable from rotation and vibration, but μ and π in the fourth and fifth terms depend on the vibrational coordinates, $\boldsymbol{Q}$. However, this rovibrational coupling is only significant for small molecules with low moments of inertia. Even for a system as small as a single water molecule, the errors incurred by neglecting the vibrational angular momentum operators are relatively small.[57–59] Therefore, a second Born-Oppenheimer-like approximation is justified, in which we neglect all but the first two terms of Eq. (1.8),

$$\hat{H}_{\text{vib}} = -\frac{1}{2}\sum_i \frac{\partial^2}{\partial Q_i^2} + V(\boldsymbol{Q}). \tag{1.9}$$

The Schrödinger equation for this Hamiltonian,

$$\hat{H}_{\text{vib}}\Psi_{\text{vib}}(\boldsymbol{Q}) = E_{\text{vib}}\Psi_{\text{vib}}(\boldsymbol{Q}), \tag{1.10}$$

is the fundamental equation of the vibrational problem of quantum chemistry. The lowest eigenvalue, E_{vib}, of Eq. (1.10) is the vibrational ZPE, also denoted as E_0, and the difference between the ZPE and a higher eigenvalue, say E_s for a state labeled s, corresponds to a vibrational frequency, identified with the symbol ν_s,

$$\nu_s \equiv E_s - E_0, \tag{1.11}$$

Throughout the remainder of this document, we drop the subscript "vib" from all factors appearing in Eq. (1.10).

1.1.4 The potential energy surface

The PES is a complicated function of all internal coordinates with no general analytical form, although approximate analytical representations are manifold. One such common representation is the Taylor series:

$$\begin{aligned} V(\boldsymbol{Q}) &= V_0 + \sum_i F_i Q_i + \frac{1}{2!} \sum_{i,j} F_{ij} Q_i Q_j \\ &+ \frac{1}{3!} \sum_{i,j,k} F_{ijk} Q_i Q_j Q_k \\ &+ \frac{1}{4!} \sum_{i,j,k,l} F_{ijkl} Q_i Q_j Q_k Q_l + \ldots, \end{aligned} \tag{1.12}$$

where V_0 is the value of the potential at some reference geometry and F's are known as force constants. Note that unlike the interaction terms in the molecular Hamiltonian [Eq. (1.2)], which are all pairwise, the PES generally contains three-body, four-body, and higher-rank terms. Because of these interaction terms, Eq. (1.10) is a many-body quantum mechanical problem.

Note that a computational algorithm to solve Eq. (1.10), if it uses a Taylor series representation of the PES, must either store the force constants, F, in memory or on disk, or compute them on the fly. There are clearly $\propto M^3$ cubic force constants in the fourth term of Eq. (1.12), $\propto M^4$ quartic force constants in the fifth term, etc. Therefore, the storage and operation cost of a computational method which utilizes all force constants of up to nth order in a Taylor-series PES is at least $O(M^n)$. This is a significant computational challenge for large molecules or solids, since obtaining numerically accurate results for predicted vibrational properties usually requires retaining a Taylor-series PES up to at least $n = 4$ (which is known as a quartic force field or QFF). Furthermore, calculating force constants accurately becomes progressively more difficult as n increases, because it requires progressively more nested finite-difference calculations of the derivatives of $V(\boldsymbol{Q})$. Clearly, numerical error as well as computational cost will tend to rise as the order of a required force constant increases.

1.1.5 The harmonic approximation

If the PES is approximated as a Taylor series [Eq. (1.12)] but is truncated after the third term,

$$V(\boldsymbol{Q}) = V_0 + \sum_i F_i Q_i + \frac{1}{2!} \sum_{i,j} F_{ij} Q_i Q_j, \tag{1.13}$$

then it is possible to solve Eq. (1.10) analytically. First, we choose the center of the coordinate system, $\boldsymbol{Q} = \{0, \ldots, 0\}$, to correspond to the global minimum of the PES, which implies that

$$F_i = 0, \tag{1.14}$$

for all i. This is known as the "equilibrium geometry." Then, we diagonalize the matrix, $\mathbf{F}$, of the quadratic force-constants, F_{ij}, thereby solving

$$0 \quad = \quad \det\left\{\omega_i^2 \mathbf{1} - \mathbf{F}\right\}, \tag{1.15}$$

for ω_i^2, which will be shown to be the square of vibrational frequencies. The eigenvectors of $\mathbf{F}$ give a new set of internal coordinates known as "normal coordinates." Centering the Taylor series for the PES at the equilibrium geometry also ensures non-negative ω_i^2. In terms of normal coordinates centered at the equilibrium geometry, Eq. (1.10) with Eq. (1.13) is

$$\left[\frac{1}{2}\sum_i\left(-\frac{\partial^2}{\partial Q_i^2} + \omega_i^2 Q_i^2\right) + V_0\right]\Psi_s(\boldsymbol{Q}) \quad = \quad E_s\Psi_s(\boldsymbol{Q}), \tag{1.16}$$

where $s \geq 0$ indexes the various solutions in order of their energies, E_s. Note that Q_i in Eq. (1.16) now refers specifically to a normal coordinate; i.e., a coordinate in which system the gradient of the PES is zero and the matrix of its second derivatives is diagonal. Equation (1.16) has solutions given analytically as

$$\Psi_s(\boldsymbol{Q}) \quad = \quad \prod_i \eta_{s_i}(Q_i), \tag{1.17}$$

$$E_s \quad = \quad V_0 + \sum_i \omega_i\left(s_i + \frac{1}{2}\right), \tag{1.18}$$

with

$$\eta_{s_i}(Q_i) \quad = \quad N_{s_i} H_{s_i}\left((\omega_i)^{1/2} Q_i\right) e^{-\omega_i Q_i^2/2}, \tag{1.19}$$

where $s_i \geq 0$ is an integer for mode i in state s, N is a normalization factor, and H_{s_i} is the s_ith Hermite polynomial. This is known as the harmonic approximation, and Eq. (1.19) is the wave function of a quantum harmonic oscillator. The "fundamental" vibrational frequencies, corresponding to the state with one vibrational quantum number (s_i) equal

to 1 with all others remaining at zero, are given by ω_i, since

$$\begin{aligned} \nu_s &= E_s - E_0 \\ &= \sum_i s_i \omega_i, \end{aligned} \tag{1.20}$$

where E_0 is the harmonic ZPE, i.e., the energy of the state with all $s_i = 0$. Frequencies for states with one nonzero quantum number which is greater than one are known as known as "overtones" and those for states with more than one nonzero vibrational quantum number are known as "combinations."

The harmonic approximation frequently gives predictions for infrared and Raman spectra and other properties which are sometimes qualitatively comparable to experiment, but its quantitative accuracy is very limited. In order to improve upon the harmonic approximation, the cubic and higher-order force constants from Eq. (1.12) must be restored. In terms of normal coordinates centered at the equilibrium geometry, the full Taylor-series PES [Eq. (1.12)] becomes

$$\begin{aligned} V(\boldsymbol{Q}) &= V_0 + \frac{1}{2!}\sum_i F_{ii} Q_i^2 + \frac{1}{3!}\sum_{i,j,k} F_{ijk} Q_i Q_j Q_k \\ &\quad + \frac{1}{4!}\sum_{i,j,k,l} F_{ijkl} Q_i Q_j Q_k Q_l + \ldots. \end{aligned} \tag{1.21}$$

Note that in normal coordinates,

$$F_{ij} = \delta_{ij}\omega_i^2. \tag{1.22}$$

As indicated above, Eq. (1.10) with this PES is analytically unsolvable. The toolkit of many-body quantum mechanics must be applied to the vibrational problem in order to achieve predictive models of molecular and crystal vibrations.

1.1.6 Second quantization algebra

The harmonic approximation provides the basis of a second-quantization algebra which is utilized in derivations in subsequent chapters. Harmonic operator ladder operators are defined as operators which change the quantum number, s_i, of harmonic operator wave functions. Considering the definition of Hermite polynomials and the values of the normalization constants, we find that

$$\hat{a}_i^\dagger \eta_{s_i}(Q_i) = (s_i + 1)^{1/2}\, \eta_{s_i+1}(Q_i), \tag{1.23}$$

$$\hat{a}_i \eta_{s_i}(Q_i) = s_i^{1/2} \eta_{s_i-1}(Q_i), \tag{1.24}$$

with

$$\hat{a}_i^\dagger = \left(\frac{\omega_i}{2}\right)^{1/2}\left(Q_i - \frac{1}{\omega_i}\frac{\partial}{\partial Q_i}\right), \tag{1.25}$$

$$\hat{a}_i = \left(\frac{\omega_i}{2}\right)^{1/2}\left(Q_i + \frac{1}{\omega_i}\frac{\partial}{\partial Q_i}\right). \tag{1.26}$$

The ladder operators obey the commutation rules,

$$\left[\hat{a}_i, \hat{a}_j^\dagger\right] = \delta_{ij}, \tag{1.27}$$

$$\left[\hat{a}_i, \hat{a}_j\right] = \left[\hat{a}_i^\dagger, \hat{a}_j^\dagger\right] = 0, \tag{1.28}$$

which identify them as creation and annihilation operators for bosonic particles,[25] appropriate for collective oscillations such as vibrational motion. Equations (1.25) and (1.26) can be inverted to give

$$Q_i = (2\omega_i)^{-1/2}\left(\hat{a}_i + \hat{a}_i^\dagger\right), \tag{1.29}$$

$$-i\frac{\partial}{\partial Q_i} = i\left(\frac{\omega_i}{2}\right)^{1/2}\left(\hat{a}_i^\dagger - \hat{a}_i\right), \tag{1.30}$$

which can be substituted into Eqs. (1.9) and (1.21) to express the vibrational Hamiltonian in terms of these ladder operators.[60]

1.2 Vibrational self-consistent field theories

For a molecule in an Abelian point-group symmetry with M vibrational degrees of freedom, the VSCF method[4–6] (see also Refs. 19,61–64) approximates the total vibrational wave function Ψ_s as a product of M one-mode wave functions ("modals") $\{\varphi_{s_m}\}$:

$$\Psi_s(\boldsymbol{Q}) = \prod_m \varphi_{s_m}(Q_m), \tag{1.31}$$

but unlike the harmonic approximation, the modal φ_{s_m} is not a harmonic oscillator wave function in general. Instead, the modals, φ_{s_m}, are variationally optimized using the entire PES operator, $V(\boldsymbol{Q})$, under the constraint that all φ_{s_m} and Φ_s overall remain normalized,

$$\delta\left[\langle\Psi_s|\hat{H}|\Psi_s\rangle - \sum_m \epsilon_{s_m}\left(\langle\varphi_{s_m}|\varphi_{s_m}\rangle - 1\right)\right] = 0, \tag{1.32}$$

where ϵ_{s_m} is a Langrange multiplier which ensures that each φ_{s_m} remains normalized. Equation (1.32) is satisfied if φ_{s_m} is the eigenfunction and ϵ_{s_m} the eigenvalue of a mean-field operator, $\hat{G}_{m,s}$,

$$\hat{G}_{m,s}|\varphi_{s_m}\rangle = \epsilon_{s_m}|\varphi_{s_m}\rangle, \tag{1.33}$$

where $\hat{G}_{m,s}$ is the expectation value of the vibrational Hamiltonian in the product of all the other $M-1$ modals,

$$\begin{aligned}\hat{G}_{m,s} &\equiv \left\langle \frac{\Psi_s}{\varphi_{s_m}} \middle| \hat{H} \middle| \frac{\Psi_s}{\varphi_{s_m}} \right\rangle_{\boldsymbol{Q}\setminus\{Q_m\}} \\ &= -\frac{1}{2}\frac{\partial^2}{\partial Q_m^2} + U_{m,s}(Q_m),\end{aligned} \tag{1.34}$$

where the subscript on the matrix element in the first line denotes integration over all normal coordinates, $\boldsymbol{Q}$, *except* for Q_m, and

$$U_{m,s}(Q_m) = -\frac{1}{2}\sum_{j\neq i}\left\langle \frac{\partial^2}{\partial Q_j^2} \right\rangle + \left\langle \frac{\Psi_s}{\varphi_{s_m}} \middle| V(\boldsymbol{Q}) \middle| \frac{\Psi_s}{\varphi_{s_m}} \right\rangle_{\boldsymbol{Q}\setminus\{Q_m\}}. \tag{1.35}$$

In the above equation and hereafter, the brackets around an operator, $f(Q_m)$, signify its expectation value in a modal φ_{s_m}, that is, $\langle\varphi_{s_m}|f(Q_m)|\varphi_{s_m}\rangle$. The eigenvalue, ϵ_{s_m}, can be easily shown to agree with the total energy, E_s, defined as the expectation value of $\hat{H}$ in Ψ_s:

$$\begin{aligned}\epsilon_{s_m} &= \langle\hat{G}_{m,s}\rangle = \langle\varphi_{s_m}|\left\langle \frac{\Psi_s}{\varphi_{s_m}} \middle| \hat{H} \middle| \frac{\Psi_s}{\varphi_{s_m}} \right\rangle_{\boldsymbol{Q}\setminus\{Q_m\}}|\varphi_{s_m}\rangle \\ &= \langle\Psi_s|\hat{H}|\Psi_s\rangle \equiv E_s.\end{aligned} \tag{1.36}$$

The VSCF equation of one mode [Eq. (1.33)] is coupled with those of all the other modes via the mean-field potential [Eq. (1.34)]. Therefore, Eq. (1.33) must be solved until self consistency across all modes, which usually is achieved by an iterative algorithm. VSCF is similar in this sense to HF, in which each electron experiences an effective one-electron potential created by nuclei and all the other electrons. They differ in that the vibrational wave function is bosonic, not fermionic, and therefore a direct product, rather than a Slater determinant, is used in defining the VSCF wave function.

VSCF is analogous to and a fundamental as the HF method for electrons, because methods such as VMP, VCI, and VCC utilize the set of VSCF Hartree product wave functions, $\{\Psi_s\}$, as a basis in which the exact vibrational wave functions can be expanded. For this reason, computational inefficiencies and theoretical problems at the VSCF level are inherited by such post-VSCF methods. As was shown by Hirata, Keçeli, and Yagi[20] and as we summarize below, the VSCF programmable equations equations contain numerous null terms in the limit of a large molecule or a crystal

and have inconsistent accuracy between systems of various sizes. Therefore, methods such as VMP, VCI, and VCC suffer from significant computational inefficiency. It is for this reason that the size-extensive VSCF or XVSCF method was developed by Keçeli and Hirata in 2011.

1.2.1 VSCF and size consistency

As discussed above, observable quantities in thermodynamics are either extensive, i.e., asymptotically proportional to K^1, where K is the size of the system, or intensive, i.e., asymptotically proportional to K^0. The total vibrational energy (E_s) of a molecule or a crystal is extensive, and a vibrational frequency (ν_s) is intensive. A method that is size-consistent must reflect these dependencies in its equations for such properties. Generally, the size dependence of a quantity in a programmable equation for an approximate many-body method for solving a Schrödiner equation is given by its polynomial dependence on the number of wave vector sampling points in the reciprocal unit cell in the corresponding formalism for a periodic solid.[17] This number is denoted as K and is proportional to the size of the solid under the periodic boundary condition; this is the reason the symbol K has been used in this chapter for system size. Any K-dependence other than K^0 or K^1 is nonphysical and if terms with such dependence are nonzero in a theoretical method, that method is not size-consistent.

For example, the harmonic approximation, whose energy and frequency expressions are given by Eq. (1.18) and (1.20), respectively, is size consistent. The harmonic frequencies, ω_m, are intensive because they are the square roots of the quadratic force constant in normal coordinates, F_{ii}, and a force constant of order n can be shown to be proportional to $K^{1-n/2}$.[20,65] The total energies are extensive because they consist of a sum of an electronic energy, V_0, which is extensive provided the underlying electronic structure approximation is size-consistent, and a sum over the (intensive) frequencies with a size equal to the number of degrees of freedom (rendering the entire term extensive, since the number of degrees of freedom is proportional to K^1, and $K^0 \times K^1 = K^1$).

In order for the VSCF method to be size-consistent, the eigenvalues of the mean-field operator, $\epsilon_{s_m} = E_s$, must consist of an extensive part common to all vibrational states and varying intensive part, like the harmonic total energies. Therefore, the mean-field operator itself must consist of a constant extensive part and a variable intensive part. In 2010, Hirata, Keçeli, and Yagi[20] investigated the size dependencies of the mean-field potential, $U_{m,s}(Q_m)$, to ascertain whether VSCF was size consistent. $U_{m,s}(Q_m)$ can be expressed with F's by substituting Eq. (1.21) into Eq. (1.35). It is convenient to rearrange the resulting equation into a Taylor expansion in Q_m:

$$\begin{aligned} U_{m,s}(Q_m) &= U^{(0)}_{m,s} + U^{(1)}_{m,s} Q_m + \frac{1}{2!} U^{(2)}_{m,s} Q_m^2 + \frac{1}{3!} U^{(3)}_{m,s} Q_m^3 \\ &\quad + \frac{1}{4!} U^{(4)}_{m,s} Q_m^4 + \cdots, \end{aligned} \tag{1.37}$$

where the definitions of the effective force constants, $U^{(k)}_{m,s}$, can be found in Ref. 20. It is readily shown that $U^{(k)}_{m,s}$ have the same size dependence as the bare force constants, F,[65] namely,

$$U^{(k)}_{m,s} \quad \propto \quad K^{1-n/2}. \tag{1.38}$$

In the bulk ($K = \infty$) limit, therefore, $U^{(3)}_{m,s}$ and all higher-order effective force constants vanish; they are not size consistent. Among the remaining effective force constants, $U^{(0)}_{m,s}$ scales extensively (K^1) and is related to the zero-point energies, while $U^{(2)}_{m,s}$ is intensive (K^0), yielding transition frequencies; they constitute size-consistent contributions in VSCF. On the other hand, the mean-field gradient, $U^{(1)}_{m,s}$, scales as $K^{1/2}$, which is nonphysical. Therefore, $U^{(1)}_{m,s}$ must vanish for VSCF to be strictly size consistent.

This analysis leads to the following predictions about how the shape of VSCF's mean-field potential varies with size. In a small molecule, the mean-field potential may have a complicated functional dependence on Q_m with contributions from cubic ($U^{(3)}_{m,s}$), quartic ($U^{(4)}_{m,s}$), and higher-order effective force constants. The vibrationally averaged geometry, that is, the expectation value of geometrical coordinates in a VSCF wave function, has no simple analytical form and needs to be evaluated numerically. As the molecule becomes larger, the mean-field potential becomes closer to a quadratic function of Q_m because the magnitudes of cubic and all higher-order force constants decrease with size. In the bulk limit, the potential becomes a pure quadratic function and hence the modals are harmonic oscillator wave functions, which are, however, distinct from those of the harmonic approximation to $V(\boldsymbol{Q})$.

The mean-field gradients, $U^{(1)}_{m,s}$, having the nonphysical $K^{1/2}$ dependence, do not vanish in the bulk. They have the effect of moving the centers of the quadratic mean-field potentials away from the coordinate origin, i.e., the equilibrium geometry. This shift in the centers of the mean-field potentials causes a basis-set convergence problem in the usual VSCF algorithm that expands modals as linear combinations of basis functions centered at the equilibrium geometry, where the modals may have low values. In short, VSCF is not size consistent and its algorithm has a considerable degree of inefficiency in the bulk limit, and methods such as VMP, VCI, and VCC will inevitably inherit this inefficiency.

1.2.2 Size-extensive VSCF

The XVSCF method was developed[21] in order to cure the size-consistency problems of the standard VSCF method. XVSCF has a mean-field potential that includes only size-consistent terms:

$$U_{m,s}(Q_m) \quad = \quad U^{(0)}_{m,s} + U^{(1)}_{m,s} Q_m + \frac{1}{2!} U^{(2)}_{m,s} Q^2_m, \tag{1.39}$$

with

$$U^{(1)}_{m,s} = 0, \tag{1.40}$$

and

$$\begin{aligned} U^{(0)}_{m,s} &= V_0 + \frac{1}{2}\sum_{i\neq m}\left\{-\left\langle\frac{\partial^2}{\partial Q_i^2}\right\rangle + F_{ii}\langle Q_i^2\rangle\right\} \\ &\quad + \frac{1}{2!2^2}{\sum_{i,j\neq m}}' F_{iijj}\langle Q_i^2\rangle\langle Q_j^2\rangle + \cdots, \end{aligned} \tag{1.41}$$

$$\begin{aligned} U^{(1)}_{m,s} &= F_m + \frac{1}{2}\sum_{i\neq m} F_{mii}\langle Q_i^2\rangle \\ &\quad + \frac{1}{2!2^2}{\sum_{i,j\neq m}}' F_{miijj}\langle Q_i^2\rangle\langle Q_j^2\rangle + \cdots, \end{aligned} \tag{1.42}$$

$$\begin{aligned} U^{(2)}_{m,s} &= F_{mm} + \frac{1}{2}\sum_{i\neq m} F_{mmii}\langle Q_i^2\rangle \\ &\quad + \frac{1}{2!2^2}{\sum_{i,j\neq m}}' F_{mmiijj}\langle Q_i^2\rangle\langle Q_j^2\rangle + \cdots, \end{aligned} \tag{1.43}$$

where sums with primes exclude equal summation indices such as $j = k$. Note that a small subset of even-order force constants appears in Eqs. (1.41) and (1.43), and a small group of odd-order force constants of certain types appears in Eq. (1.42). This is not due to an approximation; all the other force constants are associated with the terms that vanish in the bulk limit.

Equation (1.40) must be satisfied for XVSCF to exhibit proper size dependence. One way to ensure this is to approximate $V(\boldsymbol{Q})$ by $V_n(\boldsymbol{Q})$, where

$$V_n(\boldsymbol{Q}) = V_0 + \frac{1}{2}\sum_i F_{ii}Q_i^2 + \frac{1}{2!2^2}{\sum_{i,j}}' F_{iijj}Q_i^2Q_j^2 + \cdots, \tag{1.44}$$

and n is the truncation order of the potential energy surface, which may be any even number greater than 2. For example, $V_4(\boldsymbol{Q})$ consists of force constants of type F_{ii} and F_{iijj}. Since $V_n(\boldsymbol{Q})$ retains only those force constants that appear in the size-consistent definitions of $U^{(0)}_{m,s}$ and $U^{(2)}_{m,s}$ and none in the definition of $U^{(1)}_{m,s}$, Eq. (1.40) is satisfied by construction with this approximation. In other words, with no odd-order force constants, the shift in the center of the mean-field potentials cannot occur and the vibrationally averaged geometry along each normal coordinate remains at the coordinate origin. This is the approach taken in Ref. 21, which is called XVSCF(n).

Since $U_{m,s}(Q_m)$ under this approximation is a purely quadratic potential centered at the origin, Eq. (1.33) has

analytical solutions that are harmonic oscillator wave functions, Eq. (1.19), with

$$\epsilon_{s_m} = (s_m + 1/2)\omega_m + U^{(0)}_{m,s}, \tag{1.45}$$

with

$$\omega_m = \{U^{(2)}_{m,s}\}^{1/2}, \tag{1.46}$$

The integrals in Eqs. (1.41)–(1.43) thus can be evaluated analytically:

$$\langle Q_m^2 \rangle = \frac{s_m + 1/2}{\omega_m}, \tag{1.47}$$

$$\left\langle \frac{\partial^2}{\partial Q_m^2} \right\rangle = -\omega_m(s_m + 1/2), \tag{1.48}$$

and the total vibrational energy of state s in the XVSCF(n) method is

$$\begin{aligned} E_{\mathbf{s}} = {} & V_0 + \frac{1}{2}\sum_i \left\{ -\left\langle \frac{\partial^2}{\partial Q_i^2} \right\rangle + F_{ii}\langle Q_i^2 \rangle \right\} \\ & + \frac{1}{2!2^2}{\sum_{i,j}}' F_{iijj}\langle Q_i^2 \rangle \langle Q_j^2 \rangle \\ & + \frac{1}{3!2^3}{\sum_{i,j,k}}' F_{iijjkk}\langle Q_i^2 \rangle \langle Q_j^2 \rangle \langle Q_k^2 \rangle + \cdots . \end{aligned} \tag{1.49}$$

Equation (1.46) and hence (1.19), (1.45), (1.47), and (1.48) for one mode depend on all the other modals through Eq. (1.43), so these equations must be brought to self-consistency across all modes, typically by an iterative algorithm. In this way, we obtain ω_m and E_s, which are rigorously intensive and extensive, respectively. However, the XVSCF(n) and VSCF frequencies and energies do not converge at the same bulk limit unless the same approximation, $V(\boldsymbol{Q}) = V_n(\boldsymbol{Q})$, is made in VSCF (as done in Ref. 21).

The standard VSCF method usually requires a basis-set expansion of the modals, φ_{s_m}. The analytical form of the modals in XVSCF(n) therefore leads to significantly more computational efficiency, since no matrix diagonalization, e.g., for the mean-field operator $\hat{G}_{m,s}$, is required. This also means that post-XVSCF(n) "correlated" vibrational methods will inherit this relative efficiency compared to VSCF; evaluating matrix elements of products of harmonic oscillator wave functions is inherently easier than the corresponding task for arbitrary wave functions, since analytical expressions for matrix elements of position and momentum operators in a harmonic basis can be derived (see, e.g., Table I of Ref. 21). Furthermore, XVSCF with $V_n(\boldsymbol{Q})$ requires drastically fewer force constants than standard VSCF - only $O(M^{n/2})$ compared to $O(M^n)$ in a comparable VSCF calculation.

The vibrationally averaged geometry of a harmonic oscillator wave function centered at the origin remains at the origin. Therefore, the anharmonic geometry corrections by XVSCF(n) using $V(\boldsymbol{Q}) = V_n(\boldsymbol{Q})$ are null.

1.3 Manifestly size-consistent theoretical formalism for the vibrational structure problem

The XVSCF(n) method was derived by eliminating non-size-consistent terms from the programmable equations, as described in Sec. 1.2. In deriving extensions to XVSCF and correlated vibrational methods which improve on the accuracy of XVSCF, we utilize theoretical tools which ensure from the outset that programmable equations for frequencies exhibit K^0 size dependence and those for ZPE exhibit K^1 size dependence. These are found in the diagrammatic techniques of Green's functions theory for frequencies, and MBPT for ZPE.

Expressing programmable equations in terms of diagrams allows expedient evaluation of the size-dependence of the corresponding quantities.[17,27,28] Diagrams, such as those depicted in Figs. 1.2 and 1.3 below, depict programmable equations in terms of vertices, representing force constants, connected by lines, representing normal modes. These diagrams have a size dependence of $K^{1-n/2}$, where n in this case is the number of external lines; the diagrams in Fig. 1.2 have $n = 2$, and the diagrams in Fig. 1.3 have $n = 0$. Thus the former represent algebraic terms which have the correct size-dependence for a vibrational frequency, and the latter have the correct size-dependence for a vibrational total energy. Note that the programmable equations for XVSCF(n) total energies and frequencies can also be written in the form of a sum over closed and open connected diagrams, respectively, as explained by Keçeli and Hirata.[21]

In the remainder of this section we describe the Green's function and MBPT formalisms in more detail. The new vibrational many-body methods we introduce in subsequent chapters are all essentially defined by summing over various diagrammatic contributions to the Green's function and ZPE. XVSCF(n) can also be understood in terms of Green's functions, as we discuss in Chapter 3.

1.3.1 Vibrational Green's function

All of the new anharmonic vibrational methods discussed in this review calculate frequencies directly by solving the Dyson equation,[22–25] which is written for the single-particle vibrational Green's function in the frequency domain as[10]

$$\mathbf{G}(\nu) \quad = \quad \mathbf{G}_0(\nu) + \mathbf{G}_0(\nu)\boldsymbol{\Sigma}(\nu)\mathbf{G}(\nu), \tag{1.50}$$

where $\mathbf{G}$ and $\mathbf{G}_0$ respectively are the exact and zeroth-order single-particle vibrational Green's functions in the frequency domain,[23,26] and $\boldsymbol{\Sigma}$ is the Dyson self-energy. All three quantities are M-by-M matrices. The Green's function

is defined as

$$\{\mathbf{G}(\nu)\}_{ij} = 2\left(\omega_i\omega_j\right)^{1/2}\left(\sum_s \frac{\langle\Psi_0|Q_i|\Psi_s\rangle\langle\Psi_s|Q_j|\Psi_0\rangle}{\nu-(E_s-E_0)} + \sum_s \frac{\langle\Psi_0|Q_j|\Psi_s\rangle\langle\Psi_s|Q_i|\Psi_0\rangle}{-\nu-(E_s-E_0)}\right), \tag{1.51}$$

where Ψ_s and E_s are the exact vibrational wave functions and energies for state s. The zeroth-order Green's function is obtained by substituting the wave functions and energies in the harmonic approximation, leading to

$$\{\mathbf{G}_0(\nu)\}_{ij} = \frac{\delta_{ij}}{\nu-\omega_i} + \frac{\delta_{ij}}{-\nu-\omega_i}. \tag{1.52}$$

The Dyson self-energy, $\mathbf{\Sigma}$, is postulated as the function which satisfies Eq. (1.50). Equation (1.50) is depicted diagrammatically in Fig. 1.1, where the zeroth-order Green's function is represented as a thin line and the exact Green's function represented as a thick line.

The exact Green's function diverges (i.e., its matrix inverse is singular) at the exact anharmonic frequencies of the molecule, $\nu = \nu_s$, where s labels an excited vibrational state. Multiplying Eq. (1.50) by $\mathbf{G}_0^{-1}$ from the left and $\mathbf{G}^{-1}$ from the right and noting that $\det\left\{\mathbf{G}^{-1}(\nu_s)\right\} = 0$, we find

$$0 = \det\left\{\nu_s^2\mathbf{1} - \mathbf{F}(\nu_s)\right\}, \tag{1.53}$$

where

$$\{\mathbf{F}(\nu)\}_{ij} = \delta_{ij}\omega_i^2 + 2(\omega_i\omega_j)^{1/2}\{\mathbf{\Sigma}(\nu)\}_{ij}. \tag{1.54}$$

If the off-diagonal elements of the Dyson self-energy are neglected,

$$\nu_s^2 = \omega_i^2 + 2\omega_i\{\mathbf{\Sigma}(\nu_s)\}_{ii}. \tag{1.55}$$

Equations (1.53) and (1.55) are both referred to as the inverse Dyson equation. Equation (1.53) is isomorphic to Eq. (1.15), except that in this case the mass-weighted force constant matrix, $\mathbf{F}$, is 'dressed' with an energy-dependent correction that accounts for the effects of anharmonicity. The diagonalization of $\mathbf{F}$ yields vibrational coordinates (modes) and frequencies corrected by anharmonicity, whereas the diagonal approximation [Eq. (1.55)] gives anharmonic frequencies more expediently. This concept is analogous to the Dyson-equation formalism for quasi-particle energies in electronic structure theory, in which correlated orbitals and orbital energies are obtained in a formally single-particle framework by 'dressing' the Fock matrix with an energy-dependent potential term; i.e., the Dyson self-energy.[10,33,66,67]

The Green's function formalism differs from the procedure used to calculate frequencies in methods such as VCI and VMP. In these methods, vibrational frequencies are typically computed as differences in total energies between two states. This method has the drawback that it is difficult to assess whether the frequencies thus computed are thermodynamically intensive, which is required for the method to be size consistent. Methods which compute vibrational frequencies directly are more desirable in this regard, because the size dependence of the equations for the frequencies themselves can be directly assessed. The harmonic frequencies, $\{\omega_i\}$, have size dependence of K^0, as discussed in Sec. 1.2. Therefore, the anharmonic frequencies computed by Eq. (1.53) or (1.55) are also intensive so long as the Dyson self-energy, $\mathbf{\Sigma}$, also has volume dependence of K^0. This is ensured by expressing the Dyson self-energy as a sum of connected, open diagrams (see below). Furthermore, the direct calculation of frequencies allows the stochastic algorithms discussed in Chapters 5 and 6 to be employed. Small differences (frequencies) between two total energies with large statistical noise can be buried by the noise, and stochastic treatment of excited states is extremely cumbersome because their wave functions have nodes. Our Dyson-equation based formulas resolve all of these problems at once.

1.3.2 Dyson self-energy diagrams

The Dyson self-energy, $\mathbf{\Sigma}$, is expanded in a diagrammatic many-body perturbation theory (MBPT) series,

$$\mathbf{\Sigma}(\nu) \quad = \quad \mathbf{\Sigma}^{(1)}(\nu) + \mathbf{\Sigma}^{(2)}(\nu) + \ldots, \tag{1.56}$$

in which the pth-order term is defined diagrammatically as a sum of connected, irreducible, nonredundant diagrams that consist of p interaction vertices, which represent anharmonic force constants, and from which radiate edges, representing one element of the zeroth-order Green's function,[22–25] and two bare stubs, which confer an overall size dependence of K^0. These diagrams are translated into algebraic expressions involving force constants, $\{\omega_i\}$, and ν according to a set of rigorous translation rules which are presented in Chapters 2 and 4. These are inserted into Eq. (1.53) or (1.55) to obtain anharmonic frequencies. The important graphical information that these diagrams convey is that they are all connected (in the usual sense of the word[17,28,29]) and the connectedness guarantees the correct size dependence.

For example, Fig. 1.2 shows the first-order approximation to the diagonal elements of the Dyson self-energy, $\left\{\mathbf{\Sigma}^{(1)}(\nu)\right\}_{ii}$. They consist of even-order force constants, represented by filled circles radiating an even number of stubs, with all stubs except for two connected by loop edges. Figure 1.2 is interpreted algebraically as

$$\left\{\mathbf{\Sigma}^{(1)}(\nu)\right\}_{ii} \quad = \quad \frac{1}{2}\sum_j F_{iijj}(2^2\omega_i\omega_j)^{-1}$$

$$+\frac{1}{2^2 2!}\sum_{j,k} F_{iijjkk}(2^3\omega_i\omega_j\omega_k)^{-1} + \ldots, \tag{1.57}$$

where F_{iijj} is a quartic force constant along normal modes i and j, and F_{iijjkk} is a sextic force constant along normal modes i, j, and k. Approximating the Dyson self-energy by its diagonal first-order contribution,

$$\{\boldsymbol{\Sigma}(\nu)\}_{ij} \quad = \quad \delta_{ij}\left\{\boldsymbol{\Sigma}^{(1)}(\nu)\right\}_{ii}, \tag{1.58}$$

and substituting Eq. (1.57) into Eq. (1.55) gives

$$\begin{aligned} \nu_i^2 \quad &= \quad F_{ii} + \frac{1}{2}\sum_j F_{iijj}(2\omega_j)^{-1} \\ &\quad +\frac{1}{2^2 2!}\sum_{j,k} F_{iijjkk}(2^2\omega_j\omega_k)^{-1} + \ldots, \end{aligned} \tag{1.59}$$

where ν_i is the anharmonic frequency of the ith mode and we have used $F_{ii} = \omega_i^2$. Equation (1.59) is the frequency equation for the first-order perturbation theory from the harmonic approximation, which we refer to as XVH1(n), where n is the highest order of force constants in the Dyson self-energy.[1] We discuss XVH1(n) in more detail in Chapter 4.

1.3.3 Many-body perturbation theory diagrams

The standard MBPT expansion for the ground state energy (ZPE) also uses diagrams[27] to express various perturbative contributions to the total energy,

$$E_0 \quad = \quad E_0^{(0)} + E_0^{(1)} + E_0^{(2)} + E_0^{(3)} + \ldots, \tag{1.60}$$

where $E_s^{(0)}$ is the energy of state s in the harmonic approximation [Eq. (1.18)], and $E_0^{(p)}$ is the pth-order perturbation correction to the ZPE and is defined as the sum of all closed, connected diagrams with p vertices. Such diagrams can be formed by drawing a loop connecting each pair of bare stubs of the self-energy diagrams such as those depicted in Fig. 1.2. The resulting total energy diagrams, consisting of single connected pieces and no external edges or bare stubs, have a volume dependence of K^1,[17] correct for an extensive quantity such as a total energy. Diagrammatic MBPT is formally identical to RSPT, which has algebraic expressions for $E_0^{(p)}$ obtained recursively,[10]

$$E_0^{(1)} \quad = \quad \langle\Psi_0^{(0)}|\hat{H}_1|\Psi_0^{(0)}\rangle, \tag{1.61}$$

[1] Note that although Eq. (1.55) must generally be solved self-consistently due to the anharmonic frequency appearing on both the left- and right-hand sides of the equation, in this case, that is unnecessary because the first-order approximation to the Dyson self-energy does not actually depend on ν.

$$E_0^{(2)} = \sum_s{}' \frac{\langle\Psi_0^{(0)}|\hat{H}_1|\Psi_s^{(0)}\rangle\langle\Psi_s^{(0)}|\hat{H}_1|\Psi_0^{(0)}\rangle}{E_0^{(0)} - E_s^{(0)}}, \tag{1.62}$$

$$E_0^{(3)} = \sum_{s,t}{}' \frac{\langle\Psi_0^{(0)}|\hat{H}_1|\Psi_s^{(0)}\rangle\langle\Psi_s^{(0)}|\hat{H}_1|\Psi_t^{(0)}\rangle\langle\Psi_t^{(0)}|\hat{H}_1|\Psi_0^{(0)}\rangle}{(E_0^{(0)} - E_s^{(0)})(E_0^{(0)} - E_t^{(0)})} - E_0^{(1)} \sum_s{}' \frac{\langle\Psi_0^{(0)}|\hat{H}_1|\Psi_s^{(0)}\rangle\langle\Psi_s^{(0)}|\hat{H}_1|\Psi_0^{(0)}\rangle}{(E_0^{(0)} - E_s^{(0)})^2}, \tag{1.63}$$

and so forth, where the prime on the sums once again indicates the exclusion of coincident indices of summation and $\Psi_s^{(0)}$ is the wave function for the sth vibrational state in the harmonic approximation. Note that beginning at third order, so-called "disconnected" terms must be subtracted. Diagrammatic MBPT does not require this laborious subtraction.

For instance, the first-order correction to the ZPE is depicted diagrammatically in Fig. 1.3 and expressed algebraically as

$$\begin{aligned} E_0^{(1)} &= \frac{1}{2^2 2!} \sum_{i,j} F_{iijj} (2^2 \omega_i \omega_j)^{-1} \\ &\quad + \frac{1}{2^3 3!} \sum_{i,j,k} F_{iijjkk} (2^3 \omega_i \omega_j \omega_k)^{-1} + \ldots, \end{aligned} \tag{1.64}$$

and the total ZPE to first order is obtained by adding this correction to the ZPE in the harmonic approximation,

$$\begin{aligned} E_0 &= E_0^{(0)} + E_0^{(1)} \\ &= V_0 + \sum_i \frac{\omega_i}{4} + \frac{1}{2} \sum_i F_{ii} (2\omega_i)^{-1} \\ &\quad + \frac{1}{2^2 2!} \sum_{i,j} F_{iijj} (2^2 \omega_i \omega_j)^{-1} \\ &\quad + \frac{1}{2^3 3!} \sum_{i,j,k} F_{iijjkk} (2^3 \omega_i \omega_j \omega_k)^{-1} + \ldots. \end{aligned} \tag{1.65}$$

Equation (1.65) is the programmable equation for the ZPE in the XVH1(n) method.

1.4 Figures

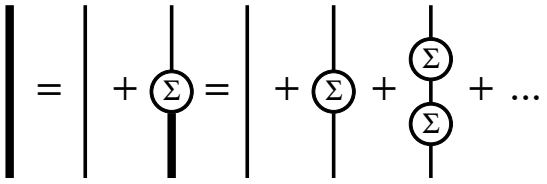

Figure 1.1: A diagrammatic representation of Eq. (1.50).

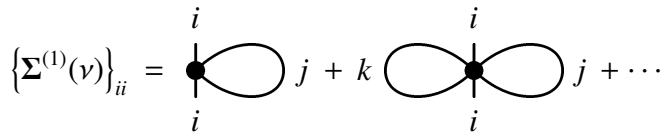

Figure 1.2: First-order diagonal self-energy diagrams.

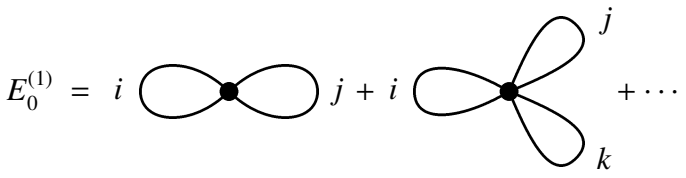

Figure 1.3: First-order energy diagrams.

Chapter 2

Anharmonic geometry corrections and XVSCF[n]

In Chapter 1, we discussed the non-size-consistency of the VSCF method, in that the programmable equations of VSCF contain many terms that are not diagrammatically size consistent and thus vanish in the bulk limit. Only the even-order anharmonic force constants of certain types, i.e., F_{iijj}, F_{iijjkk}, etc., can form closed, connected diagrams for extensive total energies and open, connected diagrams for intensive transition frequencies,[21] where i, j, and k denote distinct normal modes. The mean-field potentials of VSCF that are formed with these force constants were furthermore shown to be effectively harmonic in accordance with Makri's theorem[68] stating that interacting semi-independent oscillators are always effectively harmonic in the bulk limit.

Therefore, Keçeli and Hirata introduced[20,21] a diagrammatically size-consistent (or size-extensive) variant of VSCF, i.e., XVSCF(n), which retains only the size-consistent contributions to anharmonic total energies and anharmonic transition frequencies from the aforementioned set of even-order force constants up to the nth order. The effective harmonic form of the mean-field potentials of XVSCF(n) lends its equations to semi-analytical solutions, making a basis set, quadrature, and matrix diagonalization, which are required in any previous VSCF algorithm, unnecessary. As a result, XVSCF(n) has superior cost scaling to VSCF, is nearly three orders of magnitude faster than VSCF for medium-sized molecules,[21] and is particularly well suited, given its size consistency[17] and unmatched efficiency, for applications to large molecules and solids.

In this chapter, we report a critical extension of XVSCF(n) to anharmonic geometry corrections. We show that the odd-order force constants of the types F_{ijj}, F_{ijjkk}, etc. can be used to form open, connected diagrams isomorphic to the diagram of energy gradients (atomic forces), which, therefore, shift the minima of the mean-field potentials away from the equilibrium geometry by intensive amounts. These shifts represent the anharmonic geometry corrections and can be estimated accurately, but not exactly, by a simple formula[20] involving the mean-field gradients (determined by the odd-order force constants) and the mean-field harmonic force constants (evaluated with the even-order force constants). Here, we implement this formula and numerically test its accuracy.

We also introduce a new size-consistent VSCF method, XVSCF[n], which obtains extensive anharmonic energies and intensive anharmonic frequencies from the even-order force constants and intensive anharmonic geometry corrections from the odd-order force constants up to the nth order, fully taking into account the coupling between the

two quantities. XVSCF[n] determines the minima of the mean-field potentials by iterating XVSCF(n) cycles at the coordinate origin, which is made to progressively approach the minima. Since all the force constants that can contribute size consistently are included without any further approximation, XVSCF[n] has identical bulk limits of total energies, frequencies, and geometry corrections as VSCF, while retaining rigorous size consistency and much of the algorithmic simplicity and efficiency of XVSCF(n). We demonstrate that these theoretical expectations are supported by numerical results.

In what follows, we document the diagrammatic and algebraic definitions of the theories of XVSCF(n) and XVSCF[n] for anharmonic total energies, transition frequencies, and geometry corrections;[2,69] propose their algorithms, programmable equations, and implementations at the level of $n = 4$. We compare them with VSCF and other related methods. We also perform numerical tests of their accuracy and efficiency for the systems ranging from water and polyacenes to model one-dimensional chains consisting of 5 to 65 masses. The results are given below.

2.1 Theory

2.1.1 XVSCF(n)

In Chapter 1, we summarized the XVSCF(n) method for vibrational frequencies and total energies. This consisted of truncating the Taylor series for the VSCF mean-field potential for the mode labeled m, $U_{m,s}(Q_m)$, and approximating the Taylor-series PES, $V(\boldsymbol{Q})$, with $V_n(\boldsymbol{Q})$, where the latter contains only semidiagonal even-order force constants. This leads to an XVSCF wave function consisting of a product of harmonic oscillator wave functions centered at the equilibrium geometry, with null anharmonic geometry correction.

The VSCF method, however, predicts nonzero anharmonic geometry corrections. This is due to the odd-order semidiagonal force constants such as F_{ijj}, F_{ijjkk}, and so forth, which are omitted in XVSCF(n) because they contribute to the gradient of the mean-field potential, $U^{(1)}_{m,s}$, which has the nonphysical size dependence of $K^{1/2}$. It is possible to estimate the corrections by reinstating the odd-order force constants up to nth order *after* frequencies and energies are obtained by XVSCF with $V_n(\boldsymbol{Q})$. In other words, we can compute the nonzero value of $U^{(1)}_{m,s}$ using Eq. (1.42) and approximating $V(\boldsymbol{Q})$ by $V_{n-1}(\boldsymbol{Q})$, where the latter is defined by

$$V_{n-1}(\boldsymbol{Q}) = \sum_i F_i Q_i + \frac{1}{2}{\sum_{i,j}}' F_{ijj} Q_i Q_j^2 + \ldots, \tag{2.1}$$

with $n-1$ being an odd integer specifying the highest (truncation) order of the force constants included. The integrals in Eq. (1.42) are evaluated using Eq. (1.47) and the set of ω_m determined by XVSCF with $V_n(\boldsymbol{Q})$. Differentiating Eq. (1.39) with Q_m and equating the gradient with zero, we find[20] the minimum of the mean-field potential, $\langle Q_m \rangle$, which

equals the anharmonic geometry corrections, to occur at

$$\langle Q_m \rangle \quad = \quad -\frac{U^{(1)}_{m,s}}{U^{(2)}_{m,s}}. \tag{2.2}$$

Again, the corrections thus obtained are not the same as those of VSCF in the bulk limit because $U^{(1)}_{m,s}$ and $U^{(2)}_{m,s}$ both have complex dependence on the origin of $\boldsymbol{Q}$ and, therefore, Eqs. (1.40) and (1.46) are coupled and need to be solved simultaneously (rather than sequentially as done in the above treatment) if we are to seek the same bulk limit. The corrections are, however, diagrammatically intensive, extremely rapid to evaluate, and close to the VSCF values in the bulk limit, as we shall show in the following.

We use XVSCF(n) to refer to the use of $V_n(\boldsymbol{Q})$ to obtain vibrational energies and transition frequencies followed by the use of $V_{n-1}(\boldsymbol{Q})$ to estimate the anharmonic corrections to geometry. Keçeli and Hirata demonstrated[21] that XVSCF(4) reproduces the anharmonic frequencies of VSCF results using $V_4(\boldsymbol{Q})$ in the bulk limit at a fraction of the computational cost. Here, we propose the corresponding method for anharmonic geometry corrections, which are given by Eq. (2.2).

2.1.2 XVSCF[n]

If we do not make the approximations, $V(\boldsymbol{Q}) = V_n(\boldsymbol{Q})$ in Eq. (1.46) and $V(\boldsymbol{Q}) = V_{n-1}(\boldsymbol{Q})$ in Eq. (1.40), these two equations are coupled and must be solved simultaneously. We introduce the method that does exactly this and call it XVSCF[n] when the PES has up to the nth-order force constants. The first term in the right-hand side of Eq. (1.42), defining $U^{(1)}_{m,s}$, is zero as mentioned above. However, the sum of the subsequent terms does not vanish at the minimum of $V(\boldsymbol{Q})$.

Let $\tilde{\boldsymbol{q}} = \{\tilde{q}_1, \ldots, \tilde{q}_M\}$ be the minimum of the mean-field potential we seek. We also define the new coordinates, $\tilde{\boldsymbol{Q}}$, which are normal coordinates centered at $\tilde{\boldsymbol{q}}$, that is, $\tilde{\boldsymbol{Q}} = \boldsymbol{Q} - \tilde{\boldsymbol{q}}$. The mean-field potential in these new coordinates, $\tilde{U}_{m,s}(\tilde{Q}_m)$, is written as

$$\tilde{U}_{m,s}(\tilde{Q}_m) \quad = \quad \tilde{U}^{(0)}_{m,s} + \tilde{U}^{(1)}_{m,s}\tilde{Q}_m + \frac{1}{2}\tilde{U}^{(2)}_{m,s}\tilde{Q}^2_m, \tag{2.3}$$

where

$$\tilde{U}^{(1)}_{m,s} \quad = \quad 0, \tag{2.4}$$

by construction. In practice, of course, we solve Eq. (2.4) to determine $\tilde{\boldsymbol{q}}$.

The effective force constants $\tilde{U}^{(0)}_{m,s}$, $\tilde{U}^{(1)}_{m,s}$, and $\tilde{U}^{(2)}_{m,s}$ in these new coordinates and center are written as

$$\begin{aligned}
\tilde{U}^{(0)}_{m,s} &= V_0 + \frac{1}{2}\sum_{i\neq m}\left\{-\left\langle\frac{\partial^2}{\partial\tilde{Q}_i^2}\right\rangle + F_{ii}\langle\tilde{Q}_i^2\rangle\right\} + \sum_I F_I\tilde{q}_I + \frac{1}{2}\sum_{I,J}F_{IJ}\tilde{q}_I\tilde{q}_J + \frac{1}{3!}\sum_{I,J,K}F_{IJK}\tilde{q}_I\tilde{q}_J\tilde{q}_K \\
&\quad + \frac{1}{4!}\sum_{I,J,K,L}F_{IJKL}\tilde{q}_I\tilde{q}_J\tilde{q}_K\tilde{q}_L + \frac{1}{2}\sum_{j\neq m}\sum_I F_{Ijj}\tilde{q}_I\langle\tilde{Q}_j^2\rangle + \frac{1}{2^2}\sum_{k\neq m}\sum_{I,J}F_{IJkk}\tilde{q}_I\tilde{q}_J\langle\tilde{Q}_k^2\rangle \\
&\quad + \frac{1}{2!2^2}{\sum_{i,j\neq m}}' F_{iijj}\langle\tilde{Q}_i^2\rangle\langle\tilde{Q}_j^2\rangle + \ldots, \qquad (2.5)\\
\tilde{U}^{(1)}_{m,s} &= F_m + \sum_I F_{mI}\tilde{q}_I + \frac{1}{2}\sum_{I,J}F_{mIJ}\tilde{q}_I\tilde{q}_J + \frac{1}{3!}\sum_{I,J,K}F_{mIJK}\tilde{q}_I\tilde{q}_J\tilde{q}_K + \frac{1}{4!}\sum_{I,J,K,L}F_{mIJKL}\tilde{q}_I\tilde{q}_J\tilde{q}_K\tilde{q}_L \\
&\quad + \frac{1}{2}\sum_{i\neq m}F_{mii}\langle\tilde{Q}_i^2\rangle + \frac{1}{2}\sum_{j\neq m}\sum_I F_{mIjj}\tilde{q}_I\langle\tilde{Q}_j^2\rangle + \frac{1}{2^2}\sum_{k\neq m}\sum_{I,J}F_{mIJkk}\tilde{q}_I\tilde{q}_J\langle\tilde{Q}_k^2\rangle \\
&\quad + \frac{1}{2!2^2}{\sum_{i,j\neq m}}' F_{miijj}\langle\tilde{Q}_i^2\rangle\langle\tilde{Q}_j^2\rangle + \ldots, \qquad (2.6)
\end{aligned}$$

and

$$\begin{aligned}
\tilde{U}^{(2)}_{m,s} &= F_{mm} + \sum_I F_{mmI}\tilde{q}_I + \frac{1}{2}\sum_{I,J}F_{mmIJ}\tilde{q}_I\tilde{q}_J + \frac{1}{3!}\sum_{I,J,K}F_{mmIJK}\tilde{q}_I\tilde{q}_J\tilde{q}_K + \frac{1}{4!}\sum_{I,J,K,L}F_{mmIJKL}\tilde{q}_I\tilde{q}_J\tilde{q}_K\tilde{q}_L \\
&\quad + \frac{1}{2}\sum_{i\neq m}F_{mmii}\langle\tilde{Q}_i^2\rangle + \frac{1}{2}\sum_{j\neq m}\sum_I F_{mmIjj}\tilde{q}_I\langle\tilde{Q}_j^2\rangle + \frac{1}{2^2}\sum_{k\neq m}\sum_{I,J}F_{mmIJkk}\tilde{q}_I\tilde{q}_J\langle\tilde{Q}_k^2\rangle \\
&\quad + \frac{1}{2!2^2}{\sum_{i,j\neq m}}' F_{mmiijj}\langle\tilde{Q}_i^2\rangle\langle\tilde{Q}_j^2\rangle + \ldots, \qquad (2.7)
\end{aligned}$$

where the normal modes labeled by capital letters are those transforming as the totally symmetric irreducible representation, while those in small letters can be of any irreducible representation. We make this distinction because, for a molecule in an Abelian point-group symmetry, an anharmonic geometry correction ($\tilde{q}_I$) can be nonzero if and only if mode I transforms as the totally symmetric irreducible representation. In the above expressions, a great many force constants of types that are not seen in XVSCF(n) appear. However, they are relatively infinitesimally few in a bulk periodic solid because totally symmetric normal coordinates in such a system exist only at the Brillouin zone center. This also explains the size consistency of the above expressions, which will be discussed in greater detail in Sec. 2.1.3.

Equations (2.5)–(2.7) can furthermore be brought into forms isomorphic to Eqs. (1.41)–(1.43),

$$\begin{aligned}
\tilde{U}^{(0)}_{m,s} &= \tilde{V}_0 + \frac{1}{2}\sum_{i\neq m}\left\{-\left\langle\frac{\partial^2}{\partial\tilde{Q}_i^2}\right\rangle + \tilde{F}_{ii}\langle\tilde{Q}_i^2\rangle\right\} + \frac{1}{2!2^2}{\sum_{i,j\neq m}}'\tilde{F}_{iijj}\langle\tilde{Q}_i^2\rangle\langle\tilde{Q}_j^2\rangle + \ldots, \qquad (2.8)\\
\tilde{U}^{(1)}_{m,s} &= \tilde{F}_m + \frac{1}{2}\sum_{i\neq m}\tilde{F}_{mii}\langle\tilde{Q}_i^2\rangle + \frac{1}{2!2^2}{\sum_{i,j\neq m}}'\tilde{F}_{miijj}\langle\tilde{Q}_i^2\rangle\langle\tilde{Q}_j^2\rangle + \ldots, \qquad (2.9)\\
\tilde{U}^{(2)}_{m,s} &= \tilde{F}_{mm} + \frac{1}{2}\sum_{i\neq m}\tilde{F}_{mmii}\langle\tilde{Q}_i^2\rangle + \frac{1}{2!2^2}{\sum_{i,j\neq m}}'\tilde{F}_{mmiijj}\langle\tilde{Q}_i^2\rangle\langle\tilde{Q}_j^2\rangle + \ldots, \qquad (2.10)
\end{aligned}$$

by introducing the new force constants $\tilde{F}$ and $\tilde{V}_0$, which are related to the bare force constants by

$$\tilde{V}_0 = V_0 + \sum_I F_I \tilde{q}_I + \frac{1}{2!}\sum_{I,J} F_{IJ}\tilde{q}_I\tilde{q}_J + \frac{1}{3!}\sum_{I,J,K} F_{IJK}\tilde{q}_I\tilde{q}_J\tilde{q}_K + \ldots, \tag{2.11}$$

$$\tilde{F}_i = F_i + \sum_J F_{iJ}\tilde{q}_J + \frac{1}{2!}\sum_{J,K} F_{iJK}\tilde{q}_J\tilde{q}_K + \frac{1}{3!}\sum_{J,K,L} F_{iJKL}\tilde{q}_J\tilde{q}_K\tilde{q}_L + \ldots, \tag{2.12}$$

$$\tilde{F}_{ii} = F_{ii} + \sum_J F_{iiJ}\tilde{q}_J + \frac{1}{2!}\sum_{J,K} F_{iiJK}\tilde{q}_J\tilde{q}_K + \frac{1}{3!}\sum_{J,K,L} F_{iiJKL}\tilde{q}_J\tilde{q}_K\tilde{q}_L + \ldots, \tag{2.13}$$

$$\tilde{F}_{ijj} = F_{ijj} + \sum_K F_{ijjK}\tilde{q}_K + \frac{1}{2!}\sum_{K,L} F_{ijjKL}\tilde{q}_K\tilde{q}_L + \frac{1}{3!}\sum_{K,L,M} F_{ijjKLM}\tilde{q}_K\tilde{q}_L\tilde{q}_M + \ldots, \tag{2.14}$$

$$\tilde{F}_{iijj} = F_{iijj} + \sum_K F_{iijjK}\tilde{q}_K + \frac{1}{2!}\sum_{K,L} F_{iijjKL}\tilde{q}_K\tilde{q}_L + \frac{1}{3!}\sum_{K,L,M} F_{iijjKLM}\tilde{q}_K\tilde{q}_L\tilde{q}_M + \ldots, \tag{2.15}$$

and so forth, where the capital letters again label totally symmetric normal modes. In Sec. 2.1.3, we show that the force constants defined by Eqs. (2.11)–(2.15) have the same size dependence as the bare force constants, namely, $K^{1-n/2}$ for an nth-order force constant. This in conjunction with the fact that Eqs. (2.8)–(2.10) are isomorphic to Eqs. (1.41)–(1.43) is sufficient to prove that $\tilde{U}^{(0)}_{m,s}$, $\tilde{U}^{(1)}_{m,s}$, and $\tilde{U}^{(2)}_{m,s}$ scale as K^1, $K^{1/2}$, and K^0, respectively, as before.

In XVSCF[n], Eq. (2.4) needs to be solved to determine $\tilde{\boldsymbol{q}}$ using $\tilde{U}^{(1)}_{m,s}$ given by Eq. (2.9). The expectation values, $\langle\tilde{Q}_i^2\rangle$, appearing in this equation can be evaluated analytically by

$$\langle\tilde{Q}_m^2\rangle = \frac{s_m + 1/2}{\tilde{\omega}_m}, \tag{2.16}$$

of which the denominator is simply,

$$\tilde{\omega}_m = \{\tilde{U}^{(2)}_{m,s}\}^{1/2}. \tag{2.17}$$

Here, $\tilde{U}^{(2)}_{m,s}$ [Eq. (2.10)] in turn depends on $\tilde{\boldsymbol{q}}$ through Eqs. (2.12)–(2.15). Thus, these XVSCF[n] equations determining anharmonic frequencies and geometries are coupled with one another and must be solved self-consistently. The algorithm for achieving this is discussed in the next section. Once self-consistency is achieved, the total vibrational energy of the molecule in state s is obtained by evaluating

$$\begin{aligned} E_s = {} & \tilde{V}_0 + \frac{1}{2}\sum_i \left\{ -\left\langle \frac{\partial^2}{\partial\tilde{Q}_i^2}\right\rangle + \tilde{F}_{ii}\langle\tilde{Q}_i^2\rangle \right\} + \frac{1}{2!2^2}{\sum_{i,j}}' \tilde{F}_{iijj}\langle\tilde{Q}_i^2\rangle\langle\tilde{Q}_j^2\rangle \\ & + \frac{1}{3!2^3}{\sum_{i,j,k}}' \tilde{F}_{iijjkk}\langle\tilde{Q}_i^2\rangle\langle\tilde{Q}_j^2\rangle\langle\tilde{Q}_k^2\rangle + \ldots, \end{aligned} \tag{2.18}$$

using

$$\left\langle \frac{\partial^2}{\partial \tilde{Q}_m^2} \right\rangle = -\tilde{\omega}_m(s_m + 1/2). \tag{2.19}$$

In the bulk limit, the anharmonic frequencies and geometries of XVSCF[n] are identical to what one would obtain from VSCF using the same nth-order force field. This is because only those terms that have nonphysical size dependence and vanish in the bulk limit are removed from the former. This is confirmed numerically in Sec. 2.4.

2.1.3 Size consistency of XVSCF[n]

Force constants such as F_{ijk} and F_{ijkl} are absent in the XVSCF(n) formalism[21] because they cannot be a part of diagrammatically size-consistent contributions. However, these force constants reemerge in Eqs. (2.8)–(2.10) of XVSCF[n] as F_{IJK}, F_{IJKL}, etc., insofar as I, J, K, and L are the normal modes that transform as the totally symmetric irreducible representation. Here, we show that XVSCF[n] remains strictly size consistent despite these force constants.

The size dependence of the terms in the formalisms of electronic and vibrational structure methods is the same as their dependence on the number (K; not to be confused with one of the phonon branch indices) of the wave vector sampling points in the reciprocal unit cell in the corresponding formalisms for crystals under the periodic boundary conditions.[20] Under the conditions, each each normal mode index becomes a composite index of a phonon branch (i) and a wave vector ($\boldsymbol{k}_i$). Since an anharmonic correction must preserve the symmetry of the crystals, a geometry correction along a normal coordinate that is not totally symmetric should always be null. Therefore, the anharmonic geometry corrections are zero if $i\boldsymbol{k}_i$ involves a nuclear displacement which lifts the symmetry of the crystals. Certain phonon branches lift the symmetry of the unit cell geometry regardless of the value of $\boldsymbol{k}_i$. We use capital letters, I, J, K, and L, for the phonon branches that do not lift the symmetry of the unit cell geometry. Additionally, the normal modes with nonzero wave vectors always lift the periodic symmetry of the crystal and, hence, the anharmonic geometry corrections exist only at the Brillouin zone center ($\boldsymbol{k}_i = \boldsymbol{0}$). Together, we surmise that we only need to consider the anharmonic geometry corrections of the type $\tilde{q}_{I\boldsymbol{0}}$.

The corresponding formulas of Eqs. (2.11)–(2.15) (truncated after quartic terms for brevity) for crystals under the periodic boundary conditions are obtained by systematic replacement of each normal mode index by an appropriate composite index of a phonon branch and a wave vector:

$$\begin{aligned}\tilde{V}_0 = {} & V_0 + \sum_I F_{I\boldsymbol{0}}\tilde{q}_{I\boldsymbol{0}} + \frac{1}{2!}\sum_{I,J} F_{I\boldsymbol{0}J\boldsymbol{0}}\tilde{q}_{I\boldsymbol{0}}\tilde{q}_{J\boldsymbol{0}} + \frac{1}{3!}\sum_{I,J,K} F_{I\boldsymbol{0}J\boldsymbol{0}K\boldsymbol{0}}\tilde{q}_{I\boldsymbol{0}}\tilde{q}_{J\boldsymbol{0}}\tilde{q}_{K\boldsymbol{0}} \\ & + \frac{1}{4!}\sum_{I,J,K,L} F_{I\boldsymbol{0}J\boldsymbol{0}K\boldsymbol{0}L\boldsymbol{0}}\tilde{q}_{I\boldsymbol{0}}\tilde{q}_{J\boldsymbol{0}}\tilde{q}_{K\boldsymbol{0}}\tilde{q}_{L\boldsymbol{0}},\end{aligned} \tag{2.20}$$

$$\tilde{F}_{I\mathbf{0}} = F_{I\mathbf{0}} + \sum_J F_{I\mathbf{0}J\mathbf{0}}\tilde{q}_{J\mathbf{0}} + \frac{1}{2!}\sum_{J,K} F_{I\mathbf{0}J\mathbf{0}K\mathbf{0}}\tilde{q}_{J\mathbf{0}}\tilde{q}_{K\mathbf{0}} + \frac{1}{3!}\sum_{J,K,L} F_{I\mathbf{0}J\mathbf{0}K\mathbf{0}L\mathbf{0}}\tilde{q}_{J\mathbf{0}}\tilde{q}_{K\mathbf{0}}\tilde{q}_{L\mathbf{0}}, \tag{2.21}$$

$$\tilde{F}_{i-\boldsymbol{k}_i i\boldsymbol{k}_i} = F_{i-\boldsymbol{k}_i i\boldsymbol{k}_i} + \sum_J F_{i-\boldsymbol{k}_i i\boldsymbol{k}_i J\mathbf{0}}\tilde{q}_{J\mathbf{0}} + \frac{1}{2!}\sum_{J,K} F_{i-\boldsymbol{k}_i i\boldsymbol{k}_i J\mathbf{0}K\mathbf{0}}\tilde{q}_{J\mathbf{0}}\tilde{q}_{K\mathbf{0}}, \tag{2.22}$$

$$\tilde{F}_{I\mathbf{0}j-\boldsymbol{k}_j j\boldsymbol{k}_j} = F_{I\mathbf{0}j-\boldsymbol{k}_j j\boldsymbol{k}_j} + \sum_K F_{I\mathbf{0}j-\boldsymbol{k}_j j\boldsymbol{k}_j K\mathbf{0}}\tilde{q}_{K\mathbf{0}}, \tag{2.23}$$

and

$$\tilde{F}_{i-\boldsymbol{k}_i i\boldsymbol{k}_i j-\boldsymbol{k}_j j\boldsymbol{k}_j} = F_{i-\boldsymbol{k}_i i\boldsymbol{k}_i j-\boldsymbol{k}_j j\boldsymbol{k}_j}, \tag{2.24}$$

where we have taken into account the fact that nonzero elements of $\tilde{F}_{i\boldsymbol{k}_i}$ and $\tilde{F}_{i\boldsymbol{k}_i j-\boldsymbol{k}_j j\boldsymbol{k}_j}$ are the types given in Eqs. (2.21) and (2.23).

Notice that no summation over wave vector indices appears in these equations. Let us inspect the size dependence of these effective force constants of XVSCF[4]; the conclusion can be readily extended to a higher-ranked member of the method. A bare force constant (F) of order n has the size dependence of $K^{1-n/2}$.[17,65] Geometry corrections ($\tilde{q}$) in normal coordinates scale as $K^{1/2}$.[17,65] Using these, we find each term in Eq. (2.20) to scale consistently and correctly as K^1. That is, the first term, V_0, is obviously extensive. The second term scales as K^1 because $F_{I\mathbf{0}}$ and $\tilde{q}_{I\mathbf{0}}$ are both $K^{1/2}$ quantities. The three factors in the third term scale as K^0, $K^{1/2}$, and $K^{1/2}$, respectively, resulting in K^1 dependence for the third term. The fourth and fifth terms can also be shown to be extensive by the analogous logic: the bare nth-order force constant (the $K^{1-n/2}$ scaling) is multiplied by n geometry corrections which each scale as $K^{1/2}$. Similarly, it can be seen that each term in Eq. (2.21) scales as $K^{1/2}$, Eq. (2.22) as K^0, Eq. (2.23) as $K^{-1/2}$, and Eq. (2.24) as K^{-1}. In short, an effective force constant ($\tilde{F}$) of order n displays the same $K^{1-n/2}$ dependence as a bare nth-order force constant.

Since Eqs. (2.8)–(2.10) are isomorphic to Eqs. (1.41)–(1.43), the demonstration of the same size dependence between $\tilde{F}$ and F is sufficient to prove the size consistency of XVSCF[n], provided the fact that XVSCF(n) is diagrammatically size consistent. It should also be noted that the XVSCF[n] equations reduce exactly to those of XVSCF(n) once the origins of the normal coordinates are centered at the minima of the mean-field potentials via the iterative procedure described in Sec. 2.2.2. This also proves the size consistency of XVSCF[n].

Note also that, since Eqs. (2.20)–(2.24) have the consistent and correct size dependence term-by-term, any subset of these equations also has the same, correct size dependence. This means that the nMR approximation does not alter the size dependence of these force constants or impair the size consistency of XVSCF[n].

Finally, despite the appearance of a greater variety of force constant types in XVSCF[n], the actual number of force constants needed in a XVSCF[n] calculation for periodic solids does not grow any more rapidly than in a XVSCF(n) calculation. For instance, the number of the additional quartic force constants needed in XVSCF[4] are of the type,

$F_{\boldsymbol{l}0\boldsymbol{J}0\boldsymbol{K}0\boldsymbol{L}0}$, is only $O(N^4)$ (where N is again the number of phonon branches that do not lift the unit cell symmetry), which is infinitesimally small compared to the number of quartic force constants in XVSCF(4), $F_{i-\boldsymbol{k}_i i\boldsymbol{k}_i j-\boldsymbol{k}_j j\boldsymbol{k}_j}$, which is $O(M^2K^2)$. In fact, for periodic solids, XVSCF(n) and XVSCF[n] have the same cost scaling and are expected to be vastly faster than VSCF, which scales as $O(M^4K^4)$ with a QFF.

2.2 Algorithms and implementation

2.2.1 XVSCF(n)

Keçeli and Hirata[21] implemented XVSCF(n) with $n = 4$ only for anharmonic total energies and transition frequencies. Here, we report an implementation of XVSCF(4) for total energies and frequencies as well as for anharmonic geometry corrections. The latter are computed by Eq. (2.2).

The programmable equations of XVSCF(4) are

$$U^{(1)}_{m,s} = F_m + \sum_{i\neq m} F_{mii}\frac{s_i + 1/2}{2\omega_i}, \tag{2.25}$$

$$U^{(2)}_{m,s} = F_{mm} + \sum_{i\neq m} F_{mmii}\frac{s_i + 1/2}{2\omega_i}. \tag{2.26}$$

Equations (1.46) and (2.26) for the anharmonic transition energy for one mode (ω_i) are coupled with those of all the other modes. They are solved to reach self-consistency with an iterative algorithm outlined in Fig. 2.1. Convergence of all frequencies to within 10^{-8} cm^{-1} typically occurs after at most 15 cycles. Once self-consistent solutions for all ω_i's are obtained, Eq. (2.25) is evaluated and substituted into Eq. (2.2) to yield an anharmonic geometry correction for each mode. Finally, the total energy of the vibrational state is obtained by

$$E_s = V_0 + \sum_i \left(\omega_i^2 + F_{ii}\right)\frac{s_i + 1/2}{2\omega_i} + \frac{1}{2!}{\sum_{i,j}}' F_{iijj}\frac{s_i + 1/2}{2\omega_i}\frac{s_j + 1/2}{2\omega_j}. \tag{2.27}$$

Programmable equations for XVSCF(n) with $n > 4$ can be easily obtained by truncating Eqs. (1.41)–(1.43) after terms containing force constants of order n.

The diagrammatic expressions for $U^{(1)}_{m,s}$ and $U^{(2)}_{m,s}$ are given in Figs. 2.2 and 2.3, respectively. The same for E_s can be found in Ref. 21. The diagrams shown are for XVSCF(n) with an arbitrary value of n, but pertain to the fundamental frequency and anharmonic geometry correction along the mth mode. Note that $U^{(1)}_{m,s}$ and $U^{(2)}_{m,s}$ are divided by $\sqrt{2\omega_m}$ and $2\omega_m$, respectively, in the left-hand sides of these diagrammatic equations. This is necessary if we are to interpret these diagrams as self-energy terms in the Dyson equation for single-particle Green's functions.[23,70] The short stubs are not zeroth-order Green's functions, but are there merely to indicate the ranks (number of edges) of the vertices.

A filled circle vertex with n edges is an nth-order force constant with each edge denoting a normal mode, divided by $\sqrt{2\omega_i}$ for every edge labeled i. Short stubs are always labeled m. A loop corresponds to a factor $(s_i + 1/2)$ where i is the normal-mode index of the loop. Summations must be taken over all internal edges (the edges that are connected to vertices at both ends) including loop edges. A factor of $1/n!$ must be multiplied to the expression when there are n equivalent edges; two edges are deemed equivalent when they are connected to the same pair of vertices. The $U^{(1)}_{m,s}$ diagrams are connected and isomorphic to the gradient diagram (the first diagram in the right-hand side of Fig. 2.2), scaling as $K^{1/2}$. The $U^{(2)}_{m,s}$ diagrams are also connected and isomorphic to the harmonic force constant diagram (the first diagram in the right-hand side of Fig. 2.3), scaling as K^0.

The computational cost of vibrational structure calculations is usually dominated by the construction of the PES. The cost of evaluating a general nth-order force field scales as $O(M^n)$. Therefore, this is the overall scaling of VSCF. In contrast, XVSCF(n) uses a small number of the force constants in an nth-order Taylor expansion of $V(\boldsymbol{Q})$. For XVSCF(4), only force constants of the types, F_i, F_{ii}, F_{ijj}, and F_{iijj}, are needed. The cost of evaluating these force constants scales as only $O(M^{n/2})$.

In cases where great many vibrational states need to be considered[71] or the PES is somehow obtained inexpensively, the overall computational cost may instead be dominated by the solution of the vibrational Schrödinger equation. One cycle of the XVSCF(n) iteration, the evaluation of the total vibrational energy, and the calculation of anharmonic geometry corrections for all modes all involve only $O(M^{n/2})$ arithmetic operations. Therefore, the overall cost of XVSCF(n) scales as $O(M^{n/2})$ regardless of whether the PES scan is the cost-determining step. The number of arithmetic operations in the VSCF solver grows as $O(M^n)$ as it is implemented in virtually any program. We will, however, point out below that this is not the optimal scaling when the distinction between totally symmetric and non-totally symmetric modes is made. In either case, XVSCF(n) has a superior cost scaling as compared to VSCF for any truncation order n and this advantage grows with n.

2.2.2 XVSCF[n]

We have introduced XVSCF[n] and implemented it at $n = 4$ for anharmonic total energies and transition frequencies as well as for anharmonic geometry corrections.

The programmable equations for XVSCF[4] are Eqs. (2.4) and (2.17) as well as the following:

$$\begin{aligned}\tilde{U}^{(1)}_{m,s} &= F_m + \sum_I F_{mI}\tilde{q}_I + \frac{1}{2!}\sum_{I,J} F_{mIJ}\tilde{q}_I\tilde{q}_J + \frac{1}{3!}\sum_{I,J,K} F_{mIJK}\tilde{q}_I\tilde{q}_J\tilde{q}_K + \sum_{i\neq m} F_{mii}\frac{s_i + 1/2}{2\tilde{\omega}_i} \\ &\quad + \sum_{i\neq m}\sum_J F_{miiJ}\frac{s_i + 1/2}{2\tilde{\omega}_i}\tilde{q}_J, \qquad (2.28)\\ \tilde{U}^{(2)}_{m,s} &= F_{mm} + \sum_I F_{mmI}\tilde{q}_I + \frac{1}{2}\sum_{I,J} F_{mmIJ}\tilde{q}_I\tilde{q}_J + \sum_{i\neq m} F_{mmii}\frac{s_i + 1/2}{2\tilde{\omega}_i}, \qquad (2.29)\end{aligned}$$

and

$$
\begin{aligned}
E_s &= V_0 + \frac{1}{2}\sum_i \tilde{\omega}_i(s_i+1/2) + \sum_I F_I\tilde{q}_I + \frac{1}{2!}\sum_{I,J} F_{IJ}\tilde{q}_I\tilde{q}_J + \frac{1}{3!}\sum_{I,J,K} F_{IJK}\tilde{q}_I\tilde{q}_J\tilde{q}_K \\
&\quad + \frac{1}{4!}\sum_{I,J,K,L} F_{IJKL}\tilde{q}_I\tilde{q}_J\tilde{q}_K\tilde{q}_L + \sum_i F_{ii}\frac{s_i+1/2}{2\tilde{\omega}_i} + \sum_i\sum_J F_{iiJ}\frac{s_i+1/2}{2\tilde{\omega}_i}\tilde{q}_J \\
&\quad + \frac{1}{2!}\sum_i\sum_{J,K} F_{iiJK}\frac{s_i+1/2}{2\tilde{\omega}_i}\tilde{q}_J\tilde{q}_K + \frac{1}{2!}{\sum_{i,j}}' F_{iijj}\frac{s_i+1/2}{2\tilde{\omega}_i}\frac{s_j+1/2}{2\tilde{\omega}_j}.
\end{aligned} \tag{2.30}
$$

These are obtained by substituting Eqs. (2.16) and (2.19) into Eqs. (2.6), (2.7), and (2.18). Programmable equations for XVSCF[n] with $n > 4$ can be most straightforwardly obtained by truncating Eqs. (2.8)–(2.15) and (2.18) after higher-order terms and by generalizing Eqs. (2.11)–(2.15) to force constants of any order less than or equal to n.

Since Eq. (2.4) for anharmonic geometry corrections and Eq. (2.17) for anharmonic frequencies are coupled, we solve them simultaneously using the iterative algorithm outlined in Fig. 2.4. The initial guess for $\tilde{\boldsymbol{q}}$ can be zero. In each cycle of the iteration, the value of $\tilde{q}_m$ is updated to the new value, $\tilde{q}_m - \tilde{U}^{(1)}_{m,s}/\tilde{U}^{(2)}_{m,s}$, for all modes. The anharmonic frequencies, $\tilde{\omega}_m$'s, are also updated using Eq. (2.17). This is repeated until all $\tilde{\omega}_m$'s and $\tilde{q}_m$'s cease to change more than preset tolerances, at which point $\tilde{q}_m$ is the anharmonic correction to the equilibrium geometry along the mth normal mode.

The iterative algorithm can be based on nested two-fold loops: the inner loop solving Eq. (2.17) for $\tilde{\omega}_m$'s until convergence and the outer solving Eq. (2.4) for $\tilde{q}_m$'s. However, our preferred algorithm has just one loop solving both simultaneously (as shown in Fig. 2.4), which works well. In either algorithm, with successive cycles, the quotient, $-\tilde{U}^{(1)}_{m,s}/\tilde{U}^{(2)}_{m,s}$, approaches zero. Once all frequencies and geometries are converged, the vibrational energy is evaluated by Eq. (2.30). Convergence to within 10^{-8} cm^{-1} for frequencies and to within 10^{-10} a.u. for geometries typically requires at most 30 cycles.

The diagrammatic expressions for $\tilde{U}^{(1)}_{m,s}$, $\tilde{U}^{(2)}_{m,s}$, and E_s for XVSCF[n] are presented in Figs. 2.5–2.7, whose corresponding algebraic expressions are found in Eqs. (2.28)–(2.30), respectively. The diagrams with the same topology but having all distinct vertical orderings of nonequivalent vertices are grouped together in the parentheses. They add up to become the corresponding term in the algebraic expression. Loops and filled circle vertices are interpreted as previously discussed except $\tilde{\omega}_i$ is substituted for ω_i. Cross vertices are interpreted as $-\tilde{q}_I\tilde{\omega}_I^2/\sqrt{2\tilde{\omega}_I}$. Each diagram containing n total vertices also carries a denominator which is the product of $n-1$ terms, which are obtained by drawing a horizontal line between each vertically adjacent pair of vertices and subtracting the frequencies of the normal modes associated with each edge crossed by the line, not including loops and not including short stubs. For example, the first diagram in the second term of Fig. 2.5 has a denominator of $-\tilde{\omega}_I$. The three diagrams in the third term have denominators of $(-\tilde{\omega}_I)(-\tilde{\omega}_I-\tilde{\omega}_J)$, $(-\tilde{\omega}_I)(-\tilde{\omega}_J)$, and $(-\tilde{\omega}_I-\tilde{\omega}_J)(-\tilde{\omega}_J)$, respectively, where I is the normal mode index

associated with the edge connecting to the upper cross vertex and J to the lower.

Equations (2.28)–(2.30) involve three-, two-, and four-fold summations, respectively, over totally symmetric modes. We need to evaluate E_s only once and $\tilde{U}^{(1)}_{m,s}$ for all totally symmetric modes and, therefore, the cost of evaluating these scales as $O(N^4)$, where N is the number of the totally symmetric normal modes. On the other hand, $\tilde{U}^{(2)}_{m,s}$ must be evaluated for all modes and the associated cost grows as $O(MN^2)$, where M is the number of modes. In a nonperiodic system, N and M increase roughly proportionally with size and, hence, the overall cost scaling of the XVSCF[4] solver is $O(N^4)$. The cost of constructing the PES can also be made to scale no greater than $O(N^4)$ if the symmetries of the normal modes can be utilized in this step. Generally, the cost scaling of XVSCF[n] for molecules is, therefore, $O(N^n)$.

In the previous section, we mentioned that VSCF with a nth-order force field has the overall cost scaling of $O(M^n)$. If we can exploit the symmetries of normal modes, this is no longer the optimal scaling. It can be shown that VSCF can be carried out with just $O(N^n)$ arithmetic operations because the expectation values of normal modes that are multiplied with the nth-order force constants always vanish unless the normal modes are totally symmetric. Though our implementation of VSCF does not utilize this trick (nor does any other existing implementation to our knowledge), if it did, XVSCF[n] and VSCF with a nth-order force field have the same $O(N^n)$ scaling for molecules.

2.2.3 Comparison of methods

Table 2.4 compares XVSCF(n), XVSCF[n], and VSCF in the case of a quartic force field (QFF) ($n = 4$). The mean-field potentials of both XVSCF methods have a quadratic form, rendering the XVSCF modals analytically obtainable and removing the need for any basis-set expansion, quadrature, or matrix diagonalization from their algorithms, which are inevitable in VSCF. Consequently, both XVSCF methods are vastly faster than VSCF. The results obtained from all three are comparable with one another.

Since XVSCF[n] is defined by merely eliminating all the terms in the VSCF equations that vanish in the bulk limit, XVSCF[n] and VSCF are one and the same method in this limit; only, the latter is far less efficient than the former. XVSCF(n) may be seen as a further simplification to XVSCF[n] with substitutions $V(\boldsymbol{Q}) = V_n(\boldsymbol{Q})$ for energies and $V(\boldsymbol{Q}) = V_{n-1}(\boldsymbol{Q})$ for geometries. The primary benefit of this approximation is that the number of force constants needed is dramatically reduced and the scaling of computational cost is thus decreased from $O(N^n)$ to $O(M^{n/2})$. XVSCF(n) is, therefore, particularly well suited for practical applications on large molecules and solids. Both XVSCF(n) and XVSCF[n] are rigorously size consistent for anharmonic total energies, transition frequencies, and geometry corrections. The VSCF equations are size consistent for none of these quantities.

An alternative way to render VSCF size consistent is to express the Hamiltonian using local coordinates. Any vibrational or electronic method is size consistent when local coordinates or a local basis are used; local coordinates

render the Hamiltonian additively separable in space. An electronic example is Pulay's local CI,[72] which is size-consistent. However, insofar as normal coordinates are used in vibrational methods in practice, it is necessary to understand the intrinsic size consistency of methods in the sense of Goldstone's linked diagram theorem. See Ref. 17 for an in-depth analysis on the issue of size consistency.

XVSCF[n] is operationally similar to the effective harmonic oscillator (EHO) method developed by Spiridonov *et al.*[73,74] using finite-temperature thermodynamic perturbation theory.[75] In the EHO model, the center and frequency of harmonic oscillator wave functions are variationally optimized in a manner similar to XVSCF[n]. Roy and Prasad implemented[63] a zero-temperature EHO algorithm and showed that variationally optimized harmonic oscillator wave functions had overlaps of greater than 90% with full VSCF modals. These methods are not derived from the size-consistency arguments and thus contain terms with nonphysical size dependence, unlike XVSCF[n]. Nevertheless, this work reflects the usefulness of replacing VSCF modals by effective harmonic oscillator wave functions and foreshadows our developments.

XVSCF[n] is a diagonal approximation to the self-consistent phonon (SCP) method[31,32,76] using normal coordinates. The SCP method normally determines not only the frequencies and geometries but also the coordinates of semi-independent oscillators and can, therefore, start with arbitrary coordinates such as the Cartesian coordinates. XVSCF(n) and XVSCF[n], on the other hand, are defined for normal coordinates since they originate from VSCF using normal coordinates. Our diagrammatic equations are also similar to those of the "optimized quadratic approximation" developed by Cao and Voth[77] that maps a system with a general PES onto one with effective harmonic oscillators.

It is also noteworthy that, in the context of quantum dissipative dynamics, Makri[68] has shown that a bath of semi-independent oscillators interacting with a system in a uniform way must always be effectively harmonic in the bulk limit. This finding is consistent with our conclusion that the mean-field potentials of VSCF becomes effectively harmonic in a bulk crystal.[20] Makri's theorem is based on the size dependence of interaction parameters derived by Suarez and Silbey,[78] which is also reminiscent of the size dependence of force constants we rely on.

2.3 Numerical tests

We applied XVSCF(4), XVSCF[4], and VSCF with a QFF to a model system of unit masses connected by anharmonic springs, and the water, naphthalene, and anthracene molecules. The QFF for water was computed at the MP2/aug-cc-pVTZ level and those for the polyacenes were computed at the MP2/STO-3G level in the two-mode coupling (2MR) approximation of Gerber *et al.*[79,80] The numerical accuracy of these molecular force fields is not important here. The QFF's were obtained with SINDO,[81] running the electronic structure calculations with NWCHEM.[82]

We used the twenty lowest-lying harmonic oscillator wave functions for each mode as a basis set in all of the VSCF and vibrational configuration-interaction (VCI) (Ref. 83) calculations. There is no need for a basis set in XVSCF(4) or XVSCF[4]. We performed full VCI calculations on water using either the QFF or the modified QFF in which force constants (F_{iii}, F_{iij}, and F_{iiii}) that contribute to the cubic ($U^{(3)}_{m,s}$) and quartic ($U^{(4)}_{m,s}$) force constants of the mean-field potentials are eliminated. The latter is denoted as VCI′.

There are two ways to obtain transition frequencies from VSCF or XVSCF. One is to perform separate (X)VSCF calculations for two vibrational states and take the energy difference. We call this the "state-specific" approach (which may be more commonly referred to as ΔSCF in electronic structure theory). The other is to perform one (X)VSCF calculation for a single vibrational state (typically the zero-point or ground state) and obtain transition frequencies as the energy differences of the eigenvalue solutions of the one-mode (X)VSCF equations [Eq. (1.33)]. We call this the "virtual" approach as it involves the energies of the unoccupied (virtual) modals.

We used both state-specific and virtual approaches in the VSCF calculations for molecular frequencies. On the other hand, the molecular frequencies of XVSCF(n) and XVSCF[n] were always computed with the virtual approach. This is because the frequencies obtained by the state-specific approach do not easily lend themselves to diagrammatic size-consistency analysis and are incongruous with the philosophy of XVSCF. However, all (X)VSCF calculations for geometries were carried out in the state-specific manner because the geometry corrections of "virtual" XVSCF would be identical for all states. The energies, frequencies, and geometry corrections of VCI for all states were obtained using a single VSCF reference wave function of the zero-point state.

The 2MR approximation employed for the force fields of the polyacenes limits force constants to only those that couple up to two modes. Thus, a QFF with 2MR does not have force constants of the types, F_{ijk}, F_{iijk}, and F_{ijkl}. This does not affect XVSCF(4) because these force constants are not used in the first place. It does not impair the size consistency of XVSCF[4], either (see Sec. 2.1.3).

2.4 One-dimensional chains

Here, we numerically analyze the size dependence of the mean-field potentials of XVSCF(n), XVSCF[n], and VSCF using a one-dimensional model consisting of $N + 1$ unit masses experiencing the nearest-neighbor interactions expressed as a QFF.

Let x_κ be the displacement of the κth mass from its equilibrium position. The potential energy, $V(\boldsymbol{x})$, is defined as

$$V(\boldsymbol{x}) = \frac{1}{2!}\sum_{\kappa=1}^{N}(x_{\kappa+1}-x_\kappa)^2 + \frac{1}{3!}\sum_{\kappa=1}^{N}(x_{\kappa+1}-x_\kappa)^3 + \frac{1}{4!}\sum_{\kappa=1}^{N}(x_{\kappa+1}-x_\kappa)^4. \tag{2.31}$$

This QFF in the Cartesian coordinates can be readily transformed into that in normal coordinates. We will examine the

mean-field potentials along the normal mode with the lowest nonzero harmonic frequency with a coordinate simply labeled as Q and a frequency labeled as ω. This mode corresponds to the "breathing" motion of the whole chain and belongs to the acoustic branch of phonon dispersion in the $N \to \infty$ limit. The symbol N denotes the size of the linear chain and is not to be confused with the number of totally symmetric normal modes discussed elsewhere.

Figure 2.8 plots the errors in the VSCF frequency from the converged value as a function of the number of the harmonic oscillator basis functions used to expand modals. As the chain becomes longer (N becomes larger), the size of the basis required to converge frequencies increases dramatically to as many as 60 functions per normal coordinate at $N = 64$. This is because, in longer chains, the minima of the mean-field potentials of VSCF shift away from the minimum of $V(\boldsymbol{Q})$ where the basis functions are centered, making the basis functions less and less effective in expanding the modals, as predicted by our analysis. This graph shows, therefore, that VSCF lacks not only size consistency but also numerical stability unless its algorithm somehow accounts for the shift by, for instance, floating or optimizing the basis functions and their centers as done by Roy and Prasad.[63] The centers of these floating basis functions should be close to vibrationally averaged geometries. Neither XVSCF(n) nor XVSCF[n] would display such pathology because they do not need a basis set.

Figures 2.9, 2.10, and 2.11 plot the VSCF, XVSCF(4), and XVSCF[4] mean-field potentials for the linear chains with $N = 4$, 16, and 64, respectively. The XVSCF(4) mean-field potentials are drawn centered at their corresponding anharmonic geometry corrections [Eq. (2.2)].

While the VSCF potential with $N = 4$ is visibly anharmonic, the potentials of the longer chains show progressively smaller degrees of anharmonicity, with the VSCF potential with $N = 64$ being in accurate agreement with the XVSCF[4] and XVSCF(4) potentials (the latter after a horizontal shift), which are both quadratic. This means that they have essentially reached the bulk limit at $N = 64$. In this limit, VSCF reduces exactly to XVSCF[4] and the anharmonic geometry correction of the latter agrees identically with the vibrationally averaged geometry of VSCF. Indeed, the potentials of VSCF and XVSCF[4] are indistinguishable from each other in Fig. 2.11 as both the centers and curvature become the same between the two potentials. The anharmonic geometry correction of XVSCF(4), on the other hand, does not coincide with the anharmonic vibrationally averaged geometry of VSCF. However, they agree reasonably well with each other, the former reproducing approximately 85% of the latter.

Figure 2.12 plots the differences in the zero-point energies per unit length (N) between XVSCF(4) or XVSCF[4] and VSCF zero-point energies as a function of N^{-1}. The XVSCF(4) error approaches a finite value at large N, suggesting that XVSCF(4) unit cell (intensive) energies differ from VSCF unit cell energies by a constant value even in the limit of infinite size. This is traced to the difference in the minima of the effective potentials between XVSCF(4) and VSCF. The XVSCF[4] error per N approaches zero as N^{-1}.

Table 2.1 summarizes the geometry corrections predicted by XVSCF(4), XVSCF[4], and VSCF for the chains in

the vibrational ground state and in the excited state in which the quantum numbers of all modes are simultaneously raised to one. If the geometry corrections are transformed from normal to internal coordinates, they are seen to converge to a constant, thus N-independent value. This is expected and reassuring as the corrections in local internal coordinates such as interatomic distances are thermodynamically intensive. This is also true for the excited state considered here because the excitation energy to this state grows as N^1 and thus has sufficient energy to cause a finite, intensive change to each of the interatomic distance (see also Sec. 2.4.2). The corrections predicted by XVSCF[4] and VSCF converge at the same values with increasing N in both the ground and excited states, as expected. The XVSCF(4) corrections are, again, approximately 85% of these converged values at $N = 64$ and are satisfactory given the ease and speed of the XVSCF(4) calculations.

It was suggested elsewhere[71] that the "virtual" (i.e. unoccupied) modals generated by traditional VSCF can be used to obtain thermally averaged properties of large molecules. Our foregoing analysis of the size dependence of the VSCF mean-field potentials indicates that this may be inappropriate if normal coordinates are used: in the bulk limit, all mean-field potentials of VSCF become quadratic, making all virtual modals have the same average geometry. A calculation of thermally averaged geometry using VSCF virtual modals is expected to produce nonphysical results that are increasingly insensitive to the temperature as the molecule becomes larger and which reduce to the zero-point geometry in the bulk limit. This is also true of XVSCF(n) and XVSCF[n] at any size, since "virtual" modals in these methods are obtained by simply changing the quantum numbers of the optimized harmonic oscillator wave functions. On the other hand, in the state-specific approach, the center of the mean-field potential varies with vibrational state, so thermally averaged geometries will remain meaningful even with quadratic mean-field potentials. The greater efficiency and superior scaling of XVSCF(n) and XVSCF[n] are valuable in this regard because in calculating thermal averages of large molecules a very large number of vibrational states must be treated. A finite-temperature extension of XVSCF, in which the mean-field operators are themselves thermally averaged, may be even more appealing.

2.4.1 The water molecule

The results for the water molecule in the vibrational ground state are given in Table 2.2. The XVSCF[4] frequencies are in remarkably good agreement with the "virtual" VSCF frequencies despite the small size of the molecule. This is in contrast with the rather poor agreement between XVSCF(4) and VSCF, which has already been documented.[21] Our earlier study[21] has concluded that this disagreement largely arises from the approximation $V(\boldsymbol{Q}) = V_4(\boldsymbol{Q})$ rather than from the small molecular size. The agreement between XVSCF[4] and VSCF supports this conclusion. It furthermore suggests that, once the odd-order force constants are included in the XVSCF[4] calculation to shift the centers of the mean-field potentials, their effects on anharmonic frequencies can also be captured surprisingly well even though the mean-field potentials are still quadratic. The largest discrepancy between XVSCF[4] and "virtual" VSCF can be seen

for the symmetric stretch (ν_2), which is expected because $U^{(3)}_{2,s}$ (or F_{222} that contributes to it) is large in VSCF whereas it is absent from XVSCF[4]. Nevertheless, the discrepancy (62 cm^{-1}) is significantly reduced from that seen between XVSCF(4) and VSCF (148 cm^{-1}). Table 2.2 (the ν_3 frequencies to be specific) also indicates that comparison of XVSCF is more appropriate with "virtual" VSCF than with "state-specific" VSCF as XVSCF frequencies are always based on the "virtual" approach.

Table 2.2 lists the vibrationally averaged OH bond length and HOH bond angle. The VSCF and VCI results are consistent with each other. Both XVSCF(4) and XVSCF[4] reproduce the signs of these anharmonic geometry corrections of VSCF and VCI; they correctly predict the elongation of the OH bond and narrowing of the HOH angle going from the equilibrium geometry to the zero-point geometry. However, they underestimate the magnitude of OH elongation by more than a factor of two and overestimate the HOH narrowing by more than a factor of four. There is evidence that this discrepancy is nearly entirely attributable to the smallness of the molecules. The VCI′ calculation excludes cubic and quartic force constants that are not part of $V_3(\boldsymbol{Q})$ or $V_4(\boldsymbol{Q})$, that is, the force constants of types, F_{iii}, F_{iiij}, and F_{iiii}. Their contributions to anharmonic frequencies or geometry corrections vanish in the bulk limit. As seen in the table, the zero-point geometries of XVSCF(4) and XVSCF[4] agree accurately with that of VCI′, indicating that the differences between XVSCF and VSCF or VCI arise from these force constants and thus are expected to vanish in the bulk. The most encouraging observation is that the XVSCF(4) results closely trace the corresponding results of XVSCF[4], which is more complete but more involved computationally.

Table 2.3 compiles the anharmonic geometry corrections obtained by XVSCF(4), XVSCF[4], and VSCF for the ground and excited states. Although XVSCF(4) and XVSCF[4] cannot reproduce the VSCF corrections quantitatively, it is again reassuring to find the XVSCF(4) and XVSCF[4] results agree accurately with each other for all states, allowing simpler and cheaper XVSCF(4) to be used interchangeably with XVSCF[4]. Interestingly, for states (000), (100), (001), and (101), the OH bond lengths of XVSCF(4) and XVSCF[4] deviate from those of VSCF by nearly a constant, indicating that XVSCF can reproduce the trend of the variation. These are the states which are not excited in the symmetric stretch mode (ν_2); in the states which are excited in this mode, the effect of the cubic diagonal force constant F_{222} on the VSCF vibrationally averaged geometry is greatest. Similarly, we find that XVSCF(4) and XVSCF[4] reproduce the trend predicted by VSCF for the HOH angle for all the states except those in which the bend (ν_1) is excited. The two states in which XVSCF fails to reproduce the sign of the VSCF geometry correction to HOH angle are both excited in this mode. The disagreement is probably due to the strong anharmonic corrections to the HOH angle caused primarily by force constant F_{111}. These cubic diagonal force constants affect the geometry of excited states in VSCF because they render the VSCF mean-field potential asymmetric, whereas XVSCF(n) and XVSCF[n] mean-field potentials are always symmetric about their minima. The force constants of the type F_{iii} cannot contribute to anharmonic frequencies or geometries in a size-consistent fashion and, therefore, we consider the disagreement to

be due to the small size of the molecule, and it is expected to vanish gradually with increasing size.

2.4.2 The naphthalene and anthracene molecules

Figures 2.13 and 2.14 plots the anharmonic geometry corrections of naphthalene and anthracene, respectively, in their ground states as a function of their normal modes. A majority of the corrections are zero because the corresponding normal modes are not totally symmetric. We computed these corrections as a check of our computer implementation and verified that they are indeed computed as zero to within machine precision in the XVSCF calculations and to within 10^{-4} a.u. in the VSCF calculations.

For these relatively large molecules, both XVSCF(4) and XVSCF[4] reproduce the anharmonic geometry corrections of VSCF within the mean absolute deviation (MAD) of 0.3 and 0.2 a.u., respectively (the statistics exclude the non-totally symmetric modes). Furthermore, XVSCF(4) and XVSCF[4] plots are barely distinguishable from each other in these figures, with the MAD between the two being 0.04 a.u. (naphthalene) and 0.05 a.u. (anthracene). The most significant disagreement between XVSCF and VSCF geometries is along the CH stretching modes, of which the anharmonic geometry corrections tend to be minimal according to these theories. These numerical results support our theoretical expectation that XVSCF[4] and VSCF-QFF converge at the same bulk limit. They also suggest that XVSCF(4) is an accurate approximation and inexpensive alternative to XVSCF[4].

Figures 2.15 and 2.16 are the same plots as Figs. 2.13 and 2.14 but for naphthalene and anthracene in their excited vibrational state in which the quantum numbers of all modes are simultaneously raised to one. Unlike the excited state in which the quantum number of only one mode is raised and which is related to an optical transition caused by a single photon, this excited state is more relevant to thermal excitations which can cause finite, intensive geometry corrections in all local coordinates simultaneously.

The anharmonicity in a PES generally affects excited-state properties more than the ground-state counterparts. The geometry corrections are indeed greater in the excited states than in the ground states. Nevertheless, the agreement between XVSCF[4] and VSCF remain accurate with the MAD being only 0.7 a.u. for naphthalene and 0.8 a.u. for anthracene, which are miniscule as compared with the magnitudes of anharmonic corrections in these units. The MAD between the XVSCF(4) and VSCF results is slightly larger (1.0 a.u. for naphthalene and 1.2 a.u. for anthracene), underscoring the fact that XVSCF[4] is the more complete method having the same bulk limit as VSCF.

Figures 2.17 and 2.18 compare the fundamental transition frequencies of XVSCF(4), XVSCF[4], and VSCF using the virtual approach for naphthalene and anthracene. The XVSCF[4] frequencies are not the same as the XVSCF(4) frequencies because XVSCF[4] takes into account the coupling between frequencies and geometry corrections, while XVSCF(4) does not. The MAD between XVSCF(4) and VSCF frequencies are 7.8 cm^{-1} (naphthalene) and 8.9 cm^{-1} (anthracene) and those between XVSCF[4] and VSCF frequencies are 7.7 cm^{-1} (naphthalene) and 9.1 cm^{-1}

(anthracene). XVSCF[4] is found to give frequencies closer to the VSCF results than does XVSCF(4) for normal modes whose harmonic frequencies are below 700 cm^{-1}, including ring breathing and large-amplitude bending modes, and are between 1200 and 1800 cm^{-1} such as CC stretching modes. For CH stretching and out-of-plane CH bending modes occurring between 800 and 1100 cm^{-1}, XVSCF[4] agrees less well with VSCF than does XVSCF(4). We have found that XVSCF[4] and XVSCF(4) occasionally give the wrong signs in the geometry corrections along CH stretching coordinates. The CH stretching modes are also known to couple strongly with the out-of-plane CH bending modes. Since XVSCF[4] accounts for the coupling of frequencies and geometry corrections, these may be the reason why XVSCF[4] is not necessarily in more accurate agreement with VSCF than is XVSCF(4) in frequencies at these molecular sizes.

The VSCF calculations on the vibrational ground states of naphthalene and anthracene took 0.40 and 0.62 seconds of CPU time, respectively, on a 2.3-GHz processor. Both calculations converged after 11 cycles of the iterative algorithm. The XVSCF(4) calculations completed in 0.02 and 0.04 seconds after 13 and 14 cycles, respectively, for naphthalene and anthracene. The XVSCF[4] calculations took 0.06 and 0.11 seconds, respectively, after 23 cycles for both molecules. The calculation of the XVSCF(4) geometry corrections completed in < 0.01 seconds for both molecules. These numbers omit the much greater computational cost of evaluating the potential energy surface, which was carried out once per molecule.

2.5 Conclusion

This chapter has presented the extensions of XVSCF to anharmonic vibrationally averaged geometries. We have introduced the theory, algorithms, programmable equations, and initial implementations of the two XVSCF methods for anharmonic geometries: XVSCF(n) and XVSCF[n]. XVSCF[n] has the same converged bulk limits as VSCF for anharmonic total energies, frequencies, and geometries. XVSCF(n) for anharmonic total energies and frequencies was reported earlier.[21] Here, XVSCF(n) for anharmonic geometry corrections has been proposed, implemented, and tested. XVSCF(n) is defined for any even integer and XVSCF[n] is defined for any integer $n > 2$, and programmable equations for $n > 4$ can be obtained easily by truncating the relevant expressions for the mean-field potential constants after terms containing higher-order force constants.

The XVSCF(n) and XVSCF[n] geometry corrections have been shown to be in close agreement with the corresponding VSCF results for molecules larger than water. In Appendix 2.4, it is shown that XVSCF[n] reproduces exactly the VSCF results for anharmonic frequencies and geometries near the bulk limit, where XVSCF(n) recovers approximately 85% of the geometry corrections of VSCF or XVSCF[n], which is satisfactory. Owing to the effective harmonic form of their mean-field potentials, neither XVSCF(n) and XVSCF[n] requires basis functions, quadrature,

or matrix diagonalization, unlike any VSCF algorithm; XVSCF(n) nor XVSCF[n] are, therefore, not only size consistent (while VSCF is not), but they are also vastly more efficient than VSCF though the results obtainable from these methods are essentially of the same quality particularly for large molecules and solids.

The derivation of both XVSCF(n) and XVSCF[n] is general in the sense that nothing in their equations restricts their applications to the ground vibrational state; anharmonic geometry corrections can be calculated for excited states, opening the important possibility of applying the methods to thermally averaged properties of large molecules and solids.

2.6 Figures

1: Input M, s, F_{ii}, F_{iijj}, F_{ijj}, etc.
2: Set $\omega_m \leftarrow \sqrt{F_{mm}}$ as initial guess for all m
3: Repeat
4: For $m = 1$ to M
5: Calculate $U^{(2)}_{m,s}$ and ω_m
6: End For
7: Until all ω_m cease to change more than a threshold
8: Calculate $U^{(1)}_{m,s}$ and $\langle Q_m \rangle = -U^{(1)}_{m,s}/U^{(2)}_{m,s}$
9: Calculate E_s

Figure 2.1: The XVSCF(n) algorithm.

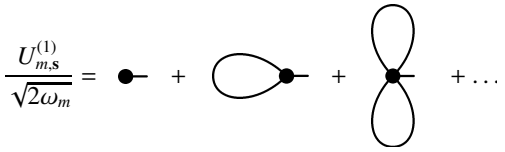

Figure 2.2: The diagrams for $U^{(1)}_{m,s}$ for the ground state.

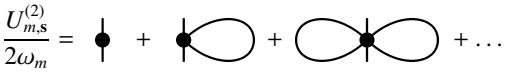

Figure 2.3: The diagrams for $U^{(2)}_{m,s}$ for the ground state.

1: Input M, s, F, etc.
2: Set $\tilde{\omega}_m \leftarrow \sqrt{F_{mm}}$ and $\tilde{q}_m \leftarrow 0$ as initial guess for all m
3: Repeat
4: For $m = 1$ to M
5: Calculate $\tilde{U}^{(1)}_{m,s}$ and $\tilde{U}^{(2)}_{m,s}$
6: Set $\tilde{\omega}_m \leftarrow \sqrt{\tilde{U}^{(2)}_{m,s}}$ and $\tilde{q}_m \leftarrow \tilde{q}_m - \tilde{U}^{(1)}_{m,s}/\tilde{U}^{(2)}_{m,s}$
7: End For
8: Until all $\tilde{\omega}_m$ and $\tilde{q}_m$ cease to change more than a threshold
9: Calculate E_s

Figure 2.4: The XVSCF[n] algorithm.

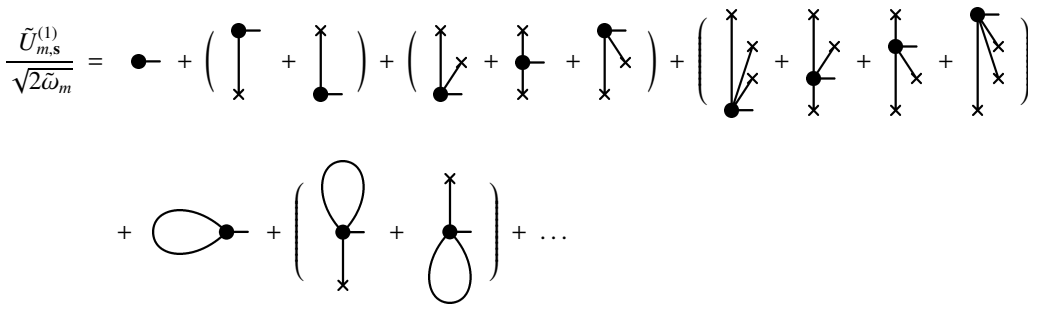

Figure 2.5: The diagrams for $\tilde{U}^{(1)}_{m,s}$ for the ground state.

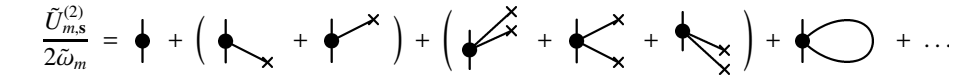

Figure 2.6: The diagrams for $\tilde{U}^{(2)}_{m,s}$ for the ground state.

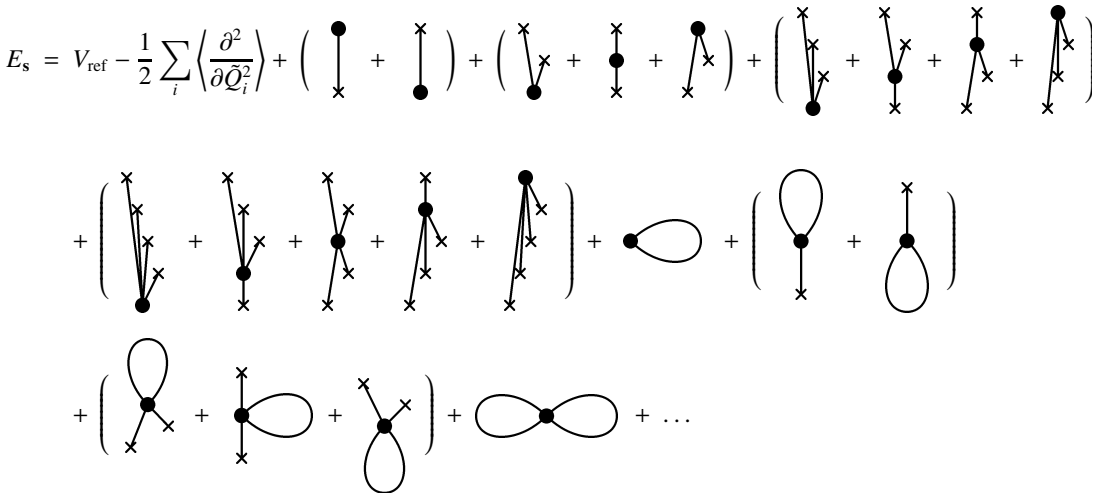

Figure 2.7: The diagrams for XVSCF[n] total energy for the ground state.

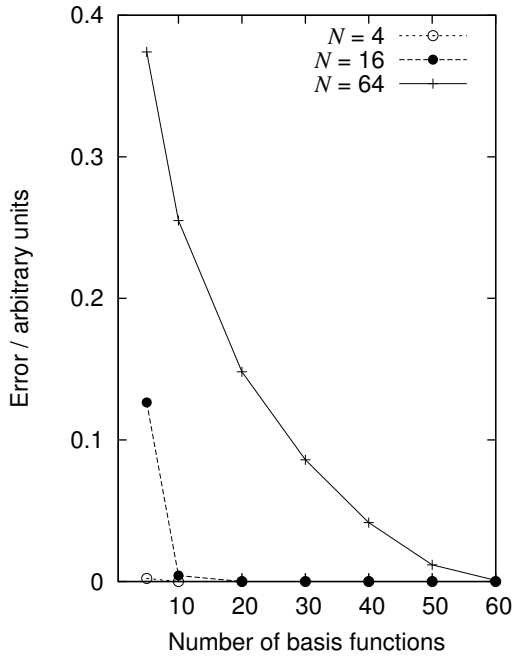

Figure 2.8: The errors in the VSCF lowest fundamental frequencies of the one-dimensional models from the converged limits as a function of the number of harmonic oscillator basis functions per normal coordinate that are used to expand the VSCF modals.

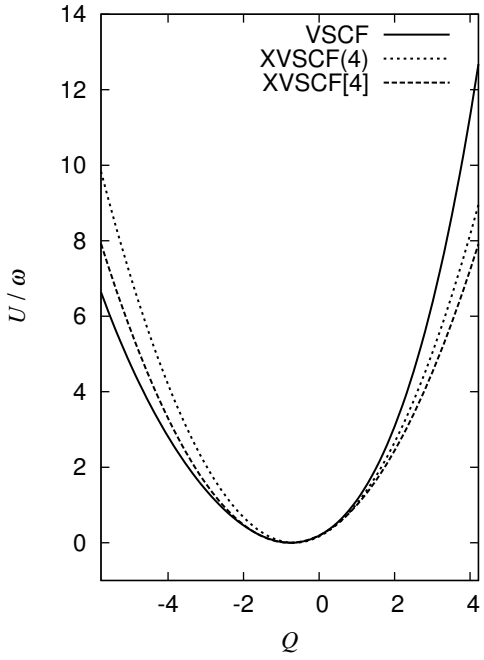

Figure 2.9: The VSCF, XVSCF(4), and XVSCF[4] mean-field potentials of the one-dimensional model with $N = 4$ along the normal mode with the lowest nonzero frequency. The potentials are given in the units of the VSCF frequency calculated with the virtual approach and evaluated relative to their minima.

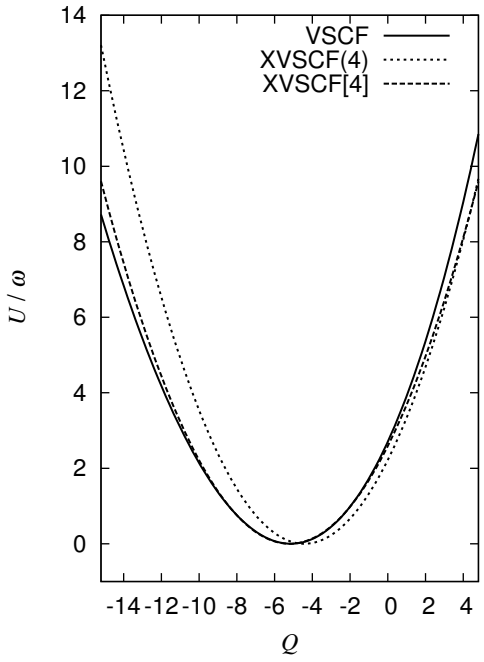

Figure 2.10: The same as Fig. 2.9, but with $N = 16$.

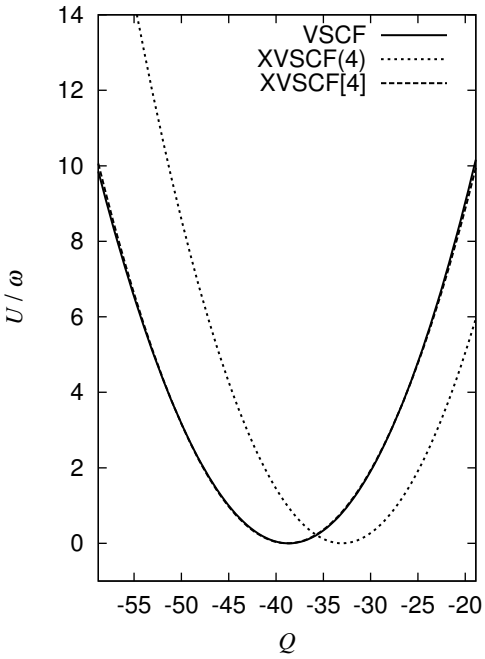

Figure 2.11: The same as Fig. 2.9, but with $N = 64$. The XVSCF[4] and VSCF mean-field potentials are indistinguishable.

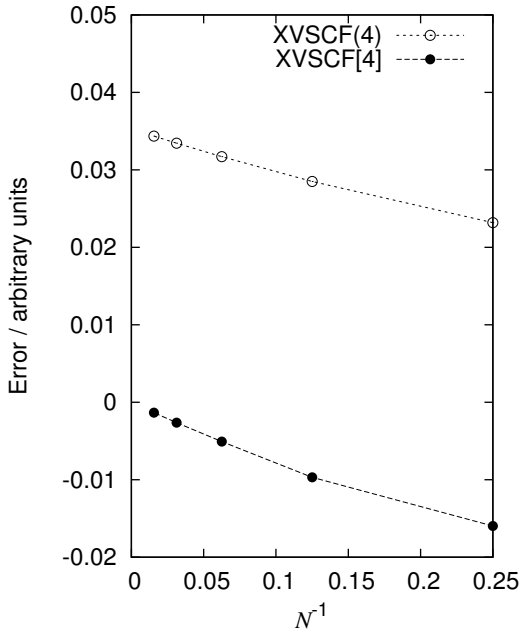

Figure 2.12: The difference between XVSCF(4) or XVSCF[4] and VSCF predictions of the zero-point energy divided by N of the one-dimensional chain plotted against N^{-1}.

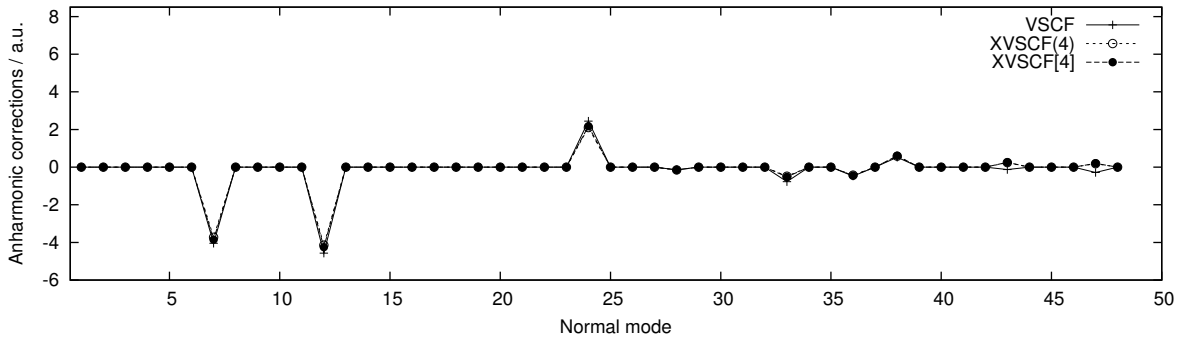

Figure 2.13: The anharmonic correction (in a.u.) in normal coordinates to the equilibrium geometry of naphthalene in the ground vibrational state obtained by XVSCF(4), XVSCF[4], and VSCF using a QFF within the 2MR approximation. The normal modes are numbered in the increasing order of the harmonic frequencies.

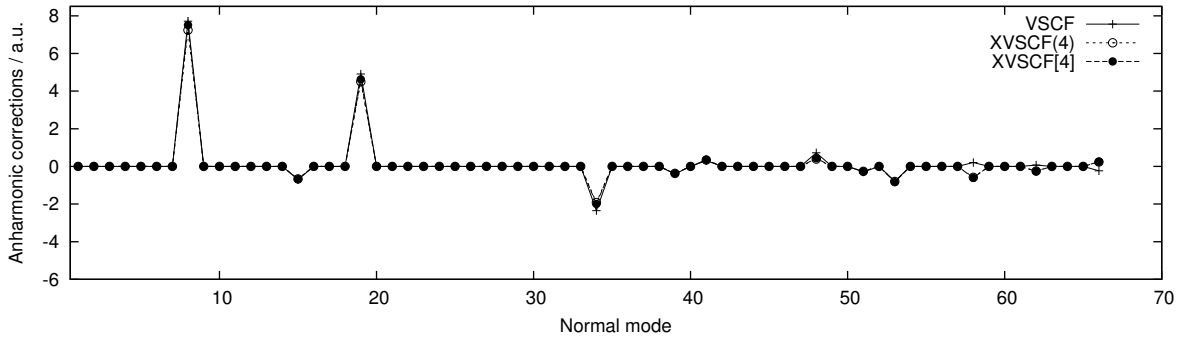

Figure 2.14: The anharmonic correction (in a.u.) in normal coordinates to the equilibrium geometry of anthracene in the ground vibrational state obtained by XVSCF(4), XVSCF[4], and VSCF using a QFF within the 2MR approximation. The normal modes are numbered in the increasing order of the harmonic frequencies.

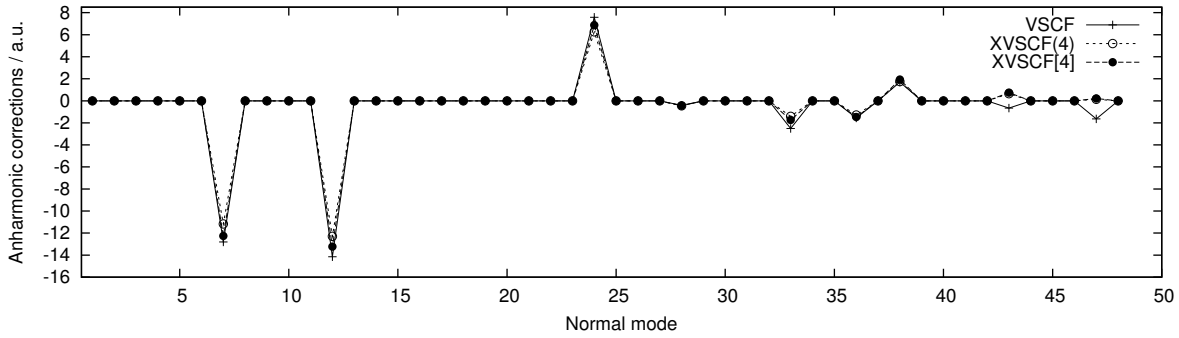

Figure 2.15: The same as Fig. 2.13 but for naphthalene in the excited vibrational state in which the quantum numbers of all modes are simultaneously raised to one.

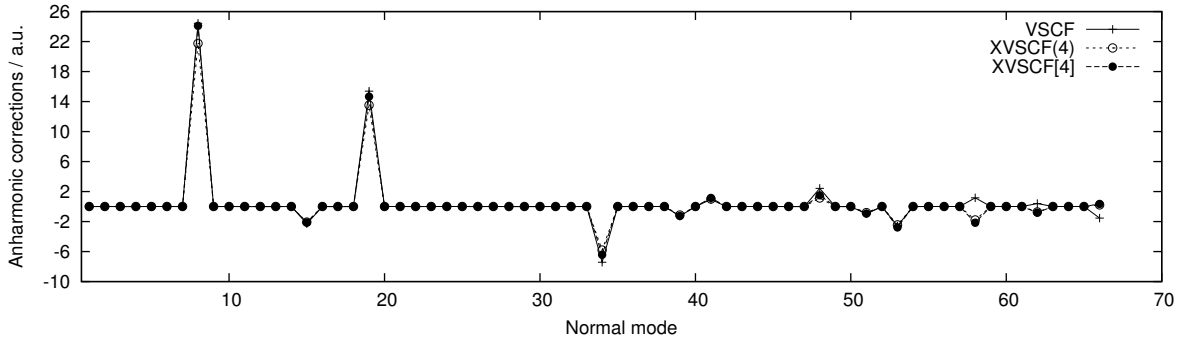

Figure 2.16: The same as Fig. 2.14 but for anthracene in the excited vibrational state in which the quantum numbers of all modes are simultaneously raised to one.

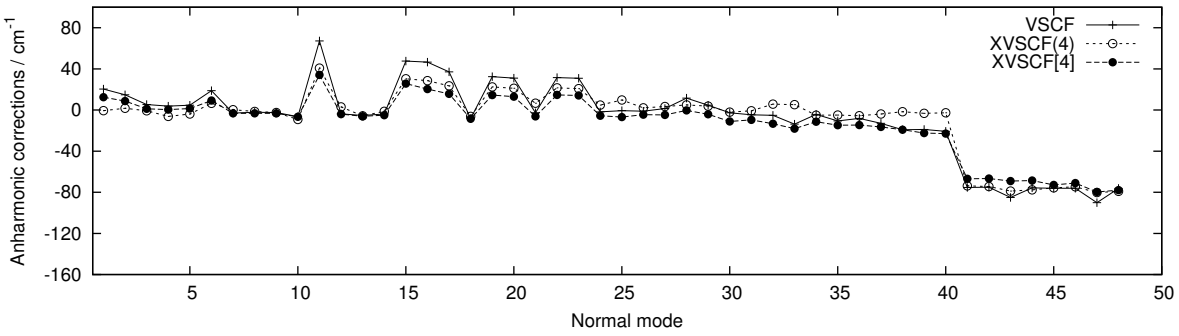

Figure 2.17: The anharmonic corrections (in cm^{-1}) to the fundamental frequencies of naphthalene obtained by XVSCF(4), XVSCF[4], and VSCF in the virtual approach using a QFF within the 2MR approximation. The normal modes are numbered in the increasing order of the harmonic frequencies.

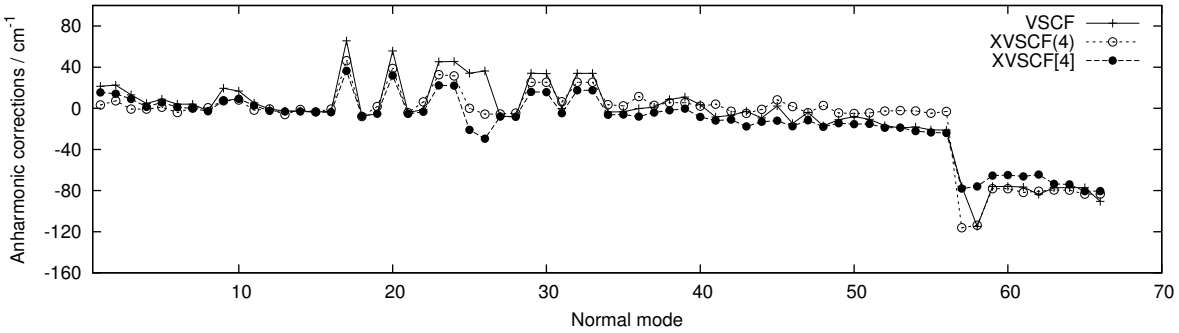

Figure 2.18: The anharmonic corrections (in cm^{-1}) to the fundamental frequencies of anthracene obtained by XVSCF(4), XVSCF[4], and VSCF in the virtual approach using a QFF within the 2MR approximation. The normal modes are numbered in the increasing order of the harmonic frequencies.

2.7 Tables

Table 2.1: The anharmonic corrections to the average interatomic distances predicted by XVSCF(4), XVSCF[4], and VSCF for the one-dimensional chains of various lengths (N) in the vibrational ground or excited state. In the excited state, the quantum numbers of all of its normal modes are simultaneously raised to one.

	The ground state			The excited state		
N	XVSCF(4)	XVSCF[4]	VSCF	XVSCF(4)	XVSCF[4]	VSCF
4	−0.2011	−0.2372	−0.2657	−0.3996	−0.4888	−0.5244
8	−0.2182	−0.2562	−0.2622	−0.4242	−0.5072	−0.5143
16	−0.2204	−0.2589	−0.2600	−0.4248	−0.5076	−0.5089
32	−0.2208	−0.2592	−0.2588	−0.4243	−0.5066	−0.5060
64	−0.2203	−0.2586	−0.2582	−0.4228	−0.5051	−0.5046

Table 2.2: The anharmonic transition frequencies (in cm^{-1}) and vibrationally averaged OH bond length (in Å) and HOH bond angle (in degrees) of water obtained with a QFF. The modes ν_1, ν_2, and ν_3 refer to the bending, symmetric stretching, and antisymmetric stretching vibrations, respectively.

	Harmonic	XVSCF(4)	XVSCF[4]	VSCF[a]	VSCF[b]	VCI	VCI′[c]
ν_1	1628[d]	1543[d]	1563	1565	1562[d]	1557[d]	1547
ν_2	3822[d]	3875[d]	3789	3727	3727[d]	3682[d]	3818
ν_3	3948[d]	3993[d]	3903	3908	3815[d]	3791[d]	3771
r_{OH}	0.9614	0.9680	0.9683	0.9758	0.9758	0.9757	0.9680
θ_{HOH}	104.1	103.4	103.5	104.0	104.0	104.0	103.4

[a]The virtual approach for frequencies (see text).

[b]The state-specific approach for frequencies (see text).

[c]The force constants of the types F_{iii}, F_{iij}, and F_{iiii} are excluded from the QFF.

[d]Reference 21.

Table 2.3: The anharmonic corrections to the OH bond length (in Å) and HOH bond angle (in degrees) of water in the ground and excited vibrational states. Quantum numbers s_1, s_2, and s_3 refer to the bending (ν_1), symmetric stretching (ν_2), and antisymmetric stretching (ν_3) vibrations, respectively.

$(s_1 s_2 s_3)$	r_{OH}			θ_{HOH}		
	XVSCF(4)	XVSCF[4]	VSCF	XVSCF(4)	XVSCF[4]	VSCF
(000)	+0.0066	+0.0070	+0.0144	−0.691	−0.656	−0.152
(100)	+0.0041	+0.0044	+0.0116	−0.714	−0.691	+0.780
(010)	+0.0065	+0.0068	+0.0296	−1.096	−1.030	−0.382
(001)	+0.0210	+0.0237	+0.0296	−1.967	−1.691	−1.116
(110)	+0.0038	+0.0041	+0.0277	−1.133	−1.092	+0.453
(101)	+0.0194	+0.0223	+0.0279	−2.037	−1.770	−0.294
(011)	+0.0205	+0.0227	+0.0425	−2.496	−2.092	−1.278
(111)	+0.0187	+0.0211	+0.0416	−2.587	−2.199	−0.516

Table 2.4: Comparison of the three vibrational self-consistent field methods with a QFF.

	XVSCF(4)	XVSCF[4]	VSCF
Working equations	Eqs. (1.46), (2.2), and (2.25)–(2.27)	Eqs. (2.4), (2.17), and (2.28)–(2.30)	Eqs. (10)–(18) of Ref. 21
Algorithm	Fig. 2.1	Fig. 2.4	Fig. 2 of Ref. 21
Linear force constants needed[a]	F_I	F_I	F_i
Quadratic force constants needed[a]	F_{ii}	F_{ii}, F_{IJ}	F_{ij}
Cubic force constants needed[a]	F_{iiJ}	F_{iiJ}, F_{IJK}	F_{ijk}
Quartic force constants needed[a]	F_{iijj}	$F_{iijj}, F_{iiJK}, F_{IJKL}$	F_{ijkl}
Mean-field potential	Quadratic	Quadratic	Quartic
Basis set, quadrature, and diagonalization	Unnecessary	Unnecessary	Necessary
Size extensive for total energies[b]	Yes	Yes	No
Size intensive for transition frequencies[b]	Yes	Yes	No
Size intensive for geometry corrections[b]	Yes	Yes	No
Convergence to VSCF in the bulk limit	No[c]	Yes	Yes
Computational cost scaling[d]	$O(M^2)$	$O(N^4)$	$O(M^4)$[e]

[a] Subscripts i, j, k, and l refer to all normal modes and are distinct from one another, whereas I, J, K, and L refer to totally symmetric normal modes and are not necessarily distinct. It is assumed that VSCF does not exploit symmetries of normal modes.

[b] Whether the equations defining these quantities are diagrammatically size extensive or intensive.

[c] The XVSCF(4) energies and frequencies converge at the VSCF(QFF) values in the bulk limit if and only if VSCF uses $V_4(\boldsymbol{Q})$.

[d] M denotes the number of normal modes and N to the number of totally symmetric normal modes.

[e] It is assumed that VSCF does not exploit symmetries of normal modes. If VSCF exploits the symmetries, the scaling can in principle reduce to $O(N^4)$.

Chapter 3

Dyson coordinates and Dyson geometry

Here, we place the XVSCF(n), XVSCF[n], and SCP methods of solid-state physics in the context of Green's function theory, of which the central equation is the (inverse) Dyson equation as discussed in Chapter 1.[10,33] The inverse Dyson equation is a set of coupled one-particle equations with energy-dependent, correlated potentials known as the Dyson self-energy;[10,23,33] the equation can, in principle, describe electronic[23,84,85] and vibrational[26,86–88] many-body wave functions exactly within an apparent one-particle framework.

The Dyson self-energy is, in turn, subject to a diagrammatic perturbation expansion,[22,24,25] where only connected, irreducible, open diagrams are retained and they describe thermodynamically intensive many-body corrections to the one-particle energies. With the self-energy added to the effective one-particle potential, the inverse Dyson equation can lead to a new set of one-particle wave functions that are a unitary transformation of the original basis functions, the latter typically being the HF orbitals for electrons and harmonic oscillator wave functions along normal coordinates for vibrations. These one-particle wave functions for electrons are so-called Dyson orbitals.[33] The corresponding one-mode wave functions for vibrations are along a new set of rectilinear coordinates centered at a new geometry that generally differs from the equilibrium geometry. These new coordinates are a unitary transformation of the normal coordinates, which we propose to call the Dyson coordinates. The new geometry is referred to as the Dyson geometry.

In this chapter, we show the following:

(1) The linked and thus size consistent anharmonic contributions to the effective harmonic force constants of the one-mode potentials of VSCF correspond to the diagonal components of the first-order Dyson self-energy. The XVSCF(n) method introduced by Keçeli and Hirata[21] takes into account only such contributions in VSCF while discarding other contributions that are not size-consistent and which vanish in the bulk limit.

(2) There are also connected contributions to the gradients of the effective one-mode potentials of VSCF. They are nonzero at the equilibrium geometry and define the first-order Dyson geometry as the point on the PES at which the effective gradients all vanish. The difference between the equilibrium and Dyson geometries is the first-order anharmonic geometry correction. XVSCF[n] accounts for the diagonal first-order Dyson self-energy in the effective one-mode potentials of VSCF and uses the first-order Dyson geometry as the center of the normal coordinates.

(3) Connected contributions also exist in the off-diagonal components of the first-order Dyson self-energy, which

are neglected in VSCF, XVSCF(n), and XVSCF[n]. They can be used to define the first-order Dyson coordinates as a unitary transformation of the normal coordinates that diagonalizes the sum of quadratic force constants and the first-order Dyson self-energy which characterizes the effective one-mode potentials of VSCF and XVSCF. This method is identified as a variant of the SCP approach[31,32,89–91] and also closely related to the optimized quadratic approximation of Cao and Voth[77] (see also Refs. 92–94). It takes into account the first-order Dyson geometry as well as the diagonal and off-diagonal components of the first-order Dyson self-energy, which, in turn, define the first-order Dyson coordinates, although recognition as such has not been made until this work. We call this method SCP[n]. Another variant of SCP, referred to as SCP(n) in this chapter, uses the first-order Dyson coordinates centered at the equilibrium geometry. Numerical evidence shows that the normal coordinates are usually exceedingly close to the first-order Dyson coordinates.

(4) The Dyson coordinates are obtained by the diagonalization of an effective harmonic force constant matrix that adds to itself the Dyson self-energy and is, therefore, "dressed" with the anharmonic effects. This mathematical procedure can be rigorously derived from the Dyson equation, as discussed in Chapter 1.

3.1 Theory

Here, we briefly recapitulate the theoretical definitions of the VSCF, XVSCF(n), and XVSCF[n] methods, described in previous chapters, as well as the SCP method in order to discuss their connection to Green's function theory. We drop the subscript s, referring to a vibrational state, for brevity.

3.1.1 VSCF

The VSCF wave function[4–6] is a product of modals in normal coordinates $\{Q_i\}$ centered at the equilibrium structure,

$$\Psi = \prod_i \varphi_i(Q_i), \tag{3.1}$$

which minimizes the expectation value of energy,

$$E = \langle \Psi | \hat{H} | \Psi \rangle, \tag{3.2}$$

under the constraints that all modals remain normalized. This leads to the following coupled set of one-mode equations,

$$\left\{ -\frac{1}{2}\frac{\partial^2}{\partial Q_i^2} + U_i(Q_i) \right\} \varphi_i(Q_i) = \epsilon_i \varphi_i(Q_i), \tag{3.3}$$

involving the effective one-mode potentials,

$$U_i(Q_i) \quad = \quad \left\langle \frac{\Psi}{\varphi_i} \middle| V \middle| \frac{\Psi}{\varphi_i} \right\rangle, \tag{3.4}$$

where V is the PES and Q_i is the normal coordinate position operator for mode i. The PES Taylor series, relating V to force constants, F, is given by Eq. (1.21).

3.1.2 XVSCF(n)

While VSCF is elegant in its definition and has fundamental value as the basis of vibrational correlation theories, it is not diagrammatically size consistent when it is defined with normal coordinates. As per Makri's theorem,[68] the effective potential that each of the semi-independent oscillators in delocalized coordinates experiences must always be harmonic in the bulk limit. This suggests that the effective one-mode potential of VSCF, U_i in Eq. (3.3), has numerous redundant terms that vanish in the bulk limit (they are important and useful for smaller molecules, however).

Eliminating all such terms in Eq. (3.3) that have nonphysical size dependence, we arrive at the coupled XVSCF equations,

$$\left\{ -\frac{1}{2}\frac{\partial^2}{\partial Q_i^2} + U_i'(Q_i) \right\} \varphi_i'(Q_i) \quad = \quad \epsilon_i' \varphi_i'(Q_i), \tag{3.5}$$

with

$$U_i'(Q_i) \quad = \quad E + \frac{1}{2} U_i^{(2)} Q_i^2, \tag{3.6}$$

where E is given by Eq. (3.2). The effective harmonic force constant, $U_i^{(2)}$, is given diagrammatically in Fig. 3.1 and algebraically as

$$U_i^{(2)} \quad = \quad F_{ii} + (2\omega_i^{(0)}) \left\{ \boldsymbol{\Sigma}^{(1)}(\nu) \right\}_{ii}', \tag{3.7}$$

where here we have used the symbol $\omega_i^{(0)}$ for the harmonic frequency. The first diagram in Fig. 3.1 and the first term in the right-hand side of the above expression correspond to the diagonal quadratic force constant, and the subsequent diagrams and the second term correspond to the diagonal first-order Dyson self-energy. The first-order Dyson self-energy, $\left\{ \boldsymbol{\Sigma}^{(1)}(\nu) \right\}_{ii}'$, which "dresses" the bare potential, is given by

$$\left\{ \boldsymbol{\Sigma}^{(1)}(\nu) \right\}_{ii}' \quad = \quad \frac{1}{2(2\omega_i^{(0)})} \sum_j F_{iijj} \langle Q_j^2 \rangle + \frac{1}{8(2\omega_i^{(0)})} \sum_{j,k} F_{iijjkk} \langle Q_j^2 \rangle \langle Q_k^2 \rangle + \ldots. \tag{3.8}$$

The symbols $\langle Q_i^2 \rangle$ refer to the expectation values $\langle \varphi_i' | Q_i^2 | \varphi_i' \rangle$. Unlike Keçeli and Hirata,[21] we have lifted the restrictions on the domains of summation indexes, anticipating unitary transformations of the coordinates to be performed later, where such restrictions become cumbersome. See Sec. (3.1.7) for a justification of this treatment.

Note both the similarity and the difference to the first-order Dyson self-energy utilized in XVH1(n) as discussed in Chapter 1, given by Fig. 1.2 and Eq. (1.57). Equation (3.8) is isomorphic to Eq. (1.2), but instead of products of strictly harmonic frequencies, the former has expectation values of Q operators *in XVSCF modals*, which as we have seen amount to products of *XVSCF* frequencies. Note also that in general, the inverse Dyson equation must in general be solved self-consistently and independently for every individual frequency, since $\mathbf{\Sigma}(\nu)$ depends on the solution ν itself. However, a first-order diagrammatic approximation to the Dyson self-energy, containing only diagrams of the type shown in Fig. 3.3, is constant in ν,[23,86] and Eq. (1.53) is in that case a simple eigenvalue problem. The self-consistency required in the XVSCF(n) method is of a different nature, the modals and their frequencies must be self-consistent with one another across all coordinates. This requirement is traced to the variational definition of VSCF and is also related to the resummation of a certain class of diagrams up to an infinite order, as will be discussed further in Chapter 4.

According to the normalization theorem,,[17,29] only connected diagrams with two external edges such as those in 3.1 have size dependence proportional to K^0 and are thermodynamically intensive, which one-mode potentials should be. The identical conclusion can also be drawn algebraically.[20] On the basis of this observation, Keçeli and Hirata introduced[21] diagrammatically size-extensive VSCF or XVSCF(n) for an nth-order Taylor-series PES. It consists of solving the coupled set of the diagrammatically linked equations, Eq. (3.5)—rather than the VSCF equations, Eq. (3.3)—with the effectively harmonic one-mode potential given by Eqs. (3.6)–(3.8). Among the numerous advantages of XVSCF(n) over VSCF discussed in Keçeli and Hirata[21] is the fact that Eq. (3.5) has analytical solutions for effectively harmonic U_i'. The eigenvalue solutions of Eq. (3.5) are

$$\epsilon_i' \quad = \quad E + (s_i + 1/2)\omega_i', \tag{3.9}$$

where s_i is the nonnegative integer quantum number and

$$U_i^{(2)} \quad = \quad \omega_i'^2. \tag{3.10}$$

The eigenfunctions (modals) of Eq. (3.5) are harmonic oscillator wave functions with angular frequencies $\{\omega_i'\}$. The total energy is given by

$$E \quad = \quad -\frac{1}{2}\sum_i \left\langle \frac{\partial^2}{\partial Q_i^2} \right\rangle + V_0 + \frac{1}{2}\sum_i F_{ii}\langle Q_i^2 \rangle + \frac{1}{8}\sum_{i,j} F_{iijj}\langle Q_i^2 \rangle \langle Q_j^2 \rangle$$

$$+\frac{1}{48}\sum_{i,j,k} F_{iijjkk}\langle Q_i^2\rangle\langle Q_j^2\rangle\langle Q_k^2\rangle + \ldots, \tag{3.11}$$

with

$$\left\langle \frac{\partial^2}{\partial Q_i^2} \right\rangle = -\frac{\omega_i'}{2}, \tag{3.12}$$

Equations (3.6) and (3.9) also contain E. This is because we have lifted the restrictions in the ranges of the summation indices in the corresponding terms in Chapters 1 and 2 for consistency.

3.1.3 XVSCF[n]

It has been shown by the present authors with coauthors[20] that Eq. (3.5) neglects more than just the terms that vanish in the bulk limit. Diagrams that are isomorphic to those of bare potential gradients in the one-mode effective potential of VSCF do not vanish with increasing size and are not accounted for in XVSCF(n). XVSCF equations that account for these diagrams have the form

$$\left\{-\frac{1}{2}\frac{\partial^2}{\partial \tilde{Q}_i^2} + \tilde{U}_i(\tilde{Q}_i)\right\}\tilde{\varphi}_i(\tilde{Q}_i) = \tilde{\epsilon}_i\tilde{\varphi}_i(\tilde{Q}_i), \tag{3.13}$$

where

$$\tilde{U}_i(\tilde{Q}_i) = \tilde{U}_i^{(1)}\tilde{Q}_i + \frac{1}{2}\tilde{U}_i^{(2)}\tilde{Q}_i^2, \tag{3.14}$$

with $\tilde{Q}_i$ defined below. The effective gradient and harmonic force constant in Eq. (3.14) are

$$\tilde{U}_i^{(1)} = \tilde{F}_i + (2\tilde{\omega}_i^{(0)})^{1/2}\tilde{\Sigma}_i^{(1)}, \tag{3.15}$$

$$\tilde{U}_i^{(2)} = \tilde{F}_{ii} + (2\tilde{\omega}_i^{(0)})\left\{\tilde{\mathbf{\Sigma}}^{(1)}(\nu)\right\}_{ii}, \tag{3.16}$$

where

$$\tilde{\omega}_i^{(0)} = (\tilde{F}_{ii})^{1/2}. \tag{3.17}$$

The Dyson self-energy, $\left\{\tilde{\mathbf{\Sigma}}^{(1)}(\nu)\right\}_{ii}$, is defined by the same equation as $\left\{\mathbf{\Sigma}^{(1)}(\nu)\right\}_{ii}'$ [Eq. (3.8)], but the F's, Q's, and $\omega^{(0)}$'s are systematically replaced by the corresponding $\tilde{F}$'s, $\tilde{Q}$'s, and $\tilde{\omega}^{(0)}$'s. The new force constants, $\tilde{F}$ (including $\tilde{V}_0$), are

related to the standard force constants, F, by algebraic relationships presented in Eqs. (2.11)–(2.15) of Chapter 2. The new quantity, $\tilde{\Sigma}_i^{(1)}$, is the one-edge analogue of the first-order Dyson self-energy and is given by

$$\tilde{\Sigma}_i^{(1)} = \frac{1}{2(2\tilde{\omega}_i^{(0)})^{1/2}} \sum_j \tilde{F}_{ijj} \langle \tilde{Q}_j^2 \rangle + \frac{1}{8(2\tilde{\omega}_i^{(0)})^{1/2}} \sum_{j,k} \tilde{F}_{ijjkk} \langle \tilde{Q}_j^2 \rangle \langle \tilde{Q}_k^2 \rangle + \ldots . \tag{3.18}$$

Again, we have lifted the summation restrictions in Eq. (3.18) that were present in Chapter 2. The diagrammatic representation of $\tilde{U}_i^{(1)}$ is given in Fig. 3.2.

The effective gradient, $\tilde{U}_i^{(1)}$ given in Eq. (3.15), has the size dependence of $K^{1/2}$ and is neither extensive or intensive.[20,29] It must vanish for the theory to be size-consistent and for the effective potential to consist of an extensive constant part and an intensive function part only. The XVSCF[n] method guarantees this by shifting the center of the coordinates to a new one $\{q_i\}$, such that all of the effective gradients vanish:

$$\tilde{U}_i^{(1)} = 0, \tag{3.19}$$

The tildes on various symbols indicate that the quantities represented by them are defined with this new center of coordinates,

$$\tilde{Q}_i = Q_i - q_i, \tag{3.20}$$

This center is called the first-order Dyson geometry. It coincides with the vibrationally averaged geometry of VSCF in the bulk limit.

The eigenvalue solutions of Eq. (3.13) are

$$\tilde{\epsilon}_i = \tilde{E} + \left(s_i + \frac{1}{2} \right) \tilde{\omega}_i, \tag{3.21}$$

with

$$\tilde{U}_i^{(2)} = \tilde{\omega}_i^2, \tag{3.22}$$

and

$$\begin{aligned} \tilde{E} = & -\frac{1}{2} \sum_i \left\langle \frac{\partial^2}{\partial \tilde{Q}_i^2} \right\rangle + \tilde{V}_0 + \frac{1}{2} \sum_i \tilde{F}_{ii} \langle \tilde{Q}_i^2 \rangle + \frac{1}{8} \sum_{i,j} \tilde{F}_{iijj} \langle \tilde{Q}_i^2 \rangle \langle \tilde{Q}_j^2 \rangle \\ & + \frac{1}{48} \sum_{i,j,k} \tilde{F}_{iijjkk} \langle \tilde{Q}_i^2 \rangle \langle \tilde{Q}_j^2 \rangle \langle \tilde{Q}_k^2 \rangle + \ldots , \end{aligned} \tag{3.23}$$

and where $\tilde{F}$'s and $\tilde{V}_0$ are again given by Eqs. (2.11)–(2.15).

3.1.4 SCP[n]

The XVSCF(n) and XVSCF[n] methods are defined for normal coordinates, adjusting the shapes of effective one-mode potentials with only the diagonal components of the first-order Dyson self-energy. If this diagonal approximation is lifted and the nonzero off-diagonal components of the Dyson self-energy are also taken into account, the effective potentials are no longer one-mode functions, but they contain two-mode contributions,

$$\tilde{U}_{ij}(\tilde{Q}_i, \tilde{Q}_j) \quad = \quad \frac{1}{2}\tilde{U}^{(2)}_{ij}\tilde{Q}_i\tilde{Q}_j, \tag{3.24}$$

where $i \neq j$ and

$$\tilde{U}^{(2)}_{ij} \quad = \quad \tilde{F}_{ij} + (2\tilde{\omega}^{(0)}_i)^{1/2}(2\tilde{\omega}^{(0)}_j)^{1/2}\left\{\tilde{\mathbf{\Sigma}}^{(1)}(\nu)\right\}_{ij}, \tag{3.25}$$

with

$$\begin{aligned}\left\{\tilde{\mathbf{\Sigma}}^{(1)}(\nu)\right\}_{ij} \quad &= \quad \frac{1}{2(2\tilde{\omega}^{(0)}_i)^{1/2}(2\tilde{\omega}^{(0)}_j)^{1/2}}\sum_k \tilde{F}_{ijkk}\langle\tilde{Q}^2_k\rangle \\ &\quad + \frac{1}{8(2\tilde{\omega}^{(0)}_i)^{1/2}(2\tilde{\omega}^{(0)}_j)^{1/2}}\sum_{k,l}\tilde{F}_{ijkkll}\langle\tilde{Q}^2_k\rangle\langle\tilde{Q}^2_l\rangle + \ldots.\end{aligned} \tag{3.26}$$

The diagrammatic representation of $\tilde{U}_{ij}$ is depicted in Fig. 3.3.

The two-mode nature of the effective potential of Eq. (3.24) prohibits an effective one-mode equation analogous to Eqs. (3.5) or (3.13) from being obtained. One can, however, transform coordinates to bring $\tilde{U}_{ij}$ into a diagonal form. Let $\{\bar{Q}_i\}$ be the new set of coordinates centered at the first-order Dyson geometry obtained by a unitary transformation of the normal coordinates,

$$\bar{Q}_i \quad = \quad \sum_j C_{ij}\left(Q_j - q_j\right), \tag{3.27}$$

where $\{C_{ij}\}$ (assumed real in this work) are the elements of the transformation matrix determined so as to bring the non-diagonal effective harmonic force constant matrix of Eq. (3.25) into a diagonal form, that is,

$$\begin{aligned}\bar{U}^{(2)}_{ij} \quad &= \quad \delta_{ij}\bar{\omega}^2_i \\ &= \quad \bar{F}_{ij} + \frac{1}{2}\sum_k \bar{F}_{ijkk}\langle\bar{Q}^2_k\rangle + \frac{1}{8}\sum_{k,l}\bar{F}_{ijkkll}\langle\bar{Q}^2_k\rangle\langle\bar{Q}^2_l\rangle + \ldots.\end{aligned} \tag{3.28}$$

As in XVSCF[n], we simultaneously ensure that the effective gradient potential terms remain zero:

$$\begin{aligned}\bar{U}_i^{(1)} &= 0 \\ &= \bar{F}_i + \frac{1}{2}\sum_j \bar{F}_{ijj}\langle\bar{Q}_j^2\rangle + \frac{1}{8}\sum_{j,k}\bar{F}_{ijjkk}\langle\bar{Q}_j^2\rangle\langle\bar{Q}_k^2\rangle + \ldots,\end{aligned} \tag{3.29}$$

where $\langle\bar{Q}_i^2\rangle = \langle\bar{\varphi}_i|\bar{Q}_i^2|\bar{\varphi}_i\rangle$, which is readily evaluated analytically (see Table I of Keçeli and Hirata[21]) with $\bar{\omega}$'s obtained from Eq. (3.28). The transformed force constants, $\bar{F}$'s are related to the force constants $\tilde{F}$'s and F's by

$$\bar{V}_0 = V_0 + \sum_i F_i q_i + \frac{1}{2!}\sum_{i,j} F_{ij}q_i q_j + \frac{1}{3!}\sum_{i,j,k} F_{ijk}q_i q_j q_k + \ldots, \tag{3.30}$$

$$\bar{F}_i = \sum_j C_{ij}F_j + \sum_{j,k} C_{ij}F_{jk}q_k + \frac{1}{2!}\sum_{j,k,l} C_{ij}F_{jkl}q_k q_l + \ldots, \tag{3.31}$$

$$\bar{F}_{ij} = \sum_{k,l} C_{ik}C_{jl}F_{kl} + \sum_{k,l,m} C_{ik}C_{jl}F_{klm}q_m + \ldots, \tag{3.32}$$

$$\bar{F}_{ijj} = \sum_{k,l,m} C_{ik}C_{jl}C_{jm}F_{klm} + \sum_{k,l,m,n} C_{ik}C_{jl}C_{jm}F_{klmn}q_n + \frac{1}{2!}\sum_{k,l,m,n,o} C_{ik}C_{jl}C_{jm}F_{klmno}q_n q_o + \ldots, \tag{3.33}$$

$$\bar{F}_{iijj} = \sum_{k,l,m,n} C_{ik}C_{il}C_{jm}C_{jn}F_{klmn} + \sum_{k,l,m,n,o} C_{ik}C_{il}C_{jm}C_{jn}F_{klmno}q_o + \ldots. \tag{3.34}$$

As will be shown in the next section, we avoid this costly transformation of force constants by transforming the corresponding position integrals instead.

Equations (3.28) and (3.29) are the central equations determining the first-order Dyson coordinates and geometry. They must be solved simultaneously because the force constants that appear in Eqs. (3.28) and (3.29) depend on both the geometry, $\{q_i\}$, and on the matrix elements, $\{C_{ij}\}$. Once these equations are solved, the underlying modals $\{\bar{\varphi}\}$ are to satisfy the coupled one-mode equations

$$\left\{-\frac{1}{2}\frac{\partial^2}{\partial\bar{Q}_i^2} + \bar{U}_i(\bar{Q}_i)\right\}\bar{\varphi}_i(\bar{Q}_i) = \bar{\epsilon}_i\bar{\varphi}_i(\bar{Q}_i), \tag{3.35}$$

with

$$\bar{U}_i(\bar{Q}_i) = \bar{U}_i^{(1)}\bar{Q}_i + \frac{1}{2}\bar{U}_i^{(2)}\bar{Q}_i^2, \tag{3.36}$$

and

$$\bar{\epsilon}_i = \bar{E} + \left(s_i + \frac{1}{2}\right)\bar{\omega}_i, \tag{3.37}$$

and

$$\begin{aligned}\bar{E} &= -\frac{1}{2}\sum_i \left\langle \frac{\partial^2}{\partial \bar{Q}_i^2} \right\rangle + \bar{V}_0 + \frac{1}{2}\sum_i \bar{F}_{ii}\langle \bar{Q}_i^2\rangle + \frac{1}{8}\sum_{i,j} \bar{F}_{iijj}\langle \bar{Q}_i^2\rangle\langle \bar{Q}_j^2\rangle \\ &\quad + \frac{1}{48}\sum_{i,j,k} \bar{F}_{iijjkk}\langle \bar{Q}_i^2\rangle\langle \bar{Q}_j^2\rangle\langle \bar{Q}_k^2\rangle + \ldots . \end{aligned} \tag{3.38}$$

This scheme is identified as a member of the SCP family of methods.[31,32,89–91] In this method, a a wave function of crystalline lattice vibration is expressed as a product of harmonic oscillator wave functions whose frequencies are the square roots of the eigenvalues of a thermally and vibrationally averaged dynamical harmonic force constant matrix at a geometry that minimizes the free energy obtained with these frequencies. At zero temperature, this is equivalent to solving Eq. (3.35) with Eqs. (3.28) and (3.29). We call this method at zero temperature SCP[n]. It uses the first-order Dyson coordinates centered at the first-order Dyson geometry.

3.1.5 SCP(n)

When SCP is carried out at the equilibrium geometry, that is, the one that minimizes the internal energy rather than the free energy of a crystal, it is the vibrational mean-field method that uses the first-order Dyson coordinates but neglects the first-order perturbation correction to the geometry. We call this method at zero temperature SCP(n). It is defined by the equations in the previous subsection for SCP[n] with $q_i = 0$ for all i.

3.1.6 Comparison of vibrational mean-field theories

Table 3.1 summarizes the characteristics of the five vibrational mean-field methods discussed in this article.

VSCF is almost always based on normal coordinates centered at the equilibrium geometry, at which the expansion basis functions of modals are also centered (such basis functions are unnecessary in the XVSCF and SCP methods). The centers of the VSCF one-mode potentials, given by Eq. (3.4), shift away from the equilibrium geometry to the vibrationally averaged geometry. Clearly, the latter is related to the first-order Dyson geometry and, in fact, these two geometries become one and the same in the bulk limit. It may thus be argued that VSCF does take into account this geometry shift through the basis-set expansion of modals. However, it does so in a manner that is more problematic than useful because the VSCF algorithms are designed unaware of this shift and the basis functions are left behind at the original center and become increasingly ineffective in expanding these "fleeing" modals.[21]

All of the other methods are formulated with connected diagrams, and they have effective harmonic one-mode potentials. SCP[n] is the most complete (albeit least practically useful; see below) in the sense that it determines and uses both the first-order Dyson coordinates and geometry. The diagonal approximation to the Dyson self-energy

in SCP[n] is XVSCF[n], which neglects the first-order Dyson coordinates. The neglect of the first-order Dyson geometry in SCP[n] leads to SCP(n), whereas the same approximation to XVSCF[n] yields XVSCF(n). XVSCF(n) is the diagonal approximation to the Dyson self-energy of SCP(n).

In XVSCF(n), neither the coordinates nor the geometry are altered. However, in Chapter 2 we proposed an approximate method to evaluate the vibrationally averaged geometry, or the first-order Dyson geometry, by

$$q_i \approx -\frac{U_i^{(1)}}{U_i^{(2)}}, \tag{3.39}$$

where

$$U_i^{(1)} = F_i + \frac{1}{2}\sum_j F_{ijj}\langle Q_j^2\rangle + \frac{1}{8}\sum_{j,k} F_{ijjkk}\langle Q_j^2\rangle\langle Q_k^2\rangle + \ldots. \tag{3.40}$$

Here, we also propose evaluating the approximate first-order Dyson geometry of SCP(n) analogously using

$$q_i \approx -\frac{\bar{U}_i}{\bar{U}_{ii}}, \tag{3.41}$$

where $\bar{U}_i$ and $\bar{U}_{ii}$ are understood to be given by Eqs. (3.28)–(3.29) and (3.30)–(3.34) with $q_i = 0$ in the definitions of $\bar{F}$'s. The first-order Dyson geometries from XVSCF(n) and SCP(n) discussed below have been obtained by Eqs. (3.39) and (3.41), respectively.

In the calculations described below, we implement XVSCF(4) and XVSCF[4] as described in the above sections, with completely unrestricted summation in Eqs. (3.8) and (3.18), unlike previous implementations.[21] This is to facilitate the unitary transformation of coordinates. A discussion of this issue is below.

3.1.7 Summation restrictions in XVSCF

Here, we show that the XVSCF[n] and XVSCF(n) equations presented above, while yielding different numerical results from previous implementations[21] for finite molecules, become equivalent to those presented previously in the bulk limit. The XVSCF[n] equations for the effective gradient ($\tilde{U}_i^{(1)}$), effective force constant ($\tilde{U}_i^{(2)}$), and total vibrational energy (E) from Chapter 2 are

$$\tilde{U}_i^{(1)} = \tilde{F}_i + \frac{1}{2}\sum_{j\neq i}\tilde{F}_{ijj}\langle\tilde{Q}_j^2\rangle + \frac{1}{8}{\sum_{j,k\neq i}}'\tilde{F}_{ijjkk}\langle\tilde{Q}_j^2\rangle\langle\tilde{Q}_k^2\rangle + \ldots, \tag{3.42}$$

$$\tilde{U}_i^{(2)} = \tilde{F}_{ii} + \frac{1}{2}\sum_{j\neq i}\tilde{F}_{iijj}\langle\tilde{Q}_j^2\rangle + \frac{1}{8}{\sum_{j,k\neq i}}'\tilde{F}_{iijjkk}\langle\tilde{Q}_j^2\rangle\langle\tilde{Q}_k^2\rangle + \ldots, \tag{3.43}$$

$$E = \tilde{V}_0 + \frac{1}{2}\sum_i \left(-\left\langle \frac{\partial^2}{\partial \tilde{Q}_i^2} \right\rangle + \tilde{F}_{ii}\langle \tilde{Q}_i^2 \rangle \right) + \frac{1}{8}{\sum_{i,j}}' \tilde{F}_{iijj}\langle \tilde{Q}_i^2 \rangle \langle \tilde{Q}_j^2 \rangle + \ldots, \tag{3.44}$$

where primes on summation symbols specify that multiple indices of summation are restricted to distinct values. It can be demonstrated algebraically[20] as well as diagrammatically that all terms in Eq. (3.44) have the consistent volume dependence of K^1 and are, therefore, term-by-term extensive. The terms in Eq. (3.43), on the other hand, have the K^0 dependence and are thus intensive, which is appropriate for quantities determining frequencies. The terms in Eq. (3.42) have the nonphysical volume dependence of $K^{1/2}$, and therefore, their sum must vanish.

In this work, we have lifted all restrictions on the ranges of summation indices because such restrictions are incongruous to the coordinate transformation. To determine the effect of this change on the internal consistency of the XVSCF formalisms in the bulk limit, we examine the volume dependence of the quantities excluded by the restricted summations, that is, the differences in the XVSCF[n] equations between this work and that of Chapter 2. They are

$$\Delta\tilde{U}_i^{(1)} = \frac{1}{2}\tilde{F}_{iii}\langle \tilde{Q}_i^2 \rangle + \frac{1}{8}\sum_j \tilde{F}_{ijjj}\langle \tilde{Q}_j^2 \rangle^2 + \frac{1}{4}\sum_{j\neq i} \tilde{F}_{iijj}\langle \tilde{Q}_i^2 \rangle \langle \tilde{Q}_j^2 \rangle + \ldots, \tag{3.45}$$

$$\Delta\tilde{U}_i^{(2)} = \frac{1}{2}\tilde{F}_{iiii}\langle \tilde{Q}_i^2 \rangle + \frac{1}{8}\sum_j \tilde{F}_{iijjjj}\langle \tilde{Q}_j^2 \rangle^2 + \frac{1}{4}\sum_{j\neq i} \tilde{F}_{iiijj}\langle \tilde{Q}_i^2 \rangle \langle \tilde{Q}_j^2 \rangle + \ldots, \tag{3.46}$$

$$\Delta E = \frac{1}{8}\sum_i \tilde{F}_{iiii}\langle \tilde{Q}_i^2 \rangle^2 + \frac{1}{48}\sum_i \tilde{F}_{iiiiii}\langle \tilde{Q}_i^2 \rangle^3 + \frac{1}{16}{\sum_{i,j}}' \tilde{F}_{iijjjj}\langle \tilde{Q}_i^2 \rangle \langle \tilde{Q}_j^2 \rangle^2 + \ldots. \tag{3.47}$$

Using the well-established algebraic method described by March *et* al.[24] and discussed extensively by Hirata *et* al.,[20] it can be easily shown that the first through third terms on the right-hand side of Eq. (3.45) have the volume dependence of $K^{-1/2}$. Likewise, all shown terms on the right-hand side of Eq. (3.46) are asymptotically proportional to K^{-1}. The first and third terms on the right-hand side of Eq. (3.47) are K^0 quantities, whereas the second term is asymptotically K^{-1}.

Thus, $\Delta\tilde{U}_i^{(1)}$, $\Delta\tilde{U}_i^{(2)}$, and ΔE have overall volume dependence proportional to, at most, $K^{-1/2}$, K^{-1}, and K^0, respectively. In each case, this is one power less than the overall size dependence of the corresponding XVSCF[n] quantities. Thus, in the bulk limit, $\Delta\tilde{U}_i^{(1)}$, $\Delta\tilde{U}_i^{(2)}$, and ΔE either vanish or are infinitesimally small compared to $\tilde{U}_i^{(1)}$, $\tilde{U}_i^{(2)}$, and E. Therefore, imposing or lifting the restrictions on summation in Eqs. (3.45)–(3.47) has no effect on the bulk limit of XVSCF[n]. The same conclusion applies to XVSCF(n).

3.2 Computer implementation

This section describes an iterative algorithm to determine the first-order Dyson coordinates and geometry of SCP[n] (in the case of quartic force field, i.e., $n = 4$), which we have implemented and applied to several molecules. The

algorithms of XVSCF(4), XVSCF[4], and SCP(4) used in the calculations below can all be deduced from this SCP[4] algorithm.

The objective of the algorithm is to satisfy Eqs. (3.28) and (3.29) self-consistently. It achieves this by performing a unitary transformation of the coordinates and by shifting the coordinate origin gradually in an iterative algorithm Substituting Eqs. (3.31)–(3.34) into (3.28) and (3.29), we find the quantities we need in the nth cycle of the SCP[4] iteration as

$$\bar{U}_i^{[n]} = \sum_j C_{ij}^{[n]} \tilde{U}_j^{[n]}, \tag{3.48}$$

$$\bar{U}_{ij}^{[n]} = \sum_{k,l} C_{ik}^{[n]} C_{jl}^{[n]} \tilde{U}_{kl}^{[n]}, \tag{3.49}$$

with

$$\begin{aligned} \tilde{U}_i^{[n]} &= F_i + \sum_J F_{iJ} q_J^{[n-1]} + \frac{1}{2} \sum_{J,K} F_{iJK} q_J^{[n-1]} q_K^{[n-1]} \frac{1}{2} \sum_{j,k} F_{ijk} D_{jk}^{[n-1]} \\ &\quad + \frac{1}{3!} \sum_{J,K,L} F_{iJKL} q_J^{[n-1]} q_K^{[n-1]} q_L^{[n-1]} + \frac{1}{2} \sum_J \sum_{k,l} F_{iJkl} q_J^{[n-1]} D_{kl}^{[n-1]}, \end{aligned} \tag{3.50}$$

$$\tilde{U}_{ij}^{[n]} = F_{ij} + \sum_K F_{ijK} q_K^{[n-1]} + \frac{1}{2} \sum_{K,L} F_{ijKL} q_K^{[n-1]} q_L^{[n-1]} \frac{1}{2} \sum_{k,l} F_{ijkl} D_{kl}^{[n-1]}, \tag{3.51}$$

and, in the zero-point vibrational state,

$$\begin{aligned} D_{ij}^{[n-1]} &= \sum_k \langle \bar{Q}_k^2 \rangle C_{ki}^{[n-1]} C_{kj}^{[n-1]}, \\ &= \sum_k \frac{C_{ki}^{[n-1]} C_{kj}^{[n-1]}}{2\bar{\omega}_k^{[n-1]}}, \end{aligned} \tag{3.52}$$

where $q_I^{[n-1]}$ and $C_{ij}^{[n-1]}$ designate, respectively, the geometry shift and unitary transformation matrix element from the previous iteration (see the next paragraph for $\bar{\omega}_i^{[n]}$). The capital letters label normal coordinates that transform as totally symmetric irreducible representations; only along the totally symmetric coordinates can q_i be nonzero. Note that all quantities, (F's, ω's, and q's) in Eqs. (3.50)–(3.52) are defined unambiguously in the normal coordinates centered at the equilibrium geometry; the meanings of these quantities (if not their values) never change even as we alter both the coordinates and their origins during iterations. In Eq. (3.52), we have chosen to transform the integrals rather than force constants for a substantial computational advantage.

In each cycle of the iterative algorithm, we first evaluate $\tilde{U}_i^{[n]}$ and $\tilde{U}_{ij}^{[n]}$ according to Eqs. (3.50) and (3.51). They are obtained with invariant quantities such as F's (in the normal coordinates) and the variable quantities determined in the previous iteration, i.e., $C_{ij}^{[n-1]}$, $q_I^{[n-1]}$, and $\bar{\omega}_i^{[n-1]}$. Second, we diagonalize the matrix of $\tilde{U}_{ij}^{[n]}$ to obtain $C_{ij}^{[n]}$ and $\bar{\omega}_i^{[n]}$.

The matrix of $\bar{U}_{ij}^{[n]}$ is diagonal by construction:

$$\bar{U}_{ij}^{[n]} = \delta_{ij}\left(\bar{\omega}_i^{[n]}\right)^2. \tag{3.53}$$

Third, we use Eq. (3.48) to obtain an improved estimate of the Dyson geometry by

$$\begin{aligned} q_I^{[n]} &= q_I^{[n-1]} - \sum_J \frac{\bar{U}_J^{[n]}}{\bar{U}_{JJ}^{[n]}} C_{JI}^{[n]}, \\ &= q_I^{[n-1]} - \sum_{J,K} C_{JI}^{[n]} C_{JK}^{[n]} \tilde{U}_K^{[n]} \left(\bar{\omega}_J^{[n]}\right)^{-2}, \end{aligned} \tag{3.54}$$

The summation indexes can be restricted to totally symmetric coordinates because both the normal and Dyson coordinates transform as irreducible representations. Fourth, we check the convergence by comparing $\{\bar{\omega}_i^{[n]}\}$ with $\{\bar{\omega}_i^{[n-1]}\}$ and $\{q_I^{[n]}\}$ with $\{q_I^{[n-1]}\}$. An appropriate initial guess is $q_I^{[0]} = 0$ for all I and $C_{ij}^{[0]} = \delta_{ij}$ for all i and j.

Once the convergence is achieved, we evaluate the total energy using Eq. (3.23), but avoiding costly transformations of force constants. A more computationally tractable expression for $\bar{E}$ is

$$\begin{aligned} E &= \sum_i \frac{\bar{\omega}_i}{4} + V_0 + \sum_I F_I q_I + \frac{1}{2}\sum_{I,J} F_{IJ} q_I q_J \frac{1}{2}\sum_{i,j} F_{ij} D_{ij} + \frac{1}{3!}\sum_{I,J,K} F_{IJK} q_I q_J q_K \\ &+ \frac{1}{2}\sum_I \sum_{j,k} F_{Ijk} q_I D_{jk} + \frac{1}{4!}\sum_{I,J,K,L} F_{IJKL} q_I q_J q_K q_L \frac{1}{4}\sum_{I,J}\sum_{k,l} F_{IJkl} q_I q_J D_{kl} \\ &+ \frac{1}{8}\sum_{i,j}\sum_{k,l} F_{ijkl} D_{ijkl}, \end{aligned} \tag{3.55}$$

with

$$\begin{aligned} D_{ij} &= \sum_m \langle \bar{Q}_m^2 \rangle C_{mi} C_{mj}, \\ &= \sum_m \frac{C_{mi} C_{mj}}{2\bar{\omega}_m}, \end{aligned} \tag{3.56}$$

$$\begin{aligned} D_{ijkl} &= \sum_m \sum_{n\neq m} \langle \bar{Q}_m^2 \rangle \langle \bar{Q}_n^2 \rangle C_{mi} C_{mj} C_{nk} C_{nl} + \sum_m \langle \bar{Q}_m^4 \rangle C_{mi} C_{mj} C_{mk} C_{ml} \\ &= 3\sum_{m,n} \frac{C_{mi} C_{mj}}{2\bar{\omega}_m} \frac{C_{nk} C_{nl}}{2\bar{\omega}_n} = 3 D_{ij} D_{kl}, \end{aligned} \tag{3.57}$$

where $\bar{\omega}_i$ is the converged frequency of the ith modal and $\langle \bar{Q}_m^2 \rangle = 1/(2\bar{\omega}_m)$ and $\langle \bar{Q}_m^4 \rangle = 3/(4\bar{\omega}_m^2)$ are used.[21] These expressions hold true only for the zero-point vibrational state.

The SCP(4) algorithm used here is obtained by setting $\tilde{U}_i^{(1)} = 0$ and $q_i = 0$ throughout the above, whereas the algorithm for XVSCF[4] can be deduced by substituting $\tilde{U}_{ij} = 0$ and $C_{ij} = \delta_{ij}$ for all $i \neq j$. The XVSCF(4) algorithm

is obtained by combining both of the above.

3.3 Numerical test

We implemented the XVSCF(4), XVSCF[4], SCP(4), and SCP[4] methods as defined in the previous section and applied them to water, naphthalene, anthracene, and *n*-butane using quartic force fields obtained either with MP2/aug-cc-pVTZ (water and *n*-butane) or HF/STO-3G (naphthalene and anthracene) electronic structure calculations. The slight differences in the XVSCF(4) and XVSCF[4] results for water between this work and that of Keçeli and Hirata[21] and Chapter 2 are due to the different ranges of the summation indices (see above and Sec. 3.1.7). The vibrational configuration-interaction (VCI) calculations on the same set of molecules with the respective, identical PES's were also carried out. The results of VCI are essentially exact for the given PES's.

The results for the water molecule are given in Table 3.2. The frequencies, total (zero-point) energies, and geometries calculated by SCP[4] and SCP(4) using the Dyson coordinates are nearly indistinguishable from those obtained by XVSCF[4] and XVSCF(4) based on normal coordinates. For instance, the total energy predicted by SCP[4] is only $4.2 \cdot 10^{-4}$ cm^{-1} lower than that the value obtained by XVSCF[4]. Likewise, the total energy predicted by SCP is only $1.4 \cdot 10^{-3}$ cm^{-1} lower than that obtained by XVSCF(4). They confirm that the calculations with the Dyson coordinates are superior (albeit very slightly) to the calculations with normal coordinates in the variational sense.

While the anharmonic effects on structural parameters are surprisingly well-reproduced by XVSCF and SCP, those on frequencies are often quite poor, occasionally having even the wrong signs. The value of these vibrational mean-field methods is, therefore, limited to their ability to serve as the basis of "correlated" treatments, to be discussed in Chapter 4. Note that VSCF reduces exactly to XVSCF[n] in the bulk limit, although the former can be much more accurate than the latter for small molecules, owing to the inclusion of more force constants in the former.[21]

The Dyson coordinates that are determined by SCP[4] and SCP(4) and are used to obtain the results in Table 3.2 are given in Table 3.3 and Table 3.4, respectively. They are nearly identical to the normal coordinates, explaining the accurate agreement in the frequencies, energies, and geometries between calculations using the two different sets of coordinates (Table 3.2). As required by symmetry, there is no mixing of the antisymmetric stretching coordinate (Q_3), which transforms as the B_2 irreducible representation of C_{2v}, with the other two coordinates, which transform as the totally symmetric A_1. The symmetric stretching (Q_2) and bending (Q_1) coordinates are mixed slightly in the Dyson coordinates.

As can be seen in Table 3.5, agreement between SCP[4] and XVSCF[4] frequencies and between SCP(4) and XVSCF(4) frequencies remains close for the larger molecules of naphthalene, anthracene, and *n*-butane.

Table 3.6 compares the total zero-point energies of naphthalene, anthracene, and *n*-butane obtained with the dif-

ferent vibrational mean-field methods. The differences between XVSCF(4) and SCP(4) and between XVSCF[4] and XVSCF[4], which are due to the use of different sets of coordinates, are again negligible. The total energy of SCP(4) is, however, significantly higher than that of SCP[4], which is caused by the calculation of the Dyson geometry in the latter. The energy reduction from using the Dyson geometry is expected to grow with molecular size, which is indeed the case with the results in Table 3.6. Generally, the order of total energies is XVSCF(n) > SCP $\gg$ XVSCF[n] > SCP[4].

Table 3.7 shows the overlap between the Dyson and normal coordinates, as measured by the smallest values of $|C_{ii}|^2$ in Eq. (3.27), where C_{ii} is the expansion coefficient for the most similar Dyson and normal coordinates. For all molecules and in both SCP[4] and SCP(4), each Dyson coordinate and its most similar normal coordinate are usually indistinguishable with the squared overlap of greater than 0.9 on average. As one notable exception, two Dyson coordinates of *n*-butane determined by SCP(4), which are C–H stretching coordinates, are significant mixtures of normal coordinates. Nevertheless, the SCP(4) frequencies of these two modes differ from the corresponding XVSCF(4) values by only +11 and −9 cm^{-1}. Therefore, it may be said that the Dyson coordinates are usually nearly parallel to the normal coordinates, and even in cases where they are not, the effect on predicted observables appears to be rather limited. This observation is consistent with the finding of Luty *et al.*, who noted that SCP coordinates are nearly identical to normal coordinates for the molecular crystal of ethylene at a temperature of up to 100 K.[91]

Finally, a remark on the computational cost is in order. An SCP[4] or SCP(4) calculation is much more expensive than XVSCF[4] or XVSCF(4). For instance, the XVSCF[4] or XVSCF(4) calculation on any of the molecules studied here takes less than one second on a 2.3-GHz processor. In contrast, the SCP[4] and SCP(4) calculations on naphthalene require 50 and 27 seconds, those on anthracene 177 and 100 seconds, and those on *n*-butane 163 and 63 seconds, respectively. This large increase in computational cost is traced both to the need to evaluate the off-diagonal as well as diagonal elements of the Dyson self-energy and to many additional iterations required to converge the Dyson coordinates. In practice, the advantage brought by the use of the Dyson coordinates and geometry is far outweighed by the added cost of determining them. This is in line with our previous conclusion in Chapter 2 that XVSCF(n) is more practical than XVSCF[n], the latter using the Dyson geometry.

3.4 Conclusion

We have introduced two mathematical constructs for molecules with anharmonic PES: the Dyson coordinates and geometry. The first-order Dyson coordinates are a unitary transform of the normal coordinates wherein the sums of the off-diagonal harmonic force constants and their first-order, linked, irreducible, diagrammatic perturbation corrections become zero. The first-order Dyson geometry is the point on the PES at which the sums of the gradients of the PES and

their first-order perturbation corrections vanish. The Dyson coordinates are the anharmonic vibrational counterpart of the Dyson orbitals in electronic structure theory. The Dyson geometry has no counterpart in electronic structure theory.

The XVSCF[n] method proposed by the present authors solves the coupled one-mode equations with the first-order Dyson self-energy in the diagonal approximation, that is, in the normal coordinates centered at the first-order Dyson geometry. The SCP[N] method solves the same equation, but without the diagonal approximation, namely, in the first-order Dyson coordinates centered at the Dyson geometry. The neglect of the Dyson geometry in SCP[n] amounts to SCP(n). The neglect of both the Dyson geometry and coordinates in SCP[n] corresponds to XVSCF(n). The numerical evidence obtained in this work has shown that the normal coordinates are exceedingly accurate approximations to the Dyson coordinates at least in the first-order approximation to the latter.

In electronic structure theory, the concept of Dyson orbitals is typically applied to perturbation theory of second order and higher.[33,34] Here, we have considered the concepts of the Dyson coordinates and geometries in relation to first-order SCF methods. They are, needless to say, also applicable to second- and higher-order perturbation treatments of the vibrational Dyson self-energy, whose effects on the calculated results are yet to be investigated.

3.5 Figures

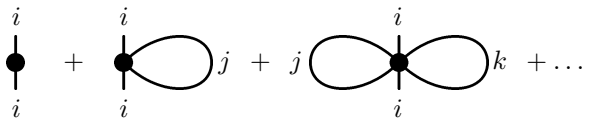

Figure 3.1: The diagrams for $U_i^{(1)}/(2\omega_i^{(0)})$.

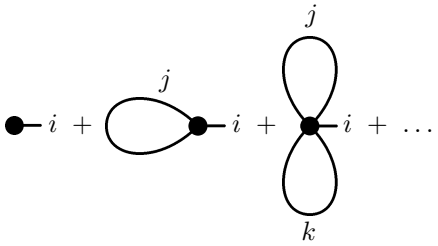

Figure 3.2: The diagrams for $\tilde{U}_i^{(1)}/(2\tilde{\omega}_i^{(0)})^{1/2}$.

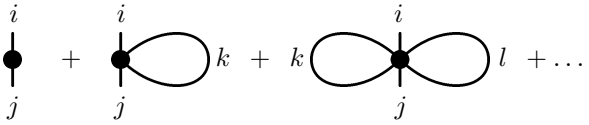

Figure 3.3: The diagrams for $\tilde{U}_{ij}^{(1)}/\{(2\tilde{\omega}_i^{(0)})(2\tilde{\omega}_j^{(0)})\}^{1/2}$.

3.6 Tables

Table 3.1: Comparison of vibrational of mean-field methods.

Method	Geometry	Coordinates
VSCF	Equilibrium[a]	Normal
XVSCF(n)	Equilibrium	Normal
XVSCF[n]	Dyson[b]	Normal
SCP(n)	Equilibrium	Dyson[c]
SCP[n]	Dyson[b]	Dyson[c]

[a] VSCF is almost always based on the normal coordinates centered at the equilibrium geometry, but the centers of its effective potentials coincide with the first-order Dyson geometry in the bulk limit.

[b] The first-order Dyson geometry is the point on the PES at which the sums of gradients and their first-order perturbation corrections vanish.

[c] The first-order Dyson coordinates are those for which the sums of off-diagonal harmonic force constants and their first-order perturbation corrections vanish.

Table 3.2: The anharmonic corrections to the frequency (ω's in cm^{-1}), total (zero-point) energy (E in cm^{-1}), OH bond length (r_{OH} in Å), and HOH bond angle (θ_{HOH} in degrees) of the water molecule.[a]

	XVSCF(4)	XVSCF[4]	SCP[4]	SCP(4)	VCI
ω_1[b]	−90	−60	−90	−60	−72
ω_2[c]	+141	−34	+141	−34	−140
ω_3[d]	+133	−40	+133	−40	−156
E	+48	−35	+48	−35	−57
r_{OH}	+0.013	+0.014	+0.013	+0.014	+0.014
θ_{HOH}	−0.12	−0.16	−0.12	−0.15	−0.15

[a] The differences form Chapter 2 are due to lifting the restrictions in the ranges of the summation indices.

[b] Bending mode.

[c] Symmetric stretching mode.

[d] Antisymmetric stretching mode.

Table 3.3: The first-order Dyson coordinates of the water molecule obtained by SCP[4].

$$\bar{Q}_1 = 1.00(Q_1 - q_1) - 6.2 \cdot 10^{-4}(Q_2 - q_2)$$
$$\bar{Q}_2 = 1.00(Q_2 - q_2) + 6.2 \cdot 10^{-4}(Q_1 - q_1)$$
$$\bar{Q}_3 = Q_3$$

Table 3.4: The first-order Dyson coordinates of the water molecule obtained by SCP(4).

$$\bar{Q}_1 = 1.00Q_1 + 1.0 \cdot 10^{-3}Q_2$$
$$\bar{Q}_2 = 1.00Q_2 - 1.0 \cdot 10^{-3}Q_1$$
$$\bar{Q}_3 = Q_3$$

Table 3.5: The mean absolute deviations in the calculated frequencies (in cm^{-1}) between two methods

Comparison	Naphthalene	Anthracene	*n*-Butane
XVSCF(4) − SCP(4)	0.9	1.2	2.4
XVSCF[4] − SCP[4]	0.7	0.8	1.6
SCP(4) − SCP[4]	7.5	6.8	10

Table 3.6: The difference in the total (zero-point) energies (in cm^{-1}) between two methods

Comparison	Naphthalene	Anthracene	*n*-Butane
XVSCF(4) − SCP(4)	+2.5	+5.1	+6.3
XVSCF[4] − SCP[4]	+2.9	+5.4	+6.1
SCP(4) − SCP[4]	+50	+61	+43

Table 3.7: The minimum value of $|C_{ii}|^2$ in Eq. (3.27).

Method	Naphthalene	Anthracene	*n*-Butane
SCP[4]	0.99	0.98	0.87
SCP(4)	0.99	0.97	0.50

Chapter 4

XVMP2

For small molecules, the XVSCF methods give noticeably different, usually poorer results than VSCF. This is readily traced to the fact that XVSCF uses far fewer force constants than VSCF. Regardless of this difference, however, both VSCF and XVSCF are limited in their ability to achieve accuracy desired in the vibrational frequencies and energies of molecules of any size. This is because the frequency calculations inevitably involve descriptions of excited states that are in general a sum of products of modals rather than a single product,[95] which VSCF and XVSCF employ to describe any state. It may be said that the primary purpose of the VSCF and XVSCF methods is, therefore, to furnish reference wave functions for vibrational *correlation* methods such as vibrational perturbation[7–9] and coupled-cluster methods,[11] which describe states as a sum of products of modals.

In this chapter, we define three XVSCF- and SCP-based vibrational perturbation theories up to second order for frequencies and zero-point energies: XVMP2$\langle n \rangle$, XVMP2[n], and XVMP2(n). They are based on the Møller–Plesset (MP) partitioning of the Hamiltonian and the SCP[n], XVSCF[n], and XVSCF(n) reference wave functions, respectively. Since the XVSCF and SCP methods take into account the first-order effects in a self-consistent fashion, XVMP1$\langle n \rangle$, XVMP1[n], and XVMP1(n) are null for both quantities. We also consider the first- and second-order vibrational perturbation theories based on the reference wave function of the harmonic approximation. These are called XVH1(n) and XVH2(n). Here, we implement and test these methods (except for XVMP2$\langle n \rangle$, whose practical utility is expected to be limited) with $n = 4$, i.e., in the case of a PES that is expressed as a quartic force field (QFF).

It must be stressed that the XVMP2 methods introduced in this work fundamentally differ from the second-order vibrational MP (VMP2) method[7–9] widely used in chemistry.

First, VMP2 is based on Rayleigh–Schrödinger perturbation theory (RSPT) with no consideration on the issue of size consistency as a critical method design guideline.[17,27] A practical consequence of this is that VMP2 relies on VSCF, which is not diagrammatically size consistent and, as a consequence, is less efficient and less numerically stable than size-consistent counterparts (XVSCF) for the aforementioned reasons. Inevitably, VMP2 inherits these shortcomings of VSCF and its algorithm must often deal with the Hamiltonian integrals in modals that are numerically defined on a quadrature grid or linear combinations of harmonic oscillator wave functions. In other words, the formalisms of VMP2 are, like those of VSCF, saddled with non-size-consistent terms, causing the corresponding

algorithms to be also bloated with inefficiency. The XVMP2 formalisms, on the other hand, avoid such algorithmic complications altogether, having simple algebraic expressions for frequencies and zero-point energies given in terms of force constants and frequencies of the reference methods.

Second, VMP2 does not offer a direct method of computing transition frequencies. It instead applies second-order RSPT to both the ground (zero-point) and excited states and calculates the energy differences, which are interpreted as the transition frequencies. There are at least two problems—formal and practical—in this approach: it is unclear whether the transition frequencies thus obtained are strictly intensive; perturbation theories tend to be unstable for excited states,[7,8] where the multi-reference or quasi-degenerate character of wave functions is more a rule than an exception.

The XVMP2 (and also XVH1 and XVH2) methods solve these two problems simultaneously and completely without resorting to quasi-degenerate perturbation theories.[96,97] Our XVMP2 methods are based on the Dyson equation, which is formally an exact theory for frequencies written in terms of coupled one-mode equations. Each mode experiences the effective potential whose definition contains the Dyson self-energy, which is frequency dependent and subject to a diagrammatic perturbation expansion. The XVMP2 algorithms solve the Dyson equation with the diagonal Dyson self-energy expressed as a sum of all connected, irreducible, and nonredundant diagrams up to second order.[23] It is a direct extension of the crystal phonon perturbation theory[70,86] developed in solid state physics to the XVSCF reference wave functions. The connected topology of the self-energy diagrams ensures the rigorous intensivity of transition frequencies, thanks to Goldstone's linked diagram theorem.[28,29] Furthermore, as shown below, the frequency dependence of the Dyson self-energy and the resulting recursive structure of the Dyson equation allows the XVMP2 and XVH2 methods to avoid instabilities due to divergent perturbation series.[88,98,99]

Together, the XVMP2 methods are shown to be algorithmically far simpler alternatives to the VMP2 method, requiring no basis functions or matrix diagonalization at any step of the calculations including the preceding XVSCF ones (though the self-consistent solution of the recursive Dyson equation may be algorithmically related to matrix diagonalization). They give frequencies and zero-point energies of small molecules which are nearly indistinguishable from VMP2. The exceptions are when excited states involved undergo Fermi resonances, where the XVMP2 methods remain accurate, while the VMP2 method shows the clear sign of divergent perturbation series with errors in frequencies in excess of hundreds of cm^{-1}. In addition, the XVMP2 methods can locate multiple roots from the Dyson equation for one mode, which correspond to the fundamental as well as its resonance counterparts, whose frequencies agree well with the corresponding values from full vibrational configuration-interaction (VCI) calculations. The XVMP2 methods can also supply, inexpensively, the relative intensities associated with the multiple roots. The same conclusion holds for XVH2 and nondiagrammatic second-order vibrational perturbation theory (VH2) based on the harmonic approximation.

The rest of this chapter is organized as follows: In Section 4.1.1, an overview of our vibrational perturbation theories based on the Dyson equation and diagrammatic perturbation expansions of the Dyson self-energy in the diagonal approximation is given. In Section 4.1.2, sets of rules to enumerate self-energy diagrams and evaluate them algebraically are provided, with applications to the XVH1 and XVH2 self-energy diagrams as examples. Section 4.1.3 generalizes the preceding subsection to the components of the total energy and their diagrams. Sections 4.1.4, 4.1.5, 4.1.6, and 4.1.7 document the precise diagrammatic and algebraic definitions of XVH$m(n)$, XVMP$m\langle n\rangle$, XVMP$m[n]$, and XVMP$m(n)$ with $m = 1$ or 2 and $n = 4$. Section 4.1.8 compares them with other vibrational perturbation theories, focusing on their second-order incarnations. Section 4.1.9 gives a partial mathematical derivation of the diagrammatic rules of Section 4.1.2 with many examples, and Sec. 4.1.10 clarifies the relationship between RSPT and the Dyson-equation-based diagrammatic perturbation theory. In Section 4.2 are described the algorithms implemented by us to solve the Dyson equation for all roots and evaluate the corresponding residues of the Green's function, which report their relative intensities. The graphical representations of the Dyson equation are given for the off-resonant and near-resonant cases, on which basis it is discussed how the Dyson equation can avoid instability of perturbation theories in the presence of strong resonance. In Section 4.3, the numerical results of XVMP2[4], XVMP2(4), and XVH2(4) for the water and formaldehyde molecules are given and compared with those of some more conventional methods (VCI, VMP2, and RSPT based on the harmonic approximation). There, it is shown that the diagrammatic methods based on the Dyson equation give far superior results for Fermi-resonant modes in formaldehyde.

4.1 Theory

4.1.1 The vibrational Dyson equation

The diagrammatic perturbation theories for anharmonic vibrations introduced in this work are based on the Dyson equation, Eq. (1.50), for the vibrational Green's function, $\mathbf{G}$, defined by Eq. (1.51), which is given in terms of the zeroth-order vibrational Green's function, $\mathbf{G}_0$, given by Eq. (1.52), and the Dyson self-energy, $\mathbf{\Sigma}$, described in Sec. 1.3.2. The ijth element of the Green's function evaluated using the Dyson equation can be written as

$$\{\mathbf{G}^{-1}(\nu)\}_{ij} = \delta_{ij}\frac{\nu^2-\omega_i^2}{2\omega_i} - \{\mathbf{\Sigma}(\nu)\}_{ij}. \tag{4.1}$$

In the diagonal approximation to the self-energy, Eq. (4.1) becomes

$$\{\mathbf{G}^{-1}(\nu)\}_{mm} = \frac{\nu^2-\omega_m^2}{2\omega_m} - \Sigma_m(\nu), \tag{4.2}$$

where $\Sigma_m(\nu) = \{\mathbf{\Sigma}(\nu)\}_{mm}$. The off-diagonal elements of $\mathbf{\Sigma}(\nu)$ in the first-order perturbation approximation have been shown to be negligible. Furthermore, we account for the second- and higher-order perturbation contributions to $\Sigma_m(\nu)$ that restore the effects of the first-order off-diagonal elements when they are neglected (see Sec. 4.1.2). The poles of $\mathbf{G}(\nu)$ occur at ν_m that satisfies,

$$\nu_m = \sqrt{\omega_m^2 + 2\omega_m \Sigma_m(\nu_m)}. \tag{4.3}$$

It is important to note that Eq. (4.3) has ν_m in both the left- and right-hand sides and, therefore, requires a self-consistent solution. It will become evident in the last section that this property enables our perturbation methods based on the Dyson equations to yield accurate frequencies even when the perturbation approximations to the self-energy $\Sigma_m(\nu)$ are divergent at many values of ν.

Furthermore, the recursive structure of Eq. (4.3) means that there can be multiple self-consistent solutions for ν_m for one equation or one mode. In the last section, we shall show that these solutions are all physical, corresponding to overtones, combinations, and/or other transitions to the states that are mutually in resonance. Therefore, the Dyson-equation-based perturbation methods not only reproduce accurate frequencies in the presence of strong anharmonic coupling, but can also account for resonance splitting, thus giving us nearly a complete description of strong correlation.

We can rewrite Eq. (4.2) as

$$\{\mathbf{G}(\nu)\}_{mm} = \frac{2\omega_m}{\nu^2 - \omega_m^2 - 2\omega_m \Sigma_m(\nu)}. \tag{4.4}$$

The residue of this function at $\nu = \nu_m$ is given by

$$\begin{aligned} \mathrm{Res}_{\nu_m}\{\mathbf{G}(\nu)\}_{mm} &= \lim_{\nu\to\nu_m} (\nu - \nu_m)\{\mathbf{G}(\nu)\}_{mm} && (4.5)\\ &= \lim_{\nu\to\nu_m} \left\{ \frac{\nu - \sqrt{\omega_m^2 + 2\omega_m \Sigma_m(\nu_m)}}{\nu - \sqrt{\omega_m^2 + 2\omega_m \Sigma_m(\nu)}} \frac{2\omega_m}{\nu + \sqrt{\omega_m^2 + 2\omega_m \Sigma_m(\nu)}} \right\}. && (4.6) \end{aligned}$$

The limit of the first factor is, according to L'Hospital's rule,

$$\begin{aligned} \lim_{\nu\to\nu_m} \frac{\nu - \sqrt{\omega_m^2 + 2\omega_m \Sigma_m(\nu_m)}}{\nu - \sqrt{\omega_m^2 + 2\omega_m \Sigma_m(\nu)}} &= \lim_{\nu\to\nu_m} \frac{(\partial/\partial\nu)\left\{\nu - \sqrt{\omega_m^2 + 2\omega_m \Sigma_m(\nu_m)}\right\}}{(\partial/\partial\nu)\left\{\nu - \sqrt{\omega_m^2 + 2\omega_m \Sigma_m(\nu)}\right\}} && (4.7)\\ &= \left\{ 1 - \frac{\omega_m}{\nu_m} \left.\frac{\partial \Sigma_m(\nu)}{\partial \nu}\right|_{\nu=\nu_m} \right\}^{-1}. && (4.8) \end{aligned}$$

Since the limit of the second factor of Eq. (4.6) is simply ω_m/ν_m, we find

$$\mathrm{Res}_{\nu_m}\{\mathbf{G}(\nu)\}_{mm} = \omega_m \left\{ \nu_m - \omega_m \left. \frac{\partial \Sigma_m(\nu)}{\partial \nu} \right|_{\nu=\nu_m} \right\}^{-1}. \tag{4.9}$$

The intensity of the transition with frequency ν_m is proportional to this residue, i.e., the numerators in Eq. (1.51) or $(2\omega_m)|\langle\Psi_0|Q_m|\Psi_s\rangle|^2$. Needless to say, the intensity also depends on various other factors such as dipole moment derivatives for infrared absorption and polarizability derivatives for vibrational Raman scattering, etc. This formula is based on the usual assumption that the dipole moments and polarizabilities depend only linearly with Q_m and, therefore, not proportional to the exact intensities even in the limit of infinite order in the perturbation theory. To obtain the latter, one must go beyond the first-order Taylor expansions of these properties in Q_m and evaluate matrix elements not considered in this work using two-particle and higher-order Green's functions.[86]

4.1.2 The vibrational Dyson self-energy

The Dyson equation, Eq. (1.50), is expressed diagrammatically in Fig. 1.1, where the thick line (edge) signifies $\mathbf{G}$, the thin edge $\mathbf{G}_0$, and the circle $\mathbf{\Sigma}$. The second equality in this figure represents,

$$\mathbf{G}(\nu) = \mathbf{G}_0(\nu) + \mathbf{G}_0(\nu)\mathbf{\Sigma}(\nu)\mathbf{G}_0(\nu) + \mathbf{G}_0(\nu)\mathbf{\Sigma}(\nu)\mathbf{G}_0(\nu)\mathbf{\Sigma}(\nu)\mathbf{G}_0(\nu) + \ldots, \tag{4.10}$$

which is obtained by substituting the Dyson equation back into itself recursively.

The Dyson self-energy, $\mathbf{\Sigma}(\nu)$, is a frequency-dependent one-mode potential that accounts for the effects of vibrational correlation.[10] It can be shown that the Dyson self-energy is the sum of all connected, irreducible, and nonredundant diagrams that consist of vertexes and edges.[22–25,86] These diagrams depict all possible ways that a vibrational mode can interact with one another through an anharmonic PES and an appropriate subset of them is taken into account in an approximate calculation.[22] These diagrammatic concepts can be best explained by examples.

First- and second-order self-energy diagrams that arise from the Hamiltonian with a QFF are drawn in Figs. 4.1–4.3. A line with both ends connected with filled circles is an edge representing $\{\mathbf{G}_0\}_{jj}$ where j is the normal-mode index associated with the edge. A line with only one of the ends terminated by a filled circle is a stub, which is there to indicate the rank of the vertex (filled circle). Every self-energy diagram has two stubs such that it has the appropriate topology in the diagrammatic Dyson equation in Fig. 1.1. A stub also carries with it a mode index.

A filled circle or a vertex represents an interaction in the perturbation, $\hat{H}_1$. When the number of the edges or stubs attached to a vertex is m, it is associated with an mth-order (effective) force constant with the corresponding mode indexes. A self-energy diagram with n vertexes thus denotes an nth-order perturbation correction.

One only needs to consider connected, irreducible, and nonredundant diagrams.

Diagram **2u** in Fig. 4.3 is an example of a disconnected diagram. A diagram is disconnected if it is not possible to go from any one vertex to any other one by following edges. Such diagrams must be excluded because they do not scale correctly with size. A connected diagram with n stubs is shown[17] to display the volume (V) dependence of $V^{1-n/2}$. Hence, a connected self-energy diagram, which has two stubs, scales as V^0 and is thermodynamically intensive as a vibrational frequency should be.

Diagrams $\mathbf{2m}^r$ and $\mathbf{2n}^r$, in which the connecting edge is labeled with the same normal mode index as the two stubs, are always reducible. A reducible diagram is the one that reduces to two connected self-energy diagrams upon the removal of an edge. Such diagrams must be excluded from consideration as their inclusion results in counting of a diagram twice because of the recursive structure of the Dyson equation. Diagram **1a** in the right-hand side of the second equality in Fig. 1.1 implies the inclusion of diagrams $\mathbf{2m}^r$ and $\mathbf{2n}^r$ as well as all higher-order reducible diagrams.

Diagram **1b** is redundant in the sense that the interaction represented by its vertex is already in $\hat{H}_0$ and not in $\hat{H}_1$. The inclusion of such redundant diagrams again results in double counting of a perturbation contribution once in the zeroth order and again in a higher order. What constitutes a redundant diagram depends on the partitioning of the Hamiltonian. As shown below, some of the diagrams in Figs. 4.1 and 4.2 are deemed redundant for the XVSCF reference wave function. Diagram **1b** is always redundant.

A set of rules to draw self-energy diagrams is given in Table 4.1. Also, the rules to transform these diagrams into algebraic expressions are summarized in Table 4.2. With the latter, diagram **1a** can, for instance, be interpreted algebraically as

$$\Sigma_m^{(\mathbf{1a})}(\nu) \quad = \quad \frac{1}{2}\sum_i F_{mmii}(2^2\omega_m\omega_i)^{-1}, \tag{4.11}$$

for the ground (zero-point) state. The precise meanings of F_{mmii}, ω_m, and ω_i depend on the choice of the reference wave function, which are clarified below. Here, m labels both stubs (in the diagonal approximation) and i labels the loop edge and the factor of $1/2$ is due to the loop. There is no resolvent line since there is only one vertex. Equation (4.11) is a part of the first-order Dyson self-energy, $\Sigma_m(\nu)$, though it does not have frequency (ν) dependence. The frequencies, ω_m and ω_i, are those of the reference wave function method to be specified in subsequent sections.

Likewise, diagrams **2a** and **2b** are evaluated as

$$\Sigma_m^{(\mathbf{2a})}(\nu) = \Sigma_m^{(\mathbf{2b})}(\nu) = \frac{1}{2}\sum_{i,j}\frac{F_{mmi}F_{ijj}(2^3\omega_m\omega_i\omega_j)^{-1}}{-\omega_i}, \tag{4.12}$$

where, in each diagram, m labels both stubs, i the edge between the two vertexes, and j the loop. The factor of $1/2$ is again due to the loop and the resolvent line gives rise to the factor of $(-\omega_i)^{-1}$. Similarly, diagrams **2c** and **2d** are given

by

$$\begin{aligned}\Sigma_m^{(\mathbf{2c})}(\nu) &= \Sigma_m^{(\mathbf{2d})}(\nu) \\ &= \frac{1}{2}\frac{1}{2!}\sum_{i,j,k}\frac{F_{mmij}F_{ijkk}(2^4\omega_m\omega_i\omega_j\omega_k)^{-1}}{-\omega_i-\omega_j},\end{aligned} \tag{4.13}$$

where m labels stubs, i and j the connecting edges, and k the loop. The factor of $1/2$ arises from the loop in each diagram and $1/2!$ from the two equivalent edges (labeled by i and j).

The algebraic interpretations of diagrams **2e** and **2f** differ in their denominators because of the different orientations of the stubs and Rule (5) of Table 4.2:

$$\Sigma_m^{(\mathbf{2e})}(\nu) = \frac{1}{2!}\sum_{i,j}\frac{F_{mij}^2(2^3\omega_m\omega_i\omega_j)^{-1}}{\nu-\omega_i-\omega_j}, \tag{4.14}$$

$$\Sigma_m^{(\mathbf{2f})}(\nu) = \frac{1}{2!}\sum_{i,j}\frac{F_{mij}^2(2^3\omega_m\omega_i\omega_j)^{-1}}{-\nu-\omega_i-\omega_j}. \tag{4.15}$$

Again m labels the stubs and i and j two equivalent edges, which are responsible for the factor of $1/2!$. Similarly, diagrams **2g** and **2h** are interpreted as

$$\Sigma_m^{(\mathbf{2g})}(\nu) = \frac{1}{3!}\sum_{i,j,k}\frac{F_{mijk}^2(2^4\omega_m\omega_i\omega_j\omega_k)^{-1}}{\nu-\omega_i-\omega_j-\omega_k}, \tag{4.16}$$

$$\Sigma_m^{(\mathbf{2h})}(\nu) = \frac{1}{3!}\sum_{i,j,k}\frac{F_{mijk}^2(2^4\omega_m\omega_i\omega_j\omega_k)^{-1}}{-\nu-\omega_i-\omega_j-\omega_k}, \tag{4.17}$$

of which the factor of $1/3!$ arises from the existence of three equivalent edges labeled by i, j, and k.

Diagrams **2i** and **2j** stand for

$$\Sigma_m^{(\mathbf{2i})}(\nu) = \Sigma_m^{(\mathbf{2j})}(\nu) = \sum_i\frac{F_{mmi}F_i(2^2\omega_m\omega_i)^{-1}}{-\omega_i}. \tag{4.18}$$

If the force constants are the "bare" ones, namely, the derivatives of PES with respect to normal coordinates centered at the equilibrium geometry, then $\Sigma_m^{(\mathbf{2i})} = \Sigma_m^{(\mathbf{2j})} = 0$ since the energy gradients at the center (F_i's) are all zero [Eq. (1.14)].

Diagrams **2k** and **2l** are the contributions from off-diagonal quadratic force constants, F_{ij} with $i \neq j$, in cases where such are nonzero, i.e., where the normal coordinates are not used and/or the center of the coordinates differs

from the equilibrium geometry. Algebraically, these contributions are,

$$\Sigma_m^{(\mathbf{2k})}(\nu) = \Sigma_m^{(\mathbf{2l})}(\nu) = \frac{1}{2!}{\sum_{i,j}}' \frac{F_{mmij}F_{ij}(2^3\omega_m\omega_i\omega_j)^{-1}}{-\omega_i - \omega_j}, \tag{4.19}$$

where the prime on the summation symbol indicates that the terms with $i = j$ are excluded from the sum. This is because the diagonal quadratic force constants, F_{ii}, are always accounted for by $\hat{H}_0$.

Diagrams **2m** and **2n** are reducible if and only if the off-diagonal contribution from **1a** is included in the self-energy. In other words, they are irreducible in the diagonal approximation of the self-energy and should be retained, while they become reducible and should be discarded when the (first-order) Dyson coordinates (see Sec. 4.1.5 and Chapter 3) are used as these coordinates take care of the effects due to the off-diagonal part of **1a**. These diagrams are interpreted as

$$\Sigma_m^{(\mathbf{2m})}(\nu) = \frac{1}{2^2}\sum_{i\neq m}\sum_{j,k} \frac{F_{mijj}F_{mikk}(2^4\omega_m\omega_i\omega_j\omega_k)^{-1}}{\nu - \omega_i}, \tag{4.20}$$

$$\Sigma_m^{(\mathbf{2n})}(\nu) = \frac{1}{2^2}\sum_{i\neq m}\sum_{j,k} \frac{F_{mijj}F_{mikk}(2^4\omega_m\omega_i\omega_j\omega_k)^{-1}}{-\nu - \omega_i}. \tag{4.21}$$

They are contrasted with $\mathbf{2m}^r$ and $\mathbf{2n}^r$ in Fig. 4.3, which are always reducible once **1a** is part of the self-energy. Diagrams **2m** and **2n** recover the effect of off-diagonal elements of the Dyson self-energy which are omitted at first order.

Similarly, diagrams **2o**, **2p**, **2q**, **2r**, **2s**, and **2t** are deemed reducible when the off-diagonal part of **1a** is taken into account by the use of the (first-order) Dyson coordinates. In addition, all six vanish if the coordinates used are the normal coordinates centered at the equilibrium geometry because of Eq. (1.22). Algebraically, they are,

$$\Sigma_m^{(\mathbf{2o})}(\nu) = \sum_{i\neq m} \frac{F_{mi}^2(2^2\omega_m\omega_i)^{-1}}{\nu - \omega_i}, \tag{4.22}$$

$$\Sigma_m^{(\mathbf{2p})}(\nu) = \sum_{i\neq m} \frac{F_{mi}^2(2^2\omega_m\omega_i)^{-1}}{-\nu - \omega_i}, \tag{4.23}$$

$$\begin{aligned}\Sigma_m^{(\mathbf{2q})}(\nu) &= \Sigma_m^{(\mathbf{2s})}(\nu) \\ &= \frac{1}{2}\sum_{i\neq m}\sum_{j} \frac{F_{mijj}F_{mi}(2^3\omega_m\omega_i\omega_j)^{-1}}{\nu - \omega_i},\end{aligned} \tag{4.24}$$

$$\begin{aligned}\Sigma_m^{(\mathbf{2r})}(\nu) &= \Sigma_m^{(\mathbf{2t})}(\nu) \\ &= \frac{1}{2}\sum_{i\neq m}\sum_{j} \frac{F_{mijj}F_{mi}(2^3\omega_m\omega_i\omega_j)^{-1}}{-\nu - \omega_i}.\end{aligned} \tag{4.25}$$

The interpretation rules in Table 4.2 used to derive these expressions are the most expedient ones. There are alternative, more rigorous interpretation rules based on assigning each edge with a zeroth-order Green's function,

$\mathbf{G}_0(\nu)$, and integrating over its frequency ν. Section 4.1.9 documents this alternative set of interpretation rules with applications. Furthermore, it is also possible to rationalize these expressions by RSPT as shown in Sec. 4.1.10.

4.1.3 The vibrational total energy

While the perturbative corrections to vibrational frequencies can be expressed by the aforementioned open diagrams of the Dyson self-energy, the corresponding corrections to total energies are related to closed diagrams, which must be connected and nonredundant. All first- and second-order diagrams for the total energies constructed from a QFF are drawn in Figs. 4.4 and 4.5. They can be enumerated by following the rules given in Table 4.3.

It may be noticed that there is correspondence between open and closed diagrams at a given perturbation order. For instance, open diagram **1a** is obtained by removing one of the edges (but leaving stubs) of closed diagram **1A**. Likewise, open diagrams **2a** and **2b** derive from closed diagram **2A** or vice versa, whereas open diagrams **2c**, **2d**, **2m**, and **2n** are obtained by variously cutting an edge of closed diagram **2B**. Open diagrams **2e** and **2f** are related to closed diagram **2C**, while open diagrams **2g** and **2h** are associated with closed diagram **2D**. Open diagrams **2i** and **2j** are obtained by cutting the loop in **2E** and **2F**, respectively. Open diagrams **2k**, **2l**, and **2q** through **2t** are obtained by cutting the loop or one of the edges in **2H** and **2I**. Finally, open diagrams **2o** and **2p** are obtained by cutting one of the edges in **2J**. Closed diagram **2G** has no corresponding self-energy diagram. When reporting both frequencies and total energies, therefore, the sets of closed diagrams and open diagrams used should correspond to each other for consistency.

A connected closed diagram is the one in which a path of edges can be found between any pair of vertexes. A redundant closed diagram must be excluded because the associated energy contribution is already accounted for by the reference wave function. Which of diagrams **1A** through **2J** are deemed redundant depends on the choice of the reference wave function and will be discussed shortly.

The closed diagrams can be interpreted algebraically by the identical set of rules already given in Table 4.2. Using them, for the ground (zero-point) state, we find the diagram **1A** to represent

$$E_0^{(\mathbf{1A})} = \frac{1}{2!2^2} \sum_{i,j} F_{iijj} (2^2 \omega_i \omega_j)^{-1}. \tag{4.26}$$

The second-order diagrams **2A** through **2J**, again for the ground state, are interpreted algebraically as

$$E_0^{(\mathbf{2A})} = \frac{1}{2^2} \sum_{i,j,k} \frac{F_{ijj} F_{ikk} (2^3 \omega_i \omega_j \omega_k)^{-1}}{-\omega_i}, \tag{4.27}$$

$$E_0^{(\mathbf{2B})} = \frac{1}{2!2^2} \sum_{i,j,k,l} \frac{F_{ijkk} F_{ijll} (2^4 \omega_i \omega_j \omega_k \omega_l)^{-1}}{-\omega_i - \omega_j}, \tag{4.28}$$

$$E_0^{(\mathbf{2C})} = \frac{1}{3!}\sum_{i,j,k}\frac{F_{ijk}^2(2^3\omega_i\omega_j\omega_k)^{-1}}{-\omega_i-\omega_j-\omega_k}, \tag{4.29}$$

$$E_0^{(\mathbf{2D})} = \frac{1}{4!}\sum_{i,j,k,l}\frac{F_{ijkl}^2(2^4\omega_i\omega_j\omega_k\omega_l)^{-1}}{-\omega_i-\omega_j-\omega_k-\omega_l}, \tag{4.30}$$

$$E_0^{(\mathbf{2E})} = E_0^{(\mathbf{2F})} \tag{4.31}$$

$$= \frac{1}{2}\sum_{i,j}\frac{F_iF_{ijj}(2^2\omega_i\omega_j)^{-1}}{-\omega_i}, \tag{4.32}$$

$$E_0^{(\mathbf{2G})} = \sum_i\frac{F_i^2(2\omega_i)^{-1}}{-\omega_i}, \tag{4.33}$$

$$E_0^{(\mathbf{2H})} = E_0^{(\mathbf{2I})} \tag{4.34}$$

$$= \frac{1}{2}\frac{1}{2!}{\sum_{i,j}}'\sum_k\frac{F_{ij}F_{ijkk}(2^3\omega_i\omega_j\omega_k)^{-1}}{-\omega_i-\omega_j}, \tag{4.35}$$

$$E_0^{(\mathbf{2J})} = \frac{1}{2}{\sum_{i,j}}'\frac{F_{ij}^2(2^2\omega_i\omega_j)^{-1}}{-\omega_i-\omega_j}. \tag{4.36}$$

Of these, $E_0^{(\mathbf{2E})}$, $E_0^{(\mathbf{2F})}$, and $E_0^{(\mathbf{2G})}$ vanish when the energy gradients are zero; $E_0^{(\mathbf{2H})}$, $E_0^{(\mathbf{2I})}$, and $E_0^{(\mathbf{2J})}$ vanish when off-diagonal quadratic force constants are zero. The same expressions can be derived by the more rigorous interpretation rules given in Section 4.1.9 or by RSPT in Sec. 4.1.10.

4.1.4 XVH1(n) and XVH2(n)

The mth-order perturbation method based on the reference wave function obtained in the harmonic approximation is referred to as XVHm(n), where n is the truncation rank of the Taylor-series PES. The partitioning of the Hamiltonian is

$$\hat{H}_0 = -\frac{1}{2}\sum_i\frac{\partial^2}{\partial Q_i^2} + V_0 + \frac{1}{2}\sum_i F_{ii}Q_i^2, \tag{4.37}$$

with $\hat{H}_1 = \hat{H} - \hat{H}_0$, where $\{Q_i\}$ is the set of the normal coordinates centered at the equilibrium geometry. Therefore, Eqs. (1.14) and (1.22) hold. The reference wave function $\Psi_0^{(0)}$ is written as

$$|\Psi_0^{(0)}\rangle = \prod_i|s_i\rangle, \tag{4.38}$$

$$\hat{H}_0|\Psi_0^{(0)}\rangle = \left\{V_0 + \sum_i(s_i+1/2)\omega_i\right\}|\Psi_0^{(0)}\rangle, \tag{4.39}$$

where $\omega_i^2 = F_{ii}$ and we use the zero-point state ($s_i = 0$ for all i) as the reference state in this work.

With this reference wave function and the partitioning of $\hat{H}$, there are nonzero first-order corrections to the zeroth-

order frequencies and energy, which are diagrammatically represented by **1a** and **1A**. Diagram **1b** is redundant as its diagonal part due to F_{ii} is already accounted for by $\hat{H}_0$ and its off-diagonal part involving F_{ij} is zero.

The working equation of XVH1(4) for frequencies is Eq. (4.3) with

$$\Sigma_m(\nu) = \Sigma_m^{(\mathbf{1a})}(\nu), \tag{4.40}$$

where F's and ω's appearing in the definition of the right-hand side are the bare force constants [as defined by Eq. (1.21)] and the harmonic frequencies. The total zero-point energy is the sum of the zeroth-order value, $E_0^{(0)}$, and the first-order correction, $E_0^{(1)}$:

$$E_0 = E_0^{(0)} + E_0^{(1)}, \tag{4.41}$$

with

$$E_0^{(0)} = \sum_i \frac{\omega_i}{2} + V_0, \tag{4.42}$$

$$E_0^{(1)} = E_0^{(\mathbf{1A})}. \tag{4.43}$$

It should not be surprising that **1a** and **1A** are the diagrams defining XVSCF.[21] Unlike XVSCF, however, the modals of XVH1(n) are unchanged from those in the harmonic approximation. In other words, XVH1(n) is what one may obtain from the first cycle of the iterative solution of XVSCF(n) starting with the harmonic approximation as an initial guess.

The second-order corrections to the frequencies and energy are characterized by all the diagrams in Figs. 4.2 and 4.5, except diagrams **2i** through **2l**, **2o** through **2t**, and **2E** through **2J** are all zero owing to Eqs. (1.14) and (1.22). Hence, XVH2(4) for frequencies is defined by Eq. (4.3) with

$$\Sigma_m(\nu) = \Sigma_m^{(1)}(\nu) + \Sigma_m^{(2)}(\nu), \tag{4.44}$$

and

$$\Sigma_m^{(1)}(\nu) = \Sigma_m^{(\mathbf{1a})}(\nu), \tag{4.45}$$

$$\begin{aligned}\Sigma_m^{(2)}(\nu) = {} & \Sigma_m^{(\mathbf{2a})}(\nu) + \Sigma_m^{(\mathbf{2b})}(\nu) + \Sigma_m^{(\mathbf{2c})}(\nu) + \Sigma_m^{(\mathbf{2d})}(\nu) + \Sigma_m^{(\mathbf{2e})}(\nu) + \Sigma_m^{(\mathbf{2f})}(\nu) \\ & + \Sigma_m^{(\mathbf{2g})}(\nu) + \Sigma_m^{(\mathbf{2h})}(\nu) + \Sigma_m^{(\mathbf{2m})}(\nu) + \Sigma_m^{(\mathbf{2n})}(\nu),\end{aligned} \tag{4.46}$$

where ω's are again the harmonic frequencies. The total zero-point energy is

$$E_0 = E_0^{(0)} + E_0^{(1)} + E_0^{(2)}, \tag{4.47}$$

and

$$E_0^{(2)} = E_0^{(\mathbf{2A})} + E_0^{(\mathbf{2B})} + E_0^{(\mathbf{2C})} + E_0^{(\mathbf{2D})}. \tag{4.48}$$

The derivatives of the self-energy with respect to ν required in calculating residues [Eq. (4.9)] can be readily and analytically obtained from Eqs. (4.11)–(4.21) and are given explicitly in Sec. 4.2.

See Tables 4.4 and 4.5 for lists of diagrams to be included in each method and Table 4.6 for a summary of the perturbation methods considered in this work.

4.1.5 XVMP1$\langle n \rangle$ and XVMP2$\langle n \rangle$

Next, we consider the first- and second-order perturbation methods based on the SCP reference wave function.[31,32] The SCP method considered here is what we have referred to as SCP[n] (where n again refers to the truncation rank of the Taylor-series PES), the precise definition of which can be found in Chapter 3 and below. We do not implement in this work the first- and second-order perturbation methods on this basis, which we call XVMP1$\langle n \rangle$ and XVMP2$\langle n \rangle$, because of the little practical utility expected from them. We nevertheless discuss these first because more practical methods to be introduced below are viewed as approximations to them.

SCP[n] is a vibrational mean-field method, whose wave function is a product of modals,

$$|\Psi_0^{(0)}\rangle = \prod_i |\bar{s}_i\rangle, \tag{4.49}$$

where $|\bar{s}_i\rangle$ is a harmonic oscillator wave function with quantum number $\bar{s}_i$ along the first-order Dyson coordinate $\bar{Q}_i$ centered at the first-order Dyson geometry. In this work, we only consider the zero-point reference state, where $\bar{s}_i = 0$ for all i. Optimizing $|\bar{s}_i\rangle$ variationally by minimizing $\langle \Psi_0^{(0)} | \hat{H} | \Psi_0^{(0)} \rangle$ leads to a set of coupled one-mode equations in which each modal experiences an effective potential. We have shown both algebraically[20] and diagrammatically[21] that this effective potential becomes harmonic in the bulk limit. The harmonic force constants of the effective potential, however, include the effects of higher-order anharmonic force constants of certain types and differ from the bare quadratic force constants.

The first-order Dyson coordinates are a unitary transformation of the normal coordinates and bring the harmonic force constant matrix of the effective potential of SCP[n] into a diagonal form, thus allowing the total wave function

to be expressed in the product form given above. These harmonic force constants (denoted by $\bar{U}^{(2)}_{ij}$) are, in turn, the sums of the bare quadratic force constants and their first-order perturbation corrections:

$$\delta_{ij}\bar{\omega}_i^2 = \bar{U}^{(2)}_{ij} = \bar{F}_{ij} + \frac{1}{2}\sum_k \bar{F}_{ijkk}(2\bar{\omega}_k)^{-1}, \tag{4.50}$$

in the case of $n = 4$, where $\bar{\omega}_i$ is the frequency of the ith first-order Dyson mode. The force constants with overbars, $\bar{F}$'s, are evaluated in the first-order Dyson coordinates centered at the first-order Dyson geometry and thus differ from the bare force constants F's evaluated in the normal coordinates centered at the equilibrium geometry. The right-hand side of the above equation is diagrammatically depicted in Fig. 4.6 (apart from some factors), where the double-lined edge represents the zeroth-order Green's function of SCP, which should be distinguished from its counterpart in the harmonic approximation drawn as a single-lined edge. It should be clear from Eq. (4.50) and Fig. 4.6 that SCP[4] accounts for the effects of anharmonicity due to the first-order self-energy diagram **1a** on the modals, frequencies, and coordinates.

It has been recognized[20] that the first-order anharmonic corrections are nonvanishing also for the geometry. Such corrections are diagrammatically represented as one-edge analogues of the Dyson self-energy. In the case of a QFF ($n = 4$), they can be depicted as Fig. 4.7. The first-order Dyson geometry is the point in the Taylor-series PES that makes all the gradients (denoted by $\bar{U}^{(1)}_i$) of the effective potential of SCP[n] vanish:

$$0 = \bar{U}^{(1)}_i = \bar{F}_i + \frac{1}{2}\sum_j \bar{F}_{ijj}(2\bar{\omega}_j)^{-1}, \tag{4.51}$$

for $n = 4$. Hence, not only the modals and coordinates, but also the *center* of coordinates of SCP[n] include the effect of anharmonicity at the first-order perturbation level.

With this reference wave function, we partition the Hamiltonian as

$$\hat{H}_0 \quad = \quad -\frac{1}{2}\sum_i \frac{\partial^2}{\partial \bar{Q}_i^2} + E_0^{(0)} + \frac{1}{2}\sum_i \bar{U}^{(2)}_{ii}\bar{Q}_i^2, - \sum_i \frac{\bar{\omega}_i}{2} \tag{4.52}$$

and $\hat{H}_1 = \hat{H} - \hat{H}_0$, where $E_0^{(0)}$ is the SCP[n] zero-point energy and $\bar{\omega}_i$ is the frequency of the ith first-order Dyson mode. The SCP[n] wave function of Eq. (4.49) is an eigenfunction of this zeroth-order Hamiltonian and satisfies,

$$\hat{H}_0|\Psi_0^{(0)}\rangle \quad = \quad \left(E_0^{(0)} + \sum_i \bar{s}_i\bar{\omega}_i\right)|\Psi_0^{(0)}\rangle. \tag{4.53}$$

This is the MP partitioning of the Hamiltonian and we call the first- and second-order perturbation theories based on this partitioning XVMP1$\langle n\rangle$ and XVMP2$\langle n\rangle$.

XVMP1⟨n⟩ and XVMP2⟨n⟩ are based on the zeroth-order Green's function, $\mathbf{G}_0$, constructed from $\{|\bar{s}_i\rangle\}$ with frequencies $\{\bar{\omega}_i\}$. Figure 4.8 relates this $\mathbf{G}_0$ of SCP[4], depicted by the double-lined edge **g1**, to $\mathbf{G}_0$ in the harmonic approximation, drawn as the single-lined edge **g2**. As indicated by **g3**, SCP[4] primarily accounts for the effect of the first-order self-energy diagram **1a** in the self-consistent-field framework. By virtue of the self-consistency, $\mathbf{G}_0$ of SCP[4] contains not only **g3** and **g4** but also **g5** and all higher-order diagrammatic contributions obtained by recursively inserting the self-energies into edges and loops. Therefore, SCP[4] and the perturbation corrections thereof implicitly perform resummation of certain classes of diagrams in the harmonic approximation to all perturbation orders. The same applies to the XVSCF methods and their perturbation corrections, which are, therefore, infinite-order perturbation theories when viewed from the harmonic reference wave function. The XVH methods, on the other hand, include diagrams such as **g3** and **g4** but not **g5**. This explains the superior numerical performance of XVMP2 over that of XVH2 (see below).

From Fig. 4.8 and the foregoing discussion, we see that **1a** as well as **2c**, **2d**, **2m**, and **2n** are already accounted for in the SCP[4] reference wave function and are redundant. Redrawing the self-energy diagrams in Fig. 4.9 with the double-lined edges denoting $\mathbf{G}_0$ of SCP[4], we can have a correct, more compact list (Table 4.4) of diagrammatic perturbation corrections to the self-energy of SCP[4]. Since **1a** is redundant, the self-energy of XVMP1⟨4⟩ is null. Likewise, XVMP2⟨4⟩ must exclude **2c′**, **2d′**, **2m′**, or **2n′** as reducible diagrams.

Another way to justify the elimination of **2c′** is to recognize that the sum of it and **2k′** vanishes because of Eq. (4.50) satisfied by the first-order Dyson coordinates used in SCP[4]. In other words, **2c′** + **2k′** contains the diagrammatic factor of Fig. 4.6, which is zero when i and j refer to distinct modes and absent from $\hat{H}_1$ otherwise [Eq. (4.52)]. Similarly, the sum of **2d′** and **2l′** and the sum of **2m′** through **2t′** both vanish. In SCP[4], furthermore, the first-order Dyson geometry is used, at which Eq. (4.51) holds. This means that the sums **2a′** + **2i′** and **2b′** + **2j′** vanish because they contain the diagrammatic factor of Fig. 4.7, which is zero. These four diagrams are, therefore, also redundant/reducible and discarded together.

In summary, there is no diagrammatic contribution in XVMP1⟨4⟩ and there are only four connected, irreducible, nonredundant diagrammatic contributions in XVMP2⟨4⟩: **2e′**, **2f′**, **2g′**, and **2h′**. Hence, the first- and second-order corrections to the Dyson self-energy of XVMP2⟨4⟩ are given by

$$\Sigma_m^{(1)}(\nu) = 0, \tag{4.54}$$

$$\Sigma_m^{(2)}(\nu) = \Sigma_m^{(\mathbf{2e'})}(\nu) + \Sigma_m^{(\mathbf{2f'})}(\nu) + \Sigma_m^{(\mathbf{2g'})}(\nu) + \Sigma_m^{(\mathbf{2h'})}(\nu), \tag{4.55}$$

where each term in the right-hand side of the last equation is given by Eqs. (4.14)–(4.17), in which F's and ω's are systematically replaced by the corresponding $\bar{F}$'s and $\bar{\omega}$'s. The relationship between $\bar{F}$'s and F's is found in Chapter

3 and $\bar{\omega}$'s are given by Eq. (4.50).

Total energy diagrams are redrawn with the SCP $\mathbf{G}_0$ in Fig. 4.10. The connected, nonredundant total energy diagrams of XVMP2⟨4⟩ are **2C′** and **2D′**. There is no diagram of type **1A** (Fig. 4.4) in XVMP1⟨4⟩ because it is already accounted for by SCP[4]. The sum of all diagrams other than **2C′** and **2D′** vanishes owing to Eqs. (4.50) and (4.51). The zeroth- through second-order parts of the total zero-point energy are, therefore, given by

$$E_0^{(0)} = \sum_i \frac{\bar{\omega}_i}{4} + \bar{V}_0 + \frac{1}{2}\sum_i \bar{F}_{ii}(2\bar{\omega}_i)^{-1} + \frac{1}{2!2^2}\sum_{i,j}\bar{F}_{iijj}(2^2\bar{\omega}_i\bar{\omega}_j)^{-1}, \tag{4.56}$$

$$E_0^{(1)} = 0, \tag{4.57}$$

$$E_0^{(2)} = E_0^{(\mathbf{2C'})} + E_0^{(\mathbf{2D'})}, \tag{4.58}$$

where $\bar{V}_0$ is the value of the Taylor-series PES at the first-order Dyson geometry and $E_0^{(\mathbf{2C'})}$ and $E_0^{(\mathbf{2D'})}$ are defined by Eqs. (4.29) and (4.30), respectively, with F's and ω's replaced by $\bar{F}$'s and $\bar{\omega}$'s. For the derivation of Eq. (4.56), see Chapter 3 and Table I of Ref. 21.

4.1.6 XVMP1[n] and XVMP2[n]

The XVMP1[n] and XVMP2[n] methods are the first- and second-order perturbation methods with the reference wave function obtained from the XVSCF[n] method. Again, n refers to the truncation rank of the Taylor-series PES. Like SCP[n], XVSCF[n] is a vibrational mean-field method, whose wave function is a product of modals,

$$|\Psi_0^{(0)}\rangle = \prod_i |\tilde{s}_i\rangle, \tag{4.59}$$

where $|\tilde{s}_i\rangle$ is a harmonic oscillator wave function along the normal coordinate $\tilde{Q}_i$ centered at the first-order Dyson geometry. Hence, XVSCF[n] is an approximation to SCP[n] and uses the normal coordinates in lieu of the first-order Dyson coordinates.

This reference wave function satisfies the Schrödinger equation,

$$\hat{H}_0|\Psi_0^{(0)}\rangle = \left(E_0^{(0)} + \sum_i \tilde{s}_i\tilde{\omega}_i\right)|\Psi_0^{(0)}\rangle, \tag{4.60}$$

with

$$\hat{H}_0 = -\frac{1}{2}\sum_i \frac{\partial^2}{\partial\tilde{Q}_i^2} + E_0^{(0)} + \frac{1}{2}\sum_i \tilde{U}_{ii}^{(2)}\tilde{Q}_i^2 - \sum_i \frac{\tilde{\omega}_i}{2}, \tag{4.61}$$

where $\tilde{U}_{ii}^{(2)}$ is related to its frequency by $\tilde{U}_{ii}^{(2)} = \tilde{\omega}_i^2$.

Hence, each modal $|\tilde{s}_i\rangle$ of XVSCF[n] is the solution of the one-mode equation with the effective potential, which is harmonic. The effective potential is, therefore, characterized by its quadratic force constants,

$$\tilde{U}^{(2)}_{ij} = \tilde{F}_{ij} + \frac{1}{2}\sum_k \tilde{F}_{ijkk}(2\tilde{\omega}_k)^{-1}, \tag{4.62}$$

and gradients,

$$0 = \tilde{U}^{(1)}_{i} = \tilde{F}_{i} + \frac{1}{2}\sum_j \tilde{F}_{ijj}(2\tilde{\omega}_j)^{-1}, \tag{4.63}$$

in the case of $n = 4$, where $\tilde{F}$'s are the normal-mode force constants evaluated at the first-order Dyson geometry and are related to F's by Eqs. (2.11)–(2.15). Equation (4.63) indicates that the center of the coordinates is shifted from the equilibrium geometry to the first-order Dyson geometry, at which gradients of the effective potential vanish. However, unlike in SCP[n], the coordinates of XVSCF[n] are unaltered from the normal coordinates and hence the off-diagonal elements of $\{\tilde{U}^{(2)}_{ij}\}$ are nonzero. The associated operator, $\tilde{U}^{(2)}_{ij}\tilde{Q}_i\tilde{Q}_j$, remains in the perturbation part of the Hamiltonian, $\hat{H}_1 = \hat{H} - \hat{H}_0$.

With this reference wave function and the partitioning of the Hamiltonian, the first- and second-order corrections to the Dyson self-energy are given by

$$\Sigma^{(1)}_m(\nu) = 0, \tag{4.64}$$

$$\begin{aligned}\Sigma^{(2)}_m(\nu) = {} & \Sigma^{(\mathbf{2c'})}_m(\nu) + \Sigma^{(\mathbf{2d'})}_m(\nu) + \Sigma^{(\mathbf{2e'})}_m(\nu) + \Sigma^{(\mathbf{2f'})}_m(\nu) + \Sigma^{(\mathbf{2g'})}_m(\nu) + \Sigma^{(\mathbf{2h'})}_m(\nu) + \Sigma^{(\mathbf{2k'})}_m(\nu) + \Sigma^{(\mathbf{2l'})}_m(\nu) \\ & + \Sigma^{(\mathbf{2m'})}_m(\nu) + \Sigma^{(\mathbf{2n'})}_m(\nu) + \Sigma^{(\mathbf{2o'})}_m(\nu) + \Sigma^{(\mathbf{2p'})}_m(\nu) + \Sigma^{(\mathbf{2q'})}_m(\nu) + \Sigma^{(\mathbf{2r'})}_m(\nu) + \Sigma^{(\mathbf{2s'})}_m(\nu) + \Sigma^{(\mathbf{2t'})}_m(\nu),\end{aligned} \tag{4.65}$$

The individual contributions are given by

$$\begin{aligned}\Sigma^{(\mathbf{2c'})}_m(\nu) &= \Sigma^{(\mathbf{2d'})}_m(\nu) \\ &= \frac{1}{2^2}{\sum_{i,j}}' \sum_k \frac{\tilde{F}_{mmij}\tilde{F}_{ijkk}(2^4\tilde{\omega}_m\tilde{\omega}_i\tilde{\omega}_j\tilde{\omega}_k)^{-1}}{-\tilde{\omega}_i - \tilde{\omega}_j},\end{aligned} \tag{4.66}$$

and Eqs. (4.14)–(4.25) with their F's and ω's replaced by $\tilde{F}$'s and $\tilde{\omega}$'s.

As in XVMP2⟨4⟩, the sum of **2a′** and **2i′** is zero and needs not be included in XVMP2[4] by virtue of the use of the first-order Dyson geometry [Eq. (4.63)]. For the same reason, **2b′** and **2j′** are excluded. Diagrams **2c′** and **2k′**, which sum to zero in XVMP2⟨4⟩, no longer vanish together when i and j in Fig. 4.9 refer to two distinct modes. This is because the off-diagonal contributions of Eq. (4.62) remain nonzero in XVMP2[4] in which the normal coordinates, rather than the first-order Dyson coordinates, are used. Similarly, diagrams **2d′** and **2l′** with $i \neq j$ and **2m′** through

2t′ with $i \neq m$ are no longer reducible and need to be included in XVMP2[4]. These contributions are often negligible because of the smallness of the off-diagonal elements of the first-order Dyson self-energy. Our implementation nevertheless includes all of the contributions listed in Eq. (4.65) and Table 4.4.

The corrections to the total zero-point energy of XVMP2[4] are given by

$$E_0^{(0)} = \sum_i \frac{\tilde{\omega}_i}{4} + \tilde{V}_0 + \frac{1}{2}\sum_i \tilde{F}_{ii}(2\tilde{\omega}_i)^{-1} + \frac{1}{2!2^2}\sum_{i,j}\tilde{F}_{iijj}(2^2\tilde{\omega}_i\tilde{\omega}_j)^{-1}, \tag{4.67}$$

$$E_0^{(1)} = 0, \tag{4.68}$$

$$E_0^{(2)} = E_0^{(\mathbf{2B'})} + E_0^{(\mathbf{2C'})} + E_0^{(\mathbf{2D'})} + E_0^{(\mathbf{2H'})} + E_0^{(\mathbf{2I'})} + E_0^{(\mathbf{2J'})}, \tag{4.69}$$

where $\tilde{V}_0$ is defined by Eq. (2.11) and the terms in the right-hand side of the above expression are defined by

$$E_0^{(\mathbf{2B'})} = \frac{1}{2!2^2}{\sum_{i,j}}' \sum_{k,l} \frac{\tilde{F}_{ijkk}\tilde{F}_{ijll}(2^4\tilde{\omega}_i\tilde{\omega}_j\tilde{\omega}_k\tilde{\omega}_l)^{-1}}{-\tilde{\omega}_i - \tilde{\omega}_j}, \tag{4.70}$$

and Eqs. (4.29), (4.30), (4.35), and (4.36), respectively, in which F's and ω's are systematically replaced by $\tilde{F}$'s and $\tilde{\omega}$'s. The connecting edges of diagram **2B′** are restricted to distinct normal modes to avoid including the redundant contributions that are already included in XVSCF.

4.1.7 XVMP1(n) and XVMP2(n)

XVSCF(n) is an approximation to SCP[n] in which the normal coordinates centered at the equilibrium geometry are used instead of the first-order Dyson coordinates centered at the first-order Dyson geometry. A wave function of XVSCF(n) thus has the product form,

$$|\Psi_0^{(0)}\rangle = \prod_i |s_i'\rangle, \tag{4.71}$$

where $|s_i'\rangle$ is a harmonic oscillator wave function along the normal coordinate Q_i centered at the equilibrium geometry. It satisfies

$$\hat{H}_0|\Psi_0^{(0)}\rangle = \left(E_0^{(0)} + \sum_i s_i'\omega_i'\right)|\Psi_0^{(0)}\rangle, \tag{4.72}$$

with

$$\hat{H}_0 = -\frac{1}{2}\sum_i \frac{\partial^2}{\partial Q_i^2} + E_0^{(0)} + \frac{1}{2}\sum_i U_{ii}^{(2)}Q_i^2 - \sum_i \frac{\omega_i'}{2}, \tag{4.73}$$

where

$$U_{ij}^{(2)} = F_{ij} + \frac{1}{2}\sum_k F_{ijkk}(2\omega'_k)^{-1}, \tag{4.74}$$

and $U_{ii}^{(2)} = (\omega'_i)^2$. The quadratic force-constant matrix of the effective potential has nonzero off-diagonal elements and the gradients of the effective potential,

$$U_i^{(1)} = F_i + \frac{1}{2}\sum_j F_{ijj}(2\omega'_j)^{-1}, \tag{4.75}$$

are also nonzero, whereas F_i all vanish at the equilibrium geometry.

The first- and second-order corrections to the Dyson self-energy are given by

$$\Sigma_m^{(1)}(\nu) = 0, \tag{4.76}$$

$$\begin{aligned}\Sigma_m^{(2)}(\nu) = {} & \Sigma_m^{(\mathbf{2a'})}(\nu) + \Sigma_m^{(\mathbf{2b'})}(\nu) + \Sigma_m^{(\mathbf{2c'})}(\nu) + \Sigma_m^{(\mathbf{2d'})}(\nu) + \Sigma_m^{(\mathbf{2e'})}(\nu) \\ & + \Sigma_m^{(\mathbf{2f'})}(\nu) + \Sigma_m^{(\mathbf{2g'})}(\nu) + \Sigma_m^{(\mathbf{2h'})}(\nu), + \Sigma_m^{(\mathbf{2m'})}(\nu) + \Sigma_m^{(\mathbf{2n'})}(\nu).\end{aligned} \tag{4.77}$$

Diagrams **2a′** and **2b′** remain because of the election of the equilibrium geometry as the center of coordinates. Diagrams **2i′** and **2j′**, on the other hand, vanish because of Eq. (1.14) and **2k′**, **2l′**, and **2o′** through **2t′** are zero owing to Eq. (1.22). The algebraic formulas for the terms in the last equation are given in Eqs. (4.12), (4.14)–(4.17), (4.20) and (4.21) with ω's replaced by ω''s and by Eq. (4.66) with $\tilde{F}$'s and $\tilde{\omega}$'s replaced by F's and ω''s.

The corresponding corrections to the XVSCF(4) zero-point energy are

$$E_0^{(0)} = \sum_i \frac{\omega'_i}{4} + V_0 + \frac{1}{2}\sum_i F_{ii}(2\omega'_i)^{-1} + \frac{1}{2!2^2}\sum_{i,j} F_{iijj}(2^2\omega'_i\omega'_j)^{-1}, \tag{4.78}$$

$$E_0^{(1)} = 0, \tag{4.79}$$

$$E_0^{(2)} = E_0^{(\mathbf{2A'})} + E_0^{(\mathbf{2B'})} + E_0^{(\mathbf{2C'})} + E_0^{(\mathbf{2D'})}, \tag{4.80}$$

where the algebraic expressions for these contributions are given by Eqs. (4.27), (4.29), and (4.30) with ω's replaced by ω''s and by Eq. (4.70) with $\tilde{F}$'s replaced by F's and $\tilde{\omega}$'s replaced by ω''s.

4.1.8 Comparisons with related methods

Our diagrammatic perturbation theories are a generalization of the crystal phonon diagrammatic formalism[23,70,86] for solids to molecules. The "improved self-consistent phonon" method,[100,101] which takes into account diagrams **2e′**

and **2f′** as well as **2C′** upon SCP, therefore, corresponds to XVMP2⟨3⟩ in our notation. In this chapter, however, we consider up to quartic anharmonicity and resulting diagrams, but using different, more streamlined reference wave functions: XVMP2(4) and XVMP2[4] as well as XVH1(4) and XVH2(4).

Stuchebrukhov *et al.*[88,98,99] made pioneering applications of a finite-temperature diagrammatic Green's function theory to anharmonic molecular vibrations and, in particular, those that were in resonance. Their work accounted for various subsets of the first- and second-order diagrams in Figs. 4.1 and 4.2 as well as an approximate resummation over higher-order diagrams related to **2e**,[88,98] from a harmonic reference. Our XVMP2(4) and XVMP2[4] methods account for all diagrams involving cubic and quartic anharmonicity up to second order as well as certain classes of diagrams (related to **1a**) up to infinite order (when viewed from the harmonic reference) through the implicit resummation of the XVSCF method.

The VMP2 method introduced by Norris *et al.*[7] is a second-order RSPT with a VSCF reference wave function. VMP2 is defined for any mathematical representation of a PES in any coordinates, whereas XVH2 and XVMP2 are defined only for a Taylor-series PES in the normal or Dyson coordinates. The latter restriction arises from the size-consistency requirement;[20,29] only such PES representation lends itself to a rigorous size-dependence analysis and a diagrammatic expression. In VMP2, the perturbation corrections to vibrational frequencies are obtained as differences in total energies between the ground and excited states calculated separately and explicitly using formulas analogous to Eqs. (4.109) and (4.110) in Sec. 4.1.10. This approach has two drawbacks. The first is the tendency for expressions like Eq. (4.110) for excited states to contain near-singularities due to vanishing denominators and become divergent owing to the prevalence of anharmonic resonances.[8,97] The second is its inability to demonstrate the intensivity of transition frequencies thus obtained. The practical consequence of the latter is the fact that VMP2 is algorithmically more complex than XVMP2 or XVH2 which are manifestly extensive and intensive and whose formalisms are the most compact in the bulk limit.

The first drawback, i.e., the instability of VMP2 in the presence of anharmonic resonances is well recognized.[7] The standard remedy for this has been to invoke a deperturbed or dressed Hamiltonian method, in which the divergent terms in the energy expression are deleted and a small Hamiltonian matrix in the basis of the corresponding states is diagonalized.[96,102–107] This procedure is closely related to the multi-reference or quasi-degenerate perturbation theories (QDPT) such as the second-order vibrational QDPT (VQDPT2) of Yagi *et al.*[97] These theories tend to encompass single-reference RSPT as a special case.[97,105] Some of the quantities used to identify important reference wave functions ("P space") in this class of methods are closely related to the Dyson self-energy. For example, the "harmonic derivatives" of Matthews and Stanton[108] are essentially the derivatives of the self-energy [Eq. (4.9)] evaluated at the harmonic frequencies. The shortcomings of these methods are that these criteria tend to be somewhat arbitrary and that the size of the P space can increase rapidly with the number of modes. We shall show that, owing to the re-

cursive structure of the Dyson equation, XVMP2 and XVH2 can eradicate the instability within a single-reference perturbation theory framework and there is no need to resort to a quasi-degenerate or dressed Hamiltonian approach.

Nonetheless, as shown in Sec. 4.1.10, it is possible to derive the identical total energy expressions of XVH and XVMP from RSPT.[20] Hence, our diagrammatic and thus many-body perturbation theories are consistent with RSPT insofar as the total energies are concerned, although the latter is not manifestly size consistent. Our diagrammatic derivation also leads to the frequency-dependent self-energy expressions as perturbation corrections to the harmonic force constants of effective one-mode potentials [Eq. (4.3)]. This is not obtainable from RSPT.

The widely used VPT2 method[96,102–107,109] is a second-order many-body perturbation theory with a harmonic reference wave function. It is nearly the same as our XVH2(4) method except that, in VPT2, diagrams **2B** and **2D** are not included (though they are at the second order according to our definition of perturbation orders) and the right-hand side of Eq. (4.3) is approximated as $\omega_m + \Sigma_m(\omega_m)$. VPT2 has the remarkable property of being exact for a one-dimensional Morse oscillator,[109] which XVH2(4) does not share. The latter, however, includes all force constants up to quartic to second order in perturbation theory and is, therefore, expected to be more accurate than VPT2 except for Morse-like PES's. Furthermore, the approximation to Eq. (4.3) eliminating the frequency dependence in the Dyson self-energy makes VPT2 unable to contain divergent behavior of the underlying perturbation series near anharmonic resonances.

4.1.9 Alternative interpretation of diagrams

Each edge in a diagram has the physical meaning of a zeroth-order Green's function.[22,24,25] In fact, the denominators in the algebraic interpretations of diagrams **2a** through **2t**, for instance, arise naturally from the integration of the frequencies of these zeroth-order Green's functions as intermediate quantities. The expedient rules of diagrammatic interpretation given in Table 4.2 bypass these mathematical steps. In this section, we document the more rigorous interpretation rules with their applications to some of the same diagrams we have considered in the main text.

The rules of algebraic interpretation of diagrams are given in Table 4.7 that apply to both open (self-energy) and closed (energy) diagrams, but only for the reference wave function that is the ground (zero-point) state. However, these rules (as opposed to those in Table 4.2) are more easily extended to reference wave functions that are excited states.

Applying them to diagram **1a** (Fig. 4.11), we obtain

$$\Sigma_m^{(\mathbf{1a})}(\nu) = \sum_i F_{mmii}\langle 0|Q_i^2/2|0\rangle|\langle 1|Q_m|0\rangle|^2 \tag{4.81}$$

$$= \frac{1}{2}\sum_i F_{mmii}(2^2\omega_m\omega_i)^{-1}, \tag{4.82}$$

where we have consulted Table I of Keçeli *et al.*[21] and used

$$\langle s_i|Q_i|s_i+1\rangle = \left(\frac{s_i+1}{2\omega_i}\right)^{1/2}, \tag{4.83}$$

$$\langle s_i|Q_i^2/2|s_i\rangle = \frac{s_i+1/2}{2\omega_i}, \tag{4.84}$$

and the fact that the Q_i operators are Hermitian. Note that the frequency associated with the loop is zero so as to satisfy the energy conservation law (the sum of energy must be ν) at any vertical position of the diagram. Hence, this diagram has no intermediate frequency to integrate over. Equation (4.82) agrees with Eq. (4.11).

Figure 4.12 indicates how edges and stubs of diagram **2a** are labeled. The frequency associated with the ith edge must be zero, as shown in the figure, because the sum of it and the frequency ν of the upgoing stub must equal ν. In this diagram also, we have no intermediate frequency with which to integrate the algebraic interpretation and thus,

$$\Sigma_m^{(\mathbf{2a})}(\nu) = \frac{1}{2!}\sum_{i,j} F_{mmi}F_{ijj}\langle 0|Q_j^2/2|0\rangle|\langle 0|Q_i|1\rangle|^2|\langle 1|Q_m|0\rangle|^2\{\mathbf{G}_0(0)\}_{ii} \tag{4.85}$$

$$= \frac{1}{2!2}\sum_{i,j} F_{mmi}F_{ijj}(2^3\omega_m\omega_i\omega_j)^{-1}\frac{2}{-\omega_i}. \tag{4.86}$$

The last expression is identical to Eq. (4.12), as it should be.

Next, we consider diagram **2c**, which is redrawn in Fig. 4.13 with all edges and stubs labeled. At a vertical position between the two vertexes, three modes exist, i, j, and m (upgoing), and the sum of their frequencies must be conserved at ν. This compels the ith and jth edges to have opposite frequencies, ν_1 and $-\nu_1$, where ν_1 can take any value between $-\infty$ and ∞. Diagram **2c** is thus algebraically written as

$$\Sigma_m^{(\mathbf{2c})}(\nu) = \frac{i}{2!2!}\sum_{i,j,k} F_{mmij}F_{ijkk}|\langle 0|Q_i|1\rangle|^2|\langle 0|Q_j|1\rangle|^2\langle 0|Q_k^2/2|0\rangle|\langle 1|Q_m|0\rangle|^2$$
$$\times\frac{1}{2\pi}\int_{-\infty}^{\infty} d\nu_1\{\mathbf{G}_0(\nu_1)\}_{ii}\{\mathbf{G}_0(-\nu_1)\}_{jj} \tag{4.87}$$

$$= \frac{i}{2!2!2}\sum_{i,j,k} F_{mmij}F_{ijkk}(2^4\omega_m\omega_i\omega_j\omega_k)^{-1}\frac{1}{2\pi}\left(I_{rr}+I_{ra}+I_{ar}+I_{aa}\right), \tag{4.88}$$

where

$$I_{rr} = \int_{-\infty}^{\infty} d\nu_1 \frac{1}{+\nu_1-\omega_i+i\delta}\frac{1}{+\nu_1-\omega_j+i\delta}, \tag{4.89}$$

$$I_{ra} = \int_{-\infty}^{\infty} d\nu_1 \frac{1}{+\nu_1-\omega_i+i\delta}\frac{1}{-\nu_1-\omega_j+i\delta}, \tag{4.90}$$

$$I_{ar} = \int_{-\infty}^{\infty} d\nu_1 \frac{1}{-\nu_1-\omega_i+i\delta}\frac{1}{+\nu_1-\omega_j+i\delta}, \tag{4.91}$$

$$I_{aa} = \int_{-\infty}^{\infty} d\nu_1 \frac{1}{-\nu_1 - \omega_i + i\delta} \frac{1}{-\nu_1 - \omega_j + i\delta}. \tag{4.92}$$

These can be evaluated most conveniently by using the contour integration using one of the two contours drawn in Fig. 4.14. The integrand in I_{rr} has both poles in the lower half of the complex plane. The integration along the upper contour immediately leads to $I_{rr} = 0$ (the integration along the semicircle of an infinite radius is zero). Likewise, $I_{aa} = 0$ since the integrand has both poles in the upper half of the complex plane. For I_{ra} and I_{ar}, integration using either contour gives us the same results, which are

$$I_{ra} = \frac{2\pi i}{\omega_i + \omega_j}, \tag{4.93}$$

$$I_{ar} = \frac{2\pi i}{\omega_i + \omega_j}. \tag{4.94}$$

Substituting these expressions into Eq. (4.88), we obtain

$$\begin{aligned} \Sigma_m^{(\mathbf{2c})}(\nu) &= \frac{i}{2!2!2} \sum_{i,j,k} F_{mmij} F_{ijkk} (2^4 \omega_m \omega_i \omega_j \omega_k)^{-1} \\ &\quad \times \frac{2i}{\omega_i + \omega_j}. \end{aligned} \tag{4.95}$$

The last expression is the same as Eq. (4.13).

We must consider diagrams **2e** and **2f** together for reasons that become evident shortly. They are drawn in Figs. 4.15 and 4.16. In **2e** (Fig. 4.15), for the sum of frequencies to be ν in between the two vertexes, the ith and jth edges have the frequencies of ν_1 and $\nu - \nu_1$, respectively, where ν_1 is an intermediate quantity, which must not appear in the final expression. In **2f** (Fig. 4.16), the ith and jth edges have the frequencies of ν_1 and $-\nu - \nu_1$ because the two stubs with the frequency ν also contribute to the sum in between the two vertexes.

With these notations, **2e** is interpreted as

$$\Sigma_m^{(\mathbf{2e''})}(\nu) = \frac{i}{2!2!} \sum_{i,j} F_{mij}^2 |\langle 0|Q_i|1\rangle|^2 |\langle 0|Q_j|1\rangle|^2 |\langle 0|Q_m|1\rangle|^2 \frac{1}{2\pi} \int_{-\infty}^{\infty} d\nu_1 \{\mathbf{G}_0(\nu_1)\}_{ii} \{\mathbf{G}_0(\nu - \nu_1)\}_{jj} \tag{4.96}$$

$$= \frac{i}{2!2!} \sum_{i,j} F_{mij}^2 (2^3 \omega_m \omega_i \omega_j)^{-1} \frac{1}{2\pi} \left(I'_{rr} + I'_{ra} + I'_{ar} + I'_{aa} \right), \tag{4.97}$$

where

$$I'_{rr} = \int_{-\infty}^{\infty} d\nu_1 \frac{1}{+\nu_1 - \omega_i + i\delta} \frac{1}{+\nu_1 - \nu - \omega_j + i\delta}, \tag{4.98}$$

$$I'_{ra} = \int_{-\infty}^{\infty} d\nu_1 \frac{1}{+\nu_1 - \omega_i + i\delta} \frac{1}{-\nu_1 + \nu - \omega_j + i\delta}, \tag{4.99}$$

$$I'_{ar} = \int_{-\infty}^{\infty} d\nu_1 \frac{1}{-\nu_1 - \omega_i + i\delta} \frac{1}{+\nu_1 - \nu - \omega_j + i\delta}, \tag{4.100}$$

$$I'_{aa} = \int_{-\infty}^{\infty} d\nu_1 \frac{1}{-\nu_1 - \omega_i + i\delta} \frac{1}{-\nu_1 + \nu - \omega_j + i\delta}. \tag{4.101}$$

These integrals are evaluated by contour integration using the contours shown in Fig. 4.14 and are found to be

$$I'_{rr} = 0, \tag{4.102}$$

$$I'_{ra} = \frac{2\pi i}{-\nu + \omega_i + \omega_j}, \tag{4.103}$$

$$I'_{ar} = \frac{2\pi i}{\nu + \omega_i + \omega_j}, \tag{4.104}$$

$$I'_{aa} = 0, \tag{4.105}$$

Substituting these into Eq. (4.97), we obtain

$$\Sigma_m^{(\mathbf{2e}'')}(\nu) = \frac{1}{2!2!} \sum_{i,j} F_{mij}^2 (2^3 \omega_m \omega_i \omega_j)^{-1} \left\{ \frac{1}{\nu - \omega_i - \omega_j} + \frac{1}{-\nu - \omega_i - \omega_j} \right\}. \tag{4.106}$$

Note that $\Sigma_m^{(\mathbf{2e}'')}$ does not agree with $\Sigma_m^{(\mathbf{2e})}$ given in Eq. (4.14).

Following essentially the same steps, we arrive at the algebraic expression of **2f**, which reads

$$\Sigma_m^{(\mathbf{2f}'')}(\nu) = \frac{1}{2!2!} \sum_{i,j} F_{mij}^2 (2^3 \omega_m \omega_i \omega_j)^{-1} \left\{ \frac{1}{-\nu - \omega_i - \omega_j} + \frac{1}{\nu - \omega_i - \omega_j} \right\}. \tag{4.107}$$

This also disagrees with $\Sigma_m^{(\mathbf{2f})}$ in Eq. (4.15). It may, however, be noticed that the sum of Eqs. (4.106) and (4.107) is equal to the sum of Eqs. (4.14) and (4.15), namely,

$$\Sigma_m^{(\mathbf{2e}'')}(\nu) + \Sigma_m^{(\mathbf{2f}'')}(\nu) = \Sigma_m^{(\mathbf{2e})}(\nu) + \Sigma_m^{(\mathbf{2f})}(\nu). \tag{4.108}$$

Hence, the different interpretation between **2e** and **2e**′′ and between **2f** and **2f**′′ causes no inconsistency in the actual use of these diagrams because one must include both **2e** and **2f** or neither and the sum of their algebraic expressions remains unchanged between the two sets of rules. The same holds true for the diagram pair **2g** and **2h**.

4.1.10 Relationship to Rayleigh–Schrödinger perturbation theory

Here we show that the same formulas for the perturbation corrections to the total (zero-point) energy can be obtained from RSPT. It is also shown that the difference in these perturbation corrections between the ground and excited states is consistent with (if not the same as) the corresponding self-energy expressions derived diagrammatically. In other

words, we can rationalize the methods described above from nondiagrammatic perturbation theory.

According to Ref. 20, one class of contributions in the second-order perturbation correction to the total zero-point energy arises from the sum over excited-state configurations which differ from the zero-point state in the vibrational quantum numbers of three distinct normal modes. The contribution of this class for a Taylor-series PES truncated after cubic force constants is

$$\begin{aligned} E_0^{(\mathbf{2C}'')} &= \sum_n{}'' \frac{\langle\Psi_0^{(0)}|\hat{H}_1|\Psi_n^{(0)}\rangle\langle\Psi_n^{(0)}|\hat{H}_1|\Psi_0^{(0)}\rangle}{E_0^{(0)} - E_n^{(0)}} \\ &= \frac{1}{3!}\sum_{i,j,k}{}' \frac{F_{ijk}^2|\langle 0|Q_i|1\rangle|^2|\langle 0|Q_j|1\rangle|^2|\langle 0|Q_k|1\rangle|^2}{-\omega_i - \omega_j - \omega_k} \\ &= \frac{1}{3!}\sum_{i,j,k}{}' \frac{F_{ijk}^2(2^3\omega_i\omega_j\omega_k)^{-1}}{-\omega_i - \omega_j - \omega_k}, \end{aligned} \tag{4.109}$$

where the double prime on the first summation symbol indicates that this is not the only contribution at the second order and the single prime indicates that all normal modes are distinct. This contribution can be easily identified as the diagrammatic correction due to **2C** excluding contributions involving coincident indexes. The remaining contributions to **2C** and all other omitted perturbation corrections can also be considered similarly.

Applying the above formula to the excited reference state in which the mth mode is promoted to the $s_m = 1$ level, we obtain

$$\begin{aligned} E_{s_m=1}^{(\mathbf{2C}'')} &= \sum_n{}'' \frac{\langle\Psi_{s_m=1}^{(0)}|\hat{H}_1|\Psi_n^{(0)}\rangle\langle\Psi_n^{(0)}|\hat{H}_1|\Psi_{s_m=1}^{(0)}\rangle}{E_0^{(0)} + \omega_m - E_n^{(0)}} \\ &= \frac{1}{3!}\sum_{i,j,k\neq m}{}' \frac{F_{ijk}^2|\langle 0|Q_i|1\rangle|^2|\langle 0|Q_j|1\rangle|^2|\langle 0|Q_k|1\rangle|^2}{-\omega_i - \omega_j - \omega_k} + \frac{1}{2!}\sum_{i,j\neq m}{}' \frac{F_{mij}^2|\langle 1|Q_m|2\rangle|^2|\langle 0|Q_i|1\rangle|^2|\langle 0|Q_j|1\rangle|^2}{-\omega_m - \omega_i - \omega_j} \\ &\quad + \frac{1}{2!}\sum_{i,j\neq m}{}' \frac{F_{mij}^2|\langle 1|Q_m|0\rangle|^2|\langle 0|Q_i|1\rangle|^2|\langle 0|Q_j|1\rangle|^2}{\omega_m - \omega_i - \omega_j} \\ &= \frac{1}{3!}\sum_{i,j,k\neq m}{}' \frac{F_{ijk}^2(2^3\omega_i\omega_j\omega_k)^{-1}}{-\omega_i - \omega_j - \omega_k} + \frac{1}{2!}\sum_{i,j\neq m}{}' \frac{2F_{mij}^2(2^3\omega_m\omega_i\omega_j)^{-1}}{-\omega_m - \omega_i - \omega_j} \\ &\quad + \frac{1}{2!}\sum_{i,j\neq m}{}' \frac{F_{mij}^2(2^3\omega_m\omega_i\omega_j)^{-1}}{\omega_m - \omega_i - \omega_j}. \end{aligned} \tag{4.110}$$

The difference between this and Eq. (4.109) should be a part of the second-order perturbation correction to the frequency of the mth mode. Subtracting Eq. (4.109) from Eq. (4.110), we find

$$\begin{aligned} E_{s_m=1}^{(\mathbf{2C}'')} - E_0^{(\mathbf{2C}'')} &= \frac{1}{2!}\sum_{i,j\neq m}{}' \frac{F_{mij}^2(2^3\omega_m\omega_i\omega_j)^{-1}}{-\omega_m - \omega_i - \omega_j} + \frac{1}{2!}\sum_{i,j\neq m}{}' \frac{F_{mij}^2(2^3\omega_m\omega_i\omega_j)^{-1}}{\omega_m - \omega_i - \omega_j} \\ &\approx \Sigma_m^{(\mathbf{2e})}(\omega_m) + \Sigma_m^{(\mathbf{2f})}(\omega_m), \end{aligned} \tag{4.111}$$

which is very close to the sum of diagrams **2e** and **2f**. It becomes equal to the sum when the normal mode indexes in **2e** and **2f** are restricted to take distinct values. The slight differences involving coincident indexes are again associated with other classes of perturbation corrections and can also be derived similarly. Diagrams **2e** and **2f** are, furthermore, the open diagrams corresponding to the closed one, **2C**. In this sense, we argue that the diagrammatic perturbation theory based on the Dyson equation and RSPT are consistent with each other.

There are, of course, differences. First, the above energy difference lacks frequency (ν) dependence, which is the hallmark of the Dyson equation and brings some stability to the calculated results, as illustrated in the main text. There is no provision in RSPT to introduce such dependence. The energy difference instead agrees with the diagrammatic counterparts with ν replaced by their reference frequency ω_m, which are analogous to the "one-shot" approximations discussed in Section 4.3. Second, the diagrammatic theory interprets the perturbation corrections as those to the Dyson self-energy, not necessarily to the frequencies; see Eq. (4.3). In the diagrammatic theories, there are additional steps to obtain the perturbation corrections to the frequencies from $\Sigma_m(\nu)$'s; we must solve Eq. (4.3). RSPT, in contrast, suggests simply adding $\Sigma_m(\nu)$ to the reference frequency, which, as we have seen, is prone to divergence problems.

4.2 Algorithms and implementation

There are at least three distinguishing features of the diagrammatic perturbation methods and their algorithms that separate them from the previously proposed vibrational methods in chemistry.

First, the XVH and XVMP methods as well as their underlying reference method XVSCF do not need basis functions to expand modals; the working equations are given in terms of force constants and matrix representations of operators in harmonic oscillator wave functions, which are given analytically.[21]

Second, the force constants that enter these working equations are only those that scale correctly with size. Hence, these diagrammatic methods are fundamentally more efficient in the bulk limit than other methods that are saddled with non-size-consistent contributions.

Third, because of the recursive structure of the Dyson equation, the unknown frequency appears in the definitions of the perturbation corrections to the self-energy. The working equations, therefore, require self-consistent solutions for the frequencies, which are obtained by an iterative algorithm to be described below. This may appear to be an unwanted complication in the algorithms, but this is not the case. As shown below, the recursive structure gives us access to multiple roots from a single equation, which all have valid physical meanings. It also resists divergent behavior that often plagues other perturbation theories.

The working equations for the frequencies of XVH1(4), XVH2(4), XVMP2[4], and XVMP2(4) are the same and

are given by Eq. (4.3) or, equivalently,

$$\nu_m = F(\nu_m)^{1/2}, \tag{4.112}$$

with

$$F(\nu_m) = \omega_m^2 + 2\omega_m \Sigma_m(\nu_m), \tag{4.113}$$

where $\Sigma_m(\nu)$ is defined for each method in the previous section and ω_i is the frequency of the ith normal mode for XVH1(4) and XVH2(4) or of the ith XVSCF modal for XVMP2[4] or XVMP2(4). The XVSCF(4) and XVSCF[4] methods used in this chapter are implemented as discussed in Chapter 3, but unlike as discussed in Chapter 2, in that summation indexes in our XVSCF implementation run through all normal modes without any restriction.

The physical solutions of this equation occur at the intersections of $y = \{F(x)\}^{1/2}$ and $y = x$. Two representative examples of how they intersect are drawn in Figs. 4.17 and 4.18. The function $F(x)$ is finite for all $x > 0$ except at a finite number of values $\{x_p\}$ at which it is divergent. Figure 4.17 corresponds to the situation where x is far from any such singularities and $\{F(x)\}^{1/2}$ varies only slowly with x. In contrast, $\{F(x)\}^{1/2}$ in Fig. 4.18 depends strongly on x and is divergent at two values in the domain of x used in the plot. In the latter, $y = \{F(x)\}^{1/2}$ and $y = x$ intersects multiple times, causing Eq. (4.112) to have more than one real, nonnegative solutions for ν_m, all of which are physically meaningful.

The frequency dependence of $F(x)$ arises from diagrams **2e** through **2h** and **2m** through **2t** (or their double-lined analogues). Among them, the contributions from diagrams with bare stubs pointing towards each other cause no singularities, whereas those with stubs pointing away from each other are responsible for the divergences at

$$x_p = \omega_i, \tag{4.114}$$

$$x_q = \omega_i + \omega_j, \tag{4.115}$$

$$x_r = \omega_i + \omega_j + \omega_k, \tag{4.116}$$

for any combinations of modes i, j, and/or k. As will be shown below, $F(x)$ is a monotonically decreasing function of x ($x > 0$) between two adjacent singularities. This means that there is exactly one intersection of $\{F(x)\}^{1/2}$ and x and thus one root of Eq. (4.112) per each interval between two adjacent singularities.

The procedure to solve Eq. (4.112) for each mode m to obtain multiple roots is as follows. First, we list all the singularities and sort them in the ascending order of their positions ($x_{\text{min.}} < x_1 < \ldots < x_n < x_{\text{max.}}$), where $x_{\text{min.}}$ (typically zero) and $x_{\text{max.}}$ are the boundaries of the domain within which we seek the roots. Second, for each

interval between x_p and x_{p+1}, we recursively refine the position of the intersection (if any) by evaluating $\{F(x)\}^{1/2}$ on a grid and linearly interpolating it between the two grid points nearest the intersection. In our implementation, we have placed 20 grid points evenly spaced in x^2 over a segment that encompasses the intersection. This segment is recursively and exponentially constricted. In this way, all the roots in $x_{\text{min.}} < x < x_{\text{max.}}$ can be determined with the precision of 10^{-9} cm^{-1}. Recursive equations such as Eq. (4.112) are often somehow related to a CI procedure (i.e., matrix diagonalization).[110,111] For larger molecules, therefore, the recursive structure should be exploited to allow the determination of a few important roots rather than all roots per equation.

Once Eq. (4.112) is solved for ν_m, the corresponding residue (which is related to the transition probability or band intensity) is given by Eq. (4.9) with

$$\left.\frac{\partial\Sigma_m(\nu)}{\partial\nu}\right|_{\nu=\nu_m} = 0, \tag{4.117}$$

for XVH1(4) or

$$\begin{aligned}
\left.\frac{\partial\Sigma_m(\nu)}{\partial\nu}\right|_{\nu=\nu_m} = & -\frac{1}{2}\sum_{i,j}\frac{F_{mij}^2(2^3\omega_m\omega_i\omega_j)^{-1}}{(\nu_m-\omega_i-\omega_j)^2}+\frac{1}{2}\sum_{i,j}\frac{F_{mij}^2(2^3\omega_m\omega_i\omega_j)^{-1}}{(-\nu_m-\omega_i-\omega_j)^2}-\frac{1}{6}\sum_{i,j,k}\frac{F_{mijk}^2(2^4\omega_m\omega_i\omega_j\omega_k)^{-1}}{(\nu_m-\omega_i-\omega_j-\omega_k)^2} \\
& +\frac{1}{6}\sum_{i,j,k}\frac{F_{mijk}^2(2^4\omega_m\omega_i\omega_j\omega_k)^{-1}}{(-\nu_m-\omega_i-\omega_j-\omega_k)^2}-\frac{1}{4}\sum_{i\neq m}\sum_{j,k}\frac{F_{mijj}F_{mikk}(2^4\omega_m\omega_i\omega_j\omega_k)^{-1}}{(\nu_m-\omega_i)^2} \\
& +\frac{1}{4}\sum_{i\neq m}\sum_{j,k}\frac{F_{mijj}F_{mikk}(2^4\omega_m\omega_i\omega_j\omega_k)^{-1}}{(-\nu_m-\omega_i)^2}-\sum_{i\neq m}\sum_{j}\frac{F_{mijj}F_{mi}(2^3\omega_m\omega_i\omega_j)^{-1}}{(\nu_m-\omega_i)^2} \\
& +\sum_{i\neq m}\sum_{j}\frac{F_{mijj}F_{mi}(2^3\omega_m\omega_i\omega_j)^{-1}}{(-\nu_m-\omega_i)^2}-\sum_{i\neq m}\frac{F_{mi}^2(2^2\omega_m\omega_i)^{-1}}{(\nu_m-\omega_i)^2}+\sum_{i\neq m}\frac{F_{mi}^2(2^2\omega_m\omega_i)^{-1}}{(-\nu_m-\omega_i)^2},
\end{aligned} \tag{4.118}$$

for XVH2(4), XVMP2(4), or XVMP2[4] (in the latter two cases, F's and ω's should be replaced by the appropriate quantities furnished by XVSCF; in the first two cases, the last four terms vanish). Incidentally, the right-hand side of the above expression is always negative for positive ν_m (the last six terms can be factored by common denominators into two terms with positive numerators), proving our earlier assertion that $F(x)$ is monotonically decreasing between two adjacent singularities.

The total zero-point energies of the respective method are evaluated straightforwardly using the expressions such as Eqs. (4.47) and (4.48) in the case of XVH2(4).

The most expensive steps of the whole calculations are the evaluation of the quartic force constants (F's) and their transformation to those at the first-order Dyson geometry ($\tilde{F}$'s), the evaluation of $\Sigma_m^{(\mathbf{2g})}$ [Eq. (4.16)] and $\Sigma_m^{(\mathbf{2h})}$ [Eq. (4.17)] for each mode m, which involve three-fold summation over mode indexes, and the calculation of $E^{(\mathbf{2D})}$ [Eq. (4.30)], which has four-fold summation. The operational cost of all of these steps scales as $O(N^4)$ with the number of modes N. This may be contrasted with the cost scaling of the conventional VMP2 method that is $O(M^4N^4)$, where M is

the number of basis functions per mode. Since the latter (M) need not increase with size, the overall scaling is the same between XVH2, XVMP2, and VMP2, although the prefactor multiplying the cost scaling function is certainly greater in VMP2. It should, however, be remembered that XVH2 and XVMP2 calculations require repeated evaluations of the self-energy expressions in the iterative algorithm to solve the Dyson equation self-consistently, which increases their cost (if not the size dependence of the cost). For the systems shown below, all VH2, XVH2, and XVMP2 calculations complete in less than 1 second. The VMP2 calculations take slightly longer owing to the greater prefactor on the cost function.

4.3 Numerical tests

We performed XVMP2(4), XVMP2[4] and XVH2(4) calculations on the water and formaldehyde molecules and compared the results with the VCI, VMP2, and VH2 results obtained with the same QFF's. VH2 refers to the second-order RSPT using a harmonic reference wave function. It takes into account all force constants up to quartic to second order, unlike VPT2, which does not include second-order corrections due to quartic force constants. In spite of this, VPT2 is sometimes more accurate than VH2 as the former happens to give exact results for a Morse oscillator. However, we use VH2 for comparison because it is the RSPT counterpart of XVH2(4). The equilibrium geometries and QFF's were determined at the second-order Møller–Plesset perturbation (MP2) theory with the aug-cc-pVTZ basis set using NWCHEM[82] and SINDO.[81] The VCI and VMP2 calculations were performed with MAVI,[112] using the twenty lowest-lying harmonic oscillator wave functions of each mode as the basis set. The VMP2 and VH2 frequencies were obtained as the energy differences between the zero-point and excited states determined by the respective methods, evaluated without using a dressed Hamiltonian or quasi-degenerate approach. The VCI calculations performed here were the *full* VCI with harmonic reference wave functions. Its results were converged to within 0.1 cm^{-1} of the exact solutions of the Schrödinger equations for the given QFF's.

The frequencies and zero-point energies of water and formaldehyde are presented in Tables 4.8 and 4.9, respectively. For all but ν_5 of formaldehyde, VMP2 can reproduce the VCI results within 6 cm^{-1}. VH2 performs noticeably less well, attesting to the usefulness of the VSCF reference, but its results for low-lying states are often within a few cm^{-1} of VCI. For ν_5 of formaldehyde, however, VMP2 and VH2 both fail dramatically, as has long been known.[97] The error between VCI and VMP2 is in excess of 600 cm^{-1} (see also Table 4.10 in which the errors from VCI are given). Clearly, this is caused by the Fermi resonance in ν_5, which makes the perturbation series divergent because of the occurrence of near-zero denominators in their expressions.

With the exception of ν_5 of formaldehyde, the XVMP2 and XVH2 results are similar to VMP2 and VH2, respectively, although the former methods are much simpler in both formalisms and algorithms. In fact, the XVH2(4) results

for zero-point energies are identical to the corresponding VH2 values, as their formalisms are the same (this is not the case for frequencies). XVMP2[4] is nearly systematically closer to VMP2 and VCI than XVMP2(4). This is expected as the former is based on XVSCF[4], which takes into account the shift in the center of the effective potentials of VSCF in a size-consistent manner and is less approximate than XVSCF(4). However, the differences between XVMP2[4] and XVMP2(4) are so small that the added computational cost in the former may not be justified.

It can also be seen that XVMP2(4) and XVMP2[4] are systematically (albeit slightly) closer to VCI than XVH2(4). This is traced to the fact that XVMP2 includes a subset of third- and all higher-order diagrams in the harmonic approximation through the self-consistent solution of the XVSCF equation.

The residues, which, in this case, report the weights of the fundamental transitions within the one-mode picture of the reference method, are nearly unity for all cases except for ν_5 of formaldehyde (the values slightly greater than unity are common in nonvariational methods). This means that the wave functions of the zero-point states and the destinations of the transitions (except for ν_5 of formaldehyde) are predominantly single Hartree products of modals, the deviations where from can usually be accurately captured by the second-order perturbation methods of any type.

This is of course not the case with ν_5 of formaldehyde. The weights of the Hartree products in the corresponding VCI wave function are distributed among the three products of reference modals with quantum numbers (000010), (001001), and (010001). In other words, ω_5 (with a harmonic frequency of 3048 cm^{-1}) undergoes Fermi resonance with combinations $\omega_3\omega_6$ (2807 cm^{-1}) and $\omega_2\omega_6$ (3020 cm^{-1}), giving rise to three transitions in 2700–3000 cm^{-1} that are mixtures of these. As mentioned above, VMP2 and VH2 are incapable of describing such strong coupling because the anharmonic effect is no longer a small perturbation.

The most striking finding is that all three diagrammatic perturbation methods can accurately reproduce the frequency of ν_5 as well as those of the other two Fermi-resonant counterparts; the errors from VCI are all within 30 cm^{-1} for XVMP2(4) and XVMP2[4] (see also the "self-consistent" category of Table 4.10). The ability of these perturbation theories to avoid divergence in the presence of resonance is ascribed to the recursive structure of the Dyson equation, Eq. (4.3) or Eq. (4.112). Figure 4.18 plots the right- and left-hand sides of Eq. (4.3) for XVMP2[4] near ν_5. The three intersections (indicated by open circles) of the two curves, $y = \{F(x)\}^{1/2}$ and $y = x$, are the roots of this equation, whose numerical values are given in the column of XVMP2[4] of Table 4.9. From this figure, it is evident that, despite divergent behavior in $\{F(x)\}^{1/2}$ inevitable in any perturbation theory, the solutions of the Dyson equation must stay on $y = x$, which ensures that they are not too far from the frequency of the reference modal (ω_5, in this case) and cannot be divergent.

The three intersections of Fig. 4.18 correspond to the Fermi triads, whose positions are in good agreement with the corresponding VCI frequencies indicated by filled circles. Hence, the frequency dependence in the Dyson self-energy allows the Dyson equation, which has the apparent one-mode structure, to access all many-mode states. We

thus assert that a perturbation theory can be applied to "strongly correlated" problems and locate all states that are in resonance, insofar as it is used in the context of the Dyson equation; it does not necessarily need a multi-reference or quasi-degenerate treatment, either, which may require *a priori* knowledge of resonances.

Since the reference wave functions of XVMP2 and XVH2 are (effectively) harmonic, combinations such as $\omega_3\omega_6$ and $\omega_2\omega_6$ are optically "dark" (in the first-order approximation to the dipole moment and polarizability tensors) whereas fundamentals of appropriate symmetry including ω_5 of formaldehyde (transforming as B_2 in the C_{2v} point group) are "bright." As a result of mixing of these reference modals, the Fermi triads all become partially bright through intensity borrowing. The relative intensities of the triads are proportional to the associated residues given in the parentheses in Table 4.9. They are in reasonable agreement with the weights of the fundamental transitions in the VCI results.

For modes that are far from any resonance, such as ν_4 of formaldehyde, the plots of the left- and right-hand sides of the Dyson equation look like Fig. 4.17. The Dyson self-energy for ν_4 has negligibly small frequency dependence, causing the intersection to nearly coincide with the value of $\{F(\omega_4)\}^{1/2}$. This suggests an expedient, approximate method of locating off-resonant roots of the Dyson equation, which is simply to ignore the frequency dependence of the self-energy and substitute $\Sigma_m(\nu_m) \approx \Sigma_m(\omega_m)$ in the right-hand side of Eq. (4.3).

Table 4.10 compiles the results of XVMP2(4), XVMP2[4], and XVH2(4) for formaldehyde obtained with this "one-shot" approximation, i.e., without achieving self consistency in the Dyson equation.[10] The XVMP2(4), XVMP2[4], and XVH2(4) columns in the "non-self-consistent" category give these results, whereas the VMP2 and VH2 results in the "non-self-consistent" category and all in the "self-consistent" category are the same as those in Table 4.9. As expected from the foregoing argument, these one-shot XVMP2 and XVH2 calculations are extremely accurate approximations to their self-consistent counterparts for ν_2 through ν_4 and ν_6. Also expected is the dramatic failure of these methods for ν_5; the errors in these one-shot results from VCI can be as great as -414 cm^{-1}. Somewhat surprisingly, however, one-shot XVMP2(4) performs poorly for ν_1 with the deviation from VCI being -191 cm^{-1} despite the fact that the residue of the corresponding self-consistent root is 0.97 (see Table 4.9). This underscores the importance of the self-consistent solutions of the Dyson equation; it can nearly completely suppress divergent behavior, which may or may not be easily anticipated.

4.4 Conclusion

In this work, we have given a complete, detailed description of the novel and powerful class of vibrational perturbation theories based on the Dyson equation and a diagrammatic expansion of the Dyson self-energy in the diagonal approximation. We have also documented rules of drawing and interpreting these diagrams, sometimes in more than

one ways, for self-energies and total energies. On this basis and with the reference wave functions of SCP, XVSCF, or the harmonic approximation, we have defined XVMP2$\langle n \rangle$, XVMP2[n], and XVMP2(n) as well as XVH1(n) and XVH2(n) and implemented the latter four methods with $n = 4$ (QFF's).

Unlike RSPT-based theories such as VMP2, the XVMP2 and XVH2 methods are diagrammatically size consistent for both frequencies and total energies. The practical consequence of this is the remarkable simplicity of their algorithms, which require only force constants and frequencies of the reference methods; they do not need (nor do the underlying reference wave function methods need) basis sets, quadrature, or matrix diagonalization. In spite of this algorithmic simplicity and efficiency, XVMP2 and XVH2 are shown to give equally accurate results as VMP2 and VH2 except for modes that are in strong resonance.

In the latter case, XVMP2 and XVH2 considerably outperform VMP2 and VH2 with the errors from the former methods being at least an order of magnitude smaller than those from the latter. Furthermore, XVMP2 and XVH2 can locate all the states that participate in the resonance from the single Dyson equation. They can also obtain the relative intensities of these resonant transitions as the corresponding residues of the Green's function. The stability of the transition frequencies and the access to multiple transitions of XVMP2 and XVH2 in the presence of resonance is traced to the recursive structure of the Dyson equation and is inimitable by RSPT.

4.5 Figures

1a

Figure 4.1: The first-order, connected, irreducible self-energy diagram formed with a QFF.

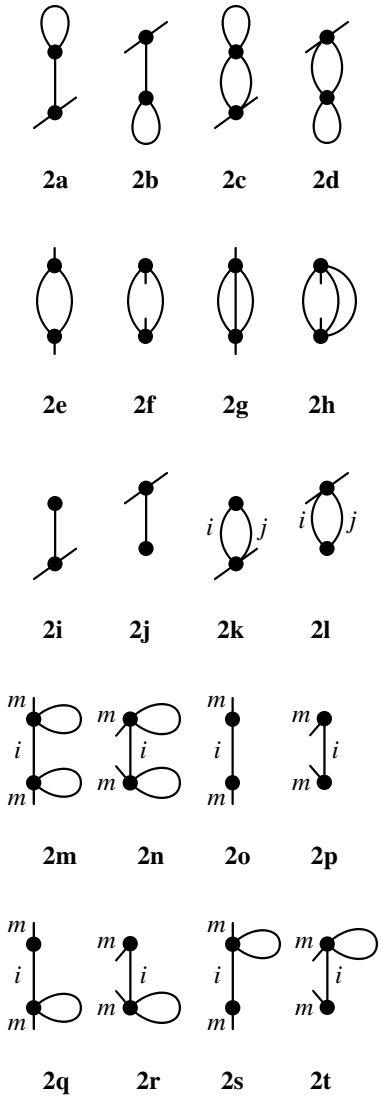

Figure 4.2: Second-order, connected, irreducible self-energy diagrams formed with a QFF. The edges or stubs with different explicit labels (m, i, and j) correspond to distinct modes.

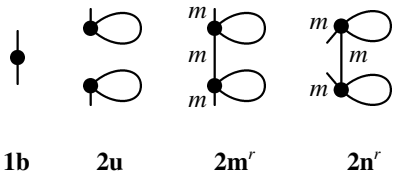

Figure 4.3: Self-energy diagrams that are redundant, disconnected, and/or reducible.

1A

Figure 4.4: The first-order, connected energy diagram formed with a QFF.

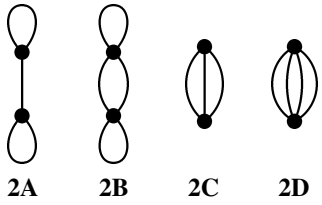

2A **2B** **2C** **2D**

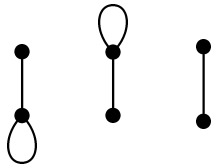

2E **2F** **2G**

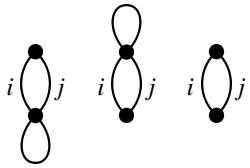

2H **2I** **2J**

Figure 4.5: Second-order, connected energy diagrams formed with a QFF. The edges or stubs with different explicit labels (m, i, and j) correspond to distinct modes.

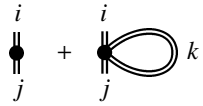

Figure 4.6: The diagrammatic expression of $\bar{U}_{ij}^{(2)}(2^2\bar{\omega}_i\bar{\omega}_j)^{-1/2}$, where $\bar{U}_{ij}^{(2)}$ is the harmonic force constant of the effective potential of SCP[4].

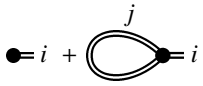

Figure 4.7: The diagrammatic expression of $\bar{U}_i^{(1)}(2\bar{\omega}_i)^{-1/2}$, where $\bar{U}_i^{(1)}$ is the gradient of the effective potential of SCP[4].

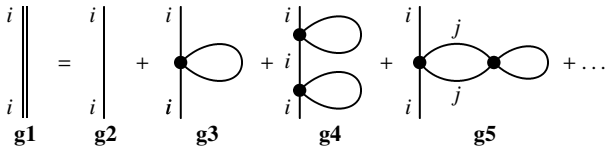

Figure 4.8: A diagrammatic representation of the Dyson equation in the SCP or XVSCF method. The double-lined edge (**g1**) represents the zeroth-order Green's function of SCP or XVSCF, whereas the single-lined edge (**g2**) the zeroth-order Green's function in the harmonic approximation. Modes *i* and *j* are not necessarily distinct.

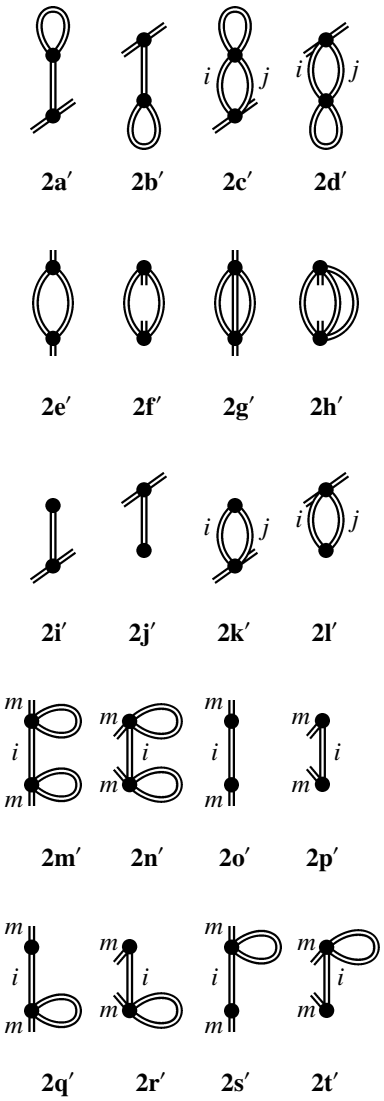

Figure 4.9: Second-order, connected self-energy diagrams in the XVMP2 family of methods. The double-lined edge denotes the zeroth-order Green's function of the corresponding SCP or XVSCF method (**g1** of Fig. 4.8). The edges or stubs labeled differently (*m*, *i*, and *j*) correspond to distinct modes.

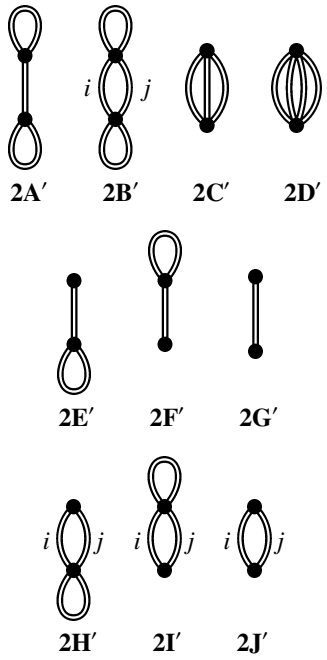

Figure 4.10: Second-order, connected energy diagrams of the XVMP2 family of methods. The double-lined edge denotes the zeroth-order Green's function of the corresponding SCP or XVSCF method (**g1** of Fig. 4.8). The edges labeled differently (*i* and *j*) correspond to distinct modes.

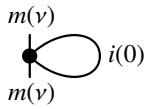

Figure 4.11: Diagram **1a** with mode and frequency (in parentheses) labels on edges and stubs.

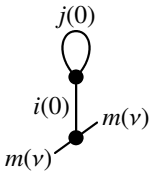

Figure 4.12: Diagram **2a** with mode and frequency (in parentheses) labels on edges and stubs.

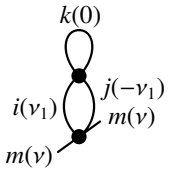

Figure 4.13: Diagram **2c** with mode and frequency (in parentheses) labels on edges and stubs.

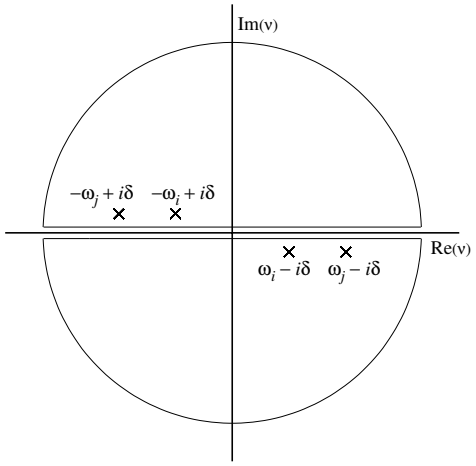

Figure 4.14: Contours in complex plane.

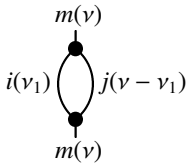

Figure 4.15: Diagram **2e** with mode and frequency (in parentheses) labels on edges and stubs.

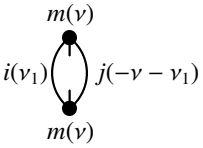

Figure 4.16: Diagram **2f** with mode and frequency (in parentheses) labels on edges and stubs.

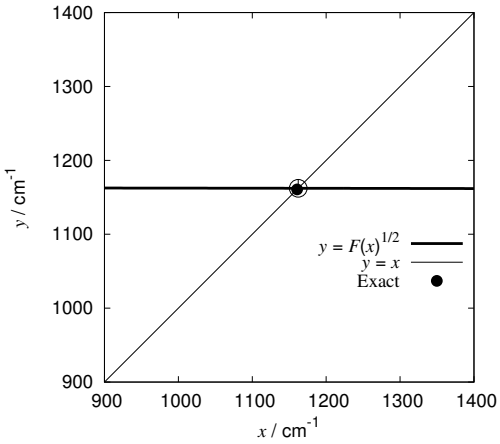

Figure 4.17: A plot of the left- and right-hand sides of Eq. (4.112) as a function of $x \equiv \nu_m$ in the XVMP2[4] calculation of formaldehyde near $x = \tilde{\omega}_4$. The open circle at the intersection of two curves corresponds to the XVMP2[4] root, whereas the filled circle is the exact solution from the VCI calculation.

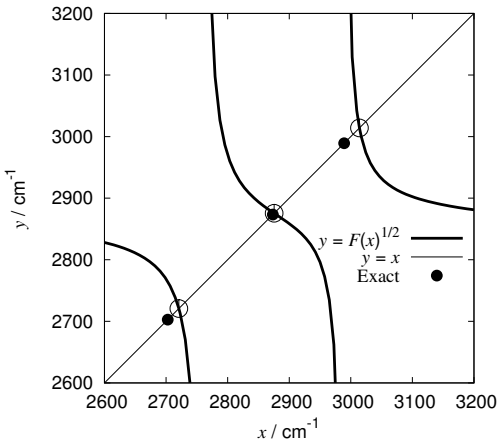

Figure 4.18: A plot of the left- and right-hand sides of Eq. (4.112) as a function of $x \equiv \nu_m$ in the XVMP2[4] calculation of formaldehyde near $x = \tilde{\omega}_5$. The open circles at the intersections of two curves correspond to the XVMP2[4] roots, whereas the filled circles are the exact solutions from the VCI calculation.

4.6 Tables

Table 4.1: Rules to draw all the nth-order self-energy diagrams for an mth-order Taylor-series PES.

(1) Draw $n + 2$ vertexes in an unambiguous vertical order. The first (bottom) and the last (top) vertexes are 'phantom' vertexes having one stub each. All the other vertexes have up to m stubs.
(2) Connect vertexes by drawing an edge between two stubs. Leave no stubs unused and enumerate all topologically distinct connections.
(3) Erase the phantom vertexes and the edges attached to them. The vertexes with a stub are called open vertexes.
(4) Eliminate all disconnected, reducible, and redundant diagrams.

Table 4.2: Rules to obtain the algebraic expression of an open (self-energy) or a closed (energy) diagram.

(1) Label all edges (including loops) and stubs with mode indexes, i_1, i_2, etc. Sum over all edge (but not stub) indexes. Restrict summations to exclude redundant or reducible contributions if necessary.
(2) For an nth-order vertex (having n edges or stubs with labels $i_1, \ldots, i_n$), associate $F_{i_1 \ldots i_n} \prod_k (2\omega_{i_k})^{-1/2}$, where $F_{i_1 \ldots i_n}$ is the nth-order force constant and ω_i is the frequency of the ith mode.
(3) For n equivalent edges, multiply $1/n!$. Two edges are equivalent when they terminate at the same vertexes.
(4) For each loop, multiply 1/2.
(5) For each pair of adjacent vertexes, draw a horizontal ("resolvent") line in between. Associate $(\zeta\nu - \sum_k \omega_{i_k})^{-1}$, where i_k runs over the indexes of all edges (not including loops or stubs) that intersect with the resolvent line. When the resolvent line lies between two open vertexes, $\zeta = \pm 1$ (with the plus sign used when the stubs point away from each other and the minus sign when the stubs point toward each other); otherwise, $\zeta = 0$.

Table 4.3: Rules to draw all the *n*th-order energy diagrams for an *m*th-order Taylor-series PES.

(1) Draw n vertexes in an unambiguous vertical order. Each vertex can have up to m stubs.

(2) Connect vertexes by drawing an edge between two stubs. Leave no stubs unused and enumerate all topologically distinct connections.

(3) Eliminate all disconnected and redundant diagrams.

Table 4.4: The self-energy diagrams included in the perturbation methods.

Method	Diagrams in Figs. 4.1, 4.2, and 4.9
XVH1(4)	**1a**
XVMP1⟨4⟩	none
XVMP1[4]	none
XVMP1(4)	none
XVH2(4)	**2a**, **2b**, **2c**, **2d**, **2e**, **2f**, **2g**, **2h**, **2m**, **2n**
XVMP2⟨4⟩	**2e′**, **2f′**, **2g′**, **2h′**
XVMP2[4]	**2c′**, **2d′**, **2e′**, **2f′**, **2g′**, **2h′**, **2k′**, **2l′**, **2m′**, **2n′**, **2o′**, **2p′**, **2q′**, **2r′**, **2s′**, **2t′**
XVMP2(4)	**2a′**, **2b′**, **2c′**, **2d′**, **2e′**, **2f′**, **2g′**, **2h′**, **2m′**, **2n′**

Table 4.5: The energy diagrams included in the perturbation methods.

Method	Diagrams in Figs. 4.4, 4.5, and 4.10
XVH1(4)	**1A**
XVMP1⟨4⟩	none
XVMP1[4]	none
XVMP1(4)	none
XVH2(4)	**2A**, **2B**, **2C**, **2D**
XVMP2⟨4⟩	**2C′**, **2D′**
XVMP2[4]	**2B′**, **2C′**, **2D′**, **2H′**, **2I′**, **2J′**
XVMP2(4)	**2A′**, **2B′**, **2C′**, **2D′**

Table 4.6: The reference wave functions and the harmonic frequencies (ω's) and force constants (F's) to be used when interpreting the self-energy and total energy diagrams with the rules in Table 4.2.

Method	Reference	Frequencies[a]	Force constants[b]
XVH$m(n)$	Harmonic	ω	F
XVMP$m\langle n\rangle$	SCP[n]	$\bar{\omega}$	$\bar{F}$
XVMP$m[n]$	XVSCF[n]	$\tilde{\omega}$	$\tilde{F}$
XVMP$m(n)$	XVSCF(n)	ω'	F

[a] A normal-mode frequency in the harmonic approximation is denoted by ω, while $\bar{\omega}$, $\tilde{\omega}$, and ω' respectively designate the effective harmonic frequencies of the reference mean-field methods, SCP[n], XVSCF[n], and XVSCF(n).

[b] F denotes a bare force constant in the normal coordinates centered at the equilibrium geometry; $\bar{F}$ is a force constant in the first-order Dyson coordinates centered at the first-order Dyson geometry; $\tilde{F}$ is a force constant in the normal coordinates centered at the first-order Dyson geometry.

Table 4.7: Rules to obtain the algebraic expression of an open (self-energy) or a closed (energy) diagram.

(1) Label the kth edge with mode index i_k and associate frequency ν_k. Label both stubs with mode index m and associate frequency ν. At any vertical position of the diagram, require that the sum of the frequencies (ν and ν_k's) be conserved.
(2) Associate the kth nonloop edge with the zeroth-order Green's function $i\{\mathbf{G}_0(\nu_k)\}_{i_k i_k}$.
(3) For an nth-order vertex (having n edges or stubs with labels $i_1, \ldots, i_n$; one or two of i_k's may be m), associate $(-i)F_{i_1 \ldots i_n}$, where $F_{i_1 \ldots i_n}$ is the nth-order force constant.
(4) For the kth nonloop edge, associate $|\langle 0|Q_{i_k}|1\rangle|^2$, where Q_{i_k} is the i_kth normal or Dyson coordinate. For the kth loop edge, associate $\langle 0|Q_{i_k}^2/2|0\rangle$. For each stub, associate $\langle 1|Q_m|0\rangle$.
(5) For n equivalent edges, multiply $1/n!$. Two edges are equivalent when they terminate at the same vertexes.
(6) Sum over all edge (but not stub) indexes. Integrate over all edge (but not stub) frequencies ν_k's. Attach $(2\pi)^{-1}$ for each integration.
(7) For an n-vertex diagram, attach a factor of $i/n!$.

Table 4.8: The zero-point energy (E_0) and frequencies (ν_i) of the fundamental transitions (in cm^{-1}) of the water molecule calculated with conventional and diagrammatic vibrational methods. The values in parentheses are the CI weights of the fundamental transitions (in the VCI column) or the residues of respective Green's functions (in the columns of XVMP2 and XVH2). The VCI results are essentially exact for the QFF.

	VCI	VMP2	VH2	XVMP2(4)	XVMP2[4]	XVH2(4)
E_0	4642	4642	4630	4647	4641	4630
ν_1	3682 (0.86)	3682	3625	3668 (1.04)	3668 (1.00)	3633 (0.98)
ν_2	1557 (0.98)	1558	1564	1560 (0.98)	1559 (1.00)	1566 (1.04)
ν_3	3791 (0.91)	3786	3728	3771 (1.06)	3774 (1.01)	3731 (1.03)

Table 4.9: The zero-point energy (E_0) and frequencies (ν_i) of the fundamental transitions (in cm^{-1}) of the formaldehyde molecule calculated with conventional and diagrammatic vibrational methods. The values in parentheses are the CI weights of the fundamental transitions (in the VCI column) or the residues of respective Green's functions (in the columns of XVMP2 and XVH2). The VCI results are essentially exact for the QFF.

	VCI	VMP2	VH2	XVMP2(4)	XVMP2[4]	XVH2(4)
E_0	5814	5814	5810	5815	5813	5810
ν_1	2837 (0.85)	2839	2811	2831 (0.97)	2828 (0.95)	2823 (0.94)
ν_2	1720 (0.94)	1720	1722	1721 (1.00)	1720 (1.00)	1722 (0.99)
ν_3	1502 (0.97)	1503	1503	1502 (1.00)	1503 (1.00)	1503 (1.01)
ν_4	1161 (0.98)	1163	1165	1163 (0.98)	1162 (1.01)	1166 (1.03)
ν_5	2873 (0.47)	3565	2983	2873 (0.68)	2875 (0.62)	2885 (0.52)
	2703 (0.17)[a]			2709 (0.23)[c]	2721 (0.24)[c]	2749 (0.42)[c]
	2989 (0.27)[b]			3019 (0.15)[d]	3014 (0.16)[d]	3039 (0.10)[d]
ν_6	1238 (0.98)	1239	1242	1240 (0.99)	1239 (1.01)	1242 (1.02)

[a]The predominant component of this excited-state wave function is the (001001) configuration.

[b]The predominant component of this excited-state wave function is the (010001) configuration.

[c]The resonance with ν_5 is caused by diagram **2e** of Fig. 4.2 with the force constant F_{356}.

[d]The resonance with ν_5 is caused by diagram **2e** of Fig. 4.2 with the force constant F_{256}.

Table 4.10: The errors (in cm^{-1}) in the calculated frequencies of formaldehyde from VCI. The "non-self-consistent" calculations mean either that VMP2 or VH2 is used or that the self-energy is evaluated with the frequency of the reference method and the Dyson equation, Eq. (4.3), is never solved for self-consistent roots. The "self-consistent" results are the same as those in Table 4.9.

	Non-self-consistent					Self-consistent		
	VMP2	VH2	XVMP2(4)	XVMP2[4]	XVH2(4)	XVMP2(4)	XVMP2[4]	XVH2(4)
ν_1	+2	−26	−191	−16	−30	−7	−9	−14
ν_2	+0	+2	+1	+0	+2	+1	+0	+2
ν_3	+2	+1	+1	+1	+1	+1	+1	+1
ν_4	+2	+4	+3	+2	+5	+3	+2	+5
ν_5	+691	+109	+33	−414	+109	−0	+2	+11
ν_6	+2	+4	+3	+2	+5	+3	+2	+5

Chapter 5

MC-XVSCF

Carrying out an XVSCF calculation requires evaluating the first three Taylor coefficients of the mean-field potential, $U_i(Q_i)$, whose diagrammatic and algebraic equations we repeat in Fig. 5.1 and below,

$$\begin{aligned} E_0 &= \sum_i \frac{\omega_i}{4} + V_0 + \frac{1}{2}\sum_i F_{ii}\,(2\omega_i)^{-1} + \frac{1}{2^2 2!}\sum_{i,j} F_{iijj}\left(2^2\omega_i\omega_j\right)^{-1} \\ &\quad + \frac{1}{2^3 3!}\sum_{i,j,k} F_{iijjkk}\left(2^3\omega_i\omega_j\omega_k\right)^{-1} + \ldots, \end{aligned} \tag{5.1}$$

$$\frac{U_i^{(1)}}{(2\omega_i)^{1/2}} = F_i\,(2\omega_i)^{-1/2} + \frac{1}{2}\sum_j F_{ijj}\left(2^3\omega_i\omega_j^2\right)^{-1/2} + \frac{1}{2^2 2!}\sum_{j,k} F_{ijjkk}\left(2^5\omega_i\omega_j^2\omega_k^2\right)^{-1/2} + \ldots, \tag{5.2}$$

$$\frac{U_{ii}^{(2)}}{2\omega_i} = F_{ii}\,(2\omega_i)^{-1} + \frac{1}{2}\sum_j F_{iijj}\left(2^2\omega_i\omega_j\right)^{-1}, + \frac{1}{2^2 2!}\sum_{j,k} F_{iijjkk}\left(2^3\omega_i\omega_j\omega_k\right)^{-1} + \ldots, \tag{5.3}$$

where ω_i are effective harmonic frequencies, and F_{ii}, F_{ijj}, and F_{iijj} are quadratic, cubic, and quartic force constants with respect to the *i*th and *j*th normal coordinates; they are obtained by performing a Taylor expansion of the bare PES centered about the equilibrium geometry in XVSCF(n) or the first-order Dyson geometry in XVSCF[n]. The constant term of the Taylor expansion of $U_i(Q_i)$, E_0, is equivalent to the XVSCF ZPE because we have lifted restrictions on indices of summations corresponding to contributions that become negligible in the bulk limit, as discussed in Chapter 3. In XVSCF(n) and XVSCF[n] calculations, the infinite sums in Eqs. (5.1)–(5.3) are truncated after terms containing nth-order force constants. The rules for translating the diagrams of Fig. 5.1 into Eqs. (5.1)–(5.3), or vice versa, are presented in Refs. 21 and Chapter 2.

An XVSCF(n) or XVSCF[n] calculation is carried out by 1) obtaining the equilibrium geometry and quadratic force constants using an electronic structure method, 2) performing a normal mode analysis to yield the harmonic oscillator approximation to the vibrational wave function, 3) evaluating anharmonic force constants in a normal mode basis, and 4) solving the SCF equations in the XVSCF(n) or XVSCF[n] approximation using Eqs. (5.1)–(5.3). The third step, the evaluation of anharmonic force constants, is the bottleneck in operation and storage cost. Both XVSCF methods only require force constants of certain types at each order, leading to an operation cost which scales as $O(m^{n/2})$.[21] This is less than in standard VSCF or second-order perturbation theory, but it is still exponential with

respect to n. Furthermore, calculations with $n > 4$ are impractical because the evaluation of sixth- and higher-order force constants suffers from the buildup of numerical error accumulated by repeated numerical differentiation. A practical method of going to higher order requires discarding the force-constant evaluation step entirely.

Here we describe an alternative implementation of the XVSCF(n) and XVSCF[n] methods which utilizes Monte Carlo (MC) integration to evaluate the effective potential coefficients, in place of force-constant calculation followed by the evaluation of diagrammatic equations. Equations (5.1)–(5.3) are re-written in the form of single high-dimensional integrals which require only the values, not the derivatives, of the PES. These integrals are evaluated with a Metropolis algorithm.[39] The entire method is thus free from any explicit differentiation of the PES at any point, except for the steps associated with constructing the initial harmonic oscillator approximation. We refer to these methods as MC-XVSCF(n) and MC-XVSCF(n). When combined with on-demand evaluation of the PES using electronic structure software, the order of force constants accounted for, n, is formally infinite.

MC-XVSCF(n) and MC-XVSCF[n] belong to a category of quantum Monte Carlo (QMC) methods[41–43] which consist of reformulating existing many-body theories so that their programmable equations center on a stochastic random walk instead of matrix-algebraic manipulation of high-dimensional arrays.[44–46] They are similar to recent stochastic implementations of the SCP method,[93,113,114] which obtains first-order Dyson coordinates in addition to the Dyson geometry. MC-XVSCF(n) and MC-XVSCF[n] also resemble vibrational QMC methods such as diffusion Monte Carlo;[115,116] however, unlike DMC, MC-XVSCF obtains all anharmonic vibrational frequencies in a single calculation without any assumption about the nodal surfaces of excited vibrational wave functions. MC-XVSCF also inherits the manifest size consistency of XVSCF,[21] making it applicable to large molecules and solids. We have also developed a second-order vibrational perturbation theory known as MC-XVMP2 along the same lines, to which MC-XVSCF is an ideal reference.

5.1 Formalism

5.1.1 XVSCF(n)

The real XVSCF(n) vibrational wave function in state $s = \{s_1, s_2, \ldots, s_M\}$, where $s_i \geq 0$ is a quantum number and M is the number of vibrational degrees of freedom, is written as

$$\Psi_s(\boldsymbol{Q}) \quad = \quad \prod_i^M \varphi_{s_i}(Q_i), \tag{5.4}$$

where $\boldsymbol{Q}$ collectively refers to all normal coordinates, $\{Q_i\}$, and the modals, $\varphi_{s_i}(Q_i)$, are the solutions to Eq. (3.3) with

$$U_i(Q_i) \quad = \quad E_0 + \frac{1}{2} U_{ii}^{(2)} Q_i^2, \tag{5.5}$$

where E_0 is given by Eq. (5.1) and $U_{ii}^{(2)}$ by Eq. (5.3). The solutions to Eq. (3.3) with Eq. (5.5) are harmonic oscillator wave functions centered at the equilibrium geometry with

$$\omega_i \quad = \quad \left(U_{ii}^{(2)}\right)^{1/2}, \tag{5.6}$$

$$\epsilon_{s_i} \quad = \quad E_0 + (s_i + 1/2)\,\omega_i. \tag{5.7}$$

There is no gradient term linear in Q_i in Eq. (5.5) because the corresponding effective force constant, $U_i^{(1)}$, has nonphysical volume dependence for a potential ($K^{1/2}$, that is, neither extensive nor intensive).[20] Therefore, the vibrationally averaged geometry of the XVSCF(n) wave function is the equilibrium geometry. However, once the XVSCF(n) wave function is obtained, an anharmonic correction to geometry can be estimated as

$$q_i \quad = \quad -U_i^{(1)}/U_{ii}^{(2)}, \tag{5.8}$$

where $U_i^{(1)}$ is given by Eq. (5.2). Equation (5.8) has the correct volume dependence for a geometry correction along normal coordinates ($K^{1/2}$).

The frequencies, ZPE, and anharmonic corrections to geometry in the XVSCF(n) approximation all depend on all frequencies, $\{\omega_i\}$. The XVSCF(n) algorithm therefore first self-consistently solves Eq. (3.3) by repeatedly evaluating $U_{ii}^{(2)}$ using Eq. (5.3) and some set of guess frequencies, $\{\omega_i^{[k]}\}$, then evaluating Eq. (5.6) to obtain an improved set, $\{\omega_i^{[k+1]}\}$. Once the frequencies are converged, E_0, $U_i^{(1)}$, and q_i are evaluated using Eq. (5.1), (5.2), and (5.8), respectively.

5.1.2 XVSCF[n]

The XVSCF[n] vibrational wave function is given by Eq. (5.4), where the modals, $\varphi_{s_i}(Q_i)$, are the solutions of Eq. (3.3) with

$$U_i(Q_i) \quad = \quad E_0 + \frac{1}{2} U_{ii}^{(2)} (Q_i - q_i)^2, \tag{5.9}$$

where the anharmonic correction to geometry, $\{q_i\}$, is obtained by solving

$$U_i^{(1)} = 0, \tag{5.10}$$

for all i. The solutions to Eq. (3.3) with Eqs. (5.9) and (5.10) are harmonic oscillator wave functions with eigenvalues given by Eq. (5.7) and frequencies given by Eq. (5.6), which are centered at $Q_i = q_i$, that is, the first-order Dyson geometry. The ZPE, E_0, and effective force constants, $U_i^{(1)}$ and $U_{ii}^{(2)}$, are given by Eqs. (5.1)–(5.3), where the force constants, F, are understood to be obtained from a Taylor expansion of the PES about $Q_i = q_i$ for all i.

The values of ω_i and q_i depend on the effective force constants, $U_i^{(1)}$ and $U_{ii}^{(2)}$, which in turn depend on all ω_i and q_i through the diagrammatic equations. Therefore all frequencies and all geometrical parameters are coupled and must be solved simultaneously. The XVSCF[n] algorithm solves Eq. (3.3) for all modes by repeatedly evaluating $U_i^{(1)}$ and $U_{ii}^{(2)}$ with some approximate set of frequencies, $\{\omega_i^{[k]}\}$, and geometrical parameters, $\{q_i^{[k]}\}$, and obtaining $\omega_i^{[k+1]}$ and $q_i^{[k+1]}$ by evaluating Eq. (5.6) and

$$q_i^{[k+1]} = q_i^{[k]} - U_i^{(1)}/U_{ii}^{(2)}. \tag{5.11}$$

The ZPE is evaluated once after all frequencies and geometries are converged.

5.1.3 Alternative integral forms of diagrammatic equations

The diagrammatic equations, Eqs. (5.1)–(5.3), which are utilized in both XVSCF(n) and XVSCF[n], require the prior evaluation of anharmonic force constants of up to nth order. These equations, however, can be rewritten as

$$E_0 = \sum_i \frac{\omega_i}{4} + \langle \Psi_0 | V(\boldsymbol{Q}) | \Psi_0 \rangle, \tag{5.12}$$

$$U_i^{(1)} = (2\omega_i)^{1/2} \left\langle \Psi_0 \left| V(\boldsymbol{Q}) \hat{a}_i^\dagger \right| \Psi_0 \right\rangle, \tag{5.13}$$

$$U_{ii}^{(2)} = (2\omega_i) \left\langle \Psi_0 \left| V(\boldsymbol{Q}) \hat{a}_i^\dagger \hat{a}_i^\dagger \right| \Psi_0 \right\rangle, \tag{5.14}$$

where $V(\boldsymbol{Q})$ is the PES and $\hat{a}_i^\dagger$ and $\hat{a}_i$ are harmonic oscillator ladder operators for mode i, which satisfy

$$\hat{a}_i \varphi_{s_i}(Q_i) = s_i^{1/2} \varphi_{s_i - 1}(Q_i), \tag{5.15}$$

$$\hat{a}_i^\dagger \varphi_{s_i}(Q_i) = (s_i + 1)^{1/2} \varphi_{s_i + 1}(Q_i). \tag{5.16}$$

The equivalence of Eqs. (5.12)–(5.14) and (5.1)–(5.3) can be shown by substituting the vibrational Hamiltonian,

$$\hat{H} = -\frac{1}{2}\sum_i \frac{\partial^2}{\partial Q_i^2} + V(\boldsymbol{Q}), \tag{5.17}$$

and a Taylor-series expansion for $V(\boldsymbol{Q})$ into Eqs. (5.12)–(5.14) and evaluating them using analytical expressions for the matrix elements of position and momentum operators in a harmonic oscillator basis with, for instance, Table 1 of Ref. 21. Equations (5.12)–(5.14), however, are simply m-dimensional integrals over $\boldsymbol{Q}$ and do not rely on the prior availability of any derivatives of the potential to evaluate. They are suitable for efficient stochastic integral evaluation algorithms such as the Metropolis MC method,[39] as described in Sec. 5.2 below. Note that it is also possible to rewrite Eqs. (5.13) and (5.14) using explicit first derivatives of the PES [cf. Eqs. (13) and (14) of Ref. 113]. This is sometimes advantageous because it reduces the variances of the corresponding integrals,[113] and several electronic structure packages include highly expedient analytical methods for calculating the first derivatives of the electronic energy with most commonly-used electronic structure methods. Nevertheless, we use Eqs. (5.13) and (5.14) as written to maintain the full generality of the algorithm, since analytical derivatives are not always available for all electronic structure methods.

MC integration can be further facilitated by partitioning $V(\boldsymbol{Q})$ into a leading-order quadratic component, the matrix elements of which can be evaluated analytically, and a fluctuation potential,

$$V(\boldsymbol{Q}) = V_0 + \frac{1}{2}\sum_i \omega_i^2 (Q_i - q_i)^2 + \Delta V(\boldsymbol{Q}), \tag{5.18}$$

where q_i in the above is understood to be fixed at zero during the course of an XVSCF(n) calculation, while it varies along with ω_i during an XVSCF[n] calculation. Substituting Eq. (5.18) into Eqs. (5.12)–(5.14), we arrive at programmable equations for a MC implementation of XVSCF(n) or XVSCF[n],

$$E_0 = V_0 + \sum_i \frac{\omega_i}{2} + \Delta\bar{V}, \tag{5.19}$$

$$U_i^{(1)} = (2\omega_i)^{1/2}\Delta\bar{V}_i, \tag{5.20}$$

$$U_{ii}^{(2)} = \omega_i^2 + (2\omega_i)\Delta\bar{V}_{ii}, \tag{5.21}$$

with

$$\Delta\bar{V} = \int d\boldsymbol{Q}\Psi_0(\boldsymbol{Q})\Delta V(\boldsymbol{Q})\Psi_0(\boldsymbol{Q}), \tag{5.22}$$

$$\Delta\bar{V}_i = \int d\boldsymbol{Q}\Psi_0(\boldsymbol{Q})\Delta V(\boldsymbol{Q})\Psi_0(\boldsymbol{Q})\frac{\varphi_1(Q_i)}{\varphi_0(Q_i)}, \tag{5.23}$$

$$\Delta\bar{V}_{ii} = \int d\boldsymbol{Q}\Psi_0(\boldsymbol{Q})\Delta V(\boldsymbol{Q})\Psi_0(\boldsymbol{Q})\frac{2^{1/2}\varphi_2(Q_i)}{\varphi_0(Q_i)}, \tag{5.24}$$

where $d\boldsymbol{Q}$ denotes simultaneous integration along all normal coordinates, $dQ_1 dQ_2 \ldots dQ_m$. Partitioning the PES using Eq. (5.18) accelerates integral evaluation by stochastic methods because the variances of the integrands of Eqs. (5.22)–(5.24) are smaller than the variances of the integrands involving $V(\boldsymbol{Q})$.[113,117] This applies to any system in which anharmonicity is small enough to be considered a perturbation; other algorithms may be better suited to other systems.[114]

5.2 Stochastic algorithm

5.2.1 MC integration

In MC-XVSCF(n) and MC-XVSCF[n], the three m-dimensional integrals, I, given by Eqs. (5.22)–(5.24) are evaluated as

$$I \approx \frac{1}{N}\sum_{i=1}^{N}\frac{f(\boldsymbol{Q}_i)}{w(\boldsymbol{Q}_i)} \equiv I_N, \tag{5.25}$$

where f is the corresponding integrand, w is a weight or importance function, $\boldsymbol{Q}_i$ is the ith sampling point in a Markov chain generated by the Metropolis algorithm,[39] and N is the total number of sampling points. These integrals are characterized by a variance, σ_I^2, and a statistical uncertainty, σ_I, which tends to zero as $O(N^{-1/2})$ and is estimated by,

$$\sigma_I^2 = \frac{1}{N(N-1)}\sum_{i=1}^{N}\left\{\frac{f(\boldsymbol{Q}_i)}{w(\boldsymbol{Q}_i)} - I_N\right\}^2. \tag{5.26}$$

This estimate is only accurate for uncorrelated samples, $f(\boldsymbol{Q}_i)/w(\boldsymbol{Q}_i)$, and the samples generated by the Metropolis random walk are correlated due to the semi-fixed radius between them. A superior estimate of the variance and statistical uncertainty is given by the blocking algorithm of Flyvbjerg and Peterson,[118] which rewrites Eq. (5.26) as

$$\sigma_I^2 = \frac{1}{N'(N'-1)}\sum_{j=1}^{N'}\left(I_j - I_N\right)^2, \tag{5.27}$$

where

$$I_j = \frac{1}{N_\mathrm{B}}\sum_{i=(j-1)N_\mathrm{B}+1}^{jN_\mathrm{B}}\frac{f(\boldsymbol{Q}_i)}{w(\boldsymbol{Q}_i)}, \tag{5.28}$$

and where $N' = N/N_B$. Setting N_B sufficiently large results in uncorrelated block estimates, I_j, leading to an accurate estimate of the variance, σ_I^2. In this work, we use $N_B = 100$.

The weight function, $w(\boldsymbol{Q})$ in Eqs. (5.25) and (5.28), guides the Metropolis random walk. It must be judiciously chosen to expedite the integration by ensuring a fast decay of the variance. The details of our weight function are discussed in Sec. 5.2.3 below.

The Metropolis algorithm for evaluating Eqs. (5.25) and (5.28) distributes the sampling points, $\boldsymbol{Q}_i$, in proportion to $w(\boldsymbol{Q})$ through a random-walk algorithm. In each MC step, a proposed $\boldsymbol{Q}_{i+1}$ is generated by displacing $\boldsymbol{Q}_i$ in a random direction, with a radius of $\beta|\langle\Psi_0|Q_j^2|\Psi_0\rangle|$ along the jth normal coordinate, where β is a semi-fixed parameter. The proposed $\boldsymbol{Q}_{i+1}$ is accepted if the ratio $w(\boldsymbol{Q}_{i+1})/w(\boldsymbol{Q}_i)$ is larger than a random number between 0 and 1; otherwise, $\boldsymbol{Q}_{i+1}$ is set equal to $\boldsymbol{Q}_i$. The parameter β is continually adjusted so that the ratio of accepted to rejected steps is as close to 1.0 as possible. During the first 10^5 MC steps of the whole calculation, the integrands of Eqs. (5.22)–(5.24) are not evaluated; the walker is repeatedly scattered without integral evaluation in order to obtain a suitable value of β and starting position.

In order to further expedite the MC integration, we have implemented the antithetic variate method for reducing the variance.[117] This method slightly modifies Eqs. (5.25) and (5.28), without changing the converged limit of I_N. Its details are presented in Sec. 5.2.4 below.

We use the Metropolis algorithm to evaluate the integrals given by Eqs. (5.22)–(5.24) because it is highly general and is usable with many kinds of weight functions. Other approaches may be more efficient in specific cases. For instance, when the weight function is chosen to be a product of Gaussian functions along normal coordinates (as in the calculations discussed below), deterministic quasi-Monte Carlo approaches, using low-discrepancy sequences instead of stochastic sampling, can be much more efficient than the Metropolis algorithm.[113] However, quasi-Monte Carlo is only practical when the inverse cumulative distribution function associated with the weight function is available analytically. This is not always possible if the weight function is more complicated than a simple product of Gaussians.

5.2.2 SCF iteration

Using some approximate set of frequencies, $\{\omega_i^{[k]}\}$, and geometrical parameters, $\{q_i^{[k]}\}$, the integrals $\Delta\bar{V}$, $\Delta\bar{V}_i$, and $\Delta\bar{V}_{ii}$ are evaluated using the Metropolis MC algorithm according to Eqs. (5.22)–(5.24). The initial ($k = 0$) values of the frequencies and geometries are given by the harmonic approximation (e.g. $q_i^{[0]} = 0$). The values of E_0, $U_i^{(1)}$, and $U_{ii}^{(2)}$ are obtained from $\Delta\bar{V}$, $\Delta\bar{V}_i$, and $\Delta\bar{V}_{ii}$ through Eqs. (5.19)–(5.21). The wave functions, Ψ_0, and φ_{s_i} which appear in Eqs. (5.22)–(5.24), are centered at $Q_i = q_i^{[k]}$ and have frequencies $\omega_i^{[k]}$. Equations (5.18)–(5.21) are all likewise evaluated by substituting $\omega_i^{[k]}$ and $q_i^{[k]}$ for ω_i and q_i whenever they appear.

The next-cycle frequencies and geometries, $\omega_i^{[k+1]}$ and $q_i^{[k+1]}$, are given by Eqs. (5.6) and (5.11). In MC-XVSCF(n),

once the statistical uncertainties of all frequencies and the ZPE fall below a threshold, the integral evaluations are restarted using $\omega_i^{[k+1]}$ in place of $\omega_i^{[k]}$, but the geometric parameter used in the integral evaluation remains fixed at $q_i^{[0]} = 0$. In MC-XVSCF[n], once the statistical uncertainties of all frequencies, ZPE, and geometries fall below a threshold, the integral evaluations are restarted with $\omega_i^{[k+1]}$ and $q_i^{[k+1]}$ in place of $\omega_i^{[k]}$ and $q_i^{[k]}$. Since even the deterministic XVSCF algorithm involves an SCF iteration, every cycle of this SCF iteration in MC-XVSCF must restart a new MC calculation using the updated sets of frequencies and geometrical parameters, discarding the results from the prior SCF cycle.

An improved estimate of the frequencies and geometries is obtained to a high degree of confidence when the statistical uncertainty, σ, of a parameter is significantly smaller than its SCF residual, δ. The statistical uncertainties are obtained by standard propagation of uncertainty rules from the statistical uncertainties of the integrals from the MC algorithm as

$$\sigma_{E_0^{[k+1]}} = \sigma_{\Delta\bar{V}}, \tag{5.29}$$

$$\sigma_{\omega_i^{[k+1]}} = \frac{\omega_i^{[k]}}{\omega_i^{[k+1]}}\sigma_{\Delta\bar{V}_{ii}}, \tag{5.30}$$

$$\sigma_{q_i^{[k+1]}} = \left|\frac{U_i^{(1)}}{U_{ii}^{(2)}}\right|\left[\left\{\frac{\sigma_{\Delta\bar{V}_i}}{\Delta\bar{V}_i}\right\}^2 + \left\{\frac{\sigma_{\Delta\bar{V}_{ii}}}{\left(\omega_i^{[k]}/2\right) + \Delta\bar{V}_{ii}}\right\}^2\right]^{1/2}, \tag{5.31}$$

where $\sigma_{E_0^{[k+1]}}$, $\sigma_{\omega_i^{[k+1]}}$, and $\sigma_{q_i^{[k+1]}}$ are the statistical uncertainties of $E_0^{[k+1]}$, $\omega_i^{[k+1]}$, and $q_i^{[k+1]}$, respectively, and the superscript $[k+1]$ on E_0 denotes its evaluation in the same SCF cycle as $\omega_i^{[k+1]}$ and $q_i^{[k+1]}$.

The SCF residuals are defined as the differences between the current (cycle k) estimate of the energies, frequencies and geometries and the running estimate of the next-cycle $(k+1)$ values of these quantities,

$$\delta_{E_0^{[k+1]}} = E_0^{[k+1]} - E_0^{[k]}, \tag{5.32}$$

$$\delta_{\omega_i^{[k+1]}} = \omega_i^{[k+1]} - \omega_i^{[k]}, \tag{5.33}$$

$$\delta_{q_i^{[k+1]}} = q_i^{[k+1]} - q_i^{[k]}. \tag{5.34}$$

In evaluating Eq. (5.32) for $k = 0$, $E_0^{[0]}$ is set to an arbitrary large number. Note that within a single SCF cycle, the first terms on the right-hand sides of Eqs. (5.32)–(5.34) vary during the course of MC integration, converging gradually to a fixed value, while the second terms are fixed. Therefore, the δ themselves gradually converge to fixed values during MC integration within a single SCF cycle.

To ensure that improved estimates of frequencies and geometries are obtained every SCF cycle, our threshold for determining when to begin a new cycle includes the criterion that for at least one frequency (in MC-XVSCF(n) or

MC-XVSCF[n]) or geometric parameter (in MC-XVSCF[n] only),

$$3\sigma_{\omega_i^{[k+1]}} < |\delta_{\omega_i^{[k+1]}}|, \tag{5.35}$$

$$3\sigma_{q_i^{[k+1]}} < |\delta_{q_i^{[k+1]}}|. \tag{5.36}$$

In order for the statistical uncertainties to be meaningful, the MC integration must have run for enough steps to obtain a good statistical distribution of sampling points of the PES. To ensure this, our threshold also contains the criterion

$$N' \geq 50, \tag{5.37}$$

where N' is the number of blocks in the Flyvbjerg–Peterson algorithm (see Sec. 5.2.1). Additionally and for the same reason, we require that for the ZPE and *all* ω_i (in both MC-XVSCF(n) and MC-XVSCF[n]) and q_i (in MC-XVSCF[n] only) the statistical uncertainties are below both an absolute threshold and the magnitude of the SCF residuals,

$$\sigma_{E_0^{[k+1]}} \leq 10\ \mathrm{cm}^{-1}, \tag{5.38}$$

$$\sigma_{\omega_i^{[k+1]}} \leq 10\ \mathrm{cm}^{-1}, \tag{5.39}$$

$$\sigma_{q_i^{[k+1]}} \leq 0.1\ \text{a.u.}, \tag{5.40}$$

$$\sigma_{E_0^{[k+1]}} \leq |\delta_{E_0^{[k+1]}}|, \tag{5.41}$$

$$\sigma_{\omega_i^{[k+1]}} \leq |\delta_{\omega_i^{[k+1]}}|, \tag{5.42}$$

$$\sigma_{q_i^{[k+1]}} \leq |\delta_{q_i^{[k+1]}}|, \tag{5.43}$$

which we have found helps to prevent oscillating SCF behavior.

To summarize, in MC-XVSCF[n] calculations, we begin a new SCF cycle when either Eq. (5.35) or (5.36) is satisfied for *at least one* mode and the conditions set by Eqs. (5.37)–(5.43) are met for *all* modes. The threshold for MC-XVSCF(n) calculations is the same except that all criteria related to q_i are ignored, since q_i is not updated during the MC-XVSCF(n) iteration.

5.2.3 Weight function

In performing Metropolis MC integration, the choice of the weight function, $w(\boldsymbol{Q})$ in Eqs. (5.25) and (5.28), is critical in determining the efficiency and feasibility of the calculation. The weight function should be positive everywhere, analytically integrable, and should have similar magnitude to the integrand over all regions of the integral, so that $|f(\boldsymbol{Q})/w(\boldsymbol{Q})|$ is as close as possible to a constant number.

The weight function we choose is the same as in our implementation of the MC-XVMP2 method,

$$w(\boldsymbol{Q}) \quad = \quad \prod_{i}^{M} \left(\frac{\alpha \omega_i^{[k]}}{\pi} \right)^{1/2} e^{-\alpha \omega_i^{[k]} (Q_i - q_i^{[k]})^2}, \tag{5.44}$$

where α is a scaling parameter, and the frequencies, $\omega_i^{[k]}$, and geometries, $q_i^{[k]}$, are the same as those in the integrands of Eqs. (5.22)–(5.24) [eg. $q_i = 0$ in MC-XVSCF(n) calculations]. Equation (5.44) with $\alpha = 1$ gives the probability density of the zero-point XVSCF wave function, and is the weight function used implicitly in, for example, stochastic SCP and vibrational configuration interaction calculations.[93,113,119] This weight function can be optimized for efficient MC integration by varying α.

5.2.4 Antithetic variate method

The integrands given by Eqs. (5.22)–(5.24) can be written as a sum of terms involving all force constants, of which the majority vanish in the integrals whose corresponding diagrammatic equations are given in Fig. 5.1 and Eqs. (5.1)–(5.3). For instance, substituting the Taylor expansion for $\Delta V(\boldsymbol{Q})$ into Eq. (5.22),

$$\begin{aligned} \Delta \bar{V} \quad = \quad & \int d\boldsymbol{Q} \left\{ \sum_i F_i Q_i + \frac{1}{2} \sum_{i,j} \left(F_{ij} - \delta_{ij} \omega_i^2 \right) Q_i Q_j \frac{1}{3!} \sum_{i,j,k} F_{ijk} Q_i Q_j Q_k + \frac{1}{4!} \sum_{i,j,k,l} F_{ijkl} Q_i Q_j Q_k Q_l + \ldots \right\} \\ & \times \prod_i \left(\frac{\omega_i}{\pi} \right)^{1/2} e^{-\omega_i Q_i^2}, \end{aligned} \tag{5.45}$$

where we define the coordinates, $\{Q_i\}$, so that $q_i = 0$ for all modes. It is clear that contributions associated with several force constants vanish by symmetry; these nonzero terms increase the variance in a MC integration, giving contributions to the integral which slowly converge at zero over a long Metropolis walk. The antithetic variate method (AVM)[117] is a method of reducing the variance by modifying the sampling of the PES to remove these oscillating terms exactly in each MC step.

The Metropolis algorithm summarized in Sec. 5.2.1 describes a method of obtaining a Markov chain of points on the PES, $\{\boldsymbol{Q}_1, \boldsymbol{Q}_2, \ldots, \boldsymbol{Q}_N\}$ which are distributed according to the weight function, $w(\boldsymbol{Q})$. The AVM consists of supplementing this Markov chain with additional chains, $\{\boldsymbol{Q}_1^s, \boldsymbol{Q}_2^s, \ldots, \boldsymbol{Q}_N^s\}$, where s denotes an operation which leaves the value of the weight function unchanged. Specifically, $\boldsymbol{Q}_i^s$ is constructed by flipping the signs of $\boldsymbol{Q}_i$ along various normal coordinates (centered about the center of the weight function).

Averaging together the integrands at these various points exactly eliminates force constants up to infinite order whose contributions to each integral vanish. For instance, in Eq. (5.45), the gradient F_i does not contribute to the value of the integral even if the value of F_i is nonzero. By averaging together sampling points of the integrand whose coordinates along mode i are Q_i and $-Q_i$, the gradient contribution vanishes identically. The same logic applies to

higher-order vanishing force constants when combinations of sign flips are averaged together. This method does not rely on the PES being evaluated in the calculation with an actual Taylor series; the Taylor series is merely used in this example to explain the concept, which relies ultimately on the symmetry of harmonic oscillator modals.

Implementing the AVM revises Eqs. (5.25) and (5.28) to

$$I_N = \frac{1}{SN} \sum_{i=1}^{N} \sum_{s}^{S} \frac{f(\boldsymbol{Q}_i^s)}{w(\boldsymbol{Q}_i^s)}, \tag{5.46}$$

$$I_j = \frac{1}{SN_\mathrm{B}} \sum_{i=(j-1)N_\mathrm{B}+1}^{jN_\mathrm{B}} \sum_{s}^{S} \frac{f(\boldsymbol{Q}_i^s)}{w(\boldsymbol{Q}_i^s)}, \tag{5.47}$$

where s is summed over sets of sign flips along normal coordinates, including the null case ($\boldsymbol{Q}_i$ as provided by the Metropolis algorithm), and S is the size of the summation. The Flyvbjerg–Peterson block length is now SN_B and all samples related by sign flips are blocked together, which is appropriate due to the strong correlation among them. This method does not inherently rely on any Abelian point-group symmetry of the molecule itself, and should be distinguished from the exploitation of point-group symmetry as well as the technique of redundant walkers[46] applied to the MC-XVMP2 method in Chapter 6.

For a molecule with M vibrational degrees of freedom and no symmetry operations other than the identity, the maximum value of S is 2^M, corresponding to the number of all possible sign flips along up to M normal coordinates for any point on the PES. This exponential dependence on molecular size is unfeasible for large molecules, since approximately $S/2$ PES calculations must be performed every MC step. An alternative is to sum over sets of points related by up to some maximum number $k \leq M$ of sign flips along normal coordinates, leading to $S = \sum_{l=0}^{k} \binom{M}{l}$. For the calculations reported in this work, we use this approach with $k = 2$. We can use Abelian point-group symmetry to further reduce S by identifying sign permutations corresponding to symmetry operations of other sign permutations and excluding them from the summations of Eqs. (5.46) and (5.47), since the value of the PES is identical at points related by symmetry operations and there is therefore no advantage to including them.

5.2.5 Parallel computer implementation

Parallelism of MC integration, described by Sec. 5.2.1, can be achieved by executing a different Metropolis process on each processor of a parallel computer. Each process computes its own set of block estimates, I_j, for all of the integrals described by Eqs. (5.22)–(5.24), which are periodically collected in order to obtain the values of the integrals and their variances. Collecting these values and statistical uncertainties is necessary in order to evaluate whether the SCF thresholds described in Sec. 5.2.2 have been achieved, and requires all-to-one communication achieved with Message-Passing Interface (MPI) commands. If the threshold has been achieved and the a new SCF cycle is to be initiated, the

new set of $\omega_i^{[k]}$ and $q_i^{[k]}$ must then be distributed to all processors using MPI one-to-all commands. This is the only inter-processor communication required in MC-XVSCF. In this implementation, we collect the values of the integrals and test for SCF iteration every 100 MC steps, corresponding to one Flyvbjerg–Peterson block for each integral on each processor. The initial equilibration step of the Metropolis algorithm is also a minor parallel bottleneck as it must be executed as many times as there are processors.

5.3 Test calculations

5.3.1 Computational details

We report the results of two sets of MC-XVSCF(n) and MC-XVSCF[n] calculations and compare them to the results of deterministic XVSCF(4) and XVSCF[4] calculations. In all these calculations, the weight function broadening parameter α is set to 0.3, and the Flyvbjerg–Peterson block length, N_B, is set to 100. The PES is evaluated at the MP2/aug-cc-pVTZ level of electronic structure theory using NWCHEM.[82] The calculations are carried out for a total of $N = 3\times10^5$ MC steps distributed across up to 10 processors, corresponding to ca. 6×10^5 evaluations of the PES (Sec. 5.2.4 above describes the actual relation of MC steps to number of PES evaluations in our implementation).

MC-XVSCF(n) and MC-XVSCF[n] calculations with $n = 4$ are also referred to as "indirect" and are carried out using a stored fourth-order Taylor series (quartic force field or QFF) representation of the PES to evaluate $V(\boldsymbol{Q})$ during MC integration. The indirect calculations are expected to reproduce the results of the deterministic calculations, and the errors can be calculated to assess the correctness and efficiency of the algorithm. However, indirect MC-XVSCF is not a practical method for applications, since the diagrammatic algorithms already developed represent the most efficient method of performing XVSCF using a precalculated and stored PES.

MC-XVSCF calculations with $n = \infty$ are also referred to as "direct" and are carried out by evaluating $V(\boldsymbol{Q})$ on the fly using NWCHEM. This method formally accounts for up to infinite-order force constants, and is not expected to reproduce the results of any deterministic calculation; exact values of the errors are not available. Direct MC-XVSCF calculations do not require the prior evaluation and storage of a Taylor-series force field.

5.3.2 Effects of different weight functions

Figure 5.2 presents the effects of using different scaling factors, α, with a weight function of the form given by Eq. (5.44), in one SCF cycle of an MC-XVSCF(4) or MC-XVSCF[4] calculation on the water molecule (using the same QFF as in Sec. 5.3 in the main text). Figure 5.2 shows that the calculated ZPE in all stochastic calculations converges towards the ZPE predicted by the first cycle of deterministic XVSCF(4) and XVSCF[4] (they are equivalent in the first SCF cycle). However, the rate of convergence and the decay of the statistical uncertainty clearly depend on α.

In the calculation with $\alpha = 0.9$, clear spikes in the statistical uncertainty are observed, which are not to be confused with the spikes in the statistical uncertainties of Figs. 5.3 and 5.6. The latter are associated with the SCF iteration, but the spikes in Fig. 5.2 correspond to near-division-by-zero behavior in the quotient $f(\boldsymbol{Q}_i)/w(\boldsymbol{Q}_i)$, indicating severe undersampling of the PES. The calculations with $\alpha = 0.7$ and $\alpha = 0.1$ show smooth, overlapping decay in the statistical uncertainty, as do the calculations with $\alpha = 0.3$ and $\alpha = 0.5$, but the uncertainties of the former two calculations are nearly twice the uncertainties of the latter. This indicates that the calculation with $\alpha = 0.7$ is slightly undersampling the PES and the one with $\alpha = 0.1$ is slightly oversampling it. Either $\alpha = 0.5$ or $\alpha = 0.3$ seem optimal. It is noteworthy that in Chapter 6, where second-order vibrational perturbation theory is discussed, the same weight function with $\alpha = 0.5$ seems to undersample the ZPE slightly compared to $\alpha = 0.3$, whereas for XVSCF (whose ZPE equation is isomorphic to first-order perturbation theory), $\alpha = 0.5$ and $\alpha = 0.3$ are indistinguishable. This is understandable in light of the higher-quantum-number modals which are involved in second-order perturbation theory, which spread the integrand further from the origin, rendering more diffuse (i.e. lower α) weight functions more desirable. All calculations discussed in the main text use $\alpha = 0.3$.

It is also worth noting that the weight function described by Eq. (5.44) is simple enough that its cumulative distribution function can be inverted analytically, enabling the use of low-discrepancy sequences to distribute integrand sampling points in lieu of Metropolis scattering. This is the technique employed in, for example, Refs. 113 and 119.

5.3.3 Impact of the antithetic variate method

Table 5.1 compares the results of the first SCF cycle of MC-XVSCF(4) and MC-XVSCF[4] calculations which do not use the AVM and have $N = 1.2 \times 10^6$ to results from calculations which do use the AVM and have $N = 3 \times 10^5$. In the former calculation, the PES is sampled approximately 6×10^5 times, because when an MC move is rejected, the value of the PES is taken from the previous step, so the total number of times the PES is sampled is approximately half the number of MC steps. In the latter calculation, the PES is again sampled approximately 6×10^5 times, because for the water molecule $S = 4$, and $SN/2 = 6 \times 10^5$. However, despite calculating the PES the same number of times, the statistical uncertainties for most quantities in the calculation using the AVM are less than 50% of the uncertainties in the calculation without the AVM.

5.3.4 Indirect ($n = 4$) calculations

Figure 5.3 shows the convergence of the ZPE of water and its statistical uncertainty calculated by MC-XVSCF(4) and MC-XVSCF[4] with respect to the total number of MC steps. After fluctuating rapidly within the first 5×10^4 MC steps, during which period the number of MC steps per SCF cycle is fewer (that is, the SCF iteration cycles frequently), the ZPE converges towards and fluctuates near the deterministic result. The statistical uncertainty decreases smoothly

as $N^{-1/2}$, but shoots up whenever a new SCF cycle begins and integral calculations are restarted. In the course of 3×10^5 MC steps, the number of SCF cycles are 2 and 4 in MC-XVSCF(4) and MC-XVSCF[4], respectively.

Figures 5.4 and 5.5 plot the SCF residuals of the XVSCF(4) and MC-XVSCF(4) frequencies and the XVSCF[4] and MC-XVSCF[4] frequencies and geometries of water. The stochastic residuals roughly follow the deterministic residuals, indicating that the MC-XVSCF calculations are replicating the evolution of the SCF cycles of the deterministic XVSCF calculations. The residuals drop during the MC calculation by at least 2 orders of magnitude, corresponding to an SCF convergence of less than 1 cm^{-1} for frequencies and at most 3% the magnitude of the anharmonic corrections to geometry (see Table 5.3).

The results of the MC-XVSCF(4) and MC-XVSCF[4] calculations are presented and compared to those of the XVSCF(4) and XVSCF[4] calculations in Table 5.2, and the statistical uncertainties, SCF residuals, and errors of the former are summarized in Table 5.3. The indirect stochastic calculations reproduce the results of the deterministic calculations to within a small fraction of the anharmonic corrections, corresponding to at most 2 cm^{-1} for ZPE and frequencies. Furthermore, both the statistical uncertainties and SCF residuals seem to be approximately equal to or larger in magnitude than the errors from the deterministic results, meaning that the uncertainties and residuals both serve as good approximations for the errors.

5.3.5 Direct ($n = \infty$) calculations

Figure 5.6 shows the convergence of the ZPE in the MC-XVSCF(∞) and the MC-XVSCF[∞] calculations. Again, the ZPE and uncertainty fluctuate strongly during the first ca. 5×10^4 MC steps before settling into mostly smooth convergence disrupted by infrequent occurrences of a new SCF cycle. After 3×10^5 MC steps, the ZPE has visibly converged to within a few cm^{-1}. Figures 5.7 and 5.8 compare the convergence of the SCF residuals with respect to the number of SCF cycles in the direct stochastic calculations to the deterministic calculations. The former is no longer expected to reproduce the latter, however, the orders of magnitudes of the SCF residuals and the speed of SCF convergence are similar between the two sets of calculations, at least during the first few cycles. The SCF residuals of the direct stochastic calculations again drop by roughly 2 orders of magnitude over 3×10^5 MC steps. Overall, the direct calculations converge with respect to both MC step and SCF cycles at a similar rate to the indirect calculations.

Tables 5.2 and 5.3 present the results of the MC-XVSCF(∞) and MC-XVSCF[∞] calculations. The uncertainties and residuals are similar in magnitude to those of the indirect stochastic calculations; however the ZPE, frequencies, and geometries themselves no longer agree with the deterministic results, as expected. The QFF approximation at the XVSCF level of theory overestimates the zero-point energy and the frequencies of the stretching modes of water by 20 to 40 cm^{-1}, underestimates the frequencies of the bending mode by up to 10 cm^{-1}, and dramatically overestimates the anharmonic correction to the HOH angle.

The direct stochastic calculations required 10^7 CPU seconds spread across 10 processors to carry out 3×10^5 MC steps, of which the large majority of the computational time consisted of 6×10^5 evaluations of the PES which succeeded in converging all frequencies and the ZPE to within 3 cm^{-1}. This is a similar number of PES evaluations and a similar convergence criteria as required by stochastic SCP calculations reported in the literature on the pyrene molecule and a water hexamer, which, however, have many more atoms than the single water molecule calculated here.[113] Our calculations also used vastly more PES evaluations than required for the SCP calculation on crystalline platinum hydride reported in Ref. 114, which used only 480 evaluations of the PES to qualitatively converge the phonon spectrum for a 16-atom supercell. Both of these implementations of the SCP method therefore exhibit greater computational efficiency than is seen in this work. This likely can be traced to substantial differences in the algorithms those works used to sample the PES. In Ref. 113, a quasi-Monte Carlo scheme using low-discrepancy sequences is employed in lieu of a standard Metropolis algorithm. In quasi-Monte Carlo, integral evaluation converges as $O(N^{-1})$, as opposed to the standard $O(N^{-1/2})$ MC convergence rate. In Ref. 114, the value and first derivatives of the PES is evaluated at a small number of randomly-distributed points on the PES and an SCF iteration is converged using only these points, after which more points are added and the process is repeated until convergence; unlike the algorithms used in this work and in Ref. 113, the integral evaluations are not converged in every SCF cycle. Both of these implementations also evaluate first derivatives of the PES analytically, unlike our implementation which only uses the values of the PES; this distinction will affect the convergence rate of the gradient and quadratic force constant integrals.[113] Because of these substantial algorithmic differences, which are not related to the underlying theoretical approximations of the XVSCF or SCP methods, it is not possible to use these data to draw conclusions comparing the computational efficiencies of MC-XVSCF and SCP as such.

5.4 Conclusion

The XVSCF(n) and XVSCF[n] methods previously developed by us require the prior evaluation and storage of a selection of force constants of up to nth order, which becomes computationally unfeasible due to both operation and storage cost and numerical instability for $n > 4$.

Here, we have developed a new scalable MC algorithm for XVSCF(n) and XVSCF[n] which substitutes stochastic evaluation of high-dimensional integrals for diagrammatic equations involving force constants, which we call MC-XVSCF(n) and MC-XVSCF[n]. This algorithm can find the XVSCF solution for a fully anharmonic PES by Metropolis sampling, thus accounting for up to infinite-order force constants, and no pre-computation of a Taylor-series force field is required.

MC-XVSCF is similar to stochastic implementations of the SCP method. It computes the zero-point energy,

vibrationally averaged geometry, and anharmonic frequencies simultaneously from a single MC run, obtaining the latter directly instead of as small differences of two noisy total energies. MC-XVSCF also inherits the manifest size consistency of XVSCF, making it suitable for applications on large molecules and solids. Furthermore, MC-XVSCF serves as a natural reference method for the MC-XVMP2 method we present in the next chapter.

5.5 Figures

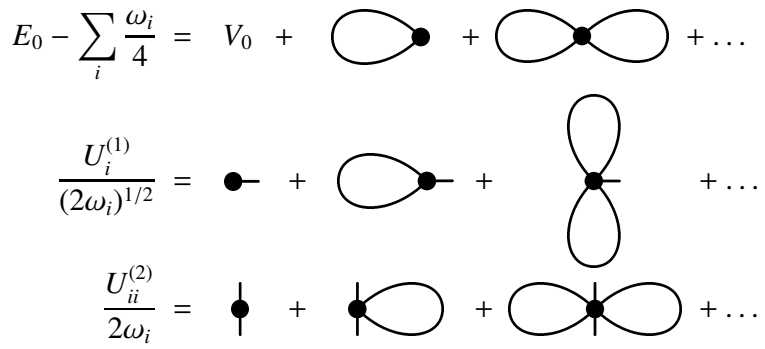

Figure 5.1: Diagrams for E_0, $U_i^{(1)}$, and $U_{ii}^{(2)}$.

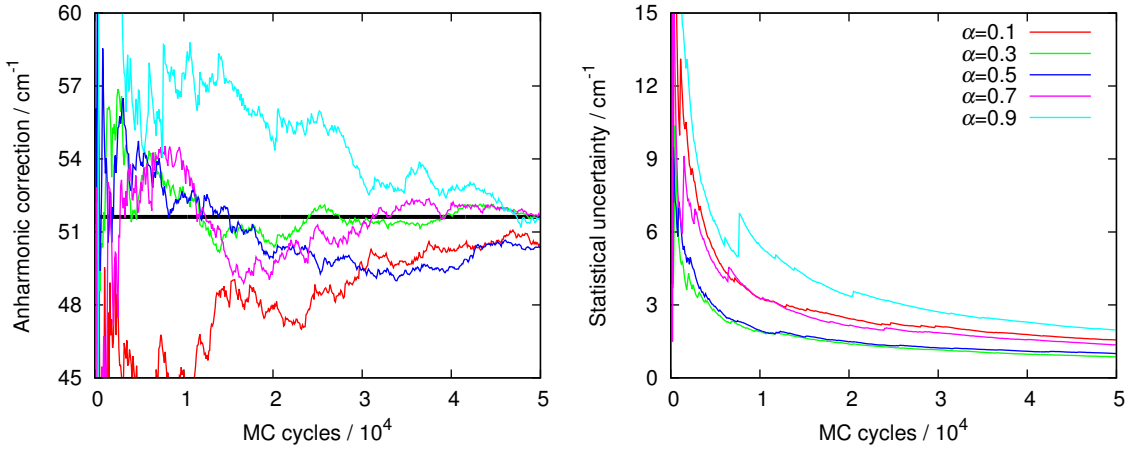

Figure 5.2: Convergence of one SCF cycle of the MC-XVSCF(4) or MC-XVSCF[4] ZPE using weight functions with various α. The left panel shows the ZPE and the right panel shows statistical uncertainty.

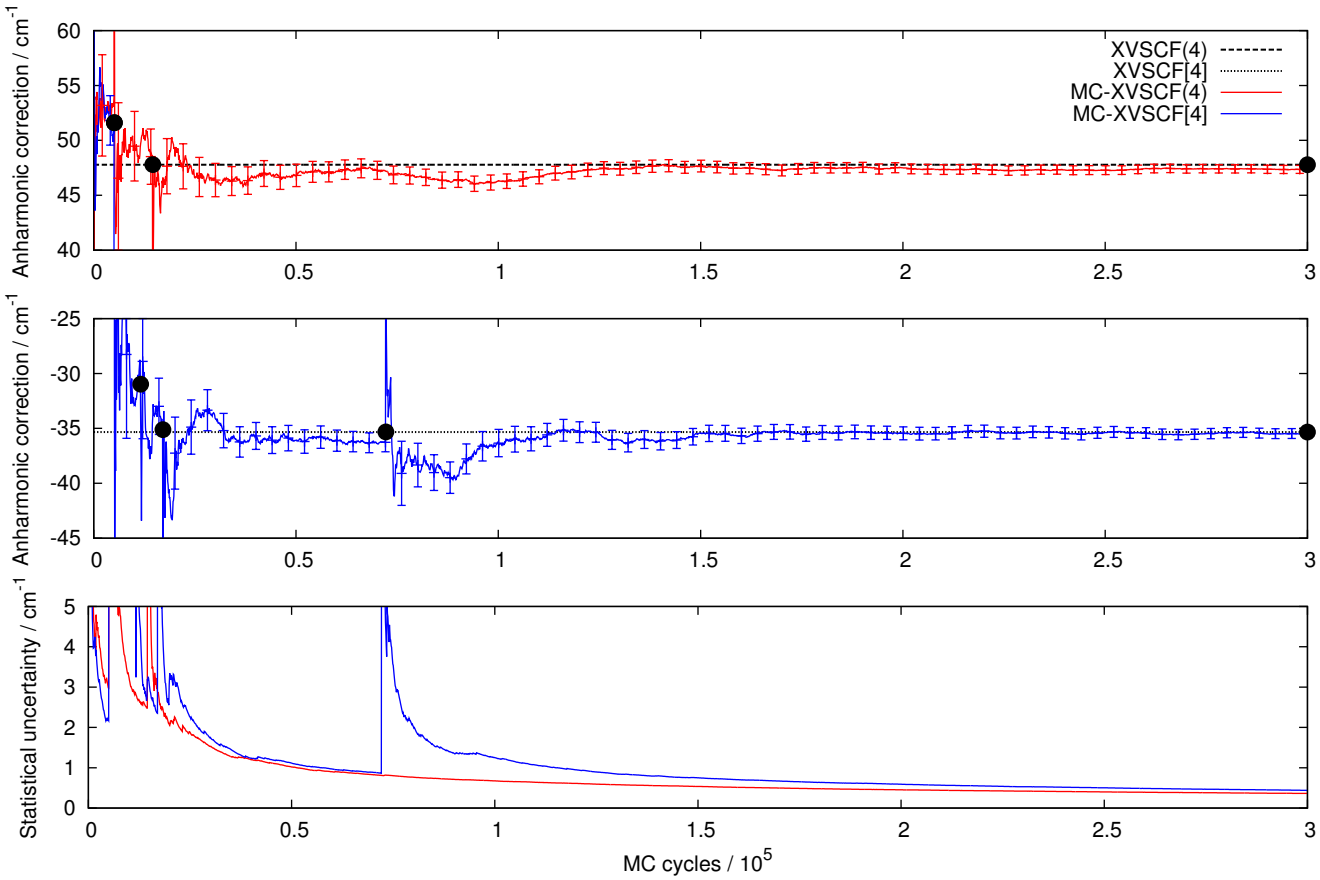

Figure 5.3: Convergence of the MC-XVSCF(4) (upper panel) and MC-XVSCF[4] (middle panel) anharmonic corrections to ZPE and the associated statistical uncertainty (lower panel and uncertainty bars on upper and middle panels). Nonconverged deterministic XVSCF(4) and XVSCF[4] ZPE estimates after 1 to 4 SCF cycles (from left to right) are plotted as solid black circles.

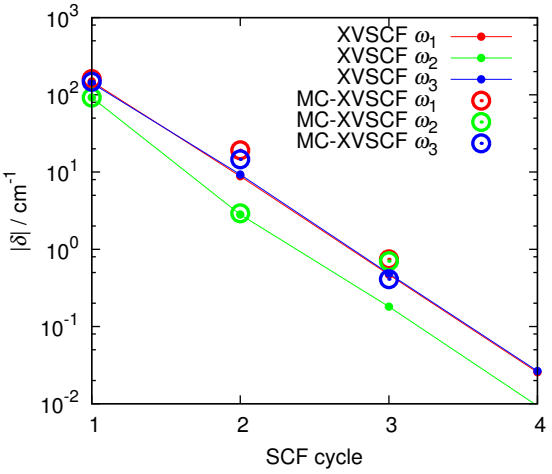

Figure 5.4: SCF residuals (δ) of the XVSCF(4) and MC-XVSCF(4) frequencies. The residuals of the stochastic calculations are evaluated from the frequencies in the last MC step of an SCF cycle.

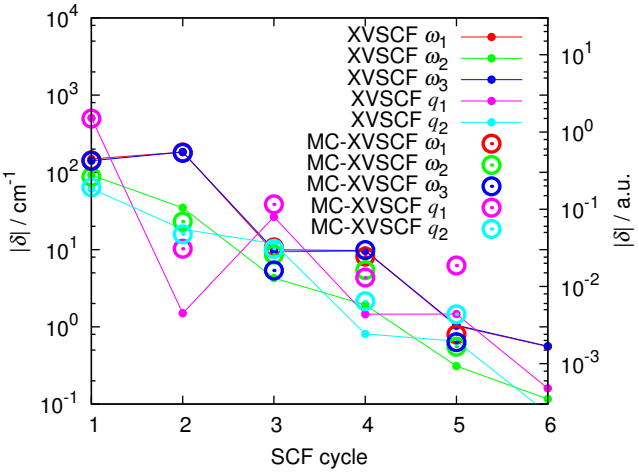

Figure 5.5: The same as Fig. 5.4, but for the frequencies in cm^{-1} and the anharmonic geometry corrections along normal coordinates in a.u. of XVSCF[4] and MC-XVSCF[4].

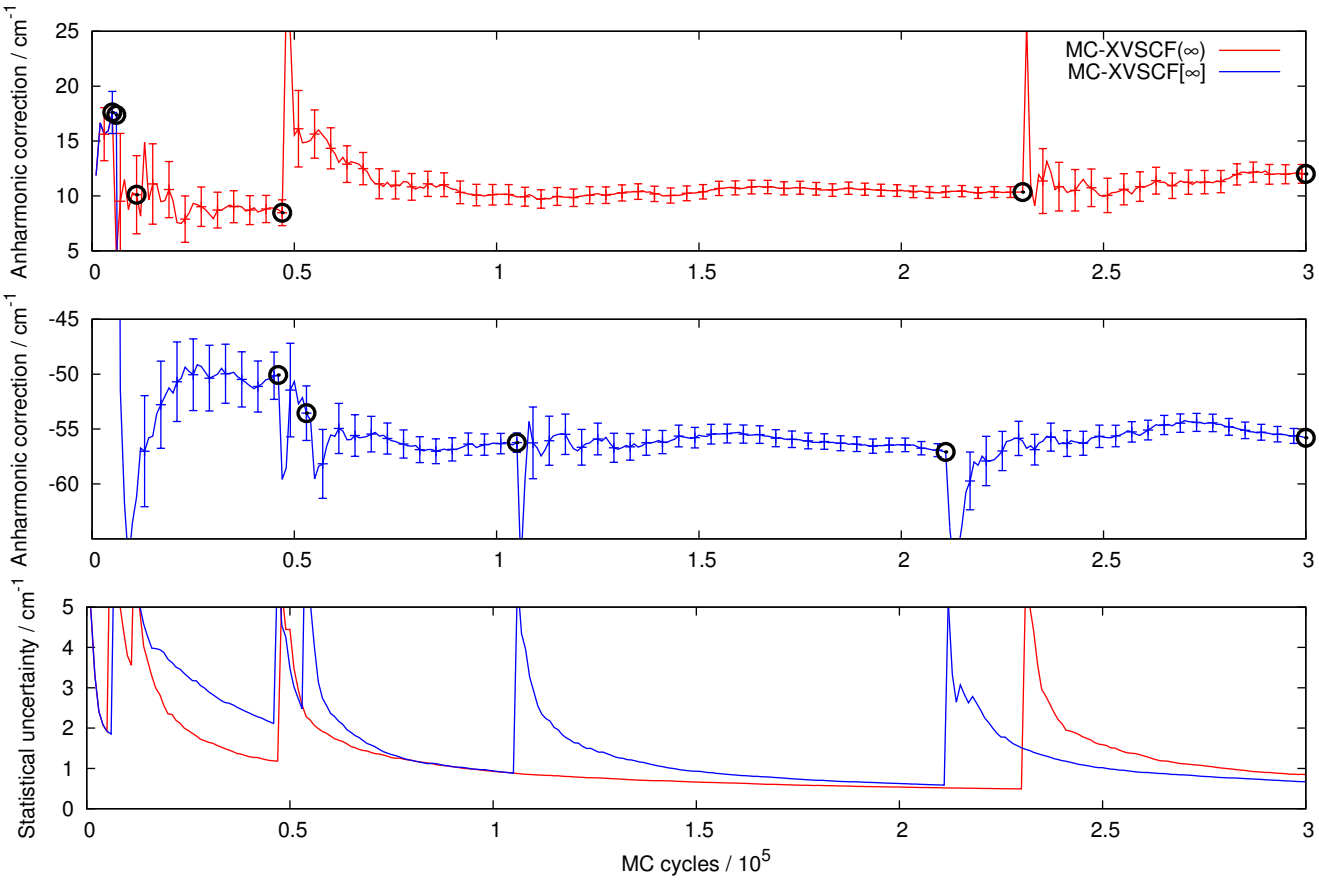

Figure 5.6: The same as Fig. 5.3, but for MC-XVSCF(∞) and MC-XVSCF[∞]. Open black circles denote the value of the ZPE in the last MC step of an SCF cycle.

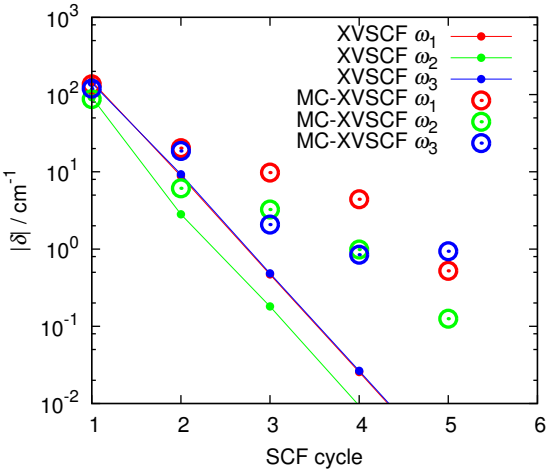

Figure 5.7: The same as Fig. 5.4, but comparing XVSCF(4) and XVSCF[4] to MC-XVSCF(∞) and MC-XVSCF[∞] calculations.

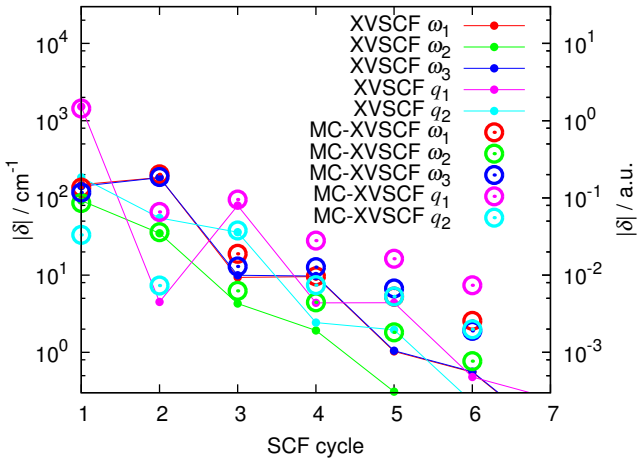

Figure 5.8: The same as Fig. 5.5, but comparing XVSCF(4) and XVSCF[4] to MC-XVSCF(∞) and MC-XVSCF[∞] calculations.

5.6 Tables

Table 5.1: The statistical uncertainties of the ZPE (in cm^{-1}), frequencies (in cm^{-1}), and geometries (in a.u. and normal coordinates) after a fixed number of MC steps in the first SCF cycle of an MC-XVSCF(4) or MC-XVSCF[4] calculation which does not use the AVM, compared to one that does. The scaling parameter for the weight function is $\alpha = 0.3$.

	No AVM; $N = 1.2 \times 10^6$	AVM; $N = 3 \times 10^5$
E_0	1.2	0.4
ω_1	3.5	1.1
ω_2	0.9	0.4
ω_3	2.1	1.1
q_1	4.5×10^{-3}	7.0×10^{-3}
q_2	7.7×10^{-3}	2.6×10^{-3}

Table 5.2: Anharmonic ZPE and frequencies (in cm^{-1}), anharmonic corrections to geometry in both normal coordinates (in a.u.) and local coordinates (bond lengths in Å and bond angles in degrees) of the water molecule in the harmonic oscillator approximation and after XVSCF(4), XVSCF[4], MC-XVSCF(4), and MC-XVSCF[4] calculations. Deterministic XVSCF calculations were run until the RMS of residuals of all frequencies and geometries between one cycle and the next is less than 10^{-9} cm^{-1} (for frequencies) or 10^{-9} a.u. (for geometries). The statistical uncertainties and SCF residuals of the stochastic calculations and the errors of the MC-XVSCF(4) and MC-XVSCF[4] calculations are presented in Table 5.3.

	E_0	ω_1	ω_2	ω_3	$q_1{}^a$	$q_2{}^b$	Δr_{OH}	$\Delta\theta_{HOH}$
Harmonic	4699.2	3822.1	1628.3	3947.9	0.000	0.000	0.000	0.000
XVSCF(4)	4746.9	3962.6	1538.7	4080.9	1.465	-0.134	0.013	-0.124
MC-XVSCF(4)	4746.5	3962.1	1538.4	4080.5	1.463	-0.137	0.013	-0.128
MC-XVSCF(∞)	4711.2	3933.1	1542.8	4048.5	1.305	-0.002	0.012	0.014
XVSCF[4]	4663.8	3787.7	1568.3	3907.6	1.608	-0.165	0.014	-0.156
MC-XVSCF[4]	4663.7	3785.9	1567.7	3905.9	1.606	-0.164	0.014	-0.155
MC-XVSCF[∞]	4643.4	3768.0	1575.5	3883.9	1.450	-0.064	0.013	-0.050

[a]Geometry along symmetric stretch coordinate.

[b]Geometry along bend coordinate.

Table 5.3: The statistical uncertainties (σ), SCF residuals (δ), and errors (ϵ) of ZPE (in cm^{-1}), frequencies (in cm^{-1}), and anharmonic geometry corrections (in normal coordinates and a.u.) in MC-XVSCF(4), MC-XVSCF[4], MC-XVSCF(∞), and MC-XVSCF[∞] calculations after 3×10^5 MC steps and k SCF cycles. The errors, labeled ϵ, are the differences between MC and deterministic XVSCF results using the same QFF ($n = 4$).

		$E_0^{[k+1]}$	$\omega_1^{[k+1]}$	$\omega_2^{[k+1]}$	$\omega_3^{[k+1]}$	$q_1^{[k+1]a}$	$q_2^{[k+1]b}$
MC-XVSCF(4) $k = 2$	σ	0.4	0.6	0.5	0.6	7.0×10^{-3}	2.8×10^{-3}
	δ	-1.3	-0.7	-0.7	-0.4	-	-
	ϵ	-0.5	-0.5	-0.3	-0.4	-1.9×10^{-3}	-3.6×10^{-3}
MC-XVSCF[4] $k = 4$	σ	0.4	0.7	0.7	0.8	6.1×10^{-3}	3.1×10^{-3}
	δ	0.8	-0.8	0.6	0.6	-1.9×10^{-2}	4.4×10^{-3}
	ϵ	-0.2	-1.8	-0.6	-1.7	-2.1×10^{-3}	5.9×10^{-4}
MC-XVSCF(∞) $k = 4$	σ	0.8	1.4	1.1	1.3	1.4×10^{-2}	6.0×10^{-3}
	δ	1.6	0.5	0.1	0.9	-	-
MC-XVSCF[∞] $k = 5$	σ	0.7	1.1	1.0	1.2	1.0×10^{-2}	5.1×10^{-3}
	δ	1.3	-2.6	0.8	-1.9	-7.4×10^{-3}	-2.0×10^{-3}

[a]Geometry along symmetric stretch coordinate.

[b]Geometry along bend coordinate.

Chapter 6

MC-XVMP2

In Chapter 4 we described vibrational MBPT, known as XVMP2, based on the Dyson equation using the reference wave function obtained either from one of the diagrammatically size-consistent variants of VSCF named XVSCF (Refs. 21, Chapters 2 and 3) or the harmonic approximation. XVMP2 has the common drawback with XVSCF of having to generate and store, at some point in a whole calculation, a high-dimensional array of the Hamiltonian matrix elements such as force constants. For instance, the evaluation and storage of all the nth-order force constants of a molecule with M vibrational degrees of freedom incur $O(M^n)$ operation and memory costs. Hence, the costs increase exponentially with n, even though the overall effect in the frequencies is observed to decay with n. There is clearly a considerable waste in computing all force constants up to a finite order or in any method that scans a PES on a product grid. The algorithms for PES scan are not as scalable on a massively parallel supercomputer as stochastic algorithms can be.

A solution to this issue is offered by stochastic methods such as quantum Monte Carlo (QMC).[40–43] QMC, particularly its variant diffusion Monte Carlo (DMC),[115,116] have been applied to anharmonic molecular vibrational problems. Their computational kernels involve nearly independent (thus highly parallel-executable) random walk of nuclei on a PES. No precomputed and stored PES or force constants are necessary as the value of PES at any nuclear geometry is evaluated on the fly and geometries are importance-sampled.[120] However, QMC has the well-known, persistent shortcoming of being limited to the ground vibrational states, which are nodeless. McCoy[115,116] has used DMC to evaluate the wave functions of a few lowest-lying excited states with assumed nodal structures, but these results inevitably suffer from fixed-node errors. Furthermore, a transition frequency needs to be evaluated as a total-energy difference with one transition at a time, which is particularly troublesome in QMC because total energies have statistical errors.

Here, we "wed" vibrational second-order MBPT (XVMP2 and XVH2) and QMC to arrive at the methods that inherit the merits of both approaches and cancel the demerits of each other, just as we did with XVSCF in Chapter 5. We call the methods MC-XVMP2 and MC-XVH2. We show that second-order corrections to zero-point energies and transition frequencies can be re-expressed as a sum of a few high-dimensional integrals of the vibrational wave functions and the PES. These integrals are, in turn, evaluated by the Monte Carlo (MC) method with nuclear geometries generated randomly by the Metropolis algorithm but according to a judiciously chosen weight function, to be specified

in this chapter. In each MC step, only the values of the vibrational wave functions and the PES at a nuclear geometry are needed, and they are computed on the fly and never stored; again, the geometries are importance-sampled according to the weight function. These MC steps are even more independent than those in DMC and should in principle be highly scalable. The new methods can compute not only the transition frequencies and zero-point energies directly (not as energy differences) but also frequency-dependent self-energies at a discrete set of frequencies, which can then be interpolated reliably and used in self-consistent solutions of the Dyson equation. Hence, MC-XVMP2 and MC-XVH2 inherit the same remarkable ability to determine multiple roots, which resist divergences near resonances, and their intensities. There is no sign problem or fixed-node error in MC-XVMP2 or MC-XVH2.

6.1 XVMP2 and XVH2

Here, we briefly review the formalisms of XVMP2 and XVH2. They are based on the inverse Dyson equation in the diagonal approximation, which solves

$$\nu^2 = \omega_i^2 + 2\omega_i \Sigma_i(\nu), \tag{6.1}$$

for ν for each mode, where ω_i is the ith-mode frequency of a reference mean-field theory and $\Sigma_i(\nu)$ is the ith diagonal element of the Dyson self-energy expanded in a diagrammatic perturbation series truncated at the second order. The reference wave function has to be a product of *effective* harmonic-oscillator functions (modals) along normal coordinates with effective harmonic frequencies $\{\omega_i\}$. It is obtained either by XVSCF (Refs. 21, Chapters 2 and 3) or the harmonic approximation. The former choice leads to XVMP2, whereas the latter defines XVH2.

Apart from being rigorously size-consistent (which is synonymous with size-extensive for total energies and with size-intensive for frequencies), these methods have unique advantages not seen in the parent second-order VMP (VMP2).[7,8] The former can obtain anharmonic transition frequencies directly from Eq. (6.1), in contrast to the latter, which calculates them as differences in total energy between the ground and excited states for one excited state at a time. Also, XVMP2 and XVH2 can resist divergence in the presence of strong anharmonic mode-mode coupling (such as a Fermi resonance) and locate multiple physically meaningful roots from the equation of one mode (with relative intensities also calculable as pole strengths of the corresponding Green's function), owing to the recursive structure of the inverse Dyson equation.

When seeking roots far from any resonances, however, one can use an even more streamlined approach and obtain an accurate approximate solution to Eq. (6.1) by evaluating

$$\nu^2 \approx \omega_i^2 + 2\omega_i \Sigma_i(\omega_i), \tag{6.2}$$

or

$$\nu^2 \approx \omega_i^2 + 2\omega_i \Sigma_i(0). \tag{6.3}$$

The self-energy in these equations is a sum of connected, irreducible, nonredundant, open diagrams with two stubs and written as

$$\Sigma_i(\nu) = \Sigma_i^{(1)}(\nu) + \Sigma_i^{(2\mathrm{p})}(\nu) + \Sigma_i^{(2\mathrm{p}')}(\nu) + \Sigma_i^{(2\mathrm{b})}(\nu) + \Sigma_i^{(2\mathrm{b}')}(\nu), \tag{6.4}$$

each of which is defined diagrammatically in Figs. 6.1–6.3, where the integer in the parenthesized superscript denotes the perturbation order. In XVMP2, the first-order term $\Sigma_i^{(1)}$ is zero as it is already included in the XVSCF reference wave function.[21] However, for reasons made clear below, we retain this term in this general expression.

These diagrams are translated straightforwardly to algebraic expressions according to the interpretation rules documented in our previous paper. The first-order self-energy diagrams in Fig. 6.1 are interpreted as

$$\begin{aligned}\Sigma_i^{(1)}(\nu) = {} & \frac{1}{2}\sum_j F_{iijj}\left(2^2\omega_i\omega_j\right)^{-1} + \frac{1}{2!2^2}\sum_{j,k} F_{iijjkk}\left(2^3\omega_i\omega_j\omega_k\right)^{-1} \\ & + \frac{1}{3!2^3}\sum_{j,k,l} F_{iijjkkll}\left(2^4\omega_i\omega_j\omega_k\omega_l\right)^{-1} + \ldots,\end{aligned} \tag{6.5}$$

where F_{iijj} is the quartic force constant with respect to the ith and jth normal coordinates and F_{iijjkk} and $F_{iijjkkll}$ the sextic and octic force constants, respectively. Likewise, the second-order diagrams in Figs. 6.2 and 6.3 are given algebraically as

$$\begin{aligned}\Sigma_i^{(2\mathrm{p})}(\nu) &= \Sigma_i^{(2\mathrm{p}')}(\nu) \\ &= \frac{1}{2}\sum_{j,k}\frac{F_{iijF_{jkk}}\left(2^3\omega_i\omega_j\omega_k\right)^{-1}}{-\omega_j} + \frac{1}{2!2^1}{\sum_{j,k,l}}'\frac{F_{iijk}F_{jkll}\left(2^4\omega_i\omega_j\omega_k\omega_l\right)^{-1}}{-\omega_j-\omega_k} \\ &\quad + \frac{1}{2^2}\sum_{j,k,l}\frac{F_{iijjk}F_{kll}\left(2^4\omega_i\omega_j\omega_k\omega_l\right)^{-1}}{-\omega_k} + \frac{1}{2!2^2}\sum_{j,k,l}\frac{F_{iij}F_{jkkll}\left(2^4\omega_i\omega_j\omega_k\omega_l\right)^{-1}}{-\omega_j} + \ldots,\end{aligned} \tag{6.6}$$

and

$$\begin{aligned}\Sigma_i^{(2\mathrm{b})}(\nu) &= \Sigma_i^{(2\mathrm{b}')}(-\nu) \\ &= \frac{1}{2!}\sum_{j,k}\frac{F_{ijk}^2\left(2^3\omega_i\omega_j\omega_k\right)^{-1}}{\nu-\omega_j-\omega_k} + \frac{1}{2^2}\sum_{j\neq i}\sum_{k,l}\frac{F_{ijkk}F_{ijll}\left(2^4\omega_i\omega_j\omega_k\omega_l\right)^{-1}}{\nu-\omega_j}\end{aligned}$$

$$+\frac{1}{3!}\sum_{j,k,l}\frac{F_{ijkl}^2\left(2^4\omega_i\omega_j\omega_k\omega_l\right)^{-1}}{\nu-\omega_j-\omega_k-\omega_l}+\frac{1}{2!2^1}\sum_{j,k,l}\frac{F_{ijk}F_{ijkll}\left(2^4\omega_i\omega_j\omega_k\omega_l\right)^{-1}}{\nu-\omega_j-\omega_k}+\ldots, \tag{6.7}$$

where the prime on the summation symbol in Eq. (6.6) indicates that $j = k$ needs to be excluded from the summation in XVMP2.

The corresponding zero-point energy expressions are given by a unified formula,

$$E_0 = E_0^{(0)} + E_0^{(1)} + E_0^{(2)}, \tag{6.8}$$

where $E_0^{(0)}$ is the energy of the zero-point (ground) state in the harmonic approximation in the case of XVH2(n) and in the XVSCF(n) approximation in the case of XVMP2(n). The first- and second-order corrections to this zeroth-order energy are written as

$$E_0^{(1)} = E_0^{(1A)} + E_0^{(1B)} + \ldots, \tag{6.9}$$

$$E_0^{(2)} = E_0^{(2A)} + E_0^{(2B)} + E_0^{(2C)} + E_0^{(2D)} + \ldots, \tag{6.10}$$

in notation similar to that used in Chapter 4. The right-hand sides are given algebraically by

$$E_0^{(1A)} = \frac{1}{2!2^2}\sum_{i,j}F_{iijj}\left(2^2\omega_i\omega_j\right)^{-1}, \tag{6.11}$$

$$E_0^{(1B)} = \frac{1}{3!2^3}\sum_{i,j,k}F_{iijjkk}\left(2^3\omega_i\omega_j\omega_k\right)^{-1}, \tag{6.12}$$

$$E_0^{(2A)} = \frac{1}{2^2}\sum_{i,j,k}\frac{F_{ijj}F_{ikk}\left(2^3\omega_i\omega_j\omega_k\right)^{-1}}{-\omega_i}, \tag{6.13}$$

$$E_0^{(2B)} = \frac{1}{2!2^2}\sum_{i,j,k,l}{}'\frac{F_{ijkk}F_{ijll}\left(2^4\omega_i\omega_j\omega_k\omega_l\right)^{-1}}{-\omega_i-\omega_j}, \tag{6.14}$$

$$E_0^{(2C)} = \frac{1}{3!}\sum_{i,j,k}\frac{F_{ijk}^2\left(2^3\omega_i\omega_j\omega_k\right)^{-1}}{-\omega_i-\omega_j-\omega_k}, \tag{6.15}$$

$$E_0^{(2D)} = \frac{1}{4!}\sum_{i,j,k,l}\frac{F_{ijkl}^2\left(2^4\omega_i\omega_j\omega_k\omega_l\right)^{-1}}{-\omega_i-\omega_j-\omega_k-\omega_l}, \tag{6.16}$$

where, again, ω's are the harmonic frequencies in XVH2(n) and the XVSCF(n) frequencies in XVMP2(n) and, in the latter case, $i = j$ is excluded in the summation of Eq. (6.14) (as designated by the prime on the summation symbol). These expressions are obtained by applying the interpretation rules stipulated in Chapter 4 to the corresponding diagrams in Fig. 6.4. Although the first-order correction is zero in XVMP2(n), we retain the corresponding term in Eq.

(6.8) for the reason given below.

In practice, the infinite sums in Eqs. (6.5)–(6.7), (6.9), and (6.10) are truncated after terms containing the nth-order force constants. With this truncation, these equations define the XVMP2(n) and XVH2(n) methods, where n is the truncation order of the Taylor-series expansion of the PES. XVMP2(n) is based on a reference wave function of XVSCF(n),[21] which, in turn, uses even-order force constants of the types appearing in Eq. (6.5) up to the nth order.

We have also introduced XVMP2[n], employing the XVSCF[n] reference wave function, in which odd-order force constants up to the nth order of certain types are additionally taken into account to define a new center of the normal coordinates known as the first-order Dyson geometry. In XVMP2[n], Eq. (6.6) for $\Sigma_i^{(2\mathrm{p})}$ and $\Sigma_i^{(2\mathrm{p}')}$ sums to zero, and $E_0^{(2\mathrm{A})}$ is part of a vanishing subset of diagrams, because these diagrams are included in the XVSCF[n] reference. In all cases, the self-energy is formally expressed by Eqs. (6.4)–(6.7), and the zero-point energy is formally expressed by Eqs. (6.8)–(6.16), with differences in the definition of ω and the coordinate center.

The derivation of MC-XVMP2(n) presented in Sec. 6.2 applies equally to MC-XVMP2[n] by simply replacing "(n)" by "[n]" everywhere it appears, and the coordinates in the latter are understood to be centered at the first-order Dyson geometry. Hereafter, we will not separately discuss MC-XVMP2[n].

A typical algorithm of the XVH2 and XVMP2 methods is as follows: (i) We first determine the equilibrium geometry and harmonic force constants of a molecule using an electronic structure method; (ii) We then perform a normal-mode analysis to obtain the normal coordinates $\{Q_i\}$ and the harmonic frequencies $\{\tilde{\omega}_i\}$; (iii) We calculate all necessary force constants up to the nth order; (iv) For XVMP2(n) or XVMP2[n], we carry out the XVSCF(n) or XVSCF[n] calculation to obtain the effective harmonic frequencies $\{\omega_i\}$ and/or adjust the geometry. For XVH2(n), this step is unnecessary as $\omega_i = \tilde{\omega}_i$ and the geometry is unchanged; (v) We solve the recursive inverse Dyson equation [Eq. (6.1)] or its nonrecursive approximations [Eq. (6.2) or (6.3)] using the self-energies defined by Eqs. (6.4)–(6.7); (vi) we evaluate the zero-point energy using Eqs. (6.8)–(6.16).

Of these, step (iii) is by far the most expensive in terms of both operation and memory costs and is also arduous to program. To obtain all nth-order force constants, one must differentiate a potential energy function with respect to normal coordinates at an $O(M^n)$ computational cost, where M is the vibrational degrees of freedom. One can alternatively compute the force constants in the Cartesian coordinates (e.g., in order to use analytical derivative capabilities[121] of *ab initio* molecular orbital theory or in order to exploit the locality of such force constants), but their transformation to the normal coordinates is an $O(M^{n+1})$ process. These become impractical for $n > 4$ not only because of the exponential scaling of cost with n but also owing to the increase in numerical errors caused by the repeated applications of finite-difference methods.[122] It is also not particularly scalable with respect to the number of processors in a modern parallel supercomputer. It is imperative that this high-order force-constant evaluation step be eliminated altogether so as to fully realize the intrinsic efficiency of XVMP2 (XVH2), especially for large molecules and solids.

6.2 MC-XVMP2 and MC-XVH2

In the stochastic implementation of these methods, we consider two scenarios (*direct* and *indirect*) for evaluating a PES and two ways (*recursive* and *nonrecursive*) of performing frequency calculations.

In a direct calculation, the value of a PES at a given geometry is calculated on demand by an electronic structure calculation, discarded after its use, and never stored. Furthermore, the geometries are generated randomly but in accordance with their probability of occurrence during vibrational motion. This is achieved by the Metropolis algorithm with a suitable weight function (see below). Hence, the overall computational cost is dominated by that of electronic structure calculations and how the rest of the integrand is evaluated is rather unimportant for the computational cost. The stochastic sampling of the PES also allows much higher-order force constants than those considered in the reference method to be implicitly included in the calculation. We call the stochastic XVMP2 methods using this algorithm MC-XVMP2(∞) and MC-XVH2(∞), emphasizing the fact that they can, in principle, include important high-order force constants up to an infinite order. This is a great advantage of these methods unmatched by any force-constant-based methods, but it also causes mismatch in the PES between the reference and perturbation methods. This is why the first-order energy and self-energy are no longer zero in MC-XVMP2(∞). This issue is discussed more fully in Sec. 6.2.5.

In an indirect calculation, a PES is precalculated and stored in the form of a mathematical function or a set of force constants, which allows the value of the PES to be rapidly evaluated at any geometry during MC integrations. The overall cost is dominated by the precalculation of the PES, which is unchanged by the stochastic algorithm introduced here. For instance, if the PES is given as a quartic force field (QFF), XVMP2(4) and XVH2(4) already constitute the most efficient, deterministic algorithms that take into account the whole QFF in the second-order perturbation theory; the stochastic counterparts, which we call MC-XVMP2(4) and MC-XVH2(4), do not offer any advantage in this case. In other words, the algorithm proposed here is meaningful only in the direct calculation. Nonetheless, we report the results of indirect calculations for the purpose of code verification and assessment of method performance.

In a recursive calculation, we solve the recursive inverse Dyson equation [Eq. (6.1)] for self-consistent solutions by an iterative algorithm such as the one proposed by us, which brings about various advantages over the conventional VMP2 method. In a nonrecursive calculation, we use the nonrecursive approximation of Eq. (6.3) to significantly reduce the computational cost and algorithm complexity at the expense of losing some of the aforementioned advantages. The total (zero-point) energy calculations are always nonrecursive.

6.2.1 First-order correction to zero-point energy

We seek a mathematical transformation that eliminates any explicit reference to force constants and thereby brings these expressions into forms that lend themselves to MC integrations. Adopting the strategy of Ref. 44, we can immediately rewrite the first-order correction to the zero-point energy, Eq. (6.9), in such a form:

$$E_0^{(1)} = \int \Psi_0(\boldsymbol{Q})\Delta V(\boldsymbol{Q})\Psi_0(\boldsymbol{Q})d\boldsymbol{Q}, \tag{6.17}$$

where $\boldsymbol{Q}$ collectively refers to all normal modes and hence $d\boldsymbol{Q}$ stands for $dQ_1 dQ_2 \cdots dQ_M$. That this is equal to Eq. (6.9) can be understood by recognizing it as the first-order correction in the Rayleigh–Schrödinger perturbation theory (RSPT), which is identical to the corresponding expression in the diagrammatic many-body perturbation theory.

Here, $\Delta V(\boldsymbol{Q})$ is the fluctuation potential in the perturbation theory and is written as

$$\Delta V(\boldsymbol{Q}) = \hat{H} - \hat{H}^{(0)}, \tag{6.18}$$

where $\hat{H}$ is the Hamiltonian containing up to the nth-order force constants and $\hat{H}^{(0)}$ is the zeroth-order Hamiltonian in the harmonic approximation in the case of MC-XVH2(n) or in the XVSCF($\tilde{n}$) approximation in the case of MC-XVMP2(n). We distinguish the highest order (n) of force constants in the Hamiltonian, which is generally undefined and can be essentially infinite in a direct calculation, from the order ($\tilde{n}$) used in the reference wave function calculation.

In MC-XVH2(n), the fluctuation potential is written as

$$\Delta V(\boldsymbol{Q}) = V(\boldsymbol{Q}) - V_0 - \frac{1}{2}\sum_{i=1}^{M} \omega_i^2 Q_i^2, \tag{6.19}$$

where $V(\boldsymbol{Q})$ is the PES containing up to the nth-order force constants and V_0 is its value at the equilibrium geometry (the minimum). $\Delta V(\boldsymbol{Q})$ is, therefore, the anharmonicity of the PES due to the cubic and higher-order force constants.

In MC-XVMP2(n), the fluctuation potential is

$$\Delta V(\boldsymbol{Q}) = V(\boldsymbol{Q}) - E_0^{(0)} + \frac{1}{2}\sum_{i=1}^{M} \omega_i - \frac{1}{2}\sum_{i=1}^{M} \omega_i^2 Q_i^2, \tag{6.20}$$

where $E_0^{(0)}$ is the energy of the zero-point (ground) state and ω_i is the ith-mode frequency of XVSCF($\tilde{n}$). All of these quantities are readily available once the reference wave function calculation is completed.

The zero-point wave function, Ψ_0, is that of the reference method and is written as

$$\Psi_0(\boldsymbol{Q}) = \prod_{i=1}^{M} \varphi_0(Q_i), \tag{6.21}$$

where $\varphi_{s_i}(Q_i)$ is the harmonic-oscillator wave function with quantum number s_i along the ith normal mode, Q_i, obtained either by the harmonic approximation in the case of MC-XVH2(n) or by XVSCF($\tilde{n}$) in the case of MC-XVMP2(n).

In a direct calculation, the cost of the calculation is determined by that of evaluating $\Delta V(\boldsymbol{Q})$ during MC integrations. The cost of evaluating the factors of the integrand other than $\Delta V(\boldsymbol{Q})$ is $O(M^1 n^0)$, where M is the vibrational degrees of freedom and n is the rank of $\Delta V(\boldsymbol{Q})$, since one must evaluate $\varphi_0(Q_i)$ for each $i = 1, \ldots, M$. This concerns the cost of evaluating the integrand, not the integral, of Eq. (6.17).

6.2.2 Second-order correction to zero-point energy

We also rewrite the second-order correction to the zero-point energy into a single high-dimensional integral. To do this, we consider the sum of all second-order corrections instead of the individual contributions and write it as

$$E_0^{(2)} = \sum_{s>0}^{s_{\max}} \frac{1}{E_0^{(0)} - E_s^{(0)}} \int \Psi_0(\boldsymbol{Q}) \Delta V(\boldsymbol{Q}) \Psi_s(\boldsymbol{Q}) d\boldsymbol{Q} \int \Psi_s(\boldsymbol{Q}') \Delta V(\boldsymbol{Q}') \Psi_0(\boldsymbol{Q}') d\boldsymbol{Q}', \tag{6.22}$$

where Ψ_s is the sth excited-state wave function of the reference method and $E_s^{(0)}$ is the associated energy. This is the second-order correction in the RSPT and is, therefore, equal to Eq. (6.10), when expanded. This is yet to have a form suitable for MC integration because it is still a sum of numerous integrals; we must interchange the order of summation and integration so that $E_0^{(2)}$ is written as a single high-dimensional integral. This can be done formally immediately as

$$E_0^{(2)} = \iint \Psi_0(\boldsymbol{Q}) \Delta V(\boldsymbol{Q}) G^{(2)}(\boldsymbol{Q}, \boldsymbol{Q}') \Delta V(\boldsymbol{Q}') \Psi_0(\boldsymbol{Q}') d\boldsymbol{Q} d\boldsymbol{Q}', \tag{6.23}$$

where $G^{(2)}(\boldsymbol{Q}, \boldsymbol{Q}')$ is a real-space Green's function given by

$$G^{(2)}(\boldsymbol{Q}, \boldsymbol{Q}') = \sum_{s>0}^{s_{\max}} \frac{\Psi_s(\boldsymbol{Q}) \Psi_s(\boldsymbol{Q}')}{E_0^{(0)} - E_s^{(0)}}. \tag{6.24}$$

The summation over s must formally go over all states that are reached by $\Delta V(\boldsymbol{Q})$ from Ψ_0. The number of such states, denoted by $s_{\max}$, is proportional to the number of force constants included in $\Delta V(\boldsymbol{Q})$, which grows as $O(M^n)$.

We can, however, reduce this $O(M^n)$ scaling by invoking the same mathematical trick used in Ref. 44. First, we note that, in the reference method, $E_s^{(0)}$ is always written as

$$E_s^{(0)} = E_0^{(0)} + \sum_{i=1}^{M} s_i \omega_i, \tag{6.25}$$

where s_i is the quantum number of the ith mode in the sth state. Second, we use the Laplace transform of $(E_0^{(0)} - E_s^{(0)})^{-1}$,

$$\frac{1}{E_0^{(0)} - E_s^{(0)}} = -\int_0^\infty e^{-\sum_i s_i \omega_i \tau} d\tau \tag{6.26}$$

$$= -\prod_{i=1}^{M} \int_0^\infty e^{-s_i \omega_i \tau} d\tau. \tag{6.27}$$

Third, we find

$$G^{(2)}(\boldsymbol{Q}, \boldsymbol{Q}') = -\int_0^\infty g^{(2)}(\boldsymbol{Q}, \boldsymbol{Q}', \tau)\, d\tau, \tag{6.28}$$

where $g^{(2)}(\boldsymbol{Q}, \boldsymbol{Q}', \tau)$ is a real-space, imaginary-time Green's function given by

$$g^{(2)}(\boldsymbol{Q}, \boldsymbol{Q}', \tau) = \prod_{i=1}^{M} \zeta_i(Q_i, Q_i', \tau) - \Psi_0(\boldsymbol{Q})\Psi_0(\boldsymbol{Q}'), \tag{6.29}$$

and

$$\zeta_i(Q_i, Q_i', \tau) = \sum_{s_i=0}^{n_{\max}} \varphi_{s_i}(Q_i)\varphi_{s_i}(Q_i') e^{-s_i \omega_i \tau}. \tag{6.30}$$

The cost of evaluating Eq. (6.28) is now reduced from $O(M^n)$ to $O(M^1 n_{\max}^1) = O(M^1 n^1)$. This Laplace-transformed expression includes all states with up to excitation rank $n_{\max}$ and some states with up to rank $Mn_{\max}$; we consider $n_{\max} \approx n$ for the cost analysis.

The last term in Eq. (6.29) corresponds to the exclusion of the $N = 0$ term from the summation in Eq. (6.22), in which it causes divergence. Diagrammatically, this term represents the sum of all disconnected diagrams; the subtraction of this term, therefore, amounts to the act of eliminating disconnected diagrams. Although the foregoing transformations may appear to be a regression from diagrammatic MBPT (Refs. 123, 124) to RSPT, the diagrammatic logic to maintain size consistency of the theory is carefully maintained.

6.2.3 First-order correction to frequencies

The first-order self-energy expression of Eq. (6.5) is converted into a single M-dimensional integral,

$$\Sigma_i^{(1)}(\nu) = \int \Psi_0(\boldsymbol{Q}) \Delta V(\boldsymbol{Q}) \hat{a}_i^\dagger \hat{a}_i^\dagger \Psi_0(\boldsymbol{Q}) d\boldsymbol{Q}, \tag{6.31}$$

where $\hat{a}_i^\dagger$ and $\hat{a}_i$ are the harmonic-oscillator ladder operators for mode i, which satisfy Eqs. (5.15) and (5.16) from Chapter 5. Therefore, the programmable expression of Eq. (6.31) is

$$\Sigma_i^{(1)}(\nu) = \int \Psi_0(\boldsymbol{Q})\Delta V(\boldsymbol{Q})\Psi_0(\boldsymbol{Q})\frac{2^{1/2}\varphi_2(Q_i)}{\varphi_0(Q_i)}d\boldsymbol{Q}, \tag{6.32}$$

which is subject to MC integration with an $O(M^1 n^0)$ cost to evaluate the integrand excluding $\Delta V(\boldsymbol{Q})$.

Equation (6.32) is equal to the infinite sum of Eq. (6.5), which can be proven algebraically by substituting the Taylor series of $\Delta V(\boldsymbol{Q})$ into Eq. (6.32) and analytically evaluating it using the formulas given in Table I of Ref. 21. In the diagrammatic language, inserting two ladder operators ($\hat{a}_i^\dagger \hat{a}_i^\dagger$) into an energy expression like Eq. (6.17) amounts to attaching two stubs to a vertex in the energy diagrams (such as the leftmost diagram in Fig. 6.4), spawning the corresponding self-energy diagrams (Fig. 6.1). Since the first-order energy diagrams are never disconnected (as there is only one vertex), the insertion of $\hat{a}_i^\dagger \hat{a}_i^\dagger$ generates only connected self-energy diagrams. This argument is not a rigorous diagrammatic rule, but a useful mnemonic invoked repeatedly in the following.

6.2.4 Second-order correction to frequencies

The second-order corrections to self-energy consist of the four terms denoted by $\Sigma_i^{(2\mathrm{p})}$, $\Sigma_i^{(2\mathrm{p}')}$, $\Sigma_i^{(2\mathrm{b})}$, and $\Sigma_i^{(2\mathrm{b}')}$. They are defined diagrammatically in Figs. 6.2 and 6.3 and algebraically in Eqs. (6.6) and (6.7).

The contributions from the "pendant" diagrams (Fig. 6.2) are written as single $2M$-dimensional integrals as follows:

$$\Sigma_i^{(2\mathrm{p})}(\nu) = \sum_{s>0}^{s_{\max}} \frac{1}{E_0^{(0)} - E_s^{(0)}} \int \Psi_0(\boldsymbol{Q})\Delta V(\boldsymbol{Q})\Psi_s(\boldsymbol{Q})d\boldsymbol{Q} \int \Psi_s(\boldsymbol{Q}')\hat{a}_i\hat{a}_i\Delta V(\boldsymbol{Q}')\Psi_0(\boldsymbol{Q}')d\boldsymbol{Q}', \tag{6.33}$$

$$\Sigma_i^{(2\mathrm{p}')}(\nu) = \sum_{s>0}^{s_{\max}} \frac{1}{E_0^{(0)} - E_s^{(0)}} \int \Psi_0(\boldsymbol{Q})\Delta V(\boldsymbol{Q})\hat{a}_i^\dagger\hat{a}_i^\dagger\Psi_s(\boldsymbol{Q})d\boldsymbol{Q} \int \Psi_s(\boldsymbol{Q}')\Delta V(\boldsymbol{Q}')\Psi_0(\boldsymbol{Q}')d\boldsymbol{Q}'. \tag{6.34}$$

Insertion of $\hat{a}_i\hat{a}_i$ into the second factor in the energy expression of $E_0^{(2)}$ [Eq. (6.22)] corresponds to attaching two stubs to the lower vertex of the second-order energy diagrams, generating the corresponding self-energy diagrams of $\Sigma_i^{(2\mathrm{p})}$ (Fig. 6.2). Likewise, insertion of $\hat{a}_i^\dagger\hat{a}_i^\dagger$ in the first factor leads to the diagrams of $\Sigma_i^{(2\mathrm{p}')}$.

The first of these equations is transformed to

$$\Sigma_i^{(2\mathrm{p})}(\nu) = \iint \Psi_0(\boldsymbol{Q})\Delta V(\boldsymbol{Q})G_i^{(2\mathrm{p})}(\boldsymbol{Q},\boldsymbol{Q}')\Delta V(\boldsymbol{Q}')\Psi_0(\boldsymbol{Q}')d\boldsymbol{Q}d\boldsymbol{Q}', \tag{6.35}$$

with

$$G_i^{(2\mathrm{p})}(\boldsymbol{Q},\boldsymbol{Q}') = \sum_{s>0}^{s_{\max}} \frac{\Psi_s(\boldsymbol{Q})\Psi_s(\boldsymbol{Q}')}{E_0^{(0)}-E_s^{(0)}} \frac{(s_i+2)^{1/2}(s_i+1)^{1/2}\varphi_{s_i+2}(Q_i')}{\varphi_{s_i}(Q_i')} \tag{6.36}$$

$$= -\int_0^\infty g_i^{(2\mathrm{p})}(\boldsymbol{Q},\boldsymbol{Q}',\tau)\,d\tau, \tag{6.37}$$

and

$$g_i^{(2\mathrm{p})}(\boldsymbol{Q},\boldsymbol{Q}',\tau) = \xi_i(Q_i,Q_i',\tau)\prod_{j\neq i}^{M}\zeta_j(Q_j,Q_j',\tau) - \Psi_0(\boldsymbol{Q})\Psi_0(\boldsymbol{Q}')\frac{2^{1/2}\varphi_2(Q_i')}{\varphi_0(Q_i')}, \tag{6.38}$$

where $\zeta_j(Q_j,Q_j',\tau)$ is already defined by Eq. (6.30) and

$$\xi_i(Q_i,Q_i',\tau) = \sum_{s_i=0}^{n_{\max}-2}\varphi_{s_i}(Q_i)\varphi_{s_i+2}(Q_i')(s_i+2)^{1/2}(s_i+1)^{1/2}e^{-s_i\omega_i\tau}. \tag{6.39}$$

The last term of Eq. (6.38) is diagrammatically interpreted as the subtraction of disconnected diagrams. Equation (6.36) costs $O(s_{\max}) = O(M^n)$ operations to evaluate, whereas Eq. (6.37) can be calculated at an $O(M^1 n_{\max}^1) = O(M^1 n^1)$ cost, again assuming $n_{\max}\approx n$. The expression for $\Sigma_i^{(2\mathrm{p}')}$ is the complex conjugate of the above.

Next, we consider the "bubble" diagrams (Fig. 6.3). They are written in integral forms as

$$\Sigma_i^{(2\mathrm{b})}(\nu) = \sum_{s\neq 0,i}^{s_{\max}}\frac{1}{\nu+E_0^{(0)}-E_s^{(0)}}\int\Psi_0(\boldsymbol{Q})\Delta V(\boldsymbol{Q})\hat{a}_i^\dagger\Psi_s(\boldsymbol{Q})d\boldsymbol{Q}\int\Psi_s(\boldsymbol{Q}')\hat{a}_i\Delta V(\boldsymbol{Q}')\Psi_0(\boldsymbol{Q}')d\boldsymbol{Q}', \tag{6.40}$$

$$\Sigma_i^{(2\mathrm{b}')}(\nu) = \sum_{s\neq 0,i}^{s_{\max}}\frac{1}{-\nu+E_0^{(0)}-E_s^{(0)}}\int\Psi_0(\boldsymbol{Q})\Delta V(\boldsymbol{Q})\hat{a}_i^\dagger\Psi_s(\boldsymbol{Q})d\boldsymbol{Q}\int\Psi_s(\boldsymbol{Q}')\hat{a}_i\Delta V(\boldsymbol{Q}')\Psi_0(\boldsymbol{Q}')d\boldsymbol{Q}'. \tag{6.41}$$

Insertion of $\hat{a}_i^\dagger$ in the first factor and of $\hat{a}_i$ in the second in the energy expression of $E_0^{(2)}$ corresponds to attaching one stub to the upper vertex and another to the lower vertex of the corresponding energy diagram, creating the bubble diagrams in Fig. 6.3.

In the summations, $s = 0$ is excluded because it corresponds to disconnected diagrams (see above). Also excluded is $s = i$, where the ith state is the one singly excited in the ith mode, i.e., $s_i = 1$ and $n_j = 0$ ($\forall j \neq i$). This exclusion amounts to the deletion of reducible diagrams, which can be understood as follows: Since Ψ_i is a singly excited state, there is only one line between the two vertexes and its mode index is i. The self-energy diagrams with this motif are, e.g., the second diagrams from the left in Fig. 6.3 with $i = j$, which are reducible.

These equations are further simplified to

$$\Sigma_i^{(2\mathrm{b})}(\nu) = \Sigma_i^{(2\mathrm{b}')}(-\nu)$$

$$= \iint \Psi_0(\boldsymbol{Q})\Delta V(\boldsymbol{Q})G_i^{(2b)}(\boldsymbol{Q},\boldsymbol{Q}',\nu)\Delta V(\boldsymbol{Q}')\Psi_0(\boldsymbol{Q}')d\boldsymbol{Q}d\boldsymbol{Q}', \tag{6.42}$$

with

$$G_i^{(2b)}(\boldsymbol{Q},\boldsymbol{Q}',\nu) = \sum_{s\neq 0,\,i}^{s_{\max}} \frac{\Psi_s(\boldsymbol{Q})\Psi_s(\boldsymbol{Q}')}{\nu + E_0^{(0)} - E_s^{(0)}} \frac{(s_i+1)\varphi_{s_i+1}(Q_i)\varphi_{s_i+1}(Q_i')}{\varphi_{s_i}(Q_i)\varphi_{s_i}(Q_i')}. \tag{6.43}$$

Unlike Eq. (6.24) or (6.36), this does not readily lend itself to a Laplace transform because the denominator, $\nu + E_0^{(0)} - E_s^{(0)}$, can go from positive to negative with increasing s; their ν-dependence prohibits the application of a Laplace transform. In a recursive calculation, where such dependence is essential, we evaluate $G_i^{(2b)}(\boldsymbol{Q},\boldsymbol{Q}',\nu)$ with the above sum-over-states expression [Eq. (6.43)] with $s_{\max}$ truncated at the states with excitation rank $\tilde{n}$ such that the scaling of the overall cost does not exceed that of the deterministic XVMP2($\tilde{n}$) or XVH2($\tilde{n}$) algorithm, which is $O(M^{\tilde{n}})$.

In a nonrecursive calculation, on the other hand, we only need $G_i^{(2b)}(\boldsymbol{Q},\boldsymbol{Q}',0)$, which is subject to a Laplace transform, yielding

$$G_i^{(2b)}(\boldsymbol{Q},\boldsymbol{Q}',0) = -\int_0^\infty g_i^{(2b)}(\boldsymbol{Q},\boldsymbol{Q}',\tau)\,d\tau, \tag{6.44}$$

and

$$\begin{aligned} g_i^{(2b)}(\boldsymbol{Q},\boldsymbol{Q}',\tau) &= \theta_i(Q_i,Q_i',\tau)\prod_{j\neq i}^{M}\zeta_j(Q_j,Q_j',\tau) - \Psi_0(\boldsymbol{Q})\Psi_0(\boldsymbol{Q}')\frac{\varphi_1(Q_i)\varphi_1(Q_i')}{\varphi_0(Q_i)\varphi_0(Q_i')} \\ &\quad -\Psi_0(\boldsymbol{Q})\Psi_0(\boldsymbol{Q}')\frac{2\varphi_2(Q_i)\varphi_2(Q_i')}{\varphi_0(Q_i)\varphi_0(Q_i')}\,e^{-\omega_i\tau}, \end{aligned} \tag{6.45}$$

where $\zeta_j(Q_j,Q_j',\tau)$ is again defined by Eq. (6.30) and

$$\begin{aligned} \theta_i(Q_i,Q_i',\tau) &= \sum_{s_i=0}^{n_{\max}-1} \varphi_{s_i+1}(Q_i)\varphi_{s_i+1}(Q_i') \\ &\quad \times(s_i+1)e^{-s_i\omega_i\tau}. \end{aligned} \tag{6.46}$$

An evaluation of Eq. (6.44) costs only $O(M^1n^1)$. The second term in the right-hand side of Eq. (6.45) subtracts the disconnected diagrams and the last term subtracts the reducible diagrams.

6.2.5 Higher-order diagrams

In a direct calculation, the PES is evaluated at geometries randomly generated by the Metropolis algorithm described in Sec. 6.3 below. Therefore, it includes the effects of higher-order force constants and their corresponding diagrammatic contributions implicitly. For instance, diagrammatic contributions in Fig. 6.5, which involves fifth-order force constants, are included in MC-XVH2(∞), MC-XVMP2(∞), and MC-XVMP2[∞] using the direct algorithm, but not in XVH2(4), XVMP2(4), or XVMP2[4], which is based on a QFF.

This is one of the advantages of the direct MC-XVMP2 methods, but it has the following side effect: the PES's used in the MC-XVMP2 and preceding XVSCF reference wave function calculations differ from each other; the partitioning is no longer the Møller–Plesset type. Hence, the first-order diagrams such as those shown in Fig. 6.6, which involve sixth-order force constants, have nonzero contributions in MC-XVMP2(∞) and MC-XVMP2[∞] when the reference wave function is XVSCF(4) or XVSCF[4]. Therefore, the first-order energy and self-energy contributions are nonzero in MC-XVMP2(∞) and MC-XVMP2[∞] calculations and need to be evaluated using Eqs. (6.17) and (6.32).

6.3 Stochastic algorithms

6.3.1 Monte Carlo integrations

Any quadrature algorithm for evaluating the M- or $2M$-dimensional integrals appearing in the preceding section would have an operation cost which grows exponentially with M (the vibrational degrees of freedom), which is prohibitive for all but the smallest molecules. On the other hand, experiences with QMC have been that the operation cost required to reach a given accuracy increases only as $O(M^3)$.[40] The trade-off is the slow $N^{-1/2}$ fall-off of the statistical error, where N is the number of MC steps of sampling points. Here, we use the MC method.

Each of the integrals I appearing in the preceding section is approximated by

$$I \approx \frac{1}{N}\sum_{i=1}^{N} I_i \equiv I_N, \tag{6.47}$$

with

$$I_i = \frac{f(\boldsymbol{Q}_i)}{w(\boldsymbol{Q}_i)}, \tag{6.48}$$

when the integral is Eq. (6.17) or (6.32), or with

$$I_i = \frac{f(\boldsymbol{Q}_i, \boldsymbol{Q}'_i)}{w(\boldsymbol{Q}_i)w(\boldsymbol{Q}'_i)}, \tag{6.49}$$

when the integral is Eq. (6.23), (6.35), or (6.42), where f refers to the integrand in one of these expressions, w is the weight function to be specified below, and $\boldsymbol{Q}_i$ is the ith sampling point in the M-dimensional space of normal coordinates generated stochastically by the Metropolis algorithm[39] according to the weight function.

More specifically, we use different formulas to evaluate the integrands depending on whether the solutions of the recursive or nonrecursive inverse Dyson equation are sought. In a recursive calculation, the integrand of $\Sigma_i^{(2b)} + \Sigma_i^{(2b')}$ is evaluated by using the sum-over-states formula of Eq. (6.43) with a severe truncation of the summation over states. In all other cases, the Laplace-transformed formulas are used, taking into account a large number of states. In the latter case, the one-dimensional integration over τ is performed by the 51-point Gauss-Kronrod quadrature,[44,125] using a change of variable to $\tilde{\tau} = (\tau + 1)^{-1}$.

The variance σ_N^2 and the statistical uncertainty σ_N are estimated by

$$\sigma_N^2 = \frac{1}{N(N-1)} \sum_{i=1}^{N} (I_i - I_N)^2. \tag{6.50}$$

This estimate is, however, accurate only when I_i is uncorrelated from one MC step to another and this is not necessarily the case here because a new sampling point is generated from an old one by a random-walk step with a semi-fixed radius (see below).

To more accurately estimate the statistical uncertainty, we use the blocking algorithm of Flyvbjerg and Petersen.[118] We thus modify the definition of σ_N as

$$\sigma_N^2 = \frac{1}{N'(N'-1)} \sum_{j=1}^{N'} (I'_j - I_N)^2, \tag{6.51}$$

where $N' = N/N_\mathrm{B}$, N_B is the block length, and

$$I'_j = \frac{1}{N_\mathrm{B}} \sum_{i=(j-1)N_\mathrm{B}+1}^{jN_\mathrm{B}} I_i. \tag{6.52}$$

In this way, we evaluate the statistical uncertainty using every N_B integrals, and these data become uncorrelated for sufficiently large N_B (we use $N_\mathrm{B} = 75$).

It has also been found that the use of Abelian point-group symmetry helps reduce the statistical uncertainty. This is discussed in Sec. 6.3.4.

6.3.2 Weight functions

The feasibility of MC integration depends critically on the quality of the weight function. An effective weight function $w(\boldsymbol{Q})$ should have a significant amplitude where $|f(\boldsymbol{Q})|$ is large, but should be negligible elsewhere. It should be positive

everywhere, be analytically integrable, and have the same singularities as the integrand. Since the integrands of the vibrational MBPT do not have any singularities, stochastic algorithms are expected to be even more efficient and well-suited for vibrational problems than for electron correlation.[44]

One candidate weight function is the zero-point wave function in the harmonic approximation or its probability density, which has been used implicitly in stochastic SCP and VCI methods[93,113,114,119] (see below). The weight function used in this study is also the probability density of the zero-point wave function of the reference method, i.e., the harmonic approximation for MC-XVH2(n) and the XVSCF($\tilde{n}$) method for MC-XVMP2(n):

$$w(\boldsymbol{Q}) = \prod_{i=1}^{M} \left(\frac{\alpha\omega_i}{\pi}\right)^{1/2} e^{-\alpha\omega_i Q_i^2}, \tag{6.53}$$

where α is a scaling parameter. This weight function is positive everywhere, integrates analytically to unity, and generally behaves like the integrands, when the PES is not too anharmonic. The weight function for the $2M$-dimensional integral is simply the product $w(\boldsymbol{Q})w(\boldsymbol{Q}')$. This weight function is ideal for all of the M and $2M$-dimensional integrals, since their integrands differ only by a polynomial factor and they all decay exponentially to zero far from the origin in normal-coordinate space.

The operation cost in a direct calculation is determined by the cost of electronic structure calculations and the memory cost is always negligible. The overall efficiency of MC-XVMP2 is, therefore, equal to the efficiency of sampling the PES, which, in turn, depends on how well the forms of the PES and weight function match with each other.

6.3.3 Metropolis algorithm

In each MC step, a new geometry, $\boldsymbol{Q}_{i+1}$, in the M-dimensional space of the normal coordinates is generated as a random-walk step from the previous geometry, $\boldsymbol{Q}_i$. The direction of this step is completely random, but the radius is semi-constant and given by $\beta|\langle\Psi_0|Q_j^2|\Psi_0\rangle|^{1/2}$ along the jth normal coordinate, where β is a parameter. The new geometry is accepted if the ratio $w(\boldsymbol{Q}_{i+1})/w(\boldsymbol{Q}_i)$ is greater than a random number between 0 and 1. If the step is accepted, the value of the PES at that geometry is evaluated; otherwise it is taken from the previous step. The value of β is continuously varied so that the acceptance rate becomes as close to 50% as possible, starting with initial geometries near the equilibrium geometry. During the first 10^5 steps (the initial equilibration stage), no PES evaluation is performed, after which the MC integration with PES evaluations starts. The same collection of walkers, guided by the same weight function, is used to evaluate all M- and $2M$-dimensional integrals.

In this study, we have also extended the redundant-walker algorithm of Willow *et al.*[46] to MC-XVMP2(n) and MC-XVH2(n). Though this algorithm is essential for the efficiency of these methods, its underlying idea is the same

as in MC-MP2 for electron correlation and its details are relegated to Sec. 6.3.5. Briefly, it involves propagating a set of N_w walkers simultaneously and exploiting a two-fold summation over walkers to accelerate the evaluation of the $2M$-dimensional integrals. In the calculations reported below, "one MC step" is defined as one random-walk step of all N_w walkers. Since the PES is evaluated roughly half as many times as a single walker is propagated, a calculation reported to have N steps evaluates the PES roughly $N_\mathrm{w}N/2$ times.

A highly scalable parallel algorithm of these methods can be readily accomplished by simply executing a Metropolis process in each processor of a parallel machine. There are nearly no inter-processor communications needed, though our implementation issues MPI commands to synchronize and collect I'_j from all processors at every N_B steps. The only step that fundamentally resists parallelization is the initial equilibration stage as it has to occur as many times as the number of processors instead of just once in a serial execution. Nevertheless, this MC algorithm naturally exposes an exceptionally high degree of parallelism in its kernel.

6.3.4 Point-group symmetry

For a molecule that belongs to an Abelian point-group symmetry, many individual contributions to the integrals become symmetrically zero. Eliminating those vanishing contributions using a symmetry logic does not change the values of the integrals or the operation cost per MC step, but it reduces the statistical uncertainty and thus increases overall efficiency of MC-XVMP2 and MC-XVH2 to a noticeable degree.

Let us illustrate the proposed symmetry algorithm by taking $\Sigma_i^{(2\mathrm{b})}$ and $\Sigma_i^{(2\mathrm{b}')}$ as an example. They are still obtained by evaluating Eq. (6.42), but with

$$G_i^{(2\mathrm{b})}(\boldsymbol{Q},\boldsymbol{Q}',\nu) \quad = \quad \sum_{s\neq 0,\,i}^{s_\mathrm{max}} \delta_{\Gamma_0\Gamma_{s_+}} \frac{\Psi_s(\boldsymbol{Q})\Psi_s(\boldsymbol{Q}')}{\nu + E_0^{(0)} - E_s^{(0)}} \frac{(s_i+1)\varphi_{s_i+1}(Q_i)\varphi_{s_i+1}(Q'_i)}{\varphi_{s_i}(Q_i)\varphi_{s_i}(Q'_i)}, \tag{6.54}$$

in a recursive calculation. Here, Γ_s stands for the irreducible representation of the sth state and the s_+th state is the one obtained by incrementing s_i by one. Hence, $\delta_{\Gamma_0\Gamma_{s_+}}$ is unity, when the s_+th and zero-point states transform as the same (i.e., totally symmetric) irreducible representation; it is zero otherwise. This has the effect of compelling symmetrically zero integral contributions to be exactly zero rather than be merely convergent towards zero after a long MC run.

In a nonrecursive calculation, we instead use the Laplace-transformed expression, Eq. (6.44), in which we no longer have individual states to which irreducible representations can be assigned. We can nonetheless use the same symmetry logic with the following modified definition of $g_i^{(2\mathrm{b})}(\boldsymbol{Q},\boldsymbol{Q}',\tau)$:

$$g_i^{(2\mathrm{b})}(\boldsymbol{Q},\boldsymbol{Q}',\tau) \quad = \quad \frac{1}{h}\sum_{R=1}^{h}\left(\theta_i^R(Q_i,Q'_i,\tau)\prod_{j\neq i}^{M}\zeta_j^R(Q_j,Q'_j,\tau) - \{\chi_{\Gamma_i}(R)\}\Psi_0(\boldsymbol{Q})\Psi_0(\boldsymbol{Q}')\frac{\varphi_1(Q_i)\varphi_1(Q'_i)}{\varphi_0(Q_i)\varphi_0(Q'_i)}\right.$$

$$-\{\chi_{\Gamma_i}(R)\}^2\Psi_0(\boldsymbol{Q})\Psi_0(\boldsymbol{Q}')\times\frac{2\varphi_2(Q_i)\varphi_2(Q_i')}{\varphi_0(Q_i)\varphi_0(Q_i')}\,e^{-\omega_i\tau}\Bigg), \tag{6.55}$$

with

$$\zeta_i^R(Q_i,Q_i',\tau) = \sum_{s_i=0}^{n_{\max}}\{\chi_{\Gamma_i}(R)\}^{s_i}\varphi_{s_i}(Q_i)\varphi_{s_i}(Q_i')e^{-s_i\omega_i\tau}, \tag{6.56}$$

$$\begin{aligned}\theta_i^R(Q_i,Q_i',\tau) &= \sum_{s_i=0}^{n_{\max}-1}\{\chi_{\Gamma_i}(R)\}^{s_i+1}\varphi_{s_i+1}(Q_i)\varphi_{s_i+1}(Q_i')\\ &\quad\times(s_i+1)e^{-s_i\omega_i\tau}.\end{aligned} \tag{6.57}$$

where R is a symmetry operation, h is the order of the symmetry group, and $\chi_{\Gamma_i}(R)$ is the character ($+1$ or -1) of the irreducible representation Γ_i under operation R. The above equations can be derived from Eq. (6.54) using the identity:

$$\delta_{\Gamma_0\Gamma_s} = \frac{1}{h}\sum_R\prod_{i=1}^{M}\{\chi_{\Gamma_i}(R)\}^{s_i}. \tag{6.58}$$

Symmetry can be applied to all the other integrals analogously.

6.3.5 Redundant-walker algorithm

At minimum, we need one random-walking point (walker), $\boldsymbol{Q}_i$, in the M-dimensional space to evaluate Eq. (6.48) and two walkers, $\boldsymbol{Q}_i$ and $\boldsymbol{Q}_i'$, to evaluate Eq. (6.49).

However, propagating much more than these minimal numbers of walkers, we can increase the efficiency of the MC integrations by many orders of magnitude; this is called the redundant-walker algorithm.[46] The only changes we need to make to the formalism are in Eqs. (6.48) and (6.49), which now read

$$I_i = \frac{1}{N_{\rm w}}\sum_{j=1}^{N_{\rm w}}\frac{f(\boldsymbol{Q}_i^{[j]})}{w(\boldsymbol{Q}_i^{[j]})}, \tag{6.59}$$

for an M-dimensional integral, and

$$I_i = \frac{2}{N_{\rm w}(N_{\rm w}-1)}\sum_{j=1}^{N_{\rm w}-1}\sum_{k=j+1}^{N_{\rm w}}\frac{f(\boldsymbol{Q}_i^{[j]},\boldsymbol{Q}_i^{[k]})}{w(\boldsymbol{Q}_i^{[j]})w(\boldsymbol{Q}_i^{[k]})}, \tag{6.60}$$

for a $2M$-dimensional integral, where $N_{\rm w}$ is the number of walkers and $\boldsymbol{Q}_i^{[j]}$ is the jth walker coordinates in the ith MC step. Hence, propagating $N_{\rm w}$ walkers instead of just two at an extra cost of $O(N_{\rm w})$, we can increase the number of MC sampling points by $O(N_{\rm w}^2)$ in Eq. (6.60), providing net $O(N_{\rm w})$ enhancement of sampling efficiency.

The block length of the Flyvbjerg–Petersen method[118] is now $N_{\rm B}N_{\rm w}(N_{\rm w}-1)/2$. It thus increases with the number

of walkers, which is appropriate, considering the strong correlation of permutations of redundant walkers used in Eq. (6.60).

6.3.6 Frequencies and pole strengths

Given the self-energy evaluated as a function of frequency, it remains to solve Eq. (6.1) for self-consistent solutions. In our implementation, the self-energy is approximated by a function of the form,

$$\Sigma_i(\nu) \approx \Sigma_i^{(1)} + \Sigma_i^{(2\mathrm{p})} + \Sigma_i^{(2\mathrm{p}')} + c_1 + c_2\nu + \sum_{s=1}^{s_{\max}} d_N \left(\frac{1}{\nu - \Omega_s} + \frac{1}{-\nu - \Omega_s} \right), \tag{6.61}$$

with

$$\Omega_s = E_s^{(0)} - E_0^{(0)}, \tag{6.62}$$

where c_1, c_2, and $\{d_N\}$ are adjustable parameters determined by a weighted linear-least-squares fit to $\Sigma_i^{(2\mathrm{b})}(\nu) + \Sigma_i^{(2\mathrm{b}')}(\nu)$ at discrete values of ν. The weight is the reciprocal of its variance. We omitted '(ν)' from the first three terms of the right-hand side to highlight their invariance with ν. In practice, the summations can be truncated much earlier than $s = s_{\max}$. Once the continuous function $\Sigma_i(\nu)$ is obtained in this way, we can determine all roots using the bisection method described in Chapter 4.

The statistical uncertainty σ_i of $\Sigma_i(\nu_i)$ obtained by the least-squares fitting is calculated by

$$\begin{aligned} \sigma_i^2 = {} & \sigma_{(1)}^2 + \sigma_{(2\mathrm{p}'')}^2 + \mathrm{cov}_{c_1c_1} + 2\nu_i \,\mathrm{cov}_{c_1c_2} + \nu_i^2 \,\mathrm{cov}_{c_2c_2} \\ & + 2 \sum_{s=1}^{s_{\max}} (\mathrm{cov}_{c_1d_N} + \nu_i \,\mathrm{cov}_{c_2d_N}) \left(\frac{1}{\nu_i - \Omega_s} + \frac{1}{-\nu_i - \Omega_s} \right) \\ & + \sum_{s=1}^{s_{\max}} \sum_{s'=1}^{s_{\max}} \mathrm{cov}_{d_N d_{N'}} \left(\frac{1}{\nu_i - \Omega_s} + \frac{1}{-\nu_i - \Omega_s} \right) \left(\frac{1}{\nu_i - \Omega_{s'}} + \frac{1}{-\nu_i - \Omega_{s'}} \right), \end{aligned} \tag{6.63}$$

where cov denotes covariance, $\sigma_{(1)}$ and $\sigma_{(2\mathrm{p}'')}$ are the statistical uncertainties associated with $\Sigma_i^{(1)}$ and $\Sigma_i^{(2\mathrm{p})} + \Sigma_i^{(2\mathrm{p}')}$, respectively, and we have used the following formula for the propagation of uncertainty:

$$\sigma_f^2 = a^2\sigma_A^2 + b^2\sigma_B^2 + 2ab \,\mathrm{cov}_{AB}, \tag{6.64}$$

with $f = aA + bB$, where a and b are constants and A and B are variables. The statistical uncertainty of ν_i is

approximately equal to σ_i since, from a Taylor expansion of Eq. (6.1), we have

$$\nu_i \approx \omega_i + \Sigma_i(\nu_i). \tag{6.65}$$

The relative intensity of this transition is proportional to the pole strength given by

$$P_i = \omega_i \left\{ \nu_i - \omega_i \left. \frac{\partial \Sigma_i(\nu)}{\partial \nu} \right|_{\nu=\nu_i} \right\}^{-1}. \tag{6.66}$$

See Chapter 4 for its derivation. To estimate its statistical uncertainty σ_{P_i}, let us first consider the first derivative of $\Sigma_i(\nu)$ that enters the formula for P_i. For the interpolated $\Sigma_i(\nu)$ given in Eq. (6.61), its first derivative is written as

$$\frac{\partial \Sigma_i(\nu)}{\partial \nu} \approx c_2 + \sum_{s=1}^{s_{\max}} d_N \left\{ -\frac{1}{(\nu - \Omega_s)^2} + \frac{1}{(\nu + \Omega_s)^2} \right\}, \tag{6.67}$$

whose associated statistical uncertainty at $\nu = \nu_i$ is

$$\begin{aligned} \sigma^2_{\partial\Sigma/\partial\nu} \approx\ & \mathrm{cov}_{c_2 c_2} + 2 \sum_{s=1}^{s_{\max}} \mathrm{cov}_{c_2 d_N} \left\{ -\frac{1}{(\nu_i - \Omega_s)^2} + \frac{1}{(\nu_i + \Omega_s)^2} \right\} \\ & + \sum_{s=1}^{s_{\max}} \sum_{s'=1}^{s_{\max}} \mathrm{cov}_{d_N d_{N'}} \left\{ -\frac{1}{(\nu_i - \Omega_s)^2} + \frac{1}{(\nu_i + \Omega_s)^2} \right\} \left\{ -\frac{1}{(\nu_i - \Omega_{s'})^2} + \frac{1}{(\nu_i + \Omega_{s'})^2} \right\}, \end{aligned} \tag{6.68}$$

where we have used Eq. (6.64). Using this with another formula for the propagation of uncertainty,

$$\sigma_f^2 \approx f^2 \frac{\sigma_A^2}{A^2}, \tag{6.69}$$

with $f = a/A$, we find

$$\sigma^2_{P_i} \approx P_i^2 \left(\sigma_i^2 + \omega_i^2 \sigma^2_{\partial\Sigma/\partial\nu} \right) \left\{ \nu_i - \omega_i \left. \frac{\partial \Sigma_i(\nu)}{\partial \nu} \right|_{\nu=\nu_i} \right\}^{-2}. \tag{6.70}$$

The formulas described here for the statistical uncertainties assume that there is no covariance between $\Sigma_i^{(1)}$, $\Sigma_i^{(2\mathrm{p})} + \Sigma_i^{(2\mathrm{p}')}$, and $\Sigma_i^{(2\mathrm{b})}(\nu) + \Sigma_i^{(2\mathrm{b}')}(\nu)$ evaluated at various ν. In fact, the several terms in the self-energy are evaluated using the same random walk in a single MC-XVH2 or MC-XVMP2 calculation, as described in Sec. 6.3, and the covariances among them are thus nonzero in principle. Equations (6.63) and (6.70) are therefore approximate, especially for MC-XVH2(n) calculations, in which the contributions to the self-energy from all three terms are significant. However, we have found in Sec. 6.5 that these estimates are reasonable, tending only to slightly overestimate the errors of the anharmonic frequencies. The covariances between $\Sigma_i^{(2\mathrm{p})}$ and $\Sigma_i^{(2\mathrm{p}')}$ and between $\Sigma_i^{(2\mathrm{b})}(\nu)$ and $\Sigma_i^{(2\mathrm{b}')}(\nu)$ are automatically

accounted for because their sums are directly evaluated by MC integrations in our implementation.

6.4 Other Monte Carlo methods

MC-XVMP2(n), MC-XVMP2[n], and MC-XVH2(n) (collectively MC-XVMP2 in this section) introduced in this work have apparent similarities with DMC for vibrations, but they differ greatly in the theoretical underpinning and the quantities that are available from the respective calculations.

The mathematical basis of DMC is the isomorphism between the Schrödinger equation and the diffusion equation for the lowest, thus nodeless, vibrational wave function.[126] However, since one is usually interested in transition frequencies in a vibrational study, excited states need to be determined by DMC. In such calculations, an approximate nodal surface has to be assumed,[115,116] leading to the so-called fixed-node errors. Procedures exist for optimizing the nodal surface with a sufficiently simple functional form,[127] but finding the latter entails defining an appropriate set of nodal coordinates,[128] which is generally difficult. Although it has been shown[129] that multiple *rotational* states can be determined simultaneously by DMC, anharmonic vibrational states must usually be calculated separately and transition frequencies are then obtained as differences between large, noisy total energies. Such a procedure is not only cumbersome, but also easily plagued by large relative errors.

MC-XVMP2, in contrast, computes energy differences directly and simultaneously, which are anharmonic corrections to zero-point energies and to transition frequencies for all modes in a single MC run; they are *not* small differences of two total energies obtained in two separate MC runs. MC-XVMP2 does not require any user-specified constraints on wave functions, while potentially achieving an even greater degree of parallelism in their computational kernel than DMC (see below). On the other hand, one of the advantages of DMC over MC-XVMP2 is that it does not presume small anharmonicity and can perform for any type of bound PES's; MC-XVMP2 is effective when the anharmonicity is small enough to be considered as a perturbation.

A variant of DMC that can compute excited states and hence transition frequencies without an assumed nodal surface is the projection operator imaginary time spectral evolution (POITSE).[130,131] POITSE computes the autocorrelation functions of various projection operators during an ordinary DMC calculation of the ground state. An inverse Laplace transform is then performed numerically on these noisy functions, yielding a quantity analogous to the vibrational Green's function, from which the locations of its poles and thus anharmonic frequencies can be obtained. While mathematically elegant and exact, it has to perform the inverse Laplace transform numerically, which is known to be computationally ill-conditioned,[130,131] making the method's practical utility limited. MC-XVMP2, on the other hand, directly compute the self-energies (which are a factor of the exact Green's function) in the frequency domain[23,24] and the Laplace transform (when applicable) is carried out by a quadrature with no noticeable systematic or statistical

error.

There is also a difference in the parallel algorithm between DMC (including POITSE) and MC-XVMP2. In DMC, the number of walkers varies during the calculation and the algorithm must make sure to prevent many walkers from "dying" at once; otherwise many processors suddenly go idle. The most common technique for this prevention requires the current best estimate of the energy to be distributed to all processors, which involves frequent all-to-all inter-processor communications and thus constitutes a bottleneck for parallel scalability.[132] In MC-XVMP2, this bottleneck does not exist because the number of (redundant) walkers is constant and no inter-processor communication is strictly required. MC integrations on different processors can be performed, in principle, completely independently and asynchronously; they can be paused and restarted at any time after the equilibration stage and some can even be allowed to halt without a catastrophic failure of the whole calculation.

The correlation function quantum Monte Carlo (CFQMC) method[133,134] is another MC method for excited states that can compute vibrational frequencies directly. It propagates a set of basis functions in imaginary time, yielding a new set with progressively more accurate eigenvalues for some lowest-lying states. It may be viewed as an MC implementation of a subspace diagonalization of the Hamiltonian matrix. The main drawback of this method seems to be the exponential growth of the statistical errors in excited-state results with imaginary time.[133] Even for semi-rigid molecules like formaldehyde, therefore, the use of initial basis functions that are already close to the exact excited-state wave functions is necessary.[134]

The most closely related to our proposed methods are the stochastic algorithms of SCP (Refs. 93, 113, 114) and of VCI with an SCP reference wave function[119] reported recently, in which high-dimensional integrals appearing in their formalisms are evaluated by MC methods. In Chapter 5, the development of a stochastic algorithm of XVSCF,[21] which is related to SCP, was described, which, when combined with MC-XVMP2, makes the whole anharmonic vibrational analysis proceed without evaluating any anharmonic force constant. Our methods have been inspired by the recent studies that aim at combining *ab initio* electron-correlation methods with QMC conducted in our laboratory[44–48] and elsewhere.[49,50,52,54,135–139]

6.5 Results and discussion

6.5.1 Computational details

Here, we report the results of 12 different types of stochastic calculations for anharmonic zero-point energy and transition frequencies of the water molecule: MC-XVH2(n), MC-XVMP2(n), and MC-XVMP2[n] using either the direct or indirect evaluation of the PES, seeking solutions of either the recursive or nonrecursive inverse Dyson equation. MC-XVH2(n), MC-XVMP2(n), and MC-XVMP2[n] are respectively based on the harmonic, XVSCF(4), and XVSCF[4]

reference wave functions.[21] These reference wave functions are obtained by their deterministic algorithms using a QFF calculated at the MP2/aug-cc-pVTZ electronic structure theory.

In the indirect calculations, the same QFF precalculated and stored is used throughout. The corresponding methods are designated as MC-XVH2(4), MC-XVMP2(4), and MC-XVMP2[4] and are expected to reproduce the numerical results of their deterministic counterparts of Chapter 4, i.e., XVH2(4), XVMP2(4), and XVMP2[4]. The direct calculations, on the other hand, evaluate the PES at random geometries on demand. They are denoted by MC-XVH2(∞), MC-XVMP2(∞), and MC-XVMP2[∞], reflecting the fact that the highest order of the force constants included implicitly is undefined, though the reference wave function methods still use the QFF. In the latter, the first-order corrections are nonzero and need to be evaluated, as discussed in Sec. 6.2.5.

In the nonrecursive calculations, the right-hand side of Eq. (6.3) is evaluated just once for each mode, giving the frequencies of the fundamental transitions and no pole strengths, but using the Laplace-transformed expressions of integrands such as Eq. (6.44). We set $n_{\max} = 8$, meaning that the effect of 24th-order force constants can in principle be included when the PES evaluation is direct. The zero-point energy calculations can always invoke the Laplace-transformed expressions (if applicable).

In the recursive calculations, Eq. (6.1) is solved using the more elaborate algorithm described in detail in Sec. 6.3.6 for frequencies of the fundamentals and overtones as well as their associated pole strengths. In this case, the sum-over-states expression must be used for $\Sigma_i^{(2b)}$ and $\Sigma_i^{(2b')}$ by evaluating Eq. (6.43) taking into account the states that can be reached by a QFF operator from the reference wave function, i.e., up to quadruply excited states (all the other integrands can still use the Laplace-transformed expressions to benefit from the inclusion of higher-order force constants).

We use the redundant-walker algorithm described in Sec. 6.3.5 with the number of walkers (N_w) equal to 20. The block length (N_B) of the Flyvbjerg–Petersen method[118] is chosen to be 75. These calculations are parallel executed with up to 9 processors using NWCHEM (Ref. 82) as the back-end electronic structure software for the on-the-fly PES evaluations.

The purpose of these calculations is primarily to establish the feasibility and accuracy of these new stochastic methods and their algorithmic behavior. The overall speed of these calculations excluding the PES evaluation step is many orders of magnitude slower than the deterministic counterpart for small molecules such as water. As mentioned above, the total performance of these methods relies more heavily on the efficiency of the Metropolis sampling of the PES, which is, in turn, determined largely by the characteristics of the PES itself and the weight function. This requires a separate systematic study covering a broad range of systems.

6.5.2 Weight functions

First, we assess the performance of the weight functions, $w(\boldsymbol{Q})$ and $w(\boldsymbol{Q})w(\boldsymbol{Q}')$ given by Eq. (6.53), by analyzing the results of the indirect MC-XVH2(4) calculations as a function of scaling parameter α. The smaller the value of α is, the more diffuse the weight function is. The anharmonic correction to the zero-point energy and associated statistical uncertainty are plotted as a function of the MC steps (N) up to $N = 5 \times 10^4$ (corresponding to *ca.* 5×10^5 PES evaluations) in Figs. 6.7 and 6.8.

The zero-point energies of MC-XVH2(4) converge towards the correct limit obtained by the deterministic XVH2(4) calculation for all values of α studied; there seems no systematic bias in the limit, with the weight function merely affecting the rate of convergence. The statistical uncertainty does depend strongly on α. With $\alpha = 0.7$ or 0.9, the plots in Fig. 6.8 display characteristic spikes on otherwise $O(N^{-1/2})$ decay, including one particularly extreme spike for $\alpha = 0.7$ near $N = 10000$. These spikes occur because Eq. (6.48) or (6.49) is experiencing "division by (near) zero" at these geometries, which, in turn, means that the weight function is decaying too fast as compared with the integrand, causing severe under-sampling. This is why they are more prevalent with greater values of α.

The statistical uncertainties with $\alpha = 0.1$ and 0.5 exhibit smooth and nearly overlapping $O(N^{-1/2})$ decay, but they are roughly twice as large as the statistical uncertainties with $\alpha = 0.3$. This means that the weight functions with $\alpha = 0.1$ and 0.5 are slightly over-sampling and under-sampling, respectively. The weight function with $\alpha = 0.3$ seems to strike a near-optimal balance.

6.5.3 Nonrecursive inverse Dyson equation

Table 6.1 lists the results of the nonrecursive calculations that evaluate Eq. (6.3).

The results of the indirect MC-XVH2(4), MC-XVMP2(4), and MC-XVMP2[4] calculations that use the precalculated QFF reproduce the corresponding results of the deterministic XVH2(4), XVMP2(4), and XVMP2[4] calculations at $N = 67500$ (*ca.* 7×10^5 PES evaluations). In all cases, the stochastic results are within a few cm^{-1} of the correct limits and these errors are also accurately estimated as the statistical uncertainties. The first-order corrections to the zero-point energy in MC-XVMP2(4) and MC-XVMP2[4] are zero to within the statistical uncertainties, as they should be.

MC-XVH2(∞), MC-XVMP2(∞), and MC-XVMP2[∞] perform on-the-fly PES evaluations in each MC step. They do not reproduce the deterministic results as they include the effect of higher-than-quartic force constants implicitly. The first-order corrections to the zero-point energy in MC-XVMP2(∞) and MC-XVMP2[∞] are no longer zero for the same reason. According to these calculations, the fifth- and higher-order force constants tend to decrease the first-order correction to the zero-point energy, to increase the second-order correction thereto, and to overall reduce the total zero-point energy by ≈ 20 cm^{-1}. Such information is exceedingly difficult to obtain by force-constant-based

methods.

The statistical uncertainties of the anharmonic frequencies are greater than those of the zero-point corrections because the integrands for the frequencies involve modals with higher quantum numbers and are more rapidly oscillating. The uncertainties of the stretching frequencies in MC-XVH2(4) and MC-XVMP2(4) also appear to be slightly overestimated, possibly due to approximations we make in evaluating these uncertainties, which are discussed in Sec. 6.3.6. However, like the zero-point energy, the statistical uncertainties of the frequencies decrease as $O(N^{-1/2})$. To reduce the uncertainties to within 1 cm^{-1} would require approximately 2×10^6 MC steps or 2×10^7 PES evaluations. Overall, the rate of convergence seems considerably faster than that in the similar method for electrons,[44] which may be ascribed to the absence of singularities in the integrands in vibrational problems.

Each of the direct calculations takes $\approx 10^7$ CPU seconds to spread across 9 processors, of which 97% is consumed by 7×10^5 electronic structure calculations at the MP2/aug-cc-pVTZ level. The overall efficiency of these calculations is greater when the proportion of the time spent by the electronic structure calculations is higher. The efficiency is also greater when the rate of convergence is faster, as judged by the decay rate of the statistical uncertainties in Fig. 6.8. It is not meaningful to compare the speed of MC-XVMP2(∞) and XVMP2(n) as the former captures a greater degree of anharmonic effects.

6.5.4 Recursive inverse Dyson equation

Figures 6.9 and 6.10 show how well MC-XVH2(4) can reproduce the self-energy for mode one (symmetric stretch) of the water molecule as a function of frequency ν. The grey curves in Fig. 6.9 are the XVH2(4) results and the green dots in Figs. 6.9 and 6.10 plot the self-energies and statistical uncertainties of MC-XVH2(4), respectively, at a discrete set of frequencies. The green curves are analytic functions obtained by the linear-least-squares fitting procedure described in Sec. 6.3.6. It can be seen that this procedure works exceedingly well with the interpolated self-energy being indistinguishable from the XVH2(4) results.

The self-energy is divergent at 1628, 3257, and 4885 cm^{-1} in the frequency domain of Fig. 6.9, corresponding to the bending fundamental (ω_2) and first and second bending overtones ($2\omega_2$ and $3\omega_2$) in the harmonic approximation (which is the reference method for XVH2). Owing to these poles, there are four roots to the recursive inverse Dyson equation of XVH2(4) in this frequency domain, only two of which have non-negligible pole strengths and thus are physically meaningful. They are the symmetric stretch fundamental (ν_1) at 3633 cm^{-1} and the first bending overtone ($2\nu_2$) at 3238 cm^{-1} with pole strengths of 0.983 and 0.051, respectively. In Fig. 6.10, the statistical uncertainty is nearly constant at 4 cm^{-1} except at these poles, where it shoots up.

Figure 6.11 illustrates these two roots of the inverse Dyson equation graphically in the salient frequency domain. They occur at the intersections (the red circles) of two curves: the left- and right-hand sides of the square root of the

inverse Dyson equation [Eq. (6.1)] drawn as the blue line and green curves, respectively. Remarkably, MC-XVH2(4) can reproduce the positions of these roots within 2 cm^{-1}. The statistical uncertainties of these frequencies are the same as those of the self-energies and they are 4.1 cm^{-1} in ν_1 and 8.7 cm^{-1} in $2\nu_2$. The latter is much greater than the others because the $2\nu_2$ root is close to the pole at $2\omega_2$. However, it is likely overestimated, considering the insensitivity of the root location of $2\nu_2$ with the vertical placement of the self-energy curve there.

The results of the direct and indirect MC-XVH2 and MC-XVMP2 calculations for the solutions of the recursive inverse Dyson equation are compiled in Table 6.2. The indirect calculations using the same QFF as the deterministic algorithms should reproduce the results (both frequencies and pole strengths) of the latter and they do so within no more than twice the corresponding statistical uncertainties, although the statistical uncertainties of some anharmonic frequencies may be slightly overestimated for reasons mentioned above. We have thus shown that it is entirely possible to solve the recursive Dyson equation for multiple roots and pole strengths using a stochastic algorithm.

A comparison of Tables 6.1 and 6.2 indicates that the nonrecursive approximation of Eq. (6.3) causes errors up to *ca.* 40 cm^{-1} in the frequencies of the fundamentals. The nonrecursive calculations do not provide any information about overtones, combinations, resonances, or their pole strengths, either. They, however, dramatically simplify the computational procedure; in the recursive algorithm, MC integration needs to be performed at each of the green dots in Fig. 6.9 for the symmetric stretching mode and at a similar spread of points for other modes, whereas a single MC integration at $\nu = 0$ per mode suffices in the nonrecursive algorithm. This is the trade-off between the two algorithms.

Interestingly, ν_1 and ν_3 predicted by MC-XVH2(4) are in more accurate agreement with the observed than those obtained by MC-XVH2(∞), even though the latter takes into account higher-than-quartic force constants. This is fortuitous and likely caused by the accidental cancellation of errors between the higher-than-quartic force constants and the higher-than-second order perturbation corrections, both neglected by MC-XVH2(4). Note that the second-order vibrational perturbation method is known to yield exact results (accidentally) for a Morse oscillator with only cubic and quartic force constants.[106,109] Note also that MC-XVMP2 takes into account a certain class of higher-order perturbation corrections (relative to the harmonic reference wave function) all the way to an infinite order, which may explain why the same cancellation of errors is hardly seen in the MC-XVMP2 results. This underscores the importance of going beyond QFF, which is exceedingly difficult with theories or algorithms specifically designed for a certain fixed representation of a PES (such as a QFF), but is achieved readily by the direct MC-XVMP2 and MC-XVH2 methods.

6.6 Conclusion

In an anharmonic vibrational analysis of a molecule, it is often the evaluation and storage of all force constants up to the nth order that constitutes the computational bottleneck. Its operational and memory costs grow exponentially with n and as a high power of M (the vibrational degrees of freedom). Computer programs for this step require an exponentially increasing effort to write with n and also tend to be numerically unstable when they are based on finite-difference formulas as they usually are.

In this work, we have introduced the whole new algorithm of the diagrammatic second-order vibrational MBPT that eradicates the need for evaluating and storing force constants, leading to a highly scalable and easily implemented algorithm that can capture anharmonic effects due to higher-order force constants essentially up to an infinite order. This has been achieved by wedding XVMP2 (XVH2) with QMC, that is, by reformulating the energy and self-energy expressions of XVMP2 (XVH2) into sums of a few high-dimensional integrals that lend themselves to brute-force MC integrations with on-the-fly electronic structure calculations of a PES.

The resulting methods, MC-XVMP2 and MC-XVH2, can directly compute the zero-point energy and transition frequencies of not only fundamentals but also overtones as well as their relative intensities all from a single MC run and *not* as small differences of noisy total energies obtained from separate MC runs. They solve the recursive inverse Dyson equation stochastically. Unlike DMC, they neither require the knowledge of nodal surfaces of excited-state wave functions nor suffer from the resulting fixed-node errors. Furthermore, the zero-point energy and transition frequencies obtained by MC-XVMP2 (MC-XVH2) are rigorously size-extensive and intensive, respectively, as their mathematical definitions obey the extensive and intensive diagram theorems,[17] while including anharmonic effects of higher-order force constants not accessible by any force-constant-based methods.

We have applied MC-XVMP2 and MC-XVH2 to a small molecule to establish their feasibility and assess their performance. We plan to extend the applications to larger molecules, where these methods are expected to become superior to their deterministic counterparts.

6.7 Figures

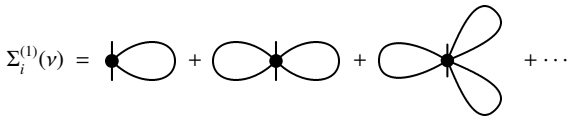

Figure 6.1: The first-order self-energy diagrams.

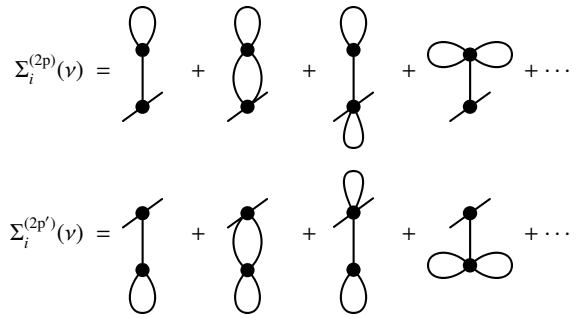

Figure 6.2: The second-order "pendant" self-energy diagrams.

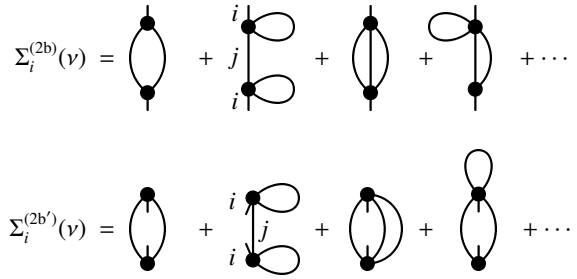

Figure 6.3: The second-order "bubble" self-energy diagrams. The diagrams with $i = j$ are reducible and excluded from the sums.

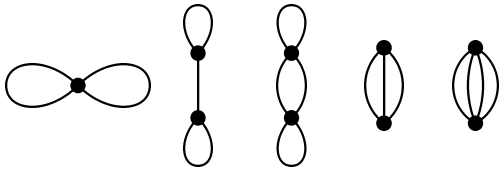

Figure 6.4: Examples of energy diagrams. From left to right, they correspond to the 1A, 2A, 2B, 2C, and 2D contributions.

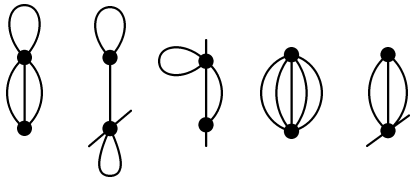

Figure 6.5: Examples of second-order diagrams with higher-order force constants included implicitly in a direct MC-XVMP2 calculation using a XVSCF(4) or XVSCF[4] reference wave function. They are also included in a direct MC-XVH2 calculation with a harmonic reference wave function.

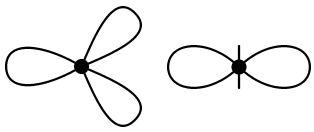

Figure 6.6: Examples of first-order diagrams with higher-order force constants included implicitly in a direct MC-XVMP1 calculation using a XVSCF(4) or XVSCF[4] reference wave function.

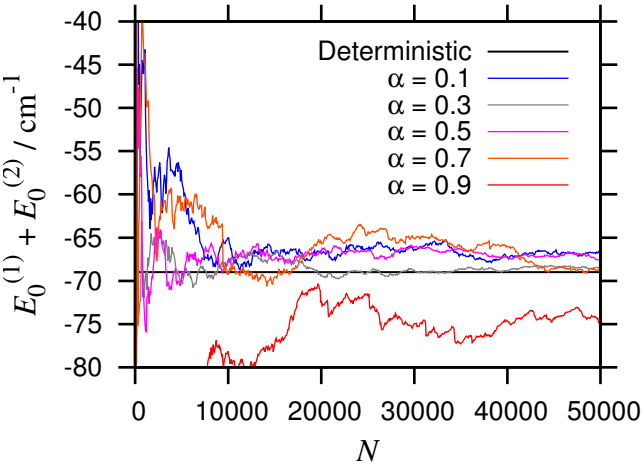

Figure 6.7: Convergence of the anharmonic correction to the zero-point energy of the water molecule obtained by indirect MC-XVH2(4) calculations with respect to the number of MC steps for a range of values of scaling parameter α in the weight functions.

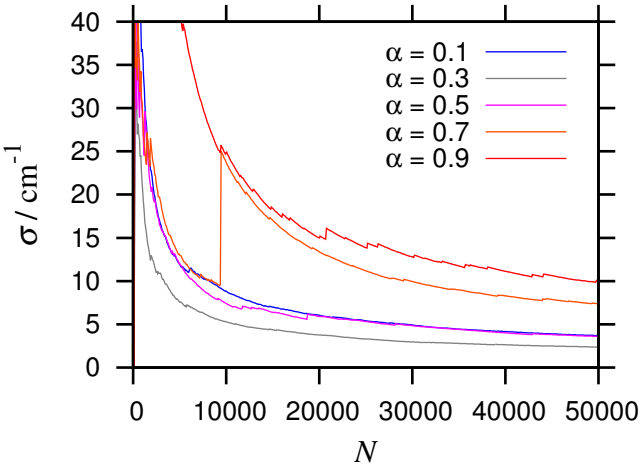

Figure 6.8: The same as Fig. 6.7, but for the statistical uncertainty.

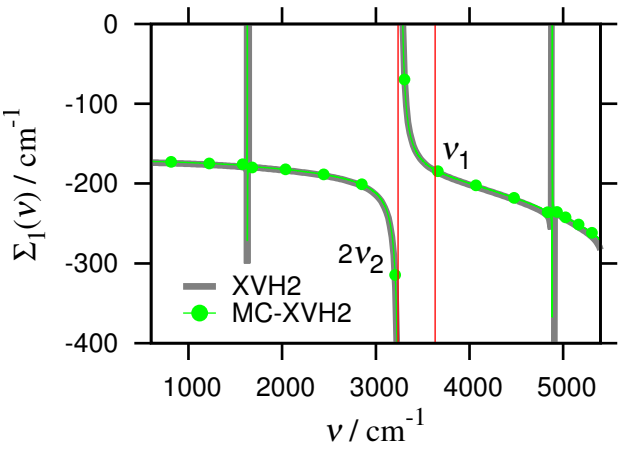

Figure 6.9: The self-energy of mode one (symmetric stretch) of the water molecule calculated by XVH2(4) and MC-XVH2(4) as a function of frequency ν. The green dots are the data obtained by MC-XVH2(4) at a discrete set of frequencies and the green curve is the linear-least-squares fit to these discrete data (see Sec. 6.3.6). The locations of two of the roots, corresponding to the symmetric stretching fundamental (ν_1) and the bending overtone ($2\nu_2$), are indicated by red lines.

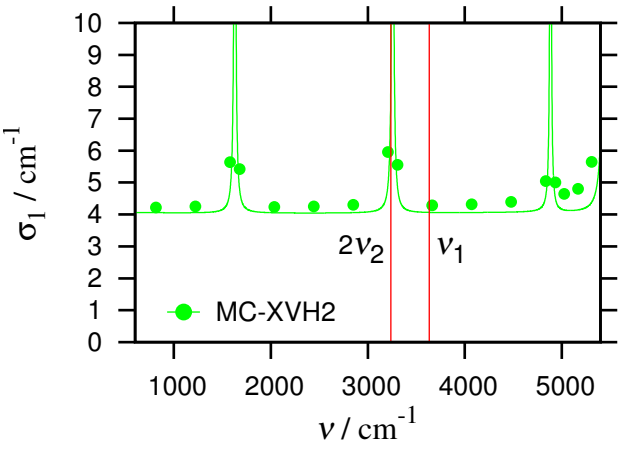

Figure 6.10: The same as Fig. 6.9, but for the statistical uncertainty of the self-energy.

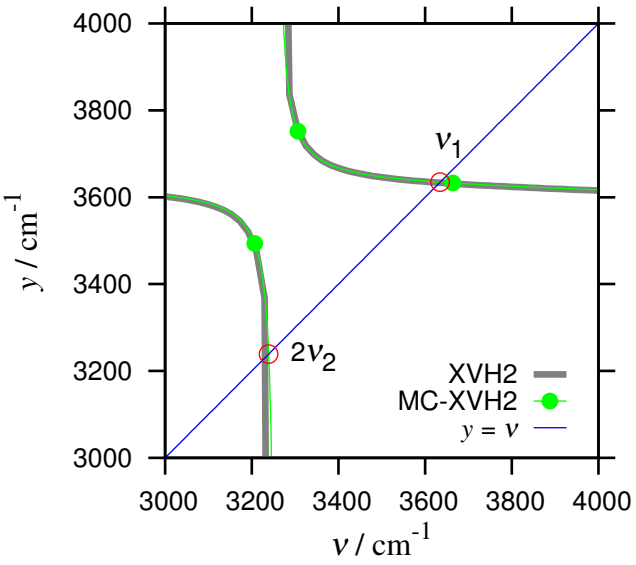

Figure 6.11: The left- and right-hand sides of the square root of the inverse Dyson equation (6.1) of mode one (symmetric stretch) as a function of frequency ν. The blue diagonal line is the left-hand side, $y = \nu$; the grey curve is the right-hand side, $y = \{\omega_1^2 + 2\omega_1\Sigma_1(\nu)\}^{1/2}$, calculated by XVH2(4); the green dots plot the right-hand side obtained by MC-XVH2(4); the green curve is the linear-least-squares fit to the green dots (see Sec. 6.3.6); the red circles indicate the locations of two of the roots, occurring at the intersections of the blue line and green curves.

6.8 Tables

Table 6.1: The first- and second-order anharmonic corrections to the zero-point energy ($E_0^{(1)}$ and $E_0^{(2)}$) and frequencies of the three fundamental transitions (ν_i) in cm^{-1} of the water molecule. The results of the stochastic calculations are obtained with $N = 67500$ solving the nonrecursive inverse Dyson equation, Eq. (3), with all integrands simplified with the Laplace transform ($n_{max} = 8$) and the weight function of Eq. (55) with $\alpha = 0.3$.

Method	$E_0^{(1)}$	$E_0^{(2)}$	ν_1	ν_2	ν_3
Experiment[a]	···	···	3657.1	1594.7	3755.9
Harmonic	±0	±0	3822.1	1628.3	3947.9
XVH2(4)[b]	+51.6	−120.6	3645.1	1566.9	3767.4
MC-XVH2(4)[b]	+51.3 ± 1.1	−119.1 ± 0.7	3646.9 ± 4.5	1566.3 ± 2.1	3768.5 ± 3.2
MC-XVH2(∞)[c]	+13.4 ± 1.0	−101.4 ± 0.6	3615.1 ± 4.3	1573.6 ± 2.1	3733.5 ± 3.2
XVMP2(4)[b]	+0.0	−100.1	3679.3	1561.9	3802.0
MC-XVMP2(4)[b]	−0.5 ± 1.1	−100.3 ± 0.5	3680.0 ± 3.8	1561.2 ± 1.8	3801.6 ± 2.6
MC-XVMP2(∞)[c]	−38.0 ± 1.0	−83.9 ± 0.4	3647.3 ± 3.6	1566.8 ± 1.7	3771.4 ± 2.5
XVMP2[4][b]	+0.0	−22.7	3686.2	1560.1	3807.6
MC-XVMP2[4][b]	+0.1 ± 0.7	−22.7 ± 0.2	3687.8 ± 1.8	1559.6 ± 1.1	3806.1 ± 1.8
MC-XVMP2[∞][c]	−17.7 ± 0.7	−25.9 ± 0.2	3656.0 ± 1.7	1568.1 ± 1.3	3771.8 ± 1.9

[a]Reference 140.

[b]Indirect calculations using a QFF.

[c]Direct calculations.

Table 6.2: The frequencies of the three fundamentals (ν_i) and one overtone ($2\nu_2 = \nu_4$) in cm^{-1} of the water molecule and their pole strengths (P_i). The results of the stochastic calculations are obtained with $N = 67500$ solving the recursive inverse Dyson equation (1) using the algorithm described in Appendix D. Only those integrands that can be simplified with the Laplace transform are so treated with $n_{max} = 8$ and the weight function of Eq. (55) with $\alpha = 0.3$.

Method	ν_1	ν_2	ν_3	$2\nu_2 \equiv \nu_4$	P_1	P_2	P_3	P_4
Experiment[a]	3657.1	1594.7	3755.9	3151.6	···	···	···	···
Harmonic	3822.1	1628.3	3947.9	3256.6	···	···	···	···
XVH2(4)[b]	3633.4	1565.6	3730.8	3238.3	0.983	1.038	1.031	0.051
MC-XVH2(4)[b]	3634.6 ± 4.1	1565.3 ± 1.7	3731.9 ± 2.7	3238.9 ± 8.7	0.985 ± 0.001	1.038 ± 0.001	1.031 ± 0.001	0.049 ± 0.001
MC-XVH2(∞)[c]	3610.3 ± 3.8	1573.5 ± 1.6	3693.2 ± 2.7	3230.2 ± 6.1	0.965 ± 0.001	1.032 ± 0.001	1.040 ± 0.001	0.076 ± 0.001
XVMP2(4)[b]	3668.1	1560.4	3770.7	3064.0	1.039	0.984	1.059	0.026
MC-XVMP2(4)[b]	3668.6 ± 3.5	1559.1 ± 1.4	3769.2 ± 2.3	3064.0 ± 9.4	1.039 ± 0.001	0.984 ± 0.001	1.060 ± 0.001	0.026 ± 0.000
MC-XVMP2(∞)[c]	3640.0 ± 3.3	1565.2 ± 1.3	3737.9 ± 2.2	3059.2 ± 7.2	1.037 ± 0.001	0.980 ± 0.001	1.067 ± 0.001	0.036 ± 0.000
XVMP2[4][b]	3667.6	1559.1	3774.5	3127.8	0.997	1.004	1.011	0.018
MC-XVMP2[4][b]	3668.5 ± 1.6	1557.5 ± 1.0	3772.5 ± 1.7	3127.8 ± 8.2	0.996 ± 0.001	1.005 ± 0.001	1.012 ± 0.000	0.018 ± 0.000
MC-XVMP2[∞][c]	3641.6 ± 1.5	1565.7 ± 1.1	3736.6 ± 1.7	3123.3 ± 6.5	0.994 ± 0.001	0.999 ± 0.001	1.020 ± 0.001	0.028 ± 0.000

[a]Reference 140.
[b]Indirect calculations using a QFF.
[c]Direct calculations.

Chapter 7

Conclusions

In Chapter 2, we presented our extension to the manifestly size-consistent XVSCF(n) method originally developed by Keçeli and Hirata,[21] enabling the former to calculate anharmonic corrections to molecular geometries as well as frequencies and total energies. XVSCF(n) with this extension is similar to the VSCF method, but not identical to it in the bulk limit. This is due to the fact that in the VSCF method, the anharmonic corrections to frequencies and geometries are coupled, whereas in the XVSCF(n) method, they are calculated separately. We also presented the formalism and implementation of the XVSCF[n] method, which calculates anharmonic corrections to frequencies and geometries simultaneously, thus recovering the identical bulk limit as the VSCF method at a fraction of the computational cost. We showed that for medium-size molecules, XVSCF(n) and XVSCF[n] are both in close agreement with VSCF for medium-size molecules, and XVSCF(n) is an efficient approximation to XVSCF[n].

In Chapter 3, we introduced the concepts of the Dyson coordinates and the Dyson geometry, vibrational analogues of the Dyson orbitals of electronic structure theory, by reformulating XVSCF(n) and XVSCF[n] in terms of the Dyson equation formalism for the single-particle vibrational Green's function. This connection also enabled us to compare XVSCF to the SCP method commonly used in solid-state physics. Test calculations on medium-size molecules showed that first-order Dyson coordinates are nearly parallel to normal coordinates, and XVSCF(n) and XVSCF[n] give results for anharmonic corrections to frequencies and energies in close agreement with SCP methods, despite being computationally cheaper.

In Chapter 4, we introduced diagrammatic second-order vibrational perturbation theories for anharmonic vibrations based on the Dyson equation formalism and using the harmonic approximation and XVSCF and SCP methods as references. We collectively named these methods XVMP2. They account for linked, open diagrammatic contributions to the Dyson self-energy and linked, closed contributions to the ZPE, ensuring size consistency for both total energies and frequencies. We showed that not only does XVMP2 calculate anharmonic frequencies directly, and in a much more efficient manner than the standard VMP2 method, it also is capable of calculating anharmonic frequencies subject to strong anharmonic resonance, such as overtones and combinations which are nearly degenerate with fundamental frequencies. This makes XVMP2 a rare example of a single-reference perturbation theory which is not necessarily defeated by strong correlation.

In Chapters 5 and 6, we formulated alternate algorithms for carrying out XVSCF and XVMP2 calculations which do not rely on the precalculation of large-dimensional arrays of high-rank force constants, and which formally account for up to infinite-order force constants by direct stochastic sampling of the PES. These MC-XVSCF and MC-XVMP2 algorithms resemble QMC methods such as DMC, but unlike the latter, they do not suffer from fixed-node errors and can compute anharmonic vibrational frequencies directly, without subtracting two noisy total energies calculated for separate vibrational states. We explored the quantitative effects of fifth- and higher-order force constants on the anharmonic frequencies and ZPE of the water molecule at the XVSCF and XVMP2 theoretical levels using direct MC-XVSCF and MC-XVMP2 calculations and quantified their effects.

Collectively, these developments represent significant progress for predictive computing of anharmonic vibrations of large molecules and solids. They directly address the two critical problems of size consistency and PES representation discussed at the beginning of this document, as manifestly size-consistent formalisms with much greater efficiency and theoretical power than common VSCF-based methods, and as algorithms which sidestep the difficult issue of PES storage though direct stochastic calculation.

References

[1] M. J. Bramley and T. J. Carrington. J. Chem. Phys. **99**, 8519 (1993).

[2] J. M. Bowman, T. Carrington, and H.-D. Meyer. Mol. Phys. **106**, 2145 (2008).

[3] L. Lodi and J. Tennyson. J. Phys. B: At. Mol. Opt. Phys. **43**, 133001 (2010).

[4] J. M. Bowman. J. Chem. Phys. **68**, 608 (1978).

[5] J. M. Bowman. Acc. Chem. Res. **19**, 202 (1986).

[6] M. A. Ratner and R. B. Gerber. J. Phys. Chem. **90**, 20 (1986).

[7] L. S. Norris, M. A. Ratner, A. E. Roitberg, and R. B. Gerber. J. Chem. Phys. **105**, 11261 (1996).

[8] O. Christiansen. J. Chem. Phys. **119**, 5773 (2003).

[9] K. Yagi, S. Hirata, and K. Hirao. J. Chem. Phys. **127**, 034111 (2007).

[10] A. Szabo and N. S. Ostlund. *Modern Quantum Chemistry: Introduction to Advanced Electronic Structure Theory* (Dover Publications, 1996).

[11] O. Christiansen. J. Chem. Phys. **120**, 2149 (2004).

[12] A. Zoccante, P. Seidler, and O. Christiansen. J. Chem. Phys. **134**, 154101 (2011).

[13] P. Seidler and O. Christiansen. J. Chem. Phys. **131**, 234109 (2009).

[14] P. Seidler, E. Matito, and O. Christiansen. J. Chem. Phys. **131**, 034115 (2009).

[15] P. Seidler, M. Sparta, and O. Christiansen. J. Chem. Phys. **134**, 054119 (2011).

[16] J. Bowman, K. Christoffel, and F. Tobin. J. Phys. Chem. **83**, 905 (1979).

[17] S. Hirata. Theor. Chem. Acc. **129**, 727 (2011).

[18] O. Christiansen. J. Chem. Phys. **120**, 2140 (2004).

[19] M. B. Hansen, M. Sparta, P. Seidler, D. Toffoli, and O. Christiansen. J. Chem. Theory Comput. **6**, 235 (2010).

[20] S. Hirata, M. Keçeli, and K. Yagi. J. Chem. Phys. **133**, 034109 (2010).

[21] M. Keçeli and S. Hirata. J. Chem. Phys. **135**, 134108 (2011).

[22] R. D. Mattuck. *A Guide to Feynman Diagrams in the Many-Body Problem* (Dover: New York, 1992).

[23] W. Jones and N. H. March. *Theoretical Solid State Physics* (Wiley, 1973).

[24] N. H. March, W. H. Young, and S. Sampanthar. *The Many-Body Problem in Quantum Mechanics* (Cambridge University Press, 1967).

[25] A. L. Fetter and J. D. Walecka. *Quantum Theory of Many-Particle Systems* (McGraw-Hill, New York, 1971, 1971).

[26] R. D. Mattuck. Ann. of Phys. **27**, 216 (1964).

[27] I. Shavitt and R. J. Bartlett. *Many-Body Methods in Chemistry and Physics: MBPT and Coupled-Cluster Theory* (Cambridge University Press, 2009).

[28] J. Goldstone. Proc. Roy. Soc. London A **239**, 267 (1957).

[29] S. Hirata, M. Keçeli, Y.-Y. Ohnishi, O. Sode, and K. Yagi. Annu. Rev. Phys. Chem. **63**, 131 (2012).

[30] M. R. Hermes, M. Keçeli, and S. Hirata. J. Chem. Phys. **136**, 234109 (2012).

[31] P. Choquard. *The Anharmonic Crystal* (W. A. Benjamin, Inc., 1967).

[32] N. S. Gillis, N. R. Werthamer, and T. R. Koehler. Phys. Rev. **165**, 951 (1968).

[33] J. V. Ortiz. Adv. Quantum Chem. **35**, 33 (1999).

[34] J. V. Ortiz. J. Chem. Phys. **104**, 7599 (1996).

[35] M. R. Hermes and S. Hirata. J. Phys. Chem. A **117**, 7179 (2013).

[36] M. R. Hermes and S. Hirata. J. Chem. Phys. **139**, 034111 (2013).

[37] M. R. Hermes and S. Hirata. J. Chem. Phys. **141**, 244111 (2014).

[38] M. R. Hermes and S. Hirata. J. Chem. Phys. **141**, 084105 (2014).

[39] N. Metropolis, A. W. Rosenbluth, M. N. Rosenbluth, A. H. Teller, and E. Teller. J. Chem. Phys. **21**, 1087 (1953).

[40] W. M. C. Foulkes, L. Mitas, R. J. Needs, and G. Rajagopal. Rev. Mod. Phys. **73**, 33 (2001).

[41] R. J. Needs, M. D. Towler, N. D. Drummond, and P. López Ríos. J. Phys.: Condens. Matter **22**, 023201 (2010).

[42] B. M. Austin, D. Y. Zubarev, and W. A. Lester Jr. Chem. Rev. **112**, 263 (2012).

[43] L. K. Wagner. Int. J. Quantum Chem. **114**, 94 (2014).

[44] S. Y. Willow, K. S. Kim, and S. Hirata. J. Chem. Phys. **137**, 204122 (2012).

[45] S. Y. Willow, K. S. Kim, and S. Hirata. J. Chem. Phys. **138**, 164111 (2013).

[46] S. Y. Willow, M. R. Hermes, K. S. Kim, and S. Hirata. J. Chem. Theory Comput. **9**, 4396 (2013).

[47] S. Y. Willow and S. Hirata. J. Chem. Phys. **140**, 024111 (2014).

[48] S. Y. Willow, J. Zhang, E. F. Valeev, and S. Hirata. J. Chem. Phys. **140**, 031101 (2014).

[49] A. Thom and A. Alavi. Phys. Rev. Lett. **99**, 143001 (2007).

[50] J. J. Shepherd, G. H. Booth, and A. Alavi. J. Chem. Phys. **136**, 244101 (2012).

[51] R. Baer, D. Neuhauser, and E. Rabani. Phys. Rev. Lett. **111**, 106402 (2013).

[52] S. Ten-no. J. Chem. Phys. **138**, 164126 (2013).

[53] D. Neuhauser, E. Rabani, and R. Baer. J. Phys. Chem. Lett. **4**, 1172 (2012).

[54] D. Neuhauser, E. Rabani, and R. Baer. J. Chem. Theory Comput. **9**, 24 (2013).

[55] Q. Ge, Y. Gao, R. Baer, E. Rabani, and D. Neuhauser. J. Phys. Chem. Lett. **5**, 185 (2014).

[56] J. K. G. Watson. Mol. Phys. **15**, 479 (1968).

[57] J. M. Bowman, S. Carter, and X. Huang. Int. Rev. Phys. Chem. **22**, 533 (2003).

[58] P. Carbonniere and V. Barone. Chem. Phys. Lett. **392**, 365 (2004).

[59] E. Mátyus, G. Czakó, B. T. Sutcliffe, and A. G. Császár. J. Chem. Phys. **127**, 084102 (2007).

[60] S. Hirata and M. R. Hermes. J. Chem. Phys. **141**, 184111 (2014).

[61] D. M. Benoit. J. Chem. Phys. **120**, 562 (2004).

[62] L. Pele and R. B. Gerber. J. Chem. Phys. **128**, 165105 (2008).

[63] T. K. Roy and M. D. Prasad. J. Chem. Sci. **121**, 805 (2009).

[64] E. Matito, D. Toffoli, and O. Christiansen. J. Chem. Phys. **130**, 134104 (2009).

[65] M. Born and K. Huang. *Dynamical Theory of Crystal Lattices* (Oxford University Press, New York, 1954).

[66] Y. Öhrn and J. V. Ortiz. Mol. Phys. **108**, 2871 (2010).

[67] V. G. Zakrzewski, O. Dolgounitcheva, A. V. Zakjevskii, and J. V. Ortiz. In J. R. Sabin and E. Brändas, editors, *Advances in Quantum Chemistry*, volume 62, chapter 3 (Elsevier Academic Press, 2011).

[68] N. Makri. J. Phys. Chem. B **103**, 2823 (1999).

[69] O. Christiansen. Phys. Chem. Chem. Phys. **9**, 2942 (2007).

[70] A. A. Maradudin and A. E. Fein. Phys. Rev. **128**, 2589 (1962).

[71] M. B. Hansen, O. Christiansen, D. Toffoli, and J. Kongsted. J. Chem. Phys. **128**, 174106 (2008).

[72] S. Saebø and P. Pulay. Chem. Phys. Lett. **113**, 13 (1985).

[73] V. P. Spiridonov, V. S. Lyutsarev, and B. S. Butayev. Chem. Phys. Lett. **110**, 32 (1984).

[74] K. V. Ermakov, B. S. Butayev, and V. P. Spiridonov. Chem. Phys. Lett. **144**, 497 (1988).

[75] D. Chandler. *Introduction to Modern Statistical Mechanics* (Oxford University Press, 1987).

[76] D. C. Wallace. *Thermodynamics of Crystals* (Wiley, New York, 1972).

[77] J. Cao and G. A. Voth. J. Chem. Phys. **102**, 3337 (1995).

[78] A. Suárez and R. Silbey. J. Chem. Phys. **95**, 9115 (1991).

[79] J. O. Jung and R. B. Gerber. J. Chem. Phys. **105**, 10332 (1996).

[80] S. Carter, S. J. Culik, and J. M. Bowman. J. Chem. Phys. **107**, 10458 (1997).

[81] K. Yagi. SINDO (The University of Tokyo, 2006).

[82] M. Valiev, E. J. Bylaska, N. Govind, K. Kowalski, T. P. Straatsma, H. J. J. Van Dam, D. Wang, J. Nieplocha, E. Apra, T. L. Windus, and W. A. de Jong. Comput. Phys. Commun. **181**, 1477 (2010).

[83] F. L. Tobin and J. M. Bowman. Chem. Phys. **47**, 151 (1980).

[84] B. T. Pickup and O. Goscinski. Mol. Phys. 37–41 (1973).

[85] J. Linderberg and Y. Öhrn. *Propagators in Quantum Chemistry* (Wiley, New York, 2004).

[86] R. A. Cowley. Adv. Phys. **12**, 421 (1963).

[87] A. A. Stuchebrukhov, M. V. Kuzmin, V. N. Bagratashvili, and V. S. Letokhov. Chem. Phys. **107**, 429 (1986).

[88] A. A. Stuchebrukhov. J. Mol. Struct. **178**, 261 (1988).

[89] D. J. Hooton. Philos. Mag. **4**, 49 (1958).

[90] T. R. Koehler. Phys. Rev. Lett. **17**, 89 (1966).

[91] T. Luty. J. Chem. Phys. **75**, 1451 (1981).

[92] L. B. Spornick, R. L. Danilowicz, A. A. Helmy, and R. D. Etters. Journal of Chemical Physics **84**, 2310 (1986).

[93] F. Calvo, P. Parneix, and N.-T. Van-Oanh. J. Chem. Phys. **133**, 074303 (2010).

[94] I. Georgescu and V. A. Mandelshtam. J. Chem. Phys. **137**, 144106 (2012).

[95] J. B. Foresman, M. Head-Gordon, J. A. Pople, and M. J. Frisch. J. Phys. Chem. **96**, 135 (1992).

[96] R. D. Amos, N. C. Handy, W. H. Green, D. Jayatilaka, A. Willetts, and P. Palmieri. J. Chem. Phys. **95**, 8323 (1991).

[97] K. Yagi, S. Hirata, and K. Hirao. Phys. Chem. Chem. Phys. **10**, 1781 (2008).

[98] M. V. Kuzmin and A. A. Stuchebrukhov. Chem. Phys. Lett. **119**, 556 (1985).

[99] O. V. Boyarkin, S. I. Ionov, A. A. Stuchebrukhov, V. N. Bagratashvili, and M. S. Djidjoev. J. Phys. Chem. **94**, 1294 (1990).

[100] V. V. Goldman, G. K. Horton, and M. Klein. Phys. Rev. Lett. **21**, 1527 (1968).

[101] T. R. Koehler. Phys. Rev. Lett. **22**, 777 (1969).

[102] J. M. L. Martin, T. J. Lee, P. R. Taylor, and J.-P. Francois. J. Chem. Phys. **103**, 2589 (1995).

[103] V. Barone and C. Minichino. J. Mol. Struct.: THEOCHEM **330**, 365 (1995).

[104] V. Barone. J. Chem. Phys. **120**, 3059 (2004).

[105] V. Barone. J. Chem. Phys. **122**, 14108 (2005).

[106] D. A. Matthews, J. Vázquez, and J. F. Stanton. Mol. Phys. **105**, 2659 (2007).

[107] J. Vázquez and J. F. Stanton. Mol. Phys. **105**, 101 (2007).

[108] D. Matthews and J. F. Stanton. Mol. Phys. **107**, 213 (2009).

[109] I. Mills and A. Robiette. Mol. Phys. **56**, 743 (1985).

[110] J. Oddershede, P. Jørgensen, and N. H. F. Beebe. Int. J. Quantum Chem. **12**, 655 (1977).

[111] S. R. Gwaltney, M. Nooijen, and R. J. Bartlett. Chem. Phys. Lett. **248**, 189 (1996).

[112] M. Keçeli. MAVI (University of Illinois at Urbana-Champaign, 2011).

[113] S. E. Brown, I. Georgescu, and V. A. Mandelshtam. J. Chem. Phys. **138**, 044317 (2013).

[114] I. Errea, M. Calandra, and F. Mauri. Phys. Rev. B **89**, 064302 (2014).

[115] A. B. McCoy. Int. Rev. Phys. Chem. **25**, 77 (2006).

[116] A. B. McCoy. In J. B. Anderson and S. M. Rothstein, editors, *Advances in Quantum Monte Carlo*, volume 953, chapter 11 (American Chemical Society, 2007).

[117] J. H. Halton. SIAM Rev. **12**, 1 (1970).

[118] H. Flyvbjerg and H. G. Petersen. J. Chem. Phys. **91**, 461 (1989).

[119] I. Georgescu, S. Jitomirskaya, and V. A. Mandelshtam. J. Chem. Phys. **139**, 204104 (2013).

[120] R. C. Grimm and R. G. Storer. J. Comput. Phys. **56**, 134 (1971).

[121] P. Pulay. Adv. Chem. Phys. **69**, 241 (1987).

[122] K. Yagi, K. Hirao, T. Taketsugu, M. W. Schmidt, and M. S. Gordon. J. Chem. Phys. **121**, 1383 (2004).

[123] R. J. Bartlett. Annu. Rev. Phys. Chem. **32**, 359 (1981).

[124] S. Hirata, X. He, M. R. Hermes, and S. Y. Willow. J. Phys. Chem. A **118**, 655 (2014).

[125] A. S. Kronrod. *Nodes and Weights of Quadrature Formulas: Sixteen-Place Tables* (Consultants Bureau, New York, 1965).

[126] J. B. Anderson. J. Chem. Phys. **63**, 1499 (1975).

[127] H.-S. Lee, J. M. Herbert, and A. B. McCoy. J. Chem. Phys. **110**, 5481 (1999).

[128] A. S. Petit and A. B. McCoy. J. Phys. Chem. A **117**, 7009 (2013).

[129] A. S. Petit, J. E. Ford, and A. B. McCoy. J. Phys. Chem. A **118**, 7206 (2014).

[130] D. Blume, M. Lewerenz, and K. B. Whaley. J. Chem. Phys. **107**, 9067 (1997).

[131] D. Blume, M. Lewerenz, P. Niyaz, and K. B. Whaley. Phys. Rev. E **55**, 3664 (1997).

[132] J. T. Krogel and D. M. Ceperley. In S. Tanaka, S. M. Rothstein, and W. A. Lester Jr., editors, *Advances in Quantum Monte Carlo*, volume 1094, chapter 2 (American Chemical Society, 2012).

[133] D. M. Ceperley and B. Bernu. J. Chem. Phys. **89**, 6316 (1988).

[134] B. Bernu, D. M. Ceperley, and W. A. Lester Jr. J. Chem. Phys. **93**, 552 (1990).

[135] R. Baer, M. Head-Gordon, and D. Neuhauser. J. Chem. Phys. **109**, 6219 (1998).

[136] S. Zhang and H. Krakauer. Phys. Rev. Lett. **90**, 136401 (2003).

[137] Y. Ohtsuka and S. Nagase. Chem. Phys. Lett. **463**, 431 (2008).

[138] G. H. Booth, A. J. W. Thom, and A. Alavi. J. Chem. Phys. **131**, 054106 (2009).

[139] D. Cleland, G. H. Booth, and A. Alavi. J. Chem. Phys. **132**, 041103 (2010).

[140] J. Tennyson, N. F. Zobov, R. Williamson, O. L. Polyansky, and P. F. Bernath. J. Phys. Chem. Ref. Data **30**, 735 (2001).